UNIVERSITY OF SURREY

Characterisation of cement microstructure and pore – water interaction by ^{1}H Nuclear Magnetic Resonance Relaxometry

by

Agata M. Gajewicz

Submitted for the degree of Doctor of Philosophy

Department of Physics

Faculty of Engineering and Physical Sciences

University of Surrey

2014

Abstract

^{1}H nuclear magnetic resonance (NMR) relaxometry is used to characterise cement paste microstructure from the stand point of the pore water. Attention focuses primarily on pore-water interactions and the morphology of calcium-silicate-hydrate (C-S-H), the active phase of cement paste. The method is non-destructive and non-invasive.

NMR allows the quantitative separation of water by confinement. The first pore-type resolved sorption isotherm of any cementitious material is measured. This provides insight into water location during drying and wetting. The C-S-H interlayer and gel pore sizes are estimated based on T_2 relaxation times (0.94 ± 0.04 and 3.1 ± 0.2 nm) and amplitudes of relaxation components during drying (1.5 ± 0.3 and 4.5 ± 1.6 nm). The specific surface areas are also evaluated.

The evolution of nanoscale porosity for underwater cured white cement pastes, with and without silica fume addition, are determined during hydration and as a function of temperature in the range 10°C to 60°C.

The C-S-H density and chemical composition are evaluated using NMR supported by X-ray diffraction and thermogravimetric analysis. The calculated C-S-H 'solid' density and composition, excluding gel pore water, in never-dried 28 days old white cement paste are 2.64 ± 0.03 g/cm^3 and $Ca_{1.53 \pm 0.02}(Si_{0.96 \pm 0.01}, Al_{0.04 \mp 0.01})O_{3.51 \pm 0.02}(H_2O)_{1.92 \pm 0.05}$. The C-S-H 'bulk' density, including gel pore water, is 1.90 ± 0.02 g/cm^3. Increase of curing temperature does not alter the Ca/(Si+Al) ratio. However, a significant decrease in C-S-H water content and increase in density is observed and attributed to the fewer locally stacked C-S-H layers.

NMR relaxation activation energies are estimated.

Insight into the mechanism of water-isopropanol exchange, used for arresting cement hydration, is provided. NMR shows that the exchange occurs in a selective manner with no C-S-H interlayer water alteration. The connectivity of the C-S-H interlayer and gel pores with interhydrate-capillary pores is evidenced.

Declaration of originality

This thesis and the work to which it refers are the results of my own efforts. Any ideas, data, images or text resulting from the work of others (whether published or unpublished) are fully identified as such within the work and attributed to their originator in the text, bibliography or in footnotes. This thesis has not been submitted in whole or in part for any other academic degree or professional qualification.

I agree that the University has the right to submit my work to the plagiarism detection service TurnitinUK for originality checks. Whether or not drafts have been so-assessed, the University reserves the right to require an electronic version of the final document (as submitted) for assessment as above.

Acknowledgements

The completion of this thesis would not be possible without help and support of several people to whom I am extremely grateful.

Foremost I extend my gratitude to my supervisor Professor Peter McDonald for his important guidance throughout this thesis, continuous support, thoughtful advice, enthusiasm and warm encouragement.

My warmest thanks also go to Doctor Radoslaw Kowalczyk for his insightful suggestions, interesting, very often exciting, discussions and sharing NMR experience with me. I am also grateful to Mr Bob Derham for his helpful hand in NMR laboratories and to Mrs Violeta Doukova for her kind support with thermogravimetric analysis. Thank you all for sharing time with me and friendly words.

I am truly grateful for the opportunity to meet the professors, researches, fellows and PhD students in the Nanocem consortium who were kind enough to share the expertise and knowledge with me.

I would also like to thank my PhD friends from Transcend project for many good times when we discussed science and when we had fun. It was great to be surrounded during the course of the project by people whose company I enjoyed very much and as such made the whole experience very positive and pleasurable.

The very special thanks go to Doctor Marek Petri and my friends, Kasia and Mikolaj; without them this journey would never have started. Thank you for your support and encouragement.

I also wish to express my gratitude to my family for love, support and care. They always believed in me even when I doubted myself.

The last, but certainly not least, I owe by loving thanks to my boyfriend Borys who was always supportive, motivating and patient. He helped me to persist through the hardest times of the PhD.

I would like to acknowledge the sponsorship from European Commission for Marie-Curie Initial Training Network Transcend 'The Understanding TRANSport for Concrete which is Eco friendly, iNnovative and Durable' (EP7/2007-2013).

Contents

Abbreviations and symbols

AFt	Ettringite – calcium sulfoaluminate
AFm	Calcium monosulfoaluminate
AMU	Atomic mass unit
BPP	Bloembergen, Purcell, Pound
BSE	Backscattered Electrons
CH	Calcium Hydroxide (Portlandite)
CPMG	Carr-Purcell-Meiboom-Gill
C-S-H	Calcium – Silicate – Hydrate
FID	Free Induction Decay
Hyd	Hydrogen
Hz	Hertz
ILT	Inverse Laplace Transform
LTC	Low Temperature Calorimetry
MIP	Mercury Intrusion Porosimetry
NMR	Nuclear Magnetic Resonance
QE	Quadrature (Quad, Solid) Echo
P_{90}	90 degree pulse
P_{180}	180 degree pulse
RH, φ	Relative humidity
SANS	Small Angle Neutron Scattering
SAXS	Small Angle X-ray Scattering
SEM	Scanning Electron Microscopy
SF	Silica Fume
SSA	Specific surface area
TEM	Transmission Electron Microscopy
TGA	Thermogravimetric Analysis
XRD	X-ray diffraction
A_{CSH}	Specific surface area of C-S-H interlayer pores per unit volume of paste
A_{gel}	Specific surface area of C-S-H gel pores per unit volume of paste
A_m	Cross section area of gas molecule
B_o	Static magnetic field
B_1	Oscillating magnetic field
c	Cement mass
d	Pore size
d_{wat}	Size of water molecule
D	Diffusion coefficient
E	Energy
E_A	Activation energy
f	Mass fraction of particular phase
G	Magnetic field gradient strength
$G^{(m)}$	Autocorrelation functions
$\hbar$	Planck constant divided by 2π
I	NMR Intensity
I	Spin quantum number
I_{SAS}	Small Angle Scattering Intensity
J	Spectral density function
k_B	Boltzmann constant
m	Mass
M	Magnetization
M^o	Magnetisation at equilibrium state
n	Molar content
p	Pressure
Q	Scattering vector
r	Radius
r_K	Kelvin radius
R	Universal gas constant
S	Surface area
S/N	Signal to noise ratio
t	Time
t_θ	Duration of excitation pulse
t_{nf}	Thickness of non-freezable layer of adsorbed water
T	Temperature
T_1	Spin-lattice relaxation time
T_2	Spin-spin relaxation time
u_m	Gas amount corresponding to monolayer coverage of surface
V	Volume
V_p	Volume of paste
V_{wp}	Volume of water in unit volume of paste
w	Water mass

w/b	Water to binder mass ratio
w/c	Water to cement mass ratio
w/c_{mix}	Water to cement mass ratio at mixing time
x	Water fraction of C-S-H
x'	Water fraction for fully saturated C-S-H gel (C-S-H and gel water)
y	Silicon fraction of C-S-H
z	Calcium fraction of C-S-H
α	Degree of hydration
α'	Mass of reacted C_3S and C_2S divided by mass of anhydrous cement
α_R	Regularisation parameter for ILT
$\beta_{CH,\,Ett}$	Reciprocal water mass fraction of Portlandite and ettringite
γ	Gyromagnetic ratio
γ_{CSH}	Reciprocal water mass fraction of C-S-H
γ_S	Surface tension
δ	Minimum distance for water molecule to approach impurity
δ_w	Reciprocal water mass fraction of pore fluid
ΔH_{fus}	Heat of fusion
$\lvert\Delta\rho_{SAS}\rvert^2$	Scattering contrast
ε	Surface layer thickness
θ	Angle of magnetization rotation
θ_c	Contact angle
θ_i	Angle of incidence
θ_{SAS}	Angle of small angle scattering
λ	Wavelength / Surface relaxivity
μ	Magnetic moment
μ_o	Vacuum permeability
υ	Frequency
ρ	Density
σ	Gaussian width
σ_S	Surface density of paramagnetic impurities
τ	Pulse gap
τ_c	Correlation time
τ_m	Correlation time associated with molecule's jumps across the surface (hopping time)
τ_{rd}	Repetition time
τ_s	Surface residency time
φ	Relative humidity
ω	Circular angular frequency
ω_o	Larmor frequency

List of tables

List of figures

"People need not fear the unknown because
they are capable of achieving what they need and want"

Paulo Coelho

Challenges have accompanied science and technology for millennia. Without them it would not be possible to achieve any progress. It is thanks to the will of learning and the perseverance in understanding the rules and laws responsible for various processes, that the enormous progress in building materials technology have been possible.

However, as time passes new questions, concerns and tasks appear, driving scientists to face them and resolve.

1. Introduction

1.1. Motivation to study cement

Concrete is a building material. Nowadays it is the most manufactured man-made material world wide with almost three tons used for each human annually [1]. It has become a crucial part of our everyday life as it is used in the majority of buildings and in many other infrastructural applications. The reasons for the large, and still increasing, consumption of concrete are various. First, concrete is unrivalled in terms of price per ton (fig. 1.1). It benefits as it is easy to make and can be formed in nearly any shape [2]. The energy consumed to produce one tonne of concrete is much less than for other building material – fig. 1.2 left. Other significant properties factors in favour of concrete are durability, strength and water-tightness [1].

Concrete is composed of anhydrous cement powder, aggregates, sand, and water. Cement, the most important component, reacts with water causing concrete setting and hardening. The formed paste bonds all the other concrete components together. Cement paste comprises of hydrates, porosity and unreacted cement grains. The main hydrate created is calcium silicate hydrate (C-S-H) that provides the binding properties.

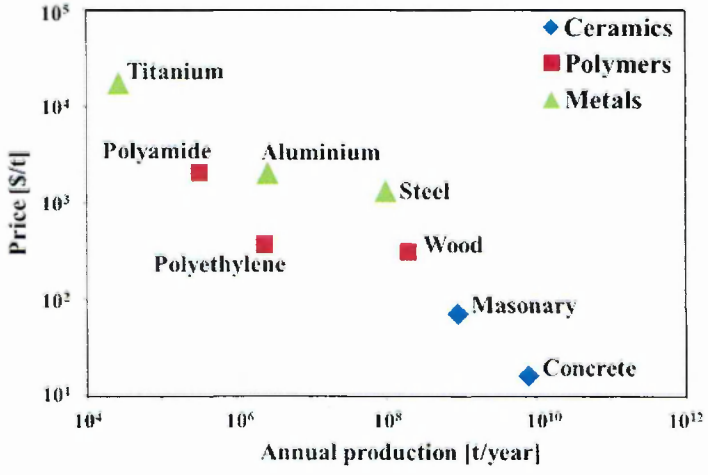

Figure 1.1 Price of materials and their annual production (adapted from [3]; quoted in [2]).

Despite all the above positive features of concrete, an important aspect to consider is the emission of carbon dioxide (CO_2) during cement production. CO_2 emissions result primarily from the burning of fuel to heat limestone to make anhydrous cement powder (~40%) and from the breakdown of the limestone itself during that process (~50%). The remaining 10% comes from electricity use and transportation.

CO_2 emission from cement production is relatively small compared to other materials on a tonne for tonne basis (fig. 1.2 right). However, the enormous amount of cement produced each year worldwide (4.0 billion tonnes in 2013 [4]) results in 5% of global non-natural CO_2

emission. [1]. Given this fact, the cement industry places high importance on the reduction of CO_2 emissions.

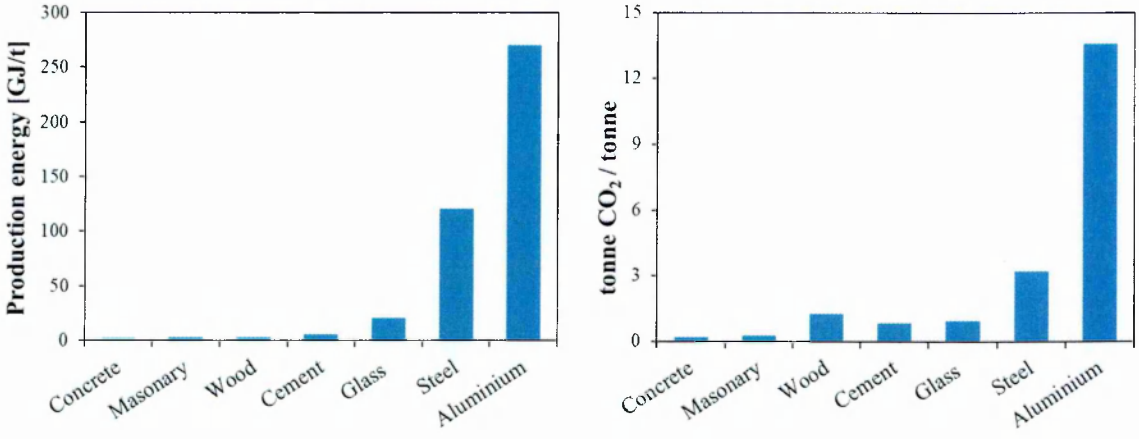

Figure 1.2 Left – Energy required for production of 1 tonne of material. Right – CO_2 emission per tonne of produced material (adapted from [1]).

Improvements have been made to cement manufacturing plant technology increasing energy efficiency to nearly 80%. Only small progress can now be made in the combustion process. Therefore, one of the biggest and the most serious challenges ahead for the cement industry is to reduce demand for cement clinker[1] production. The route to achieve that goal is production of alternative, blended cements where clinker is partially substituted by so-called Supplementary Cementitious Materials (SCMs). In a group of SCMs are by-products of different industries, like fly ash, slag and silica fume as well as the other raw materials like raw-limestone and natural puzzolans. Exploiting SCMs would facilitate making and designing cementitious materials that have as good as, or better, performance than traditional materials: rate of reaction, service life, strength, permeability and durability.

The internal porous microstructure of cement paste and the dynamics of water within it are linked to all forms of degradation as well as to mechanical properties of hydrated cementitious materials. Porosity and the state of water within it are an innate characteristic of cementitious materials. They depend hugely on the materials' water to cement ratio, age, curing conditions and degree of saturation. The porosity of cementitious materials spans over a wide range of lengths (fig. 1.3) with millimetre size air voids and micrometre capillary pores enclosed between hydrates. At the lowest nano-level there are pores within C-S-H: interlayer pores between tetrahedral silica layers and gel pores enclosed between locally aggregated stacks of layers.

A better understanding of the microstructure and pore-water interaction within cementitious materials is required to make alternative materials more commonly used and to improve durability of concrete constructions. A better understanding would also bring insight

[1] product of sintering limestone with silica, alumina and iron oxide containing materials

into hydration process, allow characterisation of materials and prediction of their properties. The establishment of rapid and non-invasive / non-destructive mean to characterise cement microstructure, with emphasis on C-S-H gel, will contribute to the great progress in cement industry and allow controlling and improving long-term performance by enabling study of the relationship between evolving microstructure and performance. The study of micro and nano structure of C-S-H and mobility of water within it is very important but, at the same time, challenging as it is a fragile, heterogeneous and nano-porous material with a lack of long range order. Moreover, the changes in its structure, morphology, density and composition occur for different cement chemistry, water to cement ratios, at various ages and curing conditions (humidity, temperature, saturation). For all of these reasons, despite ongoing extensive research in cement society [5]–[7], that C-S-H structure has been not unambiguously characterised and several alternate models have been proposed.

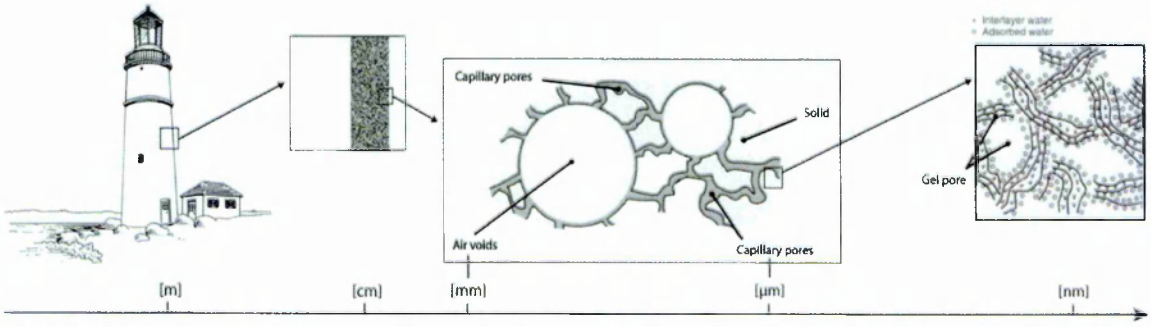

Figure 1.3 Various length scale of concrete / cement porosity [8].

1.2. TRANSCEND PROJECT

The work performed in the framework of this thesis is the part of the Marie – Curie Initial Training Network TRANSCEND; a scientific programme funded by European Commission. The programme name stands for 'The Understanding **TRANS**port for **C**oncrete which is **E**co friendly, i**N**novative and **D**urable' [9].

The main aim of the programme is to describe and predict water transport in cements and concretes. The unique characteristic of the programme is the bottom-up approach. The knowledge is gained by understanding first the transport at the lowest level and then by climbing up the hierarchy of length scales. Modelling of water dynamics is directly connected with experimental and validation studies.

The TRANSCEND programme has been divided into three specific themes.

Theme A comprises five projects on the computer modelling of water dynamics in cement. The study starts at the sub-nanometre and nanosecond level (P1) with molecular dynamics modelling of transport within C-S-H layered structure. It goes on the level of the C-S-H gel pores and paste structure with Lattice Boltzmann modelling (P2,3) and reaches the level of concrete structures measured in meters with finite elements simulations (P4,5).

Theme B concerns experimental work to provide data-base required as the input for modelling. The first group of projects is concentrated on characterisation of C-S-H

morphology (P8), cementitious materials (P7) and water transport coefficients (P6). The remaining projects focus on development and dissemination of the methods: NMR (P9), cryoporometry (P10) and micro-cracks mapping (P11).

The models are validated by the projects of Theme C. The investigation of water transport and pore connectivity has a purpose in nano and mesoscale modelling validation (P12). Development and validation of the models related to drying of particular cement phases (P13) and drying shrinkage inducing cracking (P14) are pursued. The conventional methods of examining water transport in concrete are verified by NMR profiling (P15).

The work on the themes has been performed by fifteen Early Stage Researchers hosted by academic institutions (Themes A and B) and industrial partners (Theme C). The collaboration and links between projects are presented in figure 1.4.

This thesis - project P9, is focused on Nuclear Magnetic Resonance Relaxation Analysis of Cementitious Material. The aim of the project is characterisation of water within nanoporosity of cement to provide input data for computer modelling of water dynamics in cement. The general objectives are to define the pore size distribution, pore connectivity and state of water within cement paste.

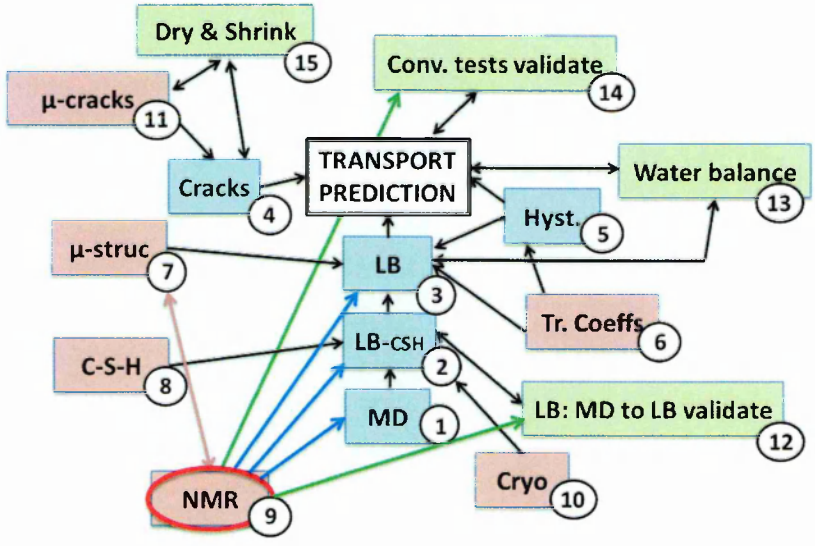

Figure 1.4 The relationship between the projects. Theme A – blue boxes, Theme B – pink, Theme C - green. Arrows show the links between projects. For project 9, the blue arrows represent the data provision, green arrows - the places of secondment and the pink arrow – collaboration on NMR method.

1.3. NMR Relaxometry as characterisation technique

Water hydrogens are sensitive to magnetic field applied in Nuclear Magnetic Resonance (NMR) technique. That gives a huge opportunity to exploit NMR to study cementitious materials. NMR probes directly hydrogen protons of water and of chemically combined OH^- groups within hydration products and pores of cement structure. The hydrogen spins mobility depends on the characteristic of the environment they are enclosed in.

The signal which follows the excitation pulse sequence in experiments provides valuable information. The signal amplitude or more accurately magnetization of relaxation time components is directly proportional to the number of spins which create a particular environmental group of protons. Therefore, NMR relaxometry can quantify those populations. NMR allows to differentiate between states of water and pore sizes as different mobility is manifested by different signal lifetimes, known as T_2 relaxation time. According to fast exchange model the observed rate of relaxation ($1/T_2$) is proportional to surface to volume ratio of the pore [10]. A second relaxation time T_1 may also be used. NMR is sensitive to the mobility of hydrogens over the wide range of time and length scale starting from nanometres level. Therefore, NMR 'sees' and responds to all water hydrogens.

NMR relaxometry is the method successfully applied to characterise microstructure and liquid dynamics in porous media. It provides valuable information for broad range of systems and material sciences: mesoporous zeolites (*e.g.* [11]); clays (*e.g.* [12]); soils and earth science (*e.g.* [13]); reservoir rocks and fluids within them for petroleum engineering (*e.g.* [14]); polymers film formation and water interactions (*e.g.* [15]); food (*e.g.* [16]); pharmaceutical and biological systems (*e.g.* [17]).

The NMR technique has the advantage for studying porous media including relevant for this thesis cementitious materials as it is non-destructive and non-invasive. It measures virgin samples - does not require drying or vacuum procedure for preparation. The delicate structure of C-S-H gel stays intact by the NMR measurement. It also benefits as samples can be study continuously during hydration.

NMR relaxation time analysis has been extensively used to investigate the microstructure of cementitious materials. The early NMR studies to follow the hydration of Portland cement and tricalcium silicate pastes were conducted by Blinc *et al* [18] in the late 1970s. Later on, in the 1990s, the first attempts to evaluate the pore size distribution in cement pastes based on NMR data were made by Halperin *et al* [10] using fast exchange model of relaxation based on the concept that water relaxes at pore surface giving an observed relaxation rate proportional to the surface to volume ratio. There followed several extensive studies of ^{1}H relaxation during cement paste hydration [19]–[24] which revealed a hierarchy of relaxation times and calculated pore sizes. However, for various reasons including variability in sample preparation, subtle differences in the measurement methods, a lack of signal intensity calibration and differences of opinion and understanding led to a broad spectrum of interpretations and assignments of T_2 to water reservoirs. The study by Holly *et al* [25] was the first to propose an assignment that essentially reflects current understanding of cement paste microstructure. Further applications and extensions of the NMR technique have been introduced and allowed to extend the knowledge on cement. They will be broadly described in this thesis.

1.4. THESIS OBJECTIVES AND OVERVIEW OF CONDUCTED WORK

The purpose of this thesis is to obtain better insight into the development of cement microstructure and pore-water interaction in cementitious materials by using ^{1}H Nuclear Magnetic Resonance Relaxometry.

The aim of this work is to demonstrate that NMR experiments are fully quantitative and deliver more detailed information about cement microstructure than other methods.

^{1}H NMR relaxometry is used to measure the first pore-type resolved sorption isotherm. In that way it is possible to assess how changes in humidity and specific processes: desorption, adsorption and secondary desorption, affect amplitude and T_2 relaxation time of water components and hence nano and microstructure of cement paste. Relaxation analysis of water in white cement paste during progressive drying and rewetting in a controlled relative humidity environment is performed. To identify and quantify all water within samples two NMR pulse sequences are applied: Quadrature echo and Carr-Purcell-Meiboom-Gill (CPMG) sequences. The signal is decomposed into chemically combined water, water in C-S-H interlayer spaces, gel and interhydrate/capillary pores. In this way a pore specific desorption / adsorption isotherm is generated. The experiments also give opportunity to compare C-S-H interlayer and gel pore sizes measured by both signal amplitude [26] and T_2 relaxation time [27]. The specific surface areas of those pores are also evaluated.

The thesis shows how quantitative data obtained by NMR relaxometry technique can provide a complete description of cement paste, C-S-H chemical composition and density. The presented calculation model is the result of collaborative work with Arnaud Muller – Transcend student placed at École Polytechnique Fédérale de Lausanne in Switzerland (P8).

The influence of curing temperature on nano and microstructure of cement pastes is of great interest. T_2 relaxation experiments are used in order to follow the evolution of particular water components – evolution of cement nanoporosity, during hydration at different temperatures (10 to 60°C) up to 90 days. The C-S-H density and composition within white cement paste are assessed at various curing temperature. The influence of cement composition is also investigated by examining white cement paste with and without addition of 10% of silica fume. Quadrature Echo and CPMG measurements are utilised in this part of thesis.

NMR relaxometry is used to evaluate the impact of solvent (isopropanol) replacement on cement paste, method used for arresting hydration. The mechanism of water – isopropanol exchange is evaluated through the observation of changes in amplitude and T_2 relaxation time of hydrogen populations. This part of thesis is the outcome of joint research between the author and Dr Radoslaw Kowalczyk. The NMR measurements are performed on cement pastes prepared with protonated and deuterated water, before and after exchange with regular and partially deuterated isopropanol. The reversibility of the exchange process and connectivity of C-S-H interlayer and gel pores with interhydrate and capillary pore network are shown.

To support computer modelling of water dynamics in cement, the activation energy for relaxation processes in associated pore types is determinate. NMR T_1 relaxation measurements of white cement paste are made as a function of temperature at which the relaxation parameters are measured.

2. Introduction to cementitious materials

2.1. CEMENT

2.1.1. Composition and chemical nomenclature

Calcium, silicon, aluminium, iron and oxygen are the five essential elements for making anhydrous cement powder. The most typical combination of raw materials to create Portland cement clinker is limestone as a source of calcium oxide and smaller amounts of clay or shale for silicon, aluminium and iron oxides [28]. Table 2.1 lists the relevant oxides in standard chemical and abbreviated cement science notation.

Table 2.1 Chemical notation in cement science.

Cement science notation	*Chemical composition*	*Oxide*
C	CaO	Calcium oxide
S	SiO_2	Silicon oxide
A	Al_2O_3	Aluminium oxide
F	Fe_2O_3	Iron (III) oxide
$\bar{S}$ / \$	SO_3	Sulphur trioxide
$\bar{C}$	CO_2	Carbon dioxide
H	H_2O	Dihydrogen oxide / Water

In cement manufacture the raw materials are blended together and ground in accurate proportions. The mix is then put in a kiln where it is heated to the temperature of 1450°C. As a result of heating, chemical and physical changes occur. The four main clinker phases are created: tricalcium silicate – C_3S called alite (50-70% of normal Portland cement clinker), dicalcium silicate – C_2S called belite (15-30%), an aluminate phase – C_3A (5-10%) and a ferrite phase – C_4AF (5-15%). In the final stage of production clinker is ground with typically five percent of gypsum to produce anhydrous cement powder. The gypsum, or an alternate source of calcium sulphate, controls the rate of cement setting by slowing-down the aluminate and ferrite reactions with water [28].

2.1.2. Hydration

Mixing cement powder with water triggers a series of dissolution-precipitation reactions which transform these solid and liquid phases into a rigid solid material with water-filled porosity. The processes which occur during hydration include: dissolution, diffusion,

nucleation, growth, complexation[2] and adsorption. The hydration process is complex as different cement phases react simultaneously with water, interact with each other and modify the chemistry of the pore liquid phase. Nevertheless, there are characteristic reactions [29], [30].

The calcium silicates, C_3S and C_2S, reactions with water result in formation of Calcium – Silicate – Hydrates (C-S-H) and Calcium Hydroxide (CH also called Portlandite) [29]:

$$\begin{aligned} C_3S + H &\rightarrow C-S-H + CH \\ C_2S + H &\rightarrow C-S-H + CH \end{aligned} \tag{2.1}$$

The exact stoichiometry of these reactions is not defined as the C/S and H/S ratios in C-S-H are not constrained and depend on the condition at which reactions occur. C-S-H is the main product of cement hydration occupying approximately 50-65% of hydrated paste. It forms mostly around cement grains. The second primary product of hydration (CH) is crystalline and has defined formula - $Ca(OH)_2$. CH constitutes about 20-25% of paste [29], [31].

The hydration of calcium aluminate, C_3A, in presence of calcium sulphate results in the creation of calcium trisulphoaluminate hydrate called ettringite (AFt). When sulphate is consumed C_3A reacts with ettringite and water to produce calcium monosulphoaluminate hydrate (AFm) [29]:

$$\begin{aligned} C_3A + 3C\$H_2 + 26H &\rightarrow C_3A \cdot 3C\$ \cdot 32H \\ 2C_3A + AFt + 4H &\rightarrow 3 \cdot C_3A \cdot C\$ \cdot 12H \end{aligned} \tag{2.2}$$

Most of hydration reactions exhibit the volume changes contributing to the chemical shrinkage of the paste and creation of porosity. It is attributed to lower specific volume of bound water in hydrates in comparison with free water [29].

In general the hydration process can be divided into four stages - figure 2.1. The first stage – initial reaction, is characterised by intensive release of heat due to wetting and dissolution of cement grains. Then heat flow decreases and reaches minimum as water becomes supersaturated. This indicates the induction - slow reaction, period. Following that, during acceleration period, the rapid increase in heat flow is observed. It is caused by rapid nucleation and growth of C-S-H and CH. The maximum level of heat flow indicates the beginning of deceleration stage. During that period the growth of C-S-H and CH is slow and believed to be controlled by diffusion of reactants through already formed hydrates. At that stage, in presence of calcium sulphate, the secondary formation of ettringite, followed by creation of AFm phase, also occurs [30].

[2] chemical reactions between ions that lead to formation of ion or molecular complexes [30]

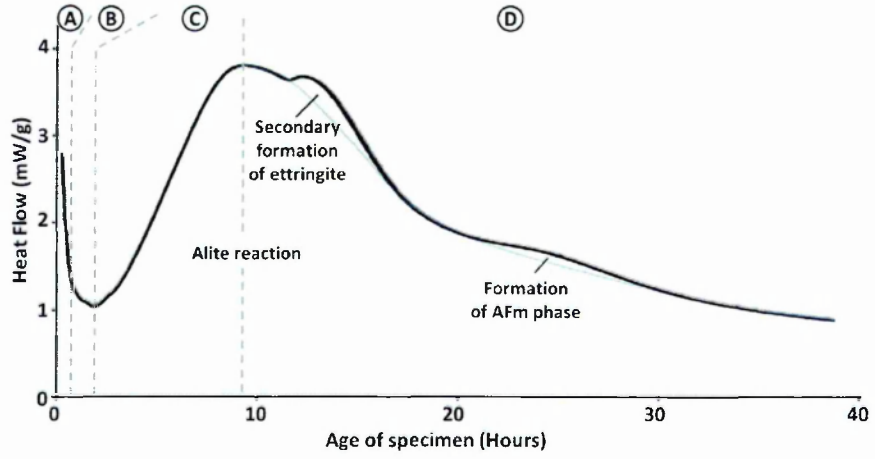

Figure 2.1 Heat evolution over time for Portland cement (adapted from [30]). A – Initial reaction, B – Induction period, C – Acceleration period, D – Deceleration period.

2.2. MICROSTRUCTURE MODELS

2.2.1. Powers and Brownyard's model of cement paste

The most widely used model of cement microstructure was developed by Powers and Brownyard in the 40's [32], [33]. This model was based on measurements of water vapour adsorption and of the non-evaporable water content. The model allows quantitative calculation of the volume composition of cement paste.

Powers and Brownyard divided the water within cement paste into non-evaporable and evaporable. Non-evaporable water is considered as that persists in paste at the pressure below $5 \cdot 10^{-5}$ mmHg at 23°C. It represents water within both non-colloidal (OH^- groups in $Ca(OH)_2$ and crystallization water in calcium sulfoaluminates) and colloidal materials (calcium silicate hydrate gel). All non-evaporable water in the model is treated as one entity. The colloidal and non-colloidal hydrates are generally called cement gel and no division into particular hydrates is made within model. The volume of non-evaporable water and cement powder is hence the absolute volume of cement gel - solid phase.

The evaporable water exists in paste at higher pressure. It is divided into gel and capillary water. The gel water is that contained in the pores of cement gel. Its amount is defined as $4 \cdot V_m$ where V_m is the volume of water required for monolayer coverage of solid phase obtained through BET theory. That value derives from two observations. First, the adsorption curves[3] for all pastes are the same at lower pressure ($RH < 0.45$). Second, they are the same in whole range of pressure for all mature pastes mix at lower water to cement ratio, $w/c < 0.32$. When the evaporable water content of saturated paste equals to $4 \cdot V_m$, the porous cement gel fills all the originally water filled space and the paste porosity is that of cement gel.

When the evaporable water content exceeds $4 \cdot V_m$ the excess water occupies the space outside of the cement gel and is called capillary water. The capillary water, if present in the

[3] w/V_m as a function of relative humidity, RH, where w is the quantity of vapour adsorbed

microstructure, fills pores at higher pressure ($RH > 0.45$). Its amount is higher for paste with bigger w/c ratio and decreases with hydration time.

As the rate of capillary water consumption is faster than the rate of filling the capillary pores with cement gel, a contraction in the volume appears called chemical shrinkage. In the case when the exterior water is available that volume becomes filled with water. However, for sealed cured paste the pores becomes partially empty.

In general Powers and Brownyard found that the content of non-evaporable water (w_n) is between 0 and ~0.25 g/g of anhydrous cement. The widely quoted value of gel porosity in cement gel, based on Powers and Brownyard model, is about 0.28 [29], [34], [35].

The cement paste as presented in original work of Powers and Brownyard's [32], [33] consists of hydration products considered together as cement gel, gel and capillary pore water as well as pores due to chemical shrinkage. In further work Powers introduced the unreacted cement as a part of the microstructure [36]. The calculations of volume composition based on the model have been repeated, used and slightly refined in further publications [28], [34], [37]. The diagrams of paste volume composition evaluated by Jensen [37] based on extended Powers and Brownyard model are presented in figure 2.2. They presents the general tendency during hydration as cement and capillary water are consumed at the expense of created cement gel with gel porosity embedment into it. Additionally, due to chemical shrinkage part of the pores becomes empty.

The important factor affecting the course of hydration is the sufficient quantity of water and space available for all hydration products and hydration to proceed. The critical, minimal, amount of water, w/c^* ratio, required for complete hydration to occur is given by Taylor [28] to be typically about 0.38. The minimum value is also determinate by Hansen [34] depending

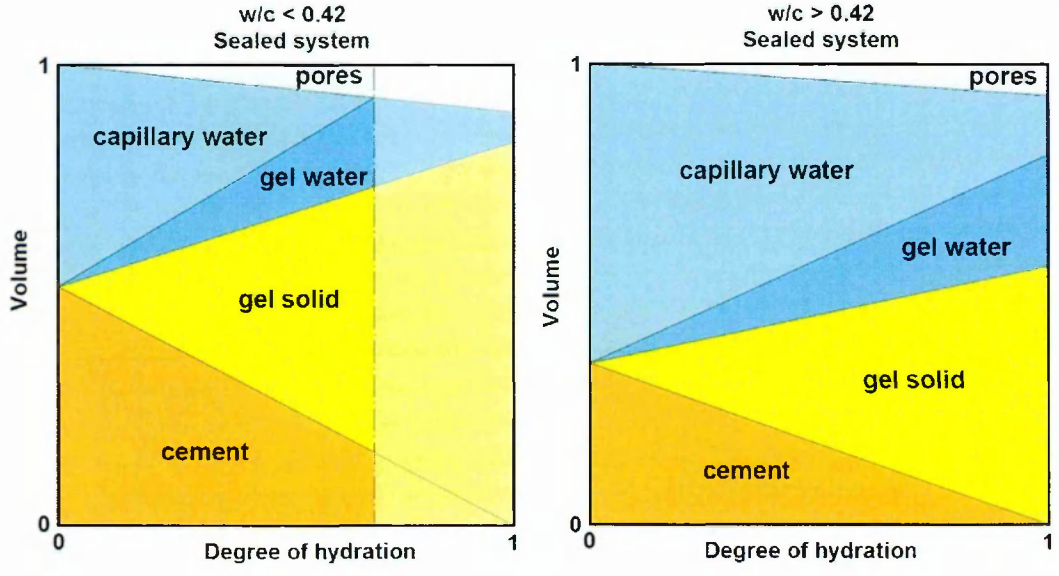

Figure 2.2. Volume phase composition diagrams by Powers for sealed cured cement paste as reworked by Jensen [37]. The dashed line in the graph for $w/c < 0.4$ indicates the degree of hydration at which hydration stops due to insufficient amount of capillary water.

on the availability of external source water. If there is supply of water from outside, underwater curing, $w/c^* = 0.36$. When no extra water is available, sealed curing, critical $w/c^* = 0.42$. As shown in fig. 2.2 above that value the paste reaches the full hydration (right graph) whereas below the hydration stops when all capillary water is used up, all capillary space is filled by cement gel, as indicated by shadow part on left graph.

2.2.2. C-S-H models

2.2.2.1. Powers model

The first C-S-H model was proposed by Powers [36]. Its origin is based on the water adsorption results obtained by Powers and Brownyard [32], [33]. Considering the high specific surface area of gel pores (~200 m^2/g of cement for mature pastes), the small gel pore (2-4 nm) and the solid unit sizes (<14 nm) Powers suggested that the solid hydrate is finely subdivided, colloidal material containing the non-evaporable water [32], [33]. Powers further defined, based on electron microscopy, the C-S-H gel particles as fibrous with straight edges. The regions of parallel particles with gel pore water between them are arranged in rigid independent blocks (figure 2.3 circle). These blocks create the cross-linked network with the amorphous material in between them. Even though the C-S-H structure is disordered it is closely similar to the crystalline mineral – tobermorite, structure [36].

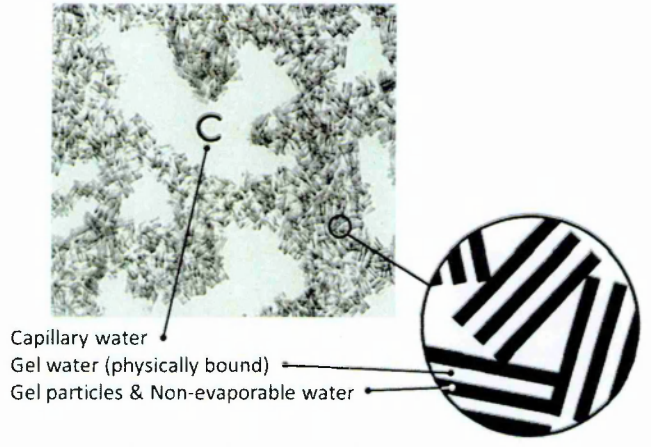

Figure 2.3 Simplified structure of hydrated paste based on electron micrograph, the zoom area (circle) presents the model of C–S–H structure by Powers (adapted from [36], [37])

2.2.2.2. Feldman-Sereda model

The next model of C-S-H has been presented by Feldman and Sereda in late 60's [38], [39]. It was based on the examination of sorption and length changes as a function of relative humidity as well as relation of mechanical properties (strength and Young' modulus) to relative humidity, porosity and method of sample preparation.

This model also considers that C-S-H is a layered structure composed of tetrahedral silica sheets with alternating layers of water and calcium ions. Nevertheless, the C-S-H layers are more connected and disorganized (figure 2.4) in comparison with Powers' model. The state of

water within C-S-H in this model has been differentiated based on reversible and irreversible behaviour of water upon scanning isotherm loops. The water between layers is inferred as the structural and chemical component of C-S-H, not as 'pore' water. This water is equivalent of the gel pore water in Powers model. It is considered irreversible water as its removal during desorption process (slow but progressive, with the biggest change at lower humidities) differs from adsorption path (gradual uptake over whole range of humidity). The reversible water is that physically held on the outer surfaces of the C-S-H layers.

The schematic representation of C-S-H proposed by Feldman and Sereda – figure 2.4, comprises also the spaces between disordered layers of C-S-H. There is no distinction regarding these spaces in the original descriptions of the model [38], [39]. In terms of current understanding and interpretation of Feldman and Sereda model the C-S-H forms stacks of quasi continuous sheets and gel pores are between imperfections in the stacking order.

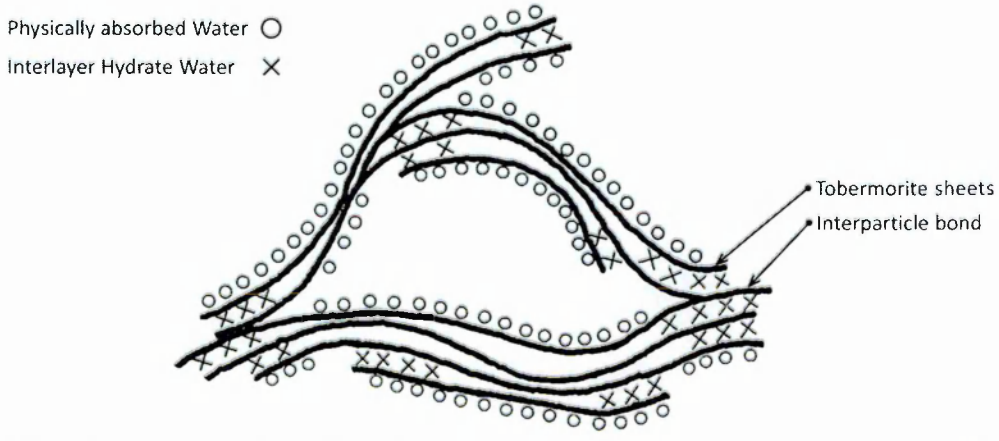

Figure 2.4 Schematic model of C-S-H morphology proposed by Feldman and Sereda (adapted from [38]).

2.2.2.3. Colloidal models by Jennings and Tennis (CM-I) and Jennings (CM-II)

Jennings and Tennis colloidal model – CM-I

The development of Jennings and Tennis colloidal model [40], [41] of C-S-H was triggered by discrepancies between different values of specific surface area (SSA) of C-S-H reported in the literature (reviewed [42]). The modelling of SSA, as measured by nitrogen sorption, led to the conclusion that there are two types of C-S-H created which are differentiated by densities. The low density (LD) C-S-H can be penetrated by nitrogen and the high density (HD) C-S-H cannot. The various SSA values obtained by different methods were also explained by not detecting HD type C-S-H.

The pictorial model presented in figure 2.5 a and b is simplified representation of the LD and HD C-S-H microstructure. In the model C-S-H units (layers) are represented by basic building blocks pictured as spheres. These units precipitate within capillary pores and flocculate to form globules. Depending on the packing arrangement of these globules, LD (fig. 2.5a) and HD (fig. 2.5b) C-S-H is created.

It is worth emphasising that Tennis and Jennings work [41] also provides a means to compute the quantitative cement phase composition. The model is based on known cement composition, *w/c* ratio and hydration equations of cement phases. Additionally, the optimized values of SSA of LD CSH and densities of LD and HD C-S-H are acquired by fits between measured and predicted values of SSA, porosity (by N_2 adsorption) and capillary porosity.

Jennings colloidal model CM-II

The C-S-H model presented in previous section was further developed by Jennings [6] based on the interpretation of water sorption isotherm, C-S-H density and small angle neutron scattering (SANS) results.

The model implies that the nature of C-S-H is particular or granular (figure 2.5c) as suggested by block C-S-H model of Powers and Brownyard [32], [33]. It consists of C-S-H layered globules (called in CM-I basic C-S-H units but not the same from structural point of view) with a thickness of about 4.2 nm [7]. The state of the water inside the C-S-H globules was inferred based on interpretation of the low pressure water isotherm hysteresis and changes of the density below 11% RH. CM-II defines two location of water within globules: interlayer space and intraglobular pores (IGP) of about 1 nm size enclosed through disordered layers. The hysteresis behaviour at the lower humidity, in the context of the model, is explained as in this range the interlayer water leaves but does not reenter globules until higher pressure is apply.

The C-S-H globules pack together into clusters and entrap the small gel pores (SGP) that are less than 3 nm wide. The water within SGP dries below 40% RH. The clusters arrange together to form the globule floc (fig 2.5 c) with the larger gel pores (LGP) in between. The LGP dry progressively between 85 and 40% RH. The volume of LGP pores reduces with time

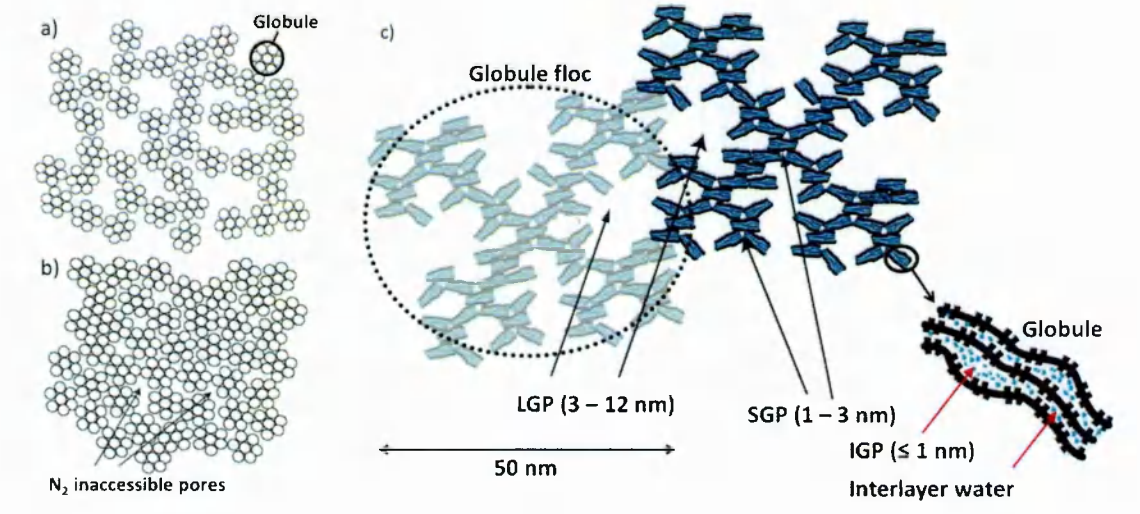

Figure 2.5 a) and b): Graphical representation of Low Density (a) and High Density (b) C–S–H as presented in colloidal model of Tennis and Jennings (adapted from [40], [41]); c) Schematic representation of CM-II C-S-H Jennings model (adapted from [6]).

by interpenetration of globule flocs - an ageing process. This process causes the formation of higher density C-S-H. The LPG pores, with the size of 3-12 nm, are considered as the intrinsic to the C-S-H gel in CM-II [6].

2.2.2.4. Relation to crystalline phases

The models of C-S-H described in the previous sections are concerned with microstructure. C-S-H has also been investigated from the composition point of view by the mean of X-ray diffraction, NMR spectroscopy and microscopic techniques. Models regarding the molecular structure, characterised by structure of silicon anion (chain length), chemical formulation and Ca/Si ratio, has been evaluated with the attempt to relate short range of C-S-H with crystalline calcium silicate hydrates.

Most of the models have been based on the structure of the 1.4 nm tobermorite [5], [43] due to similarities to C-S-H in hydrated cementitious materials in the XRD patterns, MAS NMR spectra and TEM images [29], [44] – figure 2.6.

Tobermorite (1.4 nm) consists of central Ca-O layers with silicate chains on both sides for which every third tetrahedron is bridging. The repeat distance of the layers is 1.4 nm. The

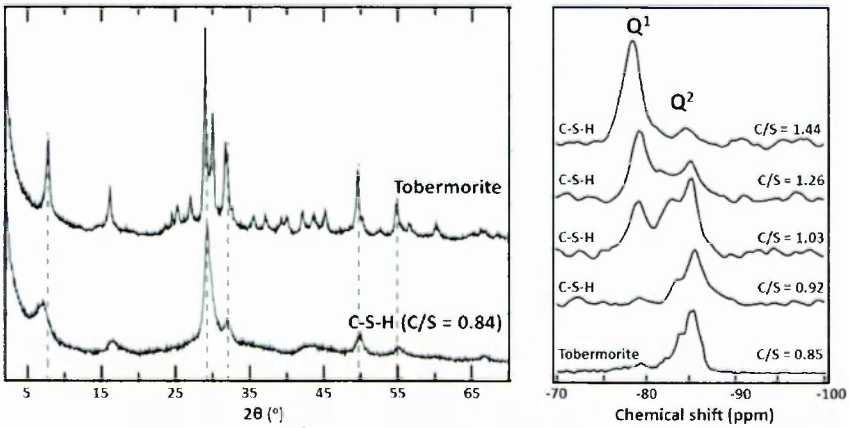

Figure 2.6 The XRD patterns (left) and ^{29}Si NMR spectra (right) for 1.4 nm tobermorite and C-S-H (adapted from [44]–[46]).

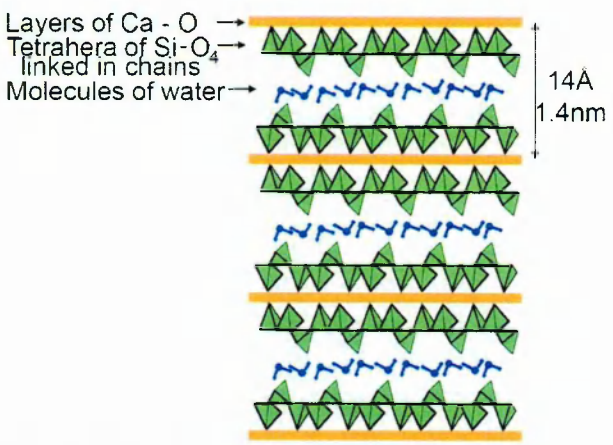

Figure 2.7 Schematic of three layers of tobermorite 1.4 nm nanostructure [29].

space between layers is filled by water and calcium ions (figure 2.7). The length of silicate chains is very long as shown by domination of Q^2 groups in NMR spectrum (fig 2.6 b) [5].

Tobermorite has well defined chemical formula: $Ca_5Si_6O_{16}(OH)_2 \cdot 7H_2O$, with the Ca to Si ratio of 0.83 [5]. The equivalent ratio in the C-S-H present in hardened cementitious material is higher, with a mean of about 1.75 [47]. Therefore, some models incorporate the intermixing of tobermorite and jennite ($Ca_9Si_6O_{18}(OH)_6 \cdot 8H_2O$) which has higher Ca/Si ratio of 1.50 and similar silicate chains [5]. Different mechanisms of changing the Ca/Si ratio have been proposed: removal of bridging tetrahedra; substitution of protons by Ca^{2+}; incorporation of Ca-OH regions [5], [29].

2.3. POROSITY AND METHODS TO CHARACTERISE PORE STRUCTURE

Porosity is most often defined as the volume of air and/or water filled space within the total volume of material. In that sense the total porosity as well as the porosity of particular pore population can be characterised. Nevertheless, in wider aspect it is the quality of being porous. A number of parameters describing porosity can be identified: specific surface area, pore size distribution, threshold pore size, connectivity and tortuosity.

Pore sizes span a wide range of sizes as is presented in figure 2.8. However, among different models and researches the divisions and nomenclature of pores varies [48].

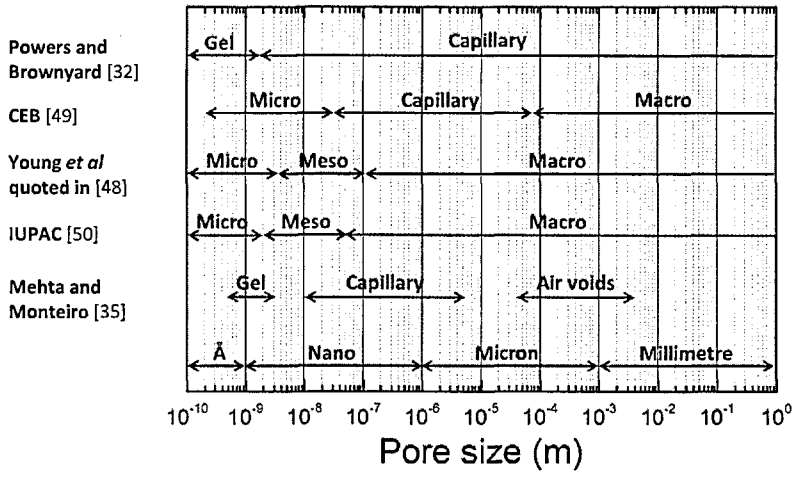

Figure 2.8 The pore nomenclature variations for cement porosity (adapted from Geiker [48]).

There are several techniques applied to characterise the porosity of cementitious materials. A brief description of selected methods follows. Different techniques are sensitive to different range of pore sizes and none can encompass the full range of pores present in cementitious materials (figure 2.8).

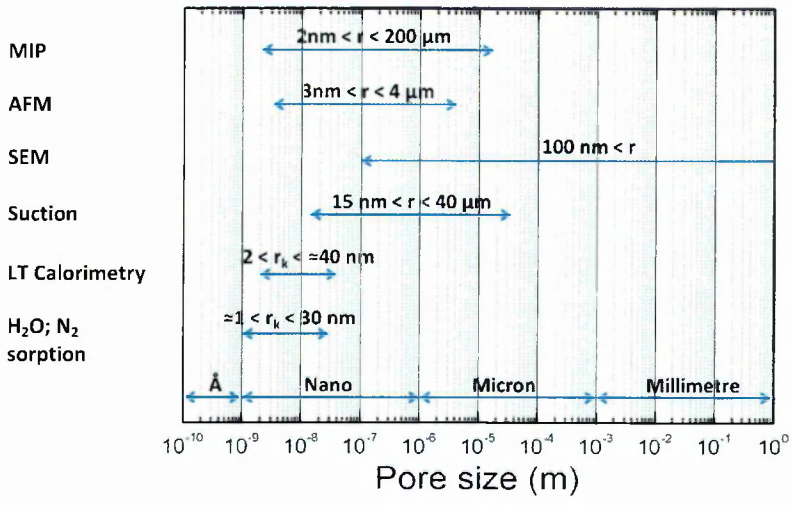

Figure 2.9 Range of pore's sizes that can be measured by specific methods – thickness of *t*-layer not included (adapted from Geiker [51]).

2.3.1. Mercury intrusion porosimetry

Liquids can interact with the surface of a solid body in two ways depending on wetting properties. If the contact angle is less than 90° then the surface is wetted (fig. 2.10 left), hence the liquid exhibits capillary rise. If it is more than 90° it does not wet surface (fig. 2.10 right) and capillary rise is not seen.

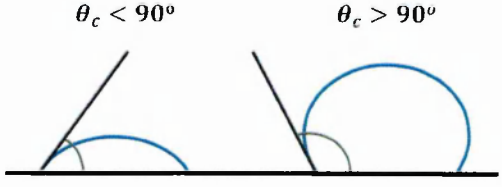

Figure 2.10 Schematic of liquid interaction with the surface. Left: surface wetted; right: surface not wetted [52].

Mercury is a liquid that does not wet the surface of cementitious material as its contact angle, at room temperature, is about 140° [52]. The procedure of using pressure to force mercury into empty pores and to define the pore size distribution is called Mercury Intrusion Porosimetry (MIP).

The procedure involves drying and then weighing of the sample, evacuation of gas from a chamber in which the sample is placed, introducing mercury to the chamber, applying a gradually increased pressure and monitoring the mercury intrusion [53]. The correlation between the size of pores (d) mercury invaded and the applied, exterior pressure (p) is expressed by the Washburn equation [54]:

$$d = \frac{2\gamma_S \cdot \cos(\theta_c)}{p} \tag{2.3}$$

where γ_S is the mercury surface tension and θ_c is the contact angle between mercury and pore surface.

The volume of the mercury that enters pores at specific pressure corresponds to the volume of pores – porosity, with the pore size defined by that pressure.

MIP has been extensively used to evaluate pore size distribution and porosity of cement based materials. Examplary data from Cook and Hover [55] are presented in figure 2.11. The results show, as expected, the decrease of the total paste porosity with passing time and smaller *w/c* ratio. The so-called equivalent pore width also declines. The measured pore width is the pore entry – threshold, size. The paste may contain 'ink-bottle' pores as well as larger pores which are connected with outside through the network of smaller pores. These can lead to erroneous conclusion about the pore size distribution and suggests that MIP data may be of limited value for small pores and actual pore sizes [53].

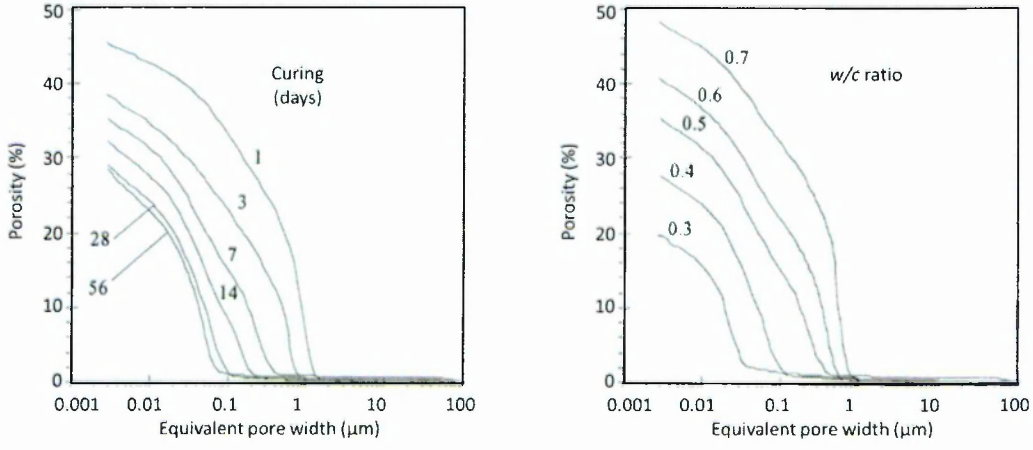

Figure 2.11 The effect of hydration time for pastes with *w/c* = 0.5 (left) and of water to cement ratio at 7 days of hydration (right) on MIP results [55].

There are other factors and assumptions that are the source of experimental errors [52], [53]. First, the Washburn model assumes that pores are cylindrical and entirely and equally accessible from the outside surface. The cement structure can be altered due to sample drying preparation and applied pressure [56]. Additionally the method itself provides limitation as samples may be not evacuated properly and contact angle differs for different material but also for different drying methods [57].

2.3.2. Scanning Electron Microscopy

Scanning Electron Microscopy (SEM) is a technique providing high resolution images of material structure. Prior to experiment, the cementitious sample is dried, impregnated with epoxy resin and polished. It is then scanned with the high energy electrons beam. As a

response of interaction between sample and incident beam different signals are emitted: secondary electrons, backscatter electrons and characteristic X-rays; with the decreasing resolution respectively [31], [58].

The secondary electrons are emitted from a region close to sample surface. They are independent of the nature of elements releasing them. This imaging of cementitious materials provides topological and morphological information about the hydration products.

The backscatter electrons (BSE) originate from higher depth than secondary electrons. The intensity - brightness, of the BSE SEM signal is strongly dependent on the average atomic number of the sample local areas. Therefore, BSE provides the reproducible phase contrast. Figure 2.12a shows the typical BSE SEM image of cement mortar where the pores filled with resin are presented as black pixels; the unreacted cement grains have the highest brightness; CH is brighter than the other hydrates.

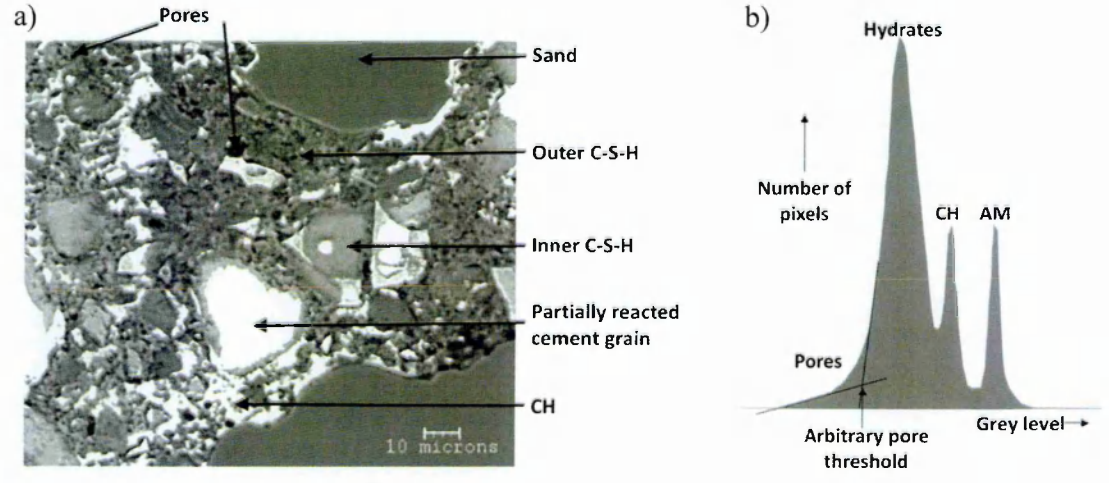

Figure 2.12 a) Examplary BSE SEM image of the Portland cement mortar; b) Grey level histogram of cement paste; AM refers to anhydrous material (adapted from[31], [58]).

The BSE SEM allows representative visualisation of the cement paste structure and observation of the pore shapes (down to 100 nm). The quantitative analysis of size distribution, total area and volume of pores is facilitated by the reproducible contrasts between particular constituents of paste. This analysis is performed by segmenting / thresholding the grey level histogram to identify the boundary grey level between pores and hydrates (fig. 2.12b). The additional advantage is possibility of combining the local chemical microanalyses by e.g. energy dispersive spectroscopy (EDS)

The key limitations of the technique arise from limited spatial resolution, variations in grey level caused by variable composition, two dimensional imaging of an inherently 3D structure and sample preparation that may disturb the structure [31], [51].

2.3.3. Gas sorption

Gas sorption measures, in the form of sorption isotherm, the amount of gas adsorbed in the sample as a function of gas pressure [59].

In this method the dry sample is exposed to the gas with specified relative humidity (φ). When sample has reached the equilibrium the humidity is step-like increased. The amount of the gas adsorbed on the sample surfaces is measured, through recorded sample mass, as a function of relative humidity. Alternative variant of the method involved measurements of changes in pressure when sample is exposed to the known volume of gas. The commonly used sorptive gases are water vapour and nitrogen [42].

The obtained sorption isotherm allows calculation of specific surface area (SSA), open porosity and pore size distribution.

The relation between adsorbed gas and humidity facilitates the calculation of its amount corresponding to monolayer coverage of surface (u_m) and in turn of SSA. The most common, and one of the earliest, method for this calculation was developed by Brunauer, Emmet and Teller (BET) [60]. It expresses the amount of adsorbed gas (u) as

$$u = \frac{K \cdot \varphi}{(1-\varphi) \cdot (1 + K \cdot \varphi - \varphi)} \cdot u_m \tag{2.4}$$

where K is constant related to heat of adsorption.

The BET theory works well at the relative humidity below ~45%. In higher humidity range the other theory can be applied e.g. extended BET, Dent equation.

The evaluated u_m together with known cross section area of gas molecule (A_m) leads to expression for specific surface area [59]:

$$A = \frac{1}{M^{AMU}} \cdot N_A \cdot A_m \cdot u_m \tag{2.5}$$

where N_A is Avogadro number, M^{AMU} –molar mass of gas.

At the higher relative humidity the capillary condensation occurs. The equality of the difference in pressure over capillary meniscus expressed as a function of relative humidity and of meniscus radius leads to Young-Laplace – Kelvin equation for so called Kelvin radius (r_K) [51], [61]:

$$r_K = -\frac{M^{AMU}}{RT\rho \cdot \ln\varphi} \cdot 2\gamma_S \tag{2.6}$$

where γ_S – the surface tension, R – universal gas constant, T – temperature and ρ – density.

Examplary water vapour adsorption isotherm of cement pastes are presented in figure 2.13. It can be seen above relative humidity of ~0.4 that the capillary condensation is more pronounced with the increase of *w/c* ratio. In the lower humidity range, isotherms are independent of *w/c* ratio. The values of SSA measured by water sorption are in the range 130-210 m^2/g of cement (equivalent to 110-175 m^2/g of dry paste) increasing with sample age from 7 to 180 days [28], [32]. The reported values of SSA by using nitrogen tend to be lower in the range of 10 - 150 m^2/g of dry paste [28], [42], [62]. The reasons for that are not fully understood, the proposed explanations are that: the size of water molecule is smaller than nitrogen's; vapour water can be re-adsorbed into C-S-H interlayer; carbonation[4] of CH and C-S-H; differences in morphology and amount between the LD and HD types of C-S-H proposed by Tennis and Jennings [42].

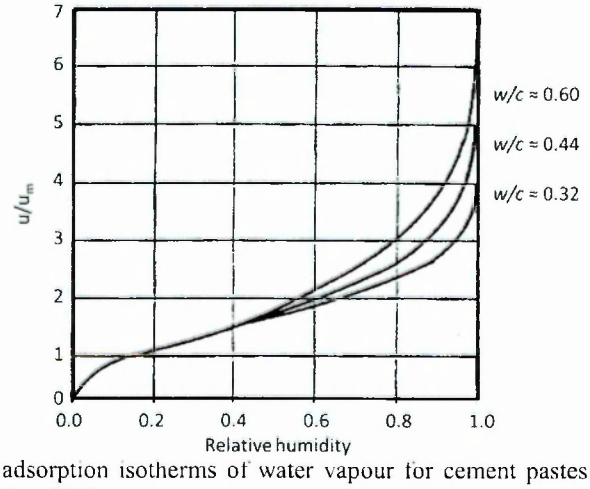

Figure 2.13 Examplary adsorption isotherms of water vapour for cement pastes mixed at different *w/c* ratios and cured for 180 days [32].

Gas sorption is a well-known method. Nevertheless, it has limitations and many aspects to consider. From experimental point of view: sample preparation involves drying that may disturb the delicate structure of C-S-H; the sample equilibration is long, especially when using salt solutions to create known relative humidity. Hence there is possibility of ongoing hydration; carbonation; shrinkage; and swelling during measurement that can alter pore structure. The balance accuracy should be very high as the mass is the actual measure in the method and the mass difference can be small. The Kelvin radius calculation assumes cylindrical shape of the pores [42], [51], [62].

[4] reaction between carbon dioxide (CO_2) and calcium compounds: CH and C-S-H; as a result calcium carbonate ($CaCO_3$) is formed

2.3.4. Low temperature Calorimetry

Low Temperature Calorimetry (LTC) is based on the fact that liquid within small pores freezes at lower temperatures in comparison with bulk fluid – so-called depression of freezing point [51], [63]. The melting point depression (ΔT) is given by equation:

$$\Delta T = \frac{2 \cdot T_0 \cdot V_l \cdot \gamma_S}{d \cdot \Delta H_{fus}} \tag{2.7}$$

where T_o is freezing temperature of bulk liquid, V_l – molar volume of liquid, γ_S – the surface tension, d – the pore size and ΔH_{fus} – the heat of fusion.

The LTC experiments are performed in the temperature range between +20°C and around -60°C and the heat flows to and from sample are measured. Plots of the heat flow present the peaks at different temperatures. The peaks' temperatures during freezing correspond to liquid freezing in pores with characteristic entry size. Melting curve peaks are correlated with actual pore sizes. It is a consequence of the freezing-melting mechanism for the structure containing 'ink-bottle' pores and bigger pores connected to surface through smaller ones [64].

The pore sizes are the sum of Kelvin radius (r_k) and t-layer thickness (non-freezable layer of adsorbed water - t_{nf}) [51], [63]:

$$r_K = -\frac{M^{AMU}}{\Delta H_{fus} \cdot \rho \cdot \ln(T/T_o)} \cdot 2\gamma_S$$
$$t_{nf} = 19.7 \cdot (273.2 - T)^{-1/3} \tag{2.8}$$

where M^{AMU} – liquid molar mass, T – freezing temperature of pore liquid and ρ – is the density of liquid.

The investigation of cement pastes during freezing scans typically show existence of three peaks corresponding to pore structure and occasionally additional peak due to bulk liquid [63], [65] – figure 2.14. The interpretation of heating scans for cementitious material is problematic as ice melts gradually [63].

LTC of cements is used to evaluate the pore thresholds and total volume of saturated porosity based on ice volume. The main advantage is measurement of 'as prepared' samples without need of drying. LTC is also relatively fast and young samples can be examined [51]. However, the position and width of peaks are affected by the rate of temperature changes and variable alkali concentration in pore solutions. The limitations are also: thawing that can cause cracking; the discrepancy between the reference and actual sample temperature; and supercooling. To overcome the latter nucleation agents are added to the samples [51], [63].

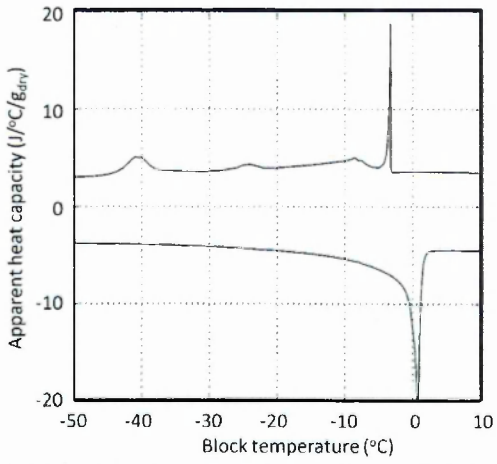

Figure 2.14 The examplary heat flow (given as apparent heat capacity) as a function of temperature for cement paste, *w/c* =0.5, after 75 days of hydration [63].

2.3.5. Small Angle Neutron Scattering and X-rays Scattering

Small Angle Scattering techniques are used to characterise the micro-structure of materials. The particle size distribution, total surface area and volume fractions of structural features, and fractal dimensionalities may be calculated. The porosity related characteristic is SSA.

During an experiment the intense beam of neutrons (SANS) or X-rays (SAXS) is directed at a sample. It passes through the sample and is elastically scattered out as a result of interaction with atomic nuclei (SANS) or cloud of electrons (SAXS) [42], [66]. Detailed models are required to relate scattering to structure. The forward problem – structure to scattering, is much easier and less ambiguous than inverse problem – scattering to structure.

The scattering vector (Q) of neutrons or X-rays is defined as:

$$Q = \frac{4\pi}{\lambda} \cdot \sin\left(\frac{\theta_{SAS}}{2}\right) \tag{2.9}$$

where θ_{SAS} is an angle of scattering and λ is the neutron or X-rays wavelength.

The resultant scattering profile presents a relation between the intensity of scattered neutrons or X-rays and scattering vector. In Porod's regime the calibrated scattering intensity (I_{SAS}) is proportional to surface area (A) per unit sample volume [42]:

$$I_{SAS} \cdot Q^4 = 2\pi \cdot |\Delta\rho_{SAS}|^2 \cdot A + C \cdot Q^4 \tag{2.10}$$

where $|\Delta\rho_{SAS}|^2$ is scattering contrast between the voids and solid phase and C is flat background intensity.

The examplary SANS data for ordinary Portland cement are presented in figure 2.15.

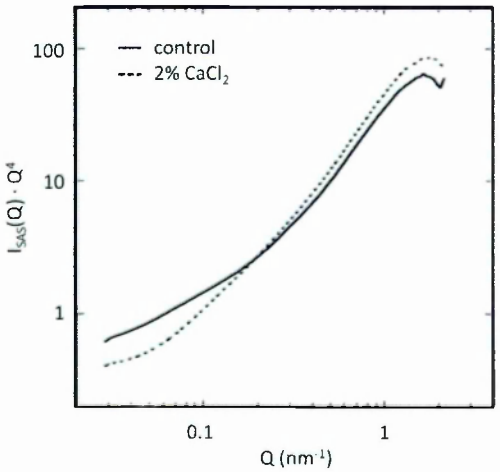

Figure 2.15 The examplary SANS data plotted as $I(Q)\cdot Q^4$ for ordinary Portland cement mixed at *w/c* ratio 0.4, with and without addition of $CaCl_2$, and hydrated for 28 days [66].

The surface areas of mature saturated cement pastes as measured by SANS and SAXS show the markable discrepancy. The SANS reported values are 60-150 m^2/g of d-dried paste while values obtained by SAXS are significantly higher, 200-600 m^2/g of d-dried paste. The probable reason is that SAXS actually probes smaller features, interlayer pores, than SANS as indicated by X-rays smaller wavelength and investigation of surface during drying [42].

The advantages of the technique are examination of saturated samples without drying and possibility of continuous study during hydration. The challenges concern primarily the strong dependence on model and analysis of data. The evolution of SSA according to presented calculation method - called the contrast method, requires the knowledge of scattering contrast for C-S-H and absolute calibration of data. The alternative analysis protocol is the scattering invariant method but brings more difficulties. The other concerns are sample preparation – the optimise thickness, and costs of equipment and its maintenance [42], [66].

2.3.6. Nuclear Magnetic Resonance Relaxometry

The work presented in this thesis is based on NMR relaxometry; hence chapter 3 is fully dedicated to provide a detailed description of relevant theory.

2.4. Characteristics of C-S-H

The investigation of the C-S-H stoichiometry provides valuable information about structure at molecular level. This serves as input for the modelling of water dynamics within nanostructure of C-S-H and its properties and lead to better understanding of its behaviour. In this thesis, the C-S-H composition is written as $Ca_z(Si_y,Al_{(1-y)})O_{(z+y/2+3/2)}(H_2O)_x$ where x is the interlayer water content. Once the gel pore water is included water content is x'.

2.4.1. C/S ratio

A primary characteristic of interest concerning C-S-H is the molar ratio of CaO to SiO_2, the so-called C/S ratio, in this thesis defined as *z/y*. The ratio in $CaO\text{-}SiO_2$ systems and for hydrated C_3S or C_2S can be calculated if the CH and amount of unreacted material is known [28]. To date, measurements of the C/S ratio has required use of complex and in some cases destructive experimental methods including e.g. the NMR spectroscopy, Electron Probe Microanalysis (EMPA), SEM and TEM with micro-analysers.

It has been reported by many researches that the C/S ratio of the C-S-H phase, in the equilibrium with Ca^{2+} solution, increases with increase of Ca^{2+} concentration [28], [43], [67], [68] – figure 2.16a. Based on this relation Taylor classified two types of the C-S-H: tobermorite-like C-S-H (I) with 0.8< C/S <1.5 and C-S-H (II) with C/S >1.5 corresponding to the mix of tobermorite-like and jennite-like phases [28] – region B and C in fig. 2.16a respectively. The highest values of C/S ratio for pure, synthetized C-S-H, samples free of CH, has been found to be about 1.5 [29], [43], [69]. This suggested that to reach higher values, as observed for C-S-H in cement pastes, the supersaturation of solution with respect to CH is necessary. Nonat [69] suggested the existence of three types of C-S-H: α-C-S-H (0.66< C/S <1) – upper part of region A in fig 2.16a; β-C-S-H (1< C/S <1.5) – region B; and γ-C-S-H (C/S >1.5) – region C. The first, α-C-S-H is typical tobermorite phase; β-C-S-H corresponds to Taylor's C-S-H (I); γ-C-S-H even though exists in the same region as C-S-H (II) shows tobermorite-like XRD pattern. The existence of single phase over whole range of C/S ratio was reported and the changes in the C/S ratio were explained by omission of bridging tetrahedra, substitution of protons by calcium ions, the presence of Ca-OH and Si-OH regions and decrease in the length of silicate chains [29], [43], [69].

Values of the C/S ratio in the C-S-H of hardened cement vary largely in the range ~1.2 to ~2.3 with the mean ~1.75 for mature pastes as measured by TEM microanalysis – figure 2.16b [47]. Recently, Allen *et al* [7] have evaluated the composition of the C–S-H by SANS analysis. They obtained the C/S ratio of 1.85 and in further analysis they assumed value of 1.70 as indicated by most studies in the cement field.

It was also noted that the C/S ratio in cement pastes changes with *w/c* ratio and age. The increase of paste *w/c* ratio lowers the C/S ratio. Additionally for younger samples the C/S present the bimodal distribution which changes to unimodal with the progress of hydration [47], [70]. This behaviour of the C/S ratio is correlated with a distinction in the C-S-H morphology (figure 2.17). The 'inner' denser C-S-H formed within the original boundary of cement grains has higher C/S ratio. The C-S-H which forms outside of these boundaries in an originally water-filled space – 'outer' C-S-H, has lower C/S. Nevertheless, with time the 'outer' C-S-H densifies, hence the single C/S ratio is reported.

The morphology of the 'outer' C-S-H is further divided into types: 'fibrillar' with intermediate C/S (fig 2.17b) and 'foil-like' with the lower values (fig 2.17c). The boundary between fibrillar and foil-like C–S-H was assigned as about 1.5 [47], [71].

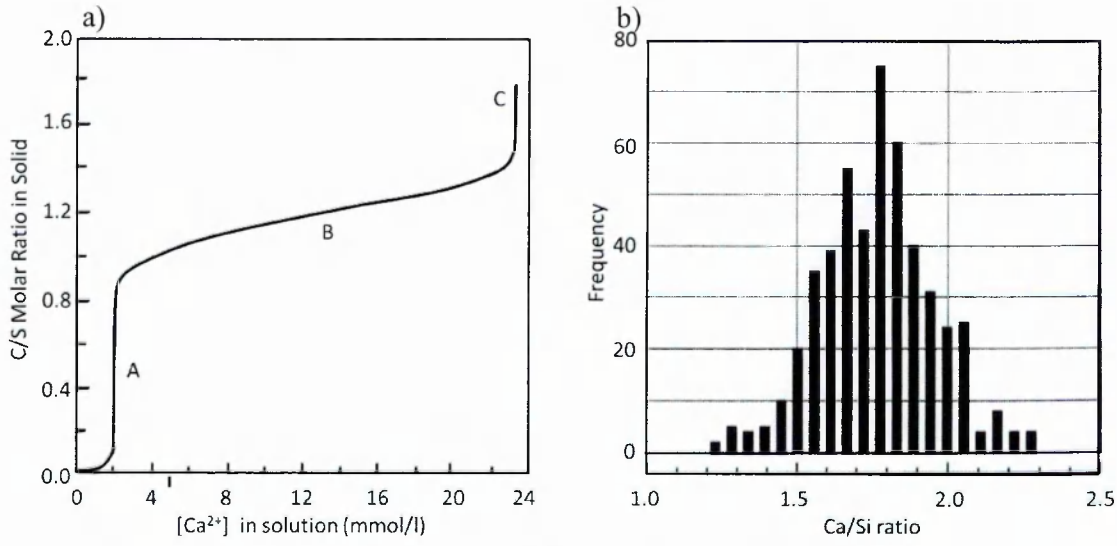

Figure 2.16 a) C/S ratio in C–S–H as a function of Ca^{2+} concentration in solution (adapted from [68]). b) Histogram of Ca/Si frequency for C-S-H in cement pastes 1 day to 3.5 year old as measured by X-ray microanalysis in the TEM (adapted from [47]).

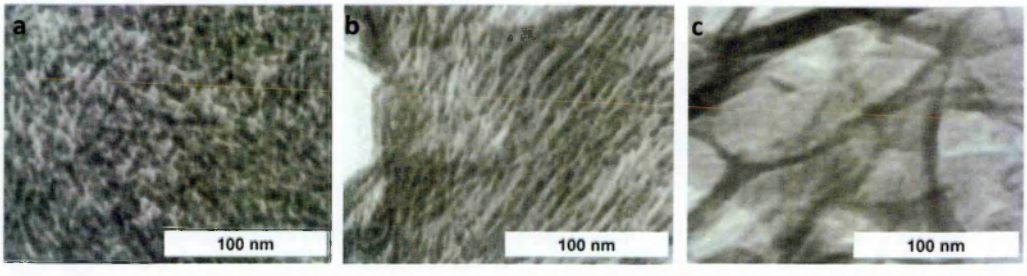

Figure 2.17 TEM micrographs of fine 'inner' C-S-H (a) and 'outer' CSH: fibrillar (b) and foil-like (c) (adapted from [71]).

2.4.2. H_2O content

As already described cement paste contains water in pores with a range of length scales and in various states. Water is present in the capillary, gel pores and C-S-H interlayer spaces as well as in the chemically combined, adsorbed and liquid states. Considering the molar H_2O content in the C-S-H the question arises as to what state of water it actually refers. Moreover, the H_2O content may also depend on the sample characteristic: *w/c* ratio, hydration time and curing conditions. When comparing the obtained values of H_2O content the types of included water or drying conditions should be clearly defined.

The water content (moles of H_2O per mole of C-S-H) for the nearly saturated C-S-H created upon hydration of C_3S (at 90% RH to not include capillary water) was defined by Hansen and Young [72]. It was 3.8 and 4.1 at *w/c* ratio of 0.4 and 0.6 respectively. Jennings has reviewed different studies and calculations of water in context of colloidal model CM-II. He reported the values for the C-S-H including water within large gel pores (LGP) with

packing density of globules 0.59 as 5. This value decreases with increase of packing density to e.g. 4 at packing density of 0.64. The drying of all LPG leads to H_2O content of 2.7 [6].

Experiments by Hansen and Young [72] and modelling by Jennings [6] showed that the removal of water through equilibration of samples at 11% relative humidity declines the H_2O content down to 2.1. At this stage it is assumed that the C-S-H globules are saturated and has water layer adsorbed on the outer surface [6], [28]. Feldman and Ramachandran measured H_2O contents in hydrated C_3S at that humidity and obtained slightly lower value of 1.96. They defined formula for C-S-H as $Ca_{z=1.64}Si_{y=1}O_{(z+y/2-3/2)=3.64}(H_2O)_{1.96}$ [73].

The SANS experiments shown that the water content of saturated globules alone is 1.80 assuming C/S value of 1.70 [7]. Upon application of d-drying[5] remaining water content in the C-S-H is 1.2-1.5 [6], [28], [73].

The other review has been performed by Chen [74]. It verified the influence of C/S ratio on the C-S-H within oven and d-dried hydrated C_3S, C_2S and CaO-SiO system. It is shown that the increase of C/S ratio is accompanied by the rise of the water molar content of C-S-H (figure 2.18).

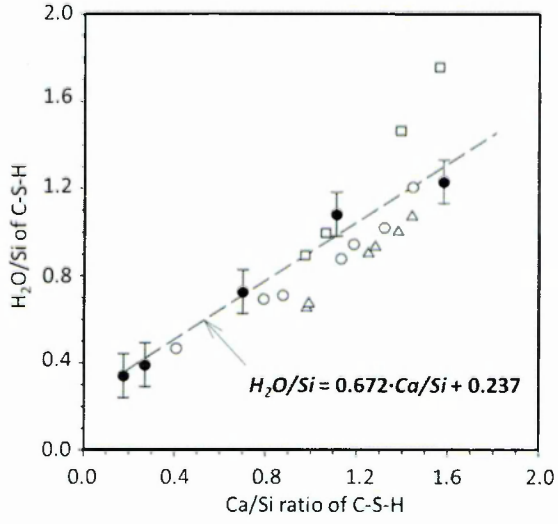

Figure 2.18 C–S–H water content (H_2O/SiO_2) as a function of Ca/Si ratio. Data obtained after: oven drying at 110°C of CaO-SiO_2 (○) and β-Ca_2SiO_4 (□) [43]; d-drying of CaO-SiO_2 (△) (reported in [74]) and Ca_3SiO_5 (●) [74].

2.4.3. Density

The same consideration as for C-S-H water content to compare like-with-like has to be exercised when considering C-S-H density. Additionally, the care must be taken as to whether or not the pore volume is excluded from calculation.

[5] equilibration with ice at -79°C by continuous evacuation with water pressure $5 \cdot 10^{-4}$ torr; equivalent to drying at 105°C in a CO_2 free atmosphere with uncontrolled humidity or 145°C with heating rate 10°C/min in dry CO_2-free N_2 [51]

The densities of C-S-H reviewed by Jennings for corresponding states of C–S-H are also given in [6]. The density including water within large gel pores (LGP) with packing density of globules 0.59 is 1.83 g/cm^3. In the reverse manner to H_2O content, density increases with increase of packing density to e.g. 2.03 g/cm^3 at packing density of 0.64. Density of saturated C-S-H based on Tennis and Jennings prediction model of high and low density C-S-H at 20°C was evaluated as 1.99 g/cm^3 [41]. The density for nearly saturated C-S-H created upon hydration of full C_3S was defined as 1.85-1.90 g/cm^3 [72].

When all LPG are dried density is 2.31 g/cm^3 and at 11% relative humidity rises to 2.47 g/cm^3 [6]. The helium piknometry gives, at the same humidity, values of 2.43-2.45 g/cm^3 for C-S-H in fully reacted C_3S paste [75]. While for CH leached, fully hydrated C_3S paste density is 2.18 g/cm^3 as measured by gas piknometry [72]. Progressive drying below that humidity, according to Jennings, actually causes increase of density. It is interpreted as the removal of water from interlayer spaces is accompanied by their collapse and hence both mass and volume decrease. For empty interlayer the density increases to 2.58 g/cm^3. Then water is dried from intraglobule space without change in the volume hence density declines to 2.25-2.53 g/cm^3 [6].

Taylor reported the density of 2.6-2.7 g/cm^3 for C-S-H dried at 110°C with corresponding H_2O content of 0.85 [28]. According to results of helium piknometry the density of d-dried C_3S and cement pastes is 2.2-2.4 g/cm^3, after correction for CH and other hydrates it is 2.4-2.5 g/cm^3 for C-S-H [28], [75], [76]. In the same conditions water piknometry shows much higher values 2.6-2.7 g/cm^3 (without correction). Feldman attributed the difference to the empty spaces entrapped between collapsed layers which water can easily penetrate but helium does very slowly [76]. Nevertheless, determination through the mass changes upon d-drying gave 2.5-2.6 g/cm^3 [28]. Hansen in his review [34] of Powers and Brownyard model evaluated the density of 2.51 g/ cm^3 for C-S-H including non-evaporable water (0.23g / g of cement) but excluding any gel water in Powers and Brownyard's terminology[6].

A recent and now widely quoted value of 2.604 g/cm^3 was evaluated for saturated C-S-H globules with water content 1.8 – no adsorb surface layer, without drying of samples by SANS experiments [7].

The summary of density review is presented in table 2.2.

[6] non-evaporable water - part of total water that persists in paste at the pressure below $5 \cdot 10^{-5}$ mmHg at 23°C; gel water - water within C-S-H gel

Table 2.2 Summary of C-S-H density values from literature; additionally the values of C/S and H/S are listed where possible.

Density [g/cm^3]	Material	Method / Model used to obtain density	C/S	H/S	Ref.
1.83	C-S-H; including water in LGP	CM-II	1.7	5	[6]
1.85-1.90	C-S-H of C_3S paste; saturated at 90% RH - no capillary water	Shrinkage weight loss curve and gas piknometry at 11% RH, ‡	1.7	3.8-4.1	[72]
1.99	C-S-H of cement paste; saturated	Tennis and Jennings model	ng	ng	[41]
2.03	C-S-H; packing density of globules 0.64	CM-II	1.7	4	[6]
2.31	C-S-H; all LPG dried	CM-II	1.7	2.7	[6]
2.47	C-S-H: saturated globule with monolayer at surface at 11% RH	CM-II	1.7	2.1	[6]
2.43-2.45	C-S-H of C_3S paste at 11% RH	Helium piknometry, #	ng	ng	[75]
2.18	C-S-H of C_3S paste at 11% RH ‡	Gas piknometry, ‡	ng	2.1	[72]
2.58	C-S-H: globule with empty interlayer spaces and full IGP	CM-II	1.7	1.85	[6]
2.25-2.53	C-S-H: empty globule	CM-II	1.7	1.3-	[6]
2.6-2.7	C-S-H dried at 110°C	(?) using water, #	ng	0.85	[28]
2.2-2.4	d-dried C_3S and cement pastes	Helium piknometry, †	–	–	[75], [76]
2.4-2.5	C-S-H of d-dried C_3S and cement pastes	Helium piknometry, #	ng	ng	[28], [75]
2.6-2.7	d-dried cement paste	Water piknometry, †	–	–	[76]
2.5-2.6	d-dried cement paste	Mass changes upon d-drying, †	–	–	[28]
2.51	C-S-H solid gel particles	Evaluation of Powers and Brownyard model	ng	ng	[34]
2.604	C-S-H: saturated globules	SANS	1.85 (1.70*)	1.87 (1.80)	[7]

‡ - CH leached paste; †- without correction for CH; # - corrected for CH (and other hydrates for cement pastes); ng - not given; '–' - not applicable; '*' – assumed;

3. NMR relaxometry

"NMR is a physical phenomenon utilized to investigate molecular properties of matter by irradiating atomic nuclei in a magnetic field with radio waves" Bernhard Blümich [77]

3.1. EXCITATION AND RELAXATION

The description of NMR relaxometry presented in this and the following sections is based on its presentation in several classic NMR texts [77]–[82].

Many atomic nuclei (e.g. ^{1}H, ^{2}H, ^{31}P, ^{14}N, ^{13}C, ^{19}F) possess non-zero spin angular momentum (spin, $\vec{I}$). Hence, they have a nuclear magnetic moment ($\vec{\mu}$) and in many ways behave like tiny magnets. The angular momentum and magnetic moment are related as $\vec{\mu} = \gamma \cdot \vec{I}$ where γ is the gyromagnetic, or more correctly magnetogyric, ratio of the nuclear species. In the absence of an applied magnetic field the nuclear magnetic moments are oriented randomly. When an external, static magnetic field (B_0) is applied the spin vectors align themselves with this field.

Quantum mechanics approach

The energy of a nuclear magnetic moment, $\vec{\mu}$, in a magnetic field, $\vec{B}_0$, depends on its orientation according to:

$$E = -\vec{\mu} \cdot \vec{B}_0 = -\gamma m_I \hbar B_0 \tag{3.1}$$

where $\hbar$ is Planck constant divided by 2π; Here m_I defines the component of I in the direction of B_0 that is universally taken as the z-direction. For ^{1}H, $I = ½$ so $m_I = \pm ½$.

There are $(2I+1)$ energy levels for each nucleus. The energy difference between different states is $\Delta E = \gamma \hbar B_0$. The parallel orientation ('up') is slightly energetically preferred. The populations of the parallel ($N_{parallel}$) and anti-parallel ($N_{anti\text{-}parallel}$) states are described by Boltzmann distribution equation:

$$\frac{N_{anti-parrallel}}{N_{parrallel}} = e^{-\Delta E/(k_B \cdot T)} \tag{3.2}$$

where k_B is Boltzmann constant and T is temperature.

The strength of the bulk nuclear magnetisation depends on the excess number of nuclei in the parallel population ($\Delta N = N_{parallel} - N_{anti\text{-}parallel}$). If the temperature decreases the

magnetisation increases, there are more parallel spins. When temperature is increased the ratio of anti-parallel to parallel populations approaches unity and magnetisation approaches zero.

Spins can change their energy state by exchanging a photon of energy with their environment. The frequency of electromagnetic radiation that induces spin transitions (υ_0) is expressed by equation $\Delta E = h\upsilon_0$. By considering the energy difference between states, $\upsilon_0 = \gamma B_0 / (2\pi)$. This leads to the Larmor equation[7] $\omega_0 = \gamma B_0$, where ω_o is angular precession frequency called the Larmor frequency.

Classical mechanics approach

For a macroscopic sample, which contains many nuclei, it is more convenient and intuitive to consider the net magnetization using a classical approach. All similar spins in the sample are considered as a group – 'packet'. Their magnetic momenta are added as vectors in x, y and z direction in the presence of an external magnetic field (B_0) oriented in z-direction, the so-called equilibrium state. The sum of magnetic moments in the x,y-plane – transverse magnetisation, is zero[8]: $M_x^o = 0$ and $M_y^o = 0$, as their transverse magnetic components cancel out. In z-direction, as there is an excess of parallel spins, the longitudinal net magnetisation is observed: $M_z^o = \Delta N \cdot \mu = \Delta N \cdot \gamma \cdot m_I \cdot \hbar$ (figure 3.1). Opposing spins pair up and cancel out their observable magnetisation.

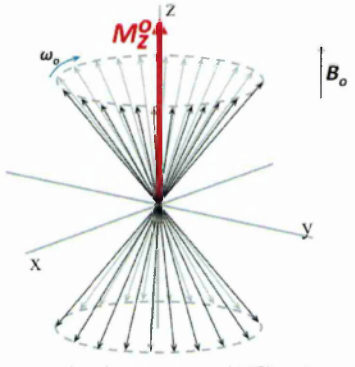

Figure 3.1 The macroscopic, net magnetization vector ($\boldsymbol{M_z^o}$) of nuclear magnetic moments (I = ½) in external magnetic field.

Excitation

When the net nuclear magnetization vector ($\vec{M}$) is disturbed, that is tipped away from alignment with the external magnetic field, it precesses coherently around the direction of the field at the Larmor frequency[7]:

$$\omega_0 = \gamma B_0 \tag{3.3}$$

---

[7] note: exact Larmor equation is written with negative sign (to compensate for a negative γ parameter)

[8] M^o indicates equilibrium state magnetisation, $M_{x,y,z}$ indicate magnetization in x, y and z direction

The rate of change of macroscopic angular momentum ($d(\vec{M}/\gamma)/dt$) depends on the torque exerted on the magnetisation by the external magnetic field, $\vec{M} \times \vec{B_0}$. The precession of the net magnetization is hence described by equation of motion:

$$\frac{d\vec{M}}{dt} = \gamma \vec{M} \times \vec{B_0} \tag{3.4}$$

In NMR experiments, the tipping of magnetisation from the z-axis 'equilibrium state' aligned with the external magnetic field is induced by the application of a short excitation pulse. An additional oscillating magnetic field (B_1) is applied in direction perpendicular to the external field B_0. The frequency of the B_1 field is set to the Larmor frequency to achieve resonant interaction. The duration of the excitation pulse (t_θ) defines the angle through which net magnetization is rotated:

$$\theta = \gamma \cdot B_1 \cdot t_\theta \tag{3.5}$$

The description of magnetisation is more convenient with reference to a rotating coordinate frame[9]. This Cartesian frame rotates at the Larmor frequency, ω_0, about B_0. In this frame of reference B_0 is transformed to zero. The net magnetisation appears stationary in the rotating frame in contrast to laboratory frame where it precesses around external magnetic field B_0. Applied B_1 is stationary and $\vec{M}$ rotates about B_1.

Following a 90° pulse applied along the y'-axis of rotating frame, the precession of net magnetisation, $\vec{M}$, over time (t) is given by

$$\begin{aligned} M_x(t) &= M_z^o \cdot \cos(\gamma \cdot B_0 \cdot t) \\ M_y(t) &= -M_z^o \cdot \sin(\gamma \cdot B_0 \cdot t) \\ M_z(t) &= 0 \end{aligned} \tag{3.6}$$

Relaxation

Equation 3.6 implies that the longitudinal magnetisation (M_z) is constant and both transverse magnetisations (M_x and M_y) precess indefinitely about the magnetic field B_0. However, experimentally it is observed that the M_z increases progressively to achieve again the equilibrium while M_x and M_y both approach zero. The reason for such a discrepancy lies in the apparent assumption that all nuclei experience exactly the same magnetic field, B_0. However, in 'real life' each nuclei 'sees' a slightly different magnetic field. The difference between B_0 and the actual field is called the local field.

[9] in the rotating coordinate frame axes are marked as x', y' and z'

There are various sources of variations in the local magnetic fields. The main ones are: interactions between nuclei within the sample as each of them experiences magnetic fields produced by neighbouring nuclei; interactions of nuclei with unpaired electrons in chemical bonds; the presence of magnetic material in a form of paramagnetic species; and magnet inhomogeneity which causes a spread of B_0 values over the sample volume. Additionally, local fields may change with time. Due to these conditions spins precess at different and changing frequencies. Therefore, as spins becomes incoherent in motion they dephase. This in turn causes relaxation.

Relaxation terms have been added to equation (3.4) by Bloch:

$$\begin{aligned}\frac{dM_x}{dt} &= \gamma|M \times B_0|_x - \frac{M_x}{T_2} \\ \frac{dM_y}{dt} &= \gamma|M \times B_0|_y - \frac{M_y}{T_2} \\ \frac{dM_z}{dt} &= \gamma|M \times B_0|_z + \frac{(M_z^o - M_z)}{T_1}\end{aligned} \tag{3.7}$$

where T_1 and T_2 are the longitudinal and transverse relaxation times, respectively.

Relaxation in the longitudinal direction is due to an exchange of energy between the nuclear spin system and the surrounding environment known as the 'lattice'. The magnetisation in the z-direction realigns with the direction of external magnetic field B_0. It relaxes to M_z^o, as the equilibrium is being reached. The rate of this process is characterised by T_1 known as spin-lattice or longitudinal relaxation time. The longitudinal relaxation process is described by

$$\frac{dM_z}{dt} = \frac{(M_z^o - M_z)}{T_1} \tag{3.8}$$

The equation governing magnetisation recovery following a 90° pulse is:

$$M_z(t) = M_z^o\left[1 - \exp\left(-\frac{t}{T_1}\right)\right] \tag{3.9}$$

Transverse relaxation is the process of direct interaction of nuclear spins to reach the thermal equilibrium amongst themselves. The time constant which describes the rate at which spins lose coherence – dephase, and magnetisation decay in the x',y'-plane is called the T_2 relaxation time. It is also known as T_2 spin-spin or transverse relaxation time. The spin relaxation process is described as

$$\frac{dM_{x,y}}{dt} = -\frac{M_{x,y}}{T_2} \tag{3.10}$$

which leads to:

$$M_{x,y}(t) = M_{x,y}(0) \cdot \exp\left(-\frac{t}{T_2}\right) \tag{3.11}$$

3.2. NMR Relaxometry measurement techniques

During experiments signal is detected along the fixed axis (x' or y') of transverse plane.

3.2.1. Free induction decay

The most basic NMR pulse sequence is free induction decay (FID) sequence. It involves application of a single 90° radio frequency pulse (P_{90}) – figure 3.2. This pulse rotates the equilibrium state magnetisation (M) along the z'-axis to the x',y'- plane. If the magnetic field B_1 lies along the x'-axis of rotating frame - pulse $P_{90}^{x'}$, magnetisation will be rotated to y'-axis – figure 3.2 (inset a). The net magnetisation in y'-direction determines the strength of observed signal called the free induction decay (FID) signal.

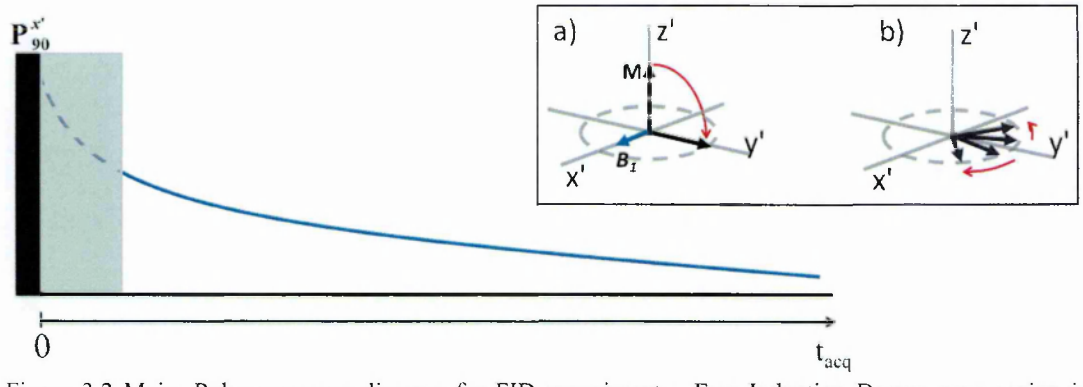

Figure 3.2 Main: Pulse sequence diagram for FID experiment – Free Induction Decay; grey region is spectrometer dead time. Inset: a) $P_{90}^{x'}$ along x'-axis rotates M from the equilibrium position to y'-axis, b) Magnetisation decreases as spins dephase.

The transverse relaxation occurs as the magnetic moments dephase - figure 3.2 (inset b). The signal decays. In perfect experimental conditions the time constant of decay would be T_2. However, in practice the FID signal has an apparent time constant (T_2^*) which includes contribution of molecular interaction (T_2) and magnet field inhomogeneity ($T_2^{\Delta B}$). The rate of relaxation due to FID decay is express as:

$$\frac{1}{T_2^*} = \frac{1}{T_2} + \frac{1}{T_2^{\Delta B}}$$

$$T_2^{\Delta B} \approx \frac{2}{\gamma \cdot \Delta B_0} \tag{3.12}$$

where ΔB_0 is magnet inhomogeneity.

The contribution of magnet inhomogeneity ($T_2^{\Delta B}$) is of order of 0.5 to 1.0 ms for low frequency bench top spectrometers. This implies that only for a very short T_2 value can the true T_2 relaxation time be measured. The excitation pulse in experiments is followed by the spectrometer dead time (grey region in fig. 3.2) during which signal is not detected. This time, even though it lasts only a few microseconds, hinders the observation of the chemically bound water with the shortest relaxation time components.

3.2.2. CPMG pulse sequence

Hahn spin-echo

Hahn [83] was the first to suggest a method for overcoming the limitation of the external magnetic field inhomogeneity. He proposed the application of 180° pulse ($P_{180}^{x'}$) at time τ – known as the pulse gap, after the initial $P_{90}^{x'}$, as shown in figure 3.3. This reverses the loss of coherence due to field inhomogeneity - figure 3.4. The magnetisation refocuses at time 2τ along the y'-axis and a spin-echo is created. The amplitude of the echo, at time 2τ, is already attenuated due to true transverse relaxation. Hence, the maximum of the echo amplitude is a function of T_2 relaxation time. It is necessary, in Hahn spin-echo experiment, to conduct separate experiments for each value of τ. Molecular diffusion is a second source of echo attenuation if there is a magnetic field gradient present. Diffusion is most significant for big τ. The magnetisation decay depends then on a combination of relaxation due to molecular interaction and diffusion. It is expressed as:

$$M_{y'}(2\tau) = M_o \cdot \exp\left[-\frac{2\tau}{T_2} - \frac{2}{3}\cdot\gamma^2\cdot G^2\cdot D\cdot\tau^3\right] \tag{3.13}$$

where G is magnetic field gradient strength and D is diffusion coefficient.

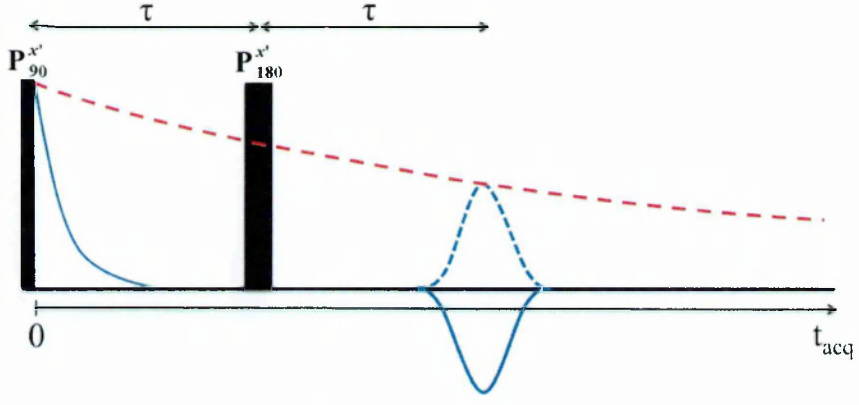

Figure 3.3 The Hahn spin-echo pulse sequence diagram. The red dash line shows the decay of transverse magnetisation.

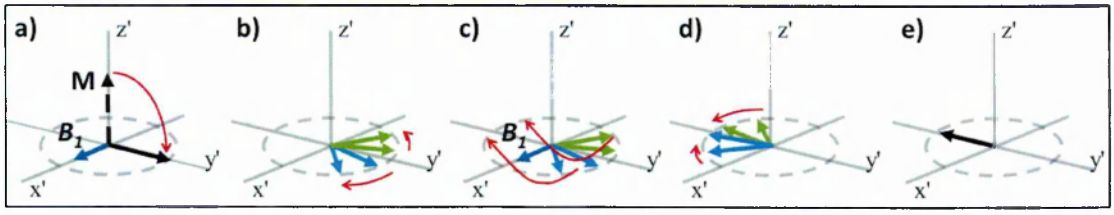

Figure 3.4 The Hahn spin-echo experiment: a) application of $P_{90}^{x'}$ along x'-axis, b) de-phasing of spins, c) application of $P_{180}^{x'}$ along x'-axis at time τ, d) re-phasing of spins, e) refocused magnetisation at time 2τ.

Carr – Purcell method

Carr and Purcell [84] provided a method that reduces the impact of diffusion on the determination of T_2 relaxation time and also allows T_2 to be measured in 'one shot'. They modified the Hahn's spin-echo pulse sequence by application of a train of P_{180} pulses as shown in figure 3.5. The Carr-Purcell sequence can be described as $P_{90}^{x'} - \tau - [P_{180}^{x'} - 2\tau]_{N_E}$ where N_E is the number of echo acquired. It shows that subsequent 180° pulses are at τ, 3τ, 5τ... whereas the amplitude of echoes appears at 2τ, 4τ, 6τ... In Carr-Purcell method, as in Hahn spin-echo, all pulses are applied along the same axis, x' in this description. Hence, echoes are alternately positive and negative. The advantages of this technique are: a shortage of experiment time and elimination of diffusion effect. Hence, the expression for decay of magnetisation (echo amplitude at time $2n\tau$, where n is the echo number) is

$$M_{y'}(t) = M_o \cdot \exp\left[-\frac{t}{T_2} - \frac{1}{3}\cdot\gamma^2\cdot G^2\cdot D\cdot\tau^2\cdot t\right]$$
$$M_{y'}(t) \cong M_o \cdot \exp\left(-\frac{t}{T_2}\right) \quad \text{for short } \tau \tag{3.14}$$

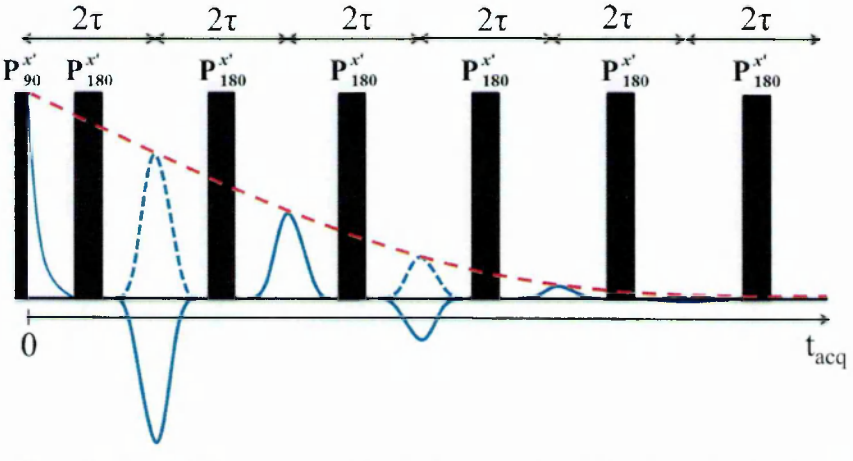

Figure 3.5 The spin-echoes pulse sequence diagram by Carr-Purcell method. The red dash line shows the decay of transverse magnetisation.

Any imperfection in the P_{180} length causes incomplete rephasing of magnetic moments. The effect is cumulative with each pulse as P_{180} is applied along x'-axis and rotates alternately the magnetisation from y' to $-y'$ direction. It is especially important during the measurements of longer T_2 as the acquisition of many P_{180} is required.

Meiboom – Gill modification

Meiboom and Gill [85] introduce a modification to the Carr-Purcell method by shifting the phase of P_{180} by 90° relatively to initial $P_{90}^{x'}$. The P_{180} pulses are applied along y' direction as shown in figure 3.6. Hence, magnetic spins are rotated about the y'-axis and all echoes are positive. Pulse sequence is described as $P_{90}^{x'} - \tau - [P_{180}^{y'} - 2\tau]_{NE}$. The pulse orientation causes that only odd echoes have slightly reduced amplitudes due to pulse imperfection, but not cumulatively.

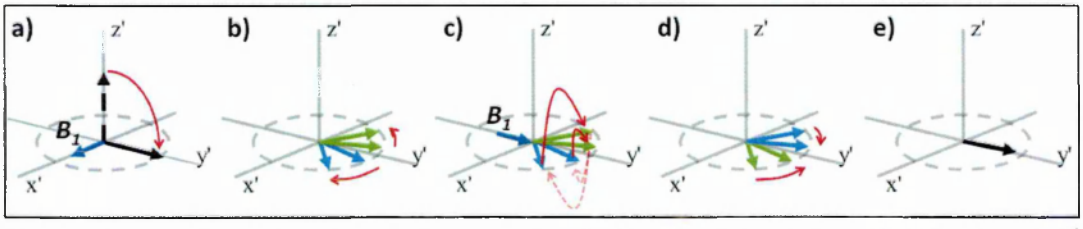

Figure 3.6 De-phasing and re-phasing of spins during the CPMG pulse sequence: a) application of $P_{90}^{x'}$ along x'-axis, b) de-phasing of spins, c) application of $P_{180}^{y'}$ along y'-axis, d) re-phasing of spins, e) refocus of magnetisation at time 2τ.

The Carr and Purcell NMR method with modification of Meilboon and Gill is called ***CPMG pulse sequence***. The CPMG diagram is presented in figure 3.7. The CPMG sequence can be described as $P_{90}^{x'} - \tau - [P_{180}^{y'} - 2\tau]_{NE}$.

The common version of CPMG pulse sequence used nowadays involves application of P_{180} alternately along y' and $-y'$-axis and can be described as $P_{90}^{x'} - \tau - [P_{180}^{y'} - 2\tau - P_{180}^{-y'} - 2\tau -]_{NE/2}$.

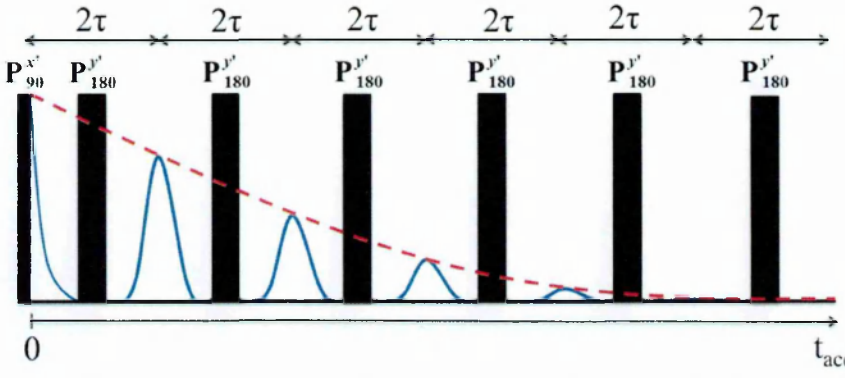

Figure 3.7 Pulse sequence diagram for CPMG sequence. The red dash line shows the decay of transverse magnetisation.

3.2.3. Quadrature echo sequence

The Quadrature echo experiment, also called the Quad or Solid echo experiment, has been designed to measure the static inter-nuclear magnetic dipole-dipole interaction [86].

The 'rigid' spins of crystalline solids coupled by such an interaction are characterised by the very short T_2 relaxation time (~few μs) due to strong dipolar coupling of the spins. They are present in chemically bound and adsorbed water (solid protons). In the elementary FID experiment the relaxation due to that component is not seen or is already significantly attenuated due to the instrument dead time. While for the CPMG experiment the first echo amplitude is even further in time to 'see' it. The Quadrature pulse sequence overcomes that limitation by refocusing dipolar interaction.

Quadrature echo sequence (fig. 3.8) comprises two P_{90} pulses shifted relatively to each other by 90°. The pulses are spaced τ pulse gap time apart: $P^{x'}_{90} - \tau - P^{y'}_{90}$. There are two phenomena observed. The more mobile spins (liquid) dephase continuously after first pulse due to spin-spin molecular interaction. The second $P^{y'}_{90}$ does not alter their magnetisation [87]. Hence, the observable signal due to these spins is FID liquid signal as shown by dash - dot line extension in figure 3.8.

The application of second $P^{y'}_{90}$ reverses the decay of solid signal - magnetic-dipolar interactions. The magnetisation of dipolar pairs of 'rigid' spins refocuses. It is partially recovered at time τ from second $P^{y'}_{90}$. The decay due to dipolar interaction is not exponential but has an approximately Gaussian shape – echo in figure 3.8.

More details on determination of the signals intensities for 'rigid' and more mobile spins is presented in section 4.3.1.

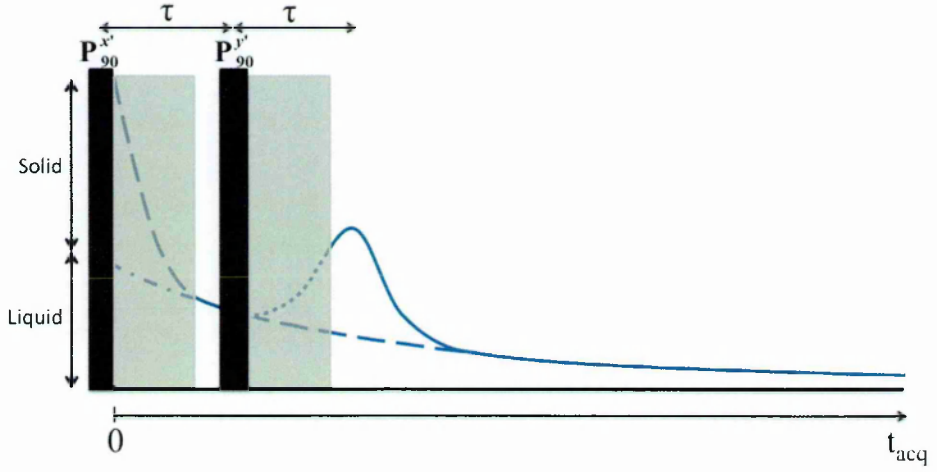

Figure 3.8 Pulse sequence diagram for Quadrature Echo sequence. The solid line presents the observable signal. Dash line shows the sum of solid and liquid signals as it would look only after $P^{x'}_{90}$. Dash – dot line shows the liquid signal. Grey region is spectrometer dead time.

3.2.4. T_1 measurements

There are two methods to measure T_1 spin-lattice relaxation time: saturation and inversion recovery.

3.2.4.1. Saturation recovery

The saturation recovery sequence (fig. 3.9) involves application of multiple $P^{x'}$ pulses. They are used to destroy, that is bring to zero, the longitudinal magnetisation. Following that, for a variable time τ_{rec}, the spin-lattice relaxation is allowed. Hence, the magnetisation recovers partially or fully depending on the τ_{rec}. A single $P^{x'}_{90}$ pulse is utilised to measure the momentary magnetisation at times τ_{rec}. The longitudinal magnetisation as a function of τ_{rec} is described as

$$M_z(t) = M_z^o\left[1 - \exp\left(-\frac{\tau_{rec}}{T_1}\right)\right] \tag{3.15}$$

where M_z^o is the equilibrium state magnetisation - aligned with the external magnetic field.

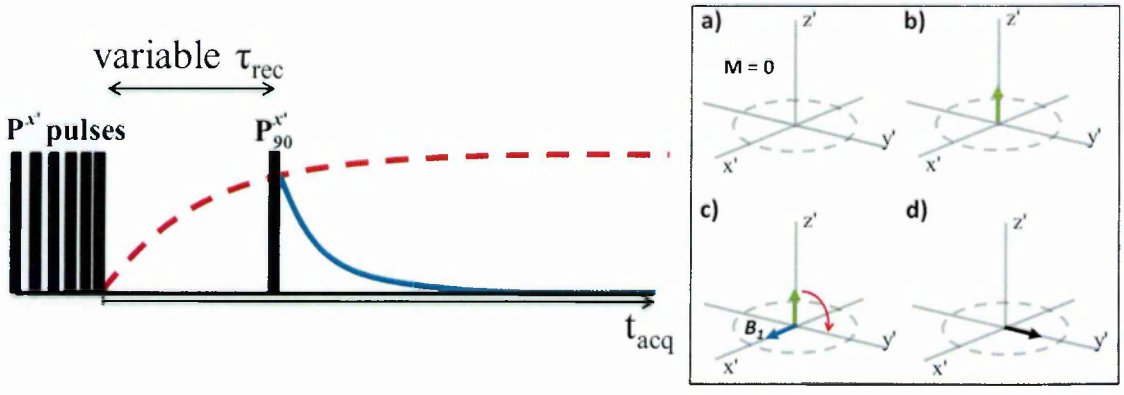

Figure 3.9 Left: Pulse sequence diagrams for T_1 saturation recovery at variable τ_{rec}. The red dash line shows the recovery of longitudinal magnetisation. Right: a) Magnetisation is saturated, $M = 0$; b) Recovery of magnetisation during τ_{rec}; c) application of $P^{x'}_{90}$; d) reverse magnetisation in transverse plane.

3.2.4.2. Inversion recovery

The inversion recovery sequence is also used to determine T_1. The difference in the pulse sequence in comparison with saturation recovery is preparation of the initial magnetisation. In this case, the $P^{x'}_{180}$ inverts the magnetisation along the z'-axis – figure 3.10. After that both sequences follow the same way. The spin-lattice relaxation process due to inversion recovery is expressed as

$$M_z(t) = M_z^o\left[1 - 2\cdot\exp\left(-\frac{\tau_{rec}}{T_1}\right)\right] \tag{3.16}$$

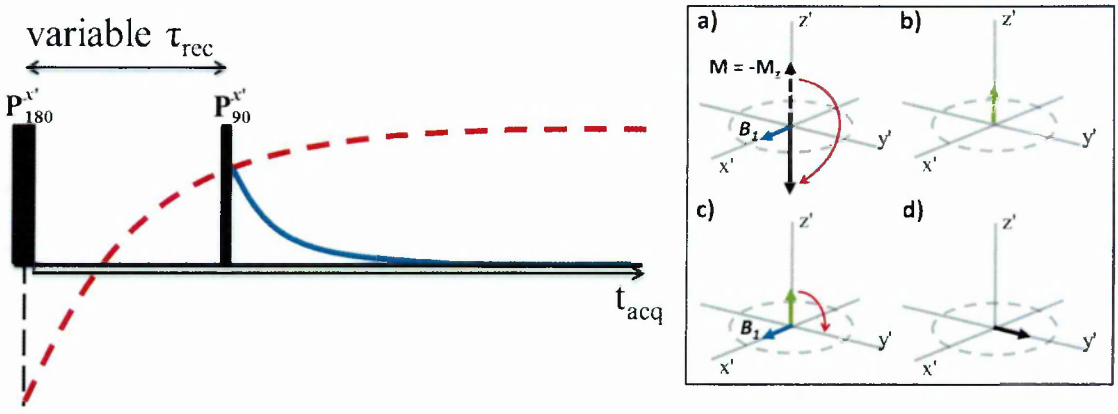

Figure 3.10 Left: Pulse sequence diagrams for T_1 inversion recovery. The red dash line shows the recovery of longitudinal magnetisation. Right: a) magnetisation is reversed by $P^{x'}_{180}$, $M = -M_z$; b) recovery of magnetisation during τ_{rec}; c) application of $P^{x'}_{90}$; d) reverse magnetisation in transverse plane.

Inversion recovery is the slower of two methods as the subsequent scans have to be performed after magnetisation fully recovers, for saturation recovery it is saturates to zero anyway at the beginning of sequence. However, as the magnetisation is reversed to $-M_z$ the sensitivity of method doubles.

T_1 measurements serve to establish the repetition time (τ_{rd}) of successive experiments as T_1 mirrors the time when magnetisation is fully recovered. Time τ_{rd} should be ~ $5 \cdot T_1$.

3.3. Theory of Relaxation

3.3.1. BBP theory

The relaxation theory is complex and the advanced analysis based on quantum statistics is outside of the scope of this work and can be found in [88], [89]. What follows here is a brief summary.

Spins undergo rotational and translational motions that modify the magnetic dipole – dipole interactions between nuclei and the other interactions contributing to the local magnetic fields in the presence of a static magnetic field. This gives rise to the fluctuations in the local magnetic fields. The relaxation processes due to these perturbations in the dipolar field for liquids was first explained by Bloemberger, Purcell and Pound in 1948. The theory of relaxation is called after them: BPP theory [89].

Changes of the intensity and direction of the local magnetic field fluctuations with time are described by autocorrelation functions describing the relative motion of spins pairs $G^{(m)}(t)$ [90]. The autocorrelation functions are given by:

$$G^{(m)}(t) = \alpha^{(m)} \cdot \left\langle \frac{Y_{2m}(\theta_o, \phi_o) \cdot Y^*_{2m}(\theta, \phi)}{r_o^3 \cdot r^3} \right\rangle \tag{3.17}$$

where $Y_{2m}(\theta_o, \phi_o)$ and $Y^*_{2m}(\theta, \phi)$ are the spherical harmonic functions of order m that has values 0, 1 and 2. The coordinates (r_o, θ_o, ϕ_o) and (r, θ, ϕ), describe the internuclear vectors at time 0 and t respectively. The $\alpha^{(m)}$ are constants such that $\alpha^{(0)}=48\pi/15$, $\alpha^{(1)}=8\pi/15$ and $\alpha^{(2)}=32\pi/15$. The * indicates the complex conjugate. The notation ‹› means the ensemble average over all pairs of the spins, I, (or, equivalently, one pair over all starting times)

In turn, the frequency dependence of intensity of fluctuation is expressed by spectral density functions $J^{(m)}(\omega)$ that are the Fourier transform of autocorrelation functions [90]:

$$J^{(m)}(\omega) = \int_{-\infty}^{\infty} G^{(m)}(t)\, e^{-i\omega t} dt \tag{3.18}$$

The relaxation times are described in terms of spectral density functions $J^{(m)}(\omega)$. For spins I associated with the same nuclear species T_1 and T_2 are expressed as [90], [79]:

$$\frac{1}{T_1} = \frac{3}{2} \cdot \left(\frac{\mu_0}{4\pi}\right)^2 \cdot \gamma^4 \cdot \hbar^2 \cdot I \cdot (I+1) \cdot \left[J^{(1)}(\omega_0) + J^{(2)}(2\omega_0)\right] \tag{3.19}$$

$$\frac{1}{T_2} = \frac{3}{2} \cdot \left(\frac{\mu_0}{4\pi}\right)^2 \cdot \gamma^4 \cdot \hbar^2 \cdot I \cdot (I+1) \cdot \left[\frac{1}{4} \cdot J^{(0)}(0) + \frac{5}{2} \cdot J^{(1)}(\omega_0) + \frac{1}{4} \cdot J^{(2)}(2\omega_0)\right] \tag{3.20}$$

where μ_0 is the vacuum permeability.

For simple Brownian diffusion and rotations the spectral density functions are [82], [79]:

$$J^{\times}(\omega) = \frac{15}{12} \cdot J^{(0)}(\omega) = \frac{15}{2} \cdot J^{(1)}(\omega) = \frac{15}{8} \cdot J^{(2)}(\omega) = \frac{1}{r^6} \cdot \frac{2 \cdot \tau_c}{1 + \omega^2 \cdot {\tau_c}^2} \tag{3.21}$$

where τ_c is correlation time of the motion and r is nuclear distance.

The dependence of T_1 and T_2 relaxation time on the correlation time τ_c can be evaluated by substitution of spectral density functions – eq. (3.21), into the expressions for relaxation rates – eq. (3.19) and (3.20). The relation is presented in figure 3.11. At the lower values of τ_c ($\omega_o \cdot \tau_c < 0.62$) molecular motion is fast and T_1 and T_2 coincide. This is called the 'extreme narrowing limit'. The T_1 goes through a minimum at $\omega_o \cdot \tau_c \approx 0.62$. With increase of correlation time T_1 and T_2 diverge. T_1 increases whereas T_2 decreases due to $J^{(0)}(0)$ contribution towards the 'rigid lattice limit' determined by the natural dipolar linewidth [82].

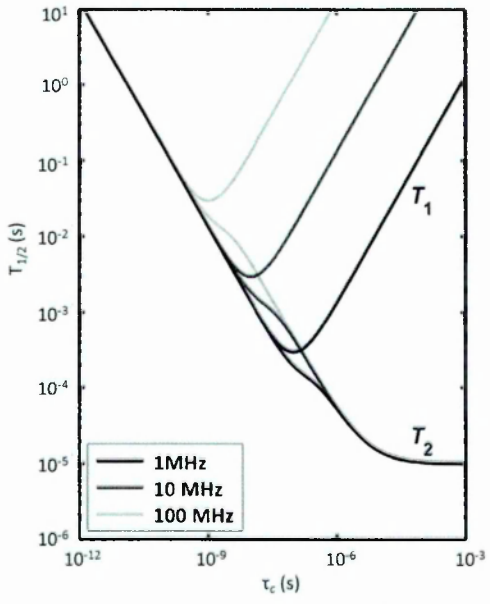

Figure 3.11 T_1 and T_2 relaxation times for hydrogen spins as a function of correlation time τ_c [82].

3.3.2. Fast exchange model of relaxation for liquids in pores and for pore size analysis

Introducing liquid to the empty space of pores in materials manifests in the increase of the relaxation rate in comparison with the bulk liquid. It implies interaction between the solid and liquid at their interface. The resulting relaxation rate of water in pores is the weighted average between slowly relaxing liquid in the pore bulk and rapidly relaxing surface water.

The equation which links the relaxation rate with the surface to volume (S/V) ratio and hence to pore size (d) for a system in which water molecules are in fast exchange is [27]:

$$\frac{1}{T_{1,2}} = \frac{V-\varepsilon S}{V}\cdot\frac{1}{T_{1,2}^{bulk}} + \frac{\varepsilon S}{V}\cdot\frac{1}{T_{1,2}^{surf}} \approx \frac{\varepsilon S}{V}\cdot\frac{1}{T_{1,2}^{surf}} \tag{3.22}$$

where $T_{1,2}$ is observed T_1 or T_2 relaxation time, $T_{1,2}^{surf}$ and $T_{1,2}^{bulk}$ are the relaxation times of surface-adsorbed and bulk liquid respectively and ε is the thickness of surface layer.

The last approximation in equation (3.22) results from the facts that surface volume is $\varepsilon S << V$ and surface relaxation time is $T_{1,2}^{surf} << T_{1,2}^{bulk}$. The surface layer thickness and relaxation time are related through the surface relaxivity $\lambda = \varepsilon / T_{1,2}^{surf}$. The pore size determination requires the knowledge of surface relaxivity. It may be established through NMR measurements of material dried to mono-layer coverage or by calculation.

An assumption of the model is the rapid exchange between molecules adsorbed on the pore surface and in the remaining part of the bulk liquid. The range of molecular diffusion should be larger than the size of measured pores: $6 \cdot D \cdot T_{1,2}^{bulk} >> d^2$, where D is the liquid self-diffusion coefficient. It ensures that each molecule experiences equally the surface-layer and

bulk-pore environments. If this condition is not fulfilled then multi-exponential decay is observed [27], [82]. Application of model to cementitious materials is presented in section 3.4.3.1.

3.3.3. Korb model

A theoretical model of surface relaxation in proximity of a pore surface was proposed by Korb and his co-workers [91]–[93]. The mechanism of spin relaxation is explained by the modulation of the magnetic dipolar interaction between proton spins, *I*, diffusing on the pore surface and static paramagnetic impurities electrons, *S*, embedded in the pore surface. The modulation is induced by the translational diffusion of the *I* spins relative to fixed *S* spins. The dynamics of molecules at the pore surface are schematically represented in figure 3.12. The coexistence of two correlation time was proposed. The molecule undergoes a 2-dimensional diffusion across the surface encountering the impurities spins *S* with translational time τ_m called the hopping time. The molecular walk across the surface lasts for characteristic surface residency time, τ_s. Desorption of molecule from the surface occurs after a time τ_s. The desorbed molecule has characteristics of bulk liquid. It is replaced on the surface by another molecule.

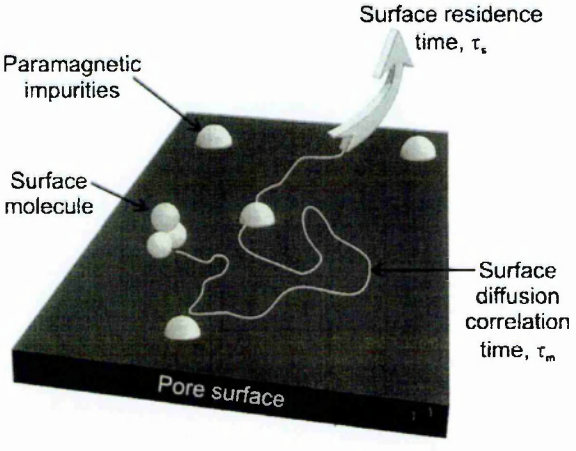

Figure 3.12 Scheme of two-dimensional diffusion process of water molecules on the pore surface containing paramagnetic impurities – Fe^{3+}. τ_s is the surface residency time, τ_m is the correlation time associated with molecule's jumps across the surface [92].

In the vicinity of the paramagnetic impurities (spins *S*) the expressions for T_1 and T_2 surface relaxation times are [91], [92]:

$$\frac{1}{T_{1,surface}} = \frac{2}{9} \cdot \gamma_I^2 \cdot \gamma_S^2 \cdot \hbar^2 \cdot S \cdot (S+1) \cdot \cdot \left[J^{(0)}(\omega_I - \omega_S) + 3 \cdot J^{(1)}(\omega_I) + 6 \cdot J^{(2)}(\omega_I + \omega_S) \right] \tag{3.23}$$

$$\frac{1}{T_{2,surface}} = \frac{4}{9}\cdot\gamma_I^2\cdot\gamma_S^2\cdot\hbar^2\cdot S\cdot(S+1)\cdot\left[J^{(0)}(0)+\frac{1}{4}\cdot J^{(0)}(\omega_I-\omega_S)\right.$$
$$\left.+\frac{3}{4}\cdot J^{(1)}(\omega_I)+\frac{3}{2}\cdot J^{(1)}(\omega_S)+\frac{3}{2}\cdot J^{(2)}(\omega_I+\omega_S)\right] \quad (3.24)$$

where γ_S and γ_I are the gyromagnetic ratio for spins I and S, $\omega_{I,S}$ is the Larmor frequency of spin I and S respectively, and $\omega_S = 658.21\cdot\omega_I$

According to the Korb model, the spectral density function for the 2-dimensional walk of spins I on the pore surface is [92]:

$$J^{(0.1.2)}(\omega) = \frac{3}{40}\cdot\frac{\pi\sigma_S\tau_m}{\delta^4}\cdot\ln\left(\frac{1+\omega^2\tau_m^2}{\left(\frac{\tau_m}{\tau_s}\right)^2+\omega^2\tau_m^2}\right) \quad (3.25)$$

where σ_S is surface density of paramagnetic impurities, δ is the minimum distance for water molecule to approach impurity, τ_s is the surface residency time, τ_m is the correlation time associated with molecule's jumps across the surface (hopping time).

3.4. NMR APPLICATION TO CEMENT BASED MATERIALS

3.4.1. Evolution of relaxation component over hydration time

The early NMR studies of cementitious materials were conducted by Blinc *et al* [18]. The experiments were performed on cement (*w/c* = 0.42) and C_3S pastes (*w/c* = 0.50) prepared with distilled water and D_2O; at frequencies 60.0 and 41.4 MHz for H_2O and D_2O respectively. The T_1 and T_2 relaxation times of single mobile component were measured by $P_{90} - \tau/2$ and Carr-Purcell pulse sequences respectively [18]. The relaxation parameters were monitored from 10 minutes to 28 days of hydration. Three distinguishable stages of hydration were observed based on the changes in relaxation times: initial stage with slow decrease of T_1 and T_2, intermediate stage (after about 2 and 8 hours for protonated and deuterated pastes respectively) identified by rapid decrease and final stage when decline slows down beyond ~40 and 80 h. The relaxation times of cement paste were systematically lower in comparison with C_3S paste indicating the influence of paramagnetic impurities on relaxation process.

Schreiner *et al* [19] examined Portland cement pastes prepared with *w/c* ratios 0.33 to 0.63 during hydration from 10 minutes to almost 1 year at 70% RH. They performed T_1, T_2 and T_2^* measurements by applying inversion recovery, Carr-Purcell and FID sequences at frequency of 38 and 19 MHz. Based on T_1 results three distinct populations of hydrogens are observed in an advance stage of hydration: solid OH groups within CH, T_1 ~ 500 ms at 38 MHz; water in micropores and layers, T_1 ~ 5 ms; and bound water within 'solid' C-S-H gel, T_1 ~ 1 ms. Four stages of hydration were identified: first, below 10 min, with a single relaxation time, T_1 ~ 30 ms; dormant period when gel mobile-water is distinguished; third stage beyond 2h when the solid component begins to grow; and final stage beyond 12 h with three components clearly distinguished. The authors noted that T_2 and T_2^* measurements for ordinary Portland cement

are not adequate as magnet inhomogeneity and paramagnetic impurities shorten relaxation times and prevent observation of all components. They suggested use of white cement paste to limit the influence of impurities and enhance the resolution.

In late 1980s, Lasic *et al* [20] monitored the evolution of T_1 relaxation times of a synthetic white cement with *w/c* = 0.42 at NMR frequency of 200 MHz. Initially two populations were observed with T_1 of about 100 ms and between 18-25 ms corresponding to water between grains of cement and early crystalline products. After 20 hours, they evolved into five distinctive hydrogen populations: hydrogens in CH, $T_1 \sim 1$ s; water in crystalline hydrates, $T_1 \sim 150$ ms; pore and adsorbed water, $T_1 \sim 30$ ms; hydrogens in C-S-H gel, $T_1 \sim 10$ ms; and water molecules in contact with paramagnetic impurities, $T_1 \sim 2$ ms.

The NMR experiments on white cement paste were also performed during the same year by Miljkovict *et al* [21]. The evolution of T_2 relaxation times of pastes with *w/c* from 0.32 to 0.62 was observed by applying CPMG and FID sequences at 90 MHz. The hydrogens were divided into liquid-like, $T_2 \sim$ 2-10 ms, and two solid-like populations, T_2 of ~10 and ~100 μs. The liquid-like T_2 decreased beyond 8h of hydration and had shorter values at lower *w/c* while solid-like T_2s stayed constant despite the hydration time and *w/c*. The intensity of solid-like hydrogens increased with time at the expense of liquid-like. The rise was higher at lower *w/c*.

In 1990s the studies were focused mainly on T_2 relaxation times and their correlation to pore size distribution based on fast exchange model as follows in section 3.4.3.1.

The new decade started with the study of T_2 relaxation time development for sealed white cement paste, *w/c* = 0.42, by Greener *et al* [24]. The authors presented a new approach to analyse FID and CPMG data. FID decay was fitted to solid like components by Gaussians and to mobile like component by single exponential. The division of solid and mobile components was set at $T_2 \sim 100$ μs. Further the mobile signal was decomposed into particular hydrogen populations based on multi-exponential fitting of CPMG decay. Authors identified five populations: protons in solid environment (CH and ettringite) with $T_2 \sim 20$ μs; interlayer water with T_2 below 100 μs; C-S-H gel water with decreasing T_2 from initial 3 ms to 200 μs at 6 days (maximum measured time); capillary pore water with T_2 reduction from ~30 ms to ~800 μs at 6 days; and the secondary hydration water with the longest T_2 of ~ 50 ms attributed to the water released due to ettringite – monosulfate conversion.

The same methodology was applied by Holly *et al* [25]. T_2 relaxation time distributions of sealed white cement pastes, *w/c* = 0.42, were measured for few months at curing temperatures of 2, 20, 60 and 100°C at 30 MHz. Authors recognised the same five hydrogen populations as Greener *et al* [24]. Mature paste hydrated for ~40 days and cured at 20°C were characterised by small quantity of capillary water, below 2%, with $T_2 \sim 1$ ms; high fraction of protons in crystalline water and OH^-, 37%, $T_2 \sim 19$ μs; two water reservoirs associated with C-S-H: interlayer and gel pore water with $T_2 \sim 90$ and 200 μs and fraction of 19 and 36%, respectively. The secondary hydration water was also detected at the hydration time of 10-20 hours. The increase of curing temperature accelerated the cement hydration process as evidenced by faster development of crystalline, interlayer and gel pore water intensities as well as supportive XRD analysis. Mature pastes (~40 days) cured at elevated temperatures were characterised by higher capillary and interlayer pore water intensities and lower gel pore

water intensity. No direct pattern influence of temperature rise was registered for the shortest T_2 component (~15-19μs) as its intensity was increasing and decreasing alternately.

3.4.2. 2D exchange experiments

T_1-T_2 and T_2-T_2 two-dimensional relaxation correlation experiments were performed on cement pastes by McDonald *et al.* [92], [94] and Monteilhet *et al* [95]. The 2D T_1-T_2 and T_2-T_2 correlation method is based on introducing an additional magnetisation storage period between encoding periods that gives hydrogens time to exchange between different environments [95]. The T_1-T_2 experiments have already been proposed in 80's [96] but were limited by lack of suitable tools for analysis which requires performing 2D inverse Laplace transform. The algorithm enabling that transform reliably was proposed by Venkataramanan [97].

T_1-T_2 experiments of white cement paste (w/c = 0.4) showed multiple discrete pore size distribution with two dominant peaks on the diagonal and one off diagonal feature – fig 3.13 left. The T_2-T_2 correlation spectra presented the same diagonal feature and two well-defined off-diagonal peaks. Two peaks at diagonal – water reservoirs, were assigned to gel porosity and separately resolved as inner and outer C-S-H or interlayer and gel pores. The presence of symmetrical off-diagonal peaks for T_2-T_2 experiment have suggested the exchange of the hydrogen or water between different pore size reservoirs [92], [95]. The alternate explanation that the exchange occurred between two reservoirs of the same size but with different Fe^{3+} concentration was investigated on synthesised C-S-H with reduced paramagnetic impurities by Valori *et al* [98]. The spectrum was shifted up the diagonal due to a decrease in paramagnetic concentration and still shown two off-diagonal peaks. It confirmed exchange between pores with different sizes occurred.

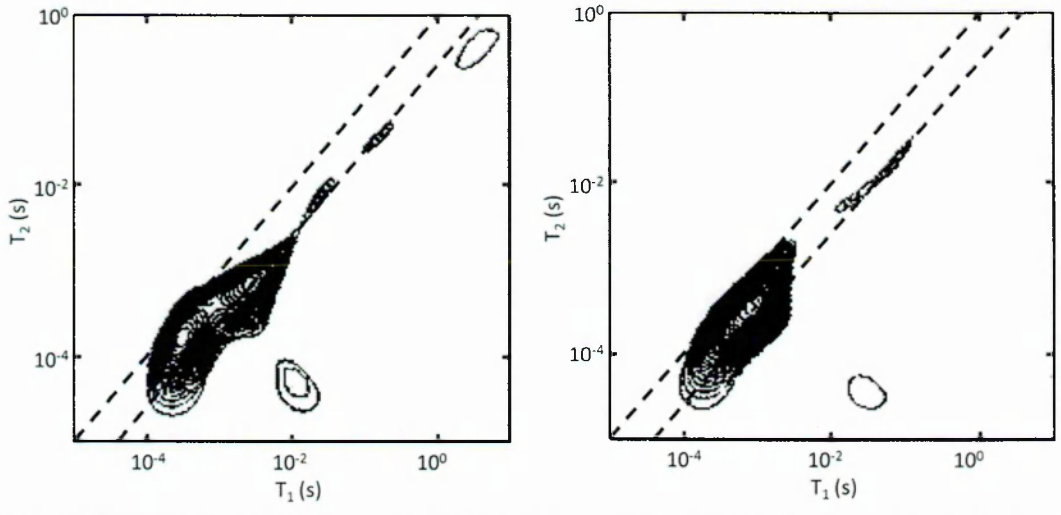

Figure 3.13 The T_1-T_2 correlation spectra of white cement paste (left) and white cemnt paste with additin of silica fume (right) cured for 7 days (adapted from[92]).

The comparison of T_1-T_2 spectra from paste of white cement and white cement with addition of 10% silica fume showed that diagonal peaks of silica fume paste are not as discrete as for white cement paste – fig. 3.13. The off-diagonal peak shifts towards longer T_1 at the earlier age for paste with silica fume which means that the hydration of this paste progresses faster [92].

The ratio of T_1 relaxation time to T_2 relaxation time was determined for cement pastes by T_1-T_2 experiment as equal to 4 at 20 MHz - components aligned along $T_1 = 4T_2$ as presented in figure 3.13. The result showed that the ratio of T_1 to T_2 is only a function of NMR Larmor frequency and two correlation times - surface resistance and hopping times - τ_s, τ_m [92]. Giving the magnet frequency and hopping time of 1.3 ns [99] the surface residency time was evaluated as ~13 μs [92], [94].

Based on T_2-T_2 correlation the exchange time was estimated as ~5 ms. The length scale of exchange, based on the cement grain size, was defined as ~4 μm and as between inner and outer product of hydration although it is no longer considered that exchange is between inner and outer product. The diffusion coefficient of exchange was calculated as $5 \cdot 10^{-10}$ m^2/s. The translation diffusion coefficient at the surface of C-S-H ($2.3 \cdot 10^{-11}$ m^2/s) was calculated from the hopping time in 2D random walk on the surface – 1 ns, and mean size of jump equalled to size of water molecule – 0.3 nm [95]. The calculated NMR diffusion coefficients – for exchange and across surface, are in good agreement with diffusion coefficients obtained by molecular dynamics simulations for water diffusing in the pore space above the internal pore surface and on the internal pore surface of tobermorite, $6 \cdot 10^{-10}$ m^2/s and $5.0 \cdot 10^{-11}$ m^2/s respectively [100].

3.4.3. Pore size distribution

3.4.3.1. Fast Exchange Model for pore size analysis

Pore size distributions in the microstructure of cement pastes can be estimated based on the fast exchange model of relaxation presented in section 3.3.2 (eq. (3.22)). The key factors in this calculation are evaluation of surface relaxation time, $T_{1,2}^{surf}$, and surface layer thickness, ε, that give together surface relaxivity, $\lambda = \varepsilon / T_{1,2}^{surf}$, and determination of the pore shape.

One approach to do so is through experiments. Bhattacharja *et al* [101] in 1993 calculated the surface relaxivity and pore size distribution of white cement paste mixed at *w/c* = 0.4. CPMG measurements were performed at 25 MHz during hydration from 1 to 28 days. The calculation of the surface relaxivity involved the additional study of partially filled (progressively dried) samples to correlate the observed T_2 and the volume fraction of water filling pores. The surface area at each hydration time was obtained through nitrogen BET analysis. The results show that λ does not vary with hydration time and is $1.6 \cdot 10^{-6}$ cm/ms. The pore sizes of two identified populations were fairly constant over hydration with diameter of 18 and 90 nm assuming cylindrical pores.

A year later the first Laplace inversion of CPMG data to yield the T_2 relaxation time and hence the pore size distribution were performed by Halperin *et al* [10]. The transverse

relaxation of water within cement paste with w/c = 0.43 was measured by application of FID and CPMG sequences. The authors correlated the thickness of water monolayer, ε = 3 Å, with the constant relaxation time observed for pastes at saturation fraction below 0.2 when all water became the mobile surface water, $T_2^{surf} \approx 40$ μs. The obtained surface relaxivity was $7.5 \cdot 10^{-7}$ cm/ms. Mobile water measured by CPMG was divided into two populations interpreted as the capillary and gel pores. The pore sizes were calculated based on spherical shape. The capillary pore size decreased from about 200 nm at 2.5 hours of hydration to 60 nm at 8 hours and 12 nm at 7 days. Beyond that time it stayed constant. The gel pore size was weakly dependent on hydration time: 3.5 nm at 2.5 hours and 2.5 nm at 59 days.

Surface relaxation time was assumed to be equalled to the relaxation time of the bound water, 10 μs, by Bohris *et al* [22]. Authors performed FID and CPMG measurements of cement pastes (w/c = 0.3 and 0.5) at 20 MHz. Results revealed the presence of three water populations: chemically bound water, gel water with T_2 = 80 μs, and capillary water, T_2 = 350 μs. The pore sizes were calculated as 2.4 and 15 nm with assumption that gel pores form layers and capillary pores are spherical and partially filled.

Valckenborg *et al* [102] measured dry sample during exposure to wet air flow and assumed that the T_2 relaxation time of first appearing signal is attributed to the surface layer. The obtained surface relaxation time for mortar was 85 μs. With monolayer of water (0.3 nm) and spherical shape of pores it led to gel and capillary pore sizes of ~6 and ~27 nm.

The other approach to evaluate surface relaxation time is through the calculation using the Korb model (eq. (3.24)-(3.25) in section 3.3.3). However, in that case the knowledge of other parameters is required: surface density of paramagnetic impurities (σ_S), the minimum distance for water molecule to approach impurity (δ), surface residency time (τ_s) and surface hopping time (τ_m). Monteilhet *et al* [95] performed analysis of the pore size distribution of white cement paste based on T_2-T_2 correlation experiments. They inferred σ_S from electron spin resonance and used τ_m and τ_s of 1.3 nm and 13 μm as obtained from frequency dependence of T_1 [99] and T_1-T_2 correlations [92] respectively. Assuming surface monolayer (0.28 nm) and value of δ = 0.2 nm, surface T_2 relaxation time is 100 μs. The smallest pores had calculated thickness of 1.0-1.7 nm assuming planar shape and the larger pore size ranged between 7-30nm depending on the shape [95].

The pore size calculation according to Fast Exchange Model can bring certain level of uncertainty due to difficulty in defining the surface relaxivity.

3.4.3.2. Amplitude Model

An alternative method to estimate the pore sizes was developed by McDonald *et al* [26] - hereafter called Amplitude Model. The estimate of pore size distribution in that model is based on the *amplitudes* of relaxation components as a function of water content rather than on the relaxation *times*.

The Amplitude Model was developed based on the layered C-S-H microstructure. In saturated pores (fig. 3.14a) the surface water molecules are in fast exchange with those in the

bulk of pore. Hence, NMR sees all molecules as mobile with one T_2 relaxation time. The drying may occur in two alternative ways. Figure 3.14b(ii) shows the scenario where no surface layer is initially created, water is removed layer by layer across the pore. All water molecules are mobile until the last layer; however the T_2 relaxation time decreases as a result of increase in S/V ratio. The second possibility is that, a water layer stays on the pore surface as drying progresses (fig. 3.14b(ii)). There are two distinguished T_2 water environments. One has the same relaxation time as mobile water in fully filled pore (same S/V) and decreasing amplitude; and second – surface layer, has shorter relaxation time, since it cannot any more exchange with bulk of pore, and increasing amplitude. This scenario is typical for the drying processes that involve considerable capillary forces. Hence, it was used to perform advance quantification.

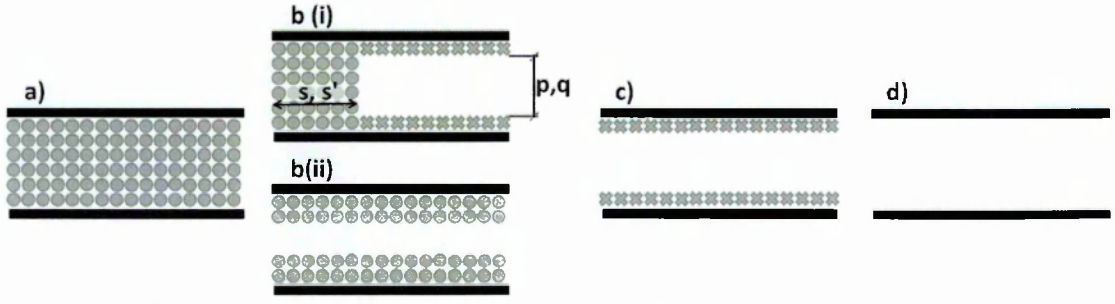

Figure 3.14 The scheme of pore drying: a) pore full of mobile water, b) two possible ways of pore drying, c) surface water layer staying, d) an empty pore [26]. Circles represent mobile water molecules, crosses are immobile, surface water molecules.

The experiments were performed for white cement paste (w/c = 0.4) by applying Quad Echo sequence. The total signal was divided into solid (I_{sol}) and mobile (I_{mob}) parts. The mobile intensity decreased successively at two different rates, above and below effective water mass fraction of 0.7. The first stage was assumed to have origin in drying of C-S-H gel pores (with specific surface area, M, and thickness, p+2, both expressed in water molecules); second - of C-S-H interlayer pores (with specific surface area, N, and thickness, q+2). During drying intensity was defined as proportional to the pore thickness and the fraction (s, s') of the specific surface area of pore still filled with liquid. The expression for normalised mass of water (m) remaining along drying was stated in the same terms. The mobile intensity and mass were expressed as:

$$\begin{aligned} I_{mob} &= M \cdot (p+2) \cdot \mathrm{s} + N \cdot (q+2) \cdot s' \\ m &= 1 - M \cdot p \cdot (1-s) - N \cdot q \cdot (1-s') \end{aligned} \tag{4.1}$$

Further, the mobile water intensity for both stages (I_{mob1} and I_{mob2}) was characterised as a function of mass through the equations: $I_{mob1} = a_1 \cdot m + b_1$ and $I_{mob2} = a_2 \cdot m + b_2$.

The equations were solved with assumption for first stage of drying that interlayer pores are full ($s' = 1$) and for second stage that gel pores were empty of mobile water ($s = 0$). This led to the expression for pore size parameters in function of the gradients of the fitting lines:

$$p = \frac{2}{a_1 - 1}; \quad q = \frac{2}{a_2 - 1}; \tag{4.2}$$

The calculated pore sizes are 1.5 and 4.1 nm for C-S-H interlayer and gel pores respectively.

3.4.4. Specific surface area

Halperin *et al* [10] presented the changes of specific surface area of cement paste (w/c = 0.43) over hydration time based on the evolution of T_2 relaxation time and its intensity recalibrated as volume of evaporable water. Calculations were performed according to the fast exchange model of relaxation. The rapid development of the surface was observed between 6 and ~50 hours when it reached the constant value of 225 m^2/g of anhydrous cement.

The surface area of cement based material was measured by application of Nuclear Magnetic Relaxation Dispersion (NMRD), so-called field cycling, experiments by Barberon *et al* [99]. This technique allows on the separation of the surface and bulk contribution towards the relaxation rate by performing measurement over the range of the nuclear Larmor frequency. Authors examined continuously the mortar sample (w/c = 0.38) up to 12 hours of hydration at frequencies values between 0.1 and 10 MHz. The rapid increase of the specific surface area was observed after 6 hours of hydration. The calculated value at 12 hours was ~100 m^2/g. The linear dependence of the area on cement degree of hydration was evidenced.

4. Experimental methods

4.1. SAMPLE PREPARATION

4.1.1. Cement composition

In this study low C_3A white Portland cement was used. This cement is characterised by an almost total lack of ferric impurities since there is minimal Ferrite content. Cement was delivered from Aalborg Portland in two separate batches. The mineralogical and chemical composition of the batches are presented in table 4.1 and 4.2.

Table 4.1 Mineralogical composition of used cements.

Phases in anhydrous cement		*Cement 1 [%]*	*Cement 2 [%]*
Alite	C_3S	66.9	64.0
Belite	C_2S	19.7	19.5
Aluminate	C_3A	3.6	3.3
Ferrite	C_4AF	0.8	0.0
Portlandite	CH	0.7	1.8
Anhydrite	C$	2.6	–
Gypsum	C$·2H	–	3.3
Bassanite	C$·0.5H	2.1	2.1
Amorphous		3.6	6.0
Total		100	100

Table 4.2 Chemical composition of used cements.

Oxides	*Cement 1 [%]*	*Cement 2 [%]*
CaO	69.3	71.6
SiO_2	24.7	21.8
Al_2O_3	2.2	1.5
Fe_2O_3	0.3	0.4
SO_3	2.1	2.0
P_2O_5	0.3	0.4
K_2O	0.1	0.1
TiO_2	0.1	0.1

4.1.2. Mixing and curing

Cement pastes were prepared at water to binder (100% white cement or 90% white cement and 10% silica fume) ratio 0.4 by mass. This ratio was agreed across Transcend projects. The mixing of cement pastes was performed in accordance with Nanocem protocols [103], [104]. According to these protocols, to prepare each white cement paste mix, 80 grams of white cement powder and 32 grams of distilled water were weighed and the water added to the cement. This was immediately followed by 3 minutes mixing at 500 rpm, 2 minutes resting during which the paste was covered and 2 minutes mixing at 2000 rpm.

The preparation of cement paste with added silica fume involved pre-dispersion of the silica fume (8g) in distilled water (32g) with Sika ViscoCrete EH 20 superplasticizer by mixing at 2000 rpm for 5 minutes. The amount of superplasticizer was 0.1% by weight of the binder. Next, 72 grams of white cement powder was added and the three stage mixing, described above, was performed.

Pastes were placed in moulds or NMR tubes as described in next section.

In all experimental parts of this work paste samples were cured under saturated Calcium Hydroxide (CH) solution. The reasons are threefold. First, the solution fills chemical shrinkage voids during curing of small samples. Second, the solution prevents sample contact with atmospheric carbon dioxide which causes carbonation. Third, CH solution approximates the cement pore liquid and prevents leaching.

4.1.3. Samples casting and specific preparation for experiments

4.1.3.1. Samples for sorption isotherm measurements

Freshly mixed cement paste was cast in cylindrical moulds 20 mm in height and 8 mm in diameter and covered with a small quantity of saturated CH solution. After 24 hours, they were removed from the moulds and further cured under solution in glass bottles at room temperature. The ratio of sample to solution volume was 1:1.

After 28 days of curing, samples were crushed to millimetre size grains with a pestle and mortar. Approximately 100 mg pieces were equilibrated to the desired relative humidity at room temperature in an IGAsorp Moisture Sorption Analyser (described in section 4.6).

In order to study the first desorption isotherm crushed pieces were first equilibrated at 80% relative humidity and then at different humidities in the range 80 to 3%. For the re-adsorption branch of the isotherm, samples were first equilibrated to 80% and then 5% RH and then re-equilibrated to higher relative humidity. The second desorption was studied following equilibration at 80, 5 and 80% RH and then at desired lower humidity. Three further samples were prepared. The first was an "as cured" material, taken to represent 100% RH. The second was a sample equilibrated directly to 90% RH. The third was a sample dried in a vacuum oven at 180°C, taken to represent 0% RH.

Once equilibrated, samples were removed from the IGAsorp chamber and quickly transferred to 5 mm diameter NMR tubes. Glass rods were added to reduce the free volume and the tubes sealed tightly with parafilm® to prevent changes in water content. Further, the

5 mm tubes were placed centrally in 10 mm diameter NMR tubes that fitted the NMR machine. The NMR tubes were made of borosilicate glass.

4.1.3.2. Samples for temperature dependent curing studies

White cement paste and white cement paste with addition of silica fume were directly deposited into NMR tubes using a plastic pipette immediately after mixing. Sample height and diameter were around 8 mm. A few drops of CH saturated solution were added to the top of samples (2-3 mm) and tubes were closed tightly.

Six curing temperatures were chosen: 10, 20, 30, 40, 50 and 60°C. Samples were stored variously in a fridge, the laboratory or a temperature controlled water baths dependent on the desired curing temperature. The stability of the temperature was: 10 ± 1°C in the fridge; 20 ± 0.5°C in the laboratory; and 30/40/50/60 ± 0.2°C in water baths.

Samples were periodically measured. For that purpose, the CH solution was removed by using a glass pipette, the tube walls and sample surface were touch-dried with tissue paper and the mass of sample was recorded. The glass rod was inserted to reduce the air volume and tube was sealed with parafilm®. After measurements in the temperature-controlled NMR probe (described in section 4.7), CH solution was back-added at the top of samples. The care was taken to put back as much as possible of the removed earlier solution. If it was not enough, fresh drops were added.

4.1.3.3. Samples for activation energy analysis

Due to the broad temperature range to be studied (-20 to +60°C) different sample preparation methods were assessed to verify the best method of performing experiments.

The chosen method comprised samples cast in the NMR tubes to a length of 5 cm. Samples were cured under saturated CH solution. During experiments the solution was left on top of samples but outside the NMR coil. Tubes were connected by a rubber pipe to a water reservoir in order to accommodate the pressure changes during the experiments.

4.1.3.4. Samples for water-isopropanol exchange experiments

Samples for collaborative research on isopropanol exchange were prepared by Dr Radoslaw Kowalczyk. Cement pastes were mixed at water to cement ratio 0.46 when prepared with H_2O and 0.51 with D_2O to introduce the same amount of hydrogen and deuterium moles. The pastes were cast as described in section 4.1.3.1. After 50 days of curing samples were crushed into millimetre size pieces to increase the surface area and accelerate ingress of solvent. The isopropanol, $(CH_3)_2CHOH$, and partially deuterated isopropanol, $(CH_3)_2CDOD$, were used as solvents. The exchange using deionised water was also performed to test reversibility. Exchange was carried out by 3 wash cycles of 24 hours each. Each cycle was performed with fresh solvent in solvent to sample volume ratio at least 20:1. More details on the sample preparation are presented in [105] (Appendix 2).

Sample casting for specific experiments is summarised in table 4.3.

Table 4.3 Characteristic of samples casting.

Experiment	*Cast*	*Cement*	*Sample dimension*		*Curing Temperature*
Sorption isotherm	Mould	1	ø = 8mm	L = 20mm	20°C (laboratory)
Temperature dependence	Tubes	2	ø = 8mm	L = ~8mm	10°C (fridge) 20°C (laboratory) 30-60°C (water baths)
Activation energy	Tubes	1	ø = 8mm	L = 50mm	20°C (laboratory)
Isopropanol	Mould	2	ø = 8mm	L = 20mm	20°C (laboratory)

4.2. NMR MEASUREMENTS

4.2.1. Spectrometers

^{1}H NMR Quad echo, CPMG and T_1 recovery measurements, described in the following sections, were made on a bench top spectrometer operating at 20 MHz. Early measurements (sorption and activation energy experiments) were performed on Resonance Instruments "Maran" spectrometer (Oxford Instruments, UK). Later work (the curing temperature and solvent exchange) used a Kea^2 spectrometer (Magritek, New Zealand).

4.2.2. Quad Echo parameters

The Quad Echo (QE) signals were acquired as a function of pulse gap (τ) between 90° radio frequency pulses. Typically eight QE experiments were performed with pulse gaps in the range 12-54 μs. The 90° excitation pulse length was 2-2.5 μs (Maran) and 4-5 μs (Kea^2). Following the second 90° pulse the spectrometer dead time was 10 μs for most experiments. However, in the case of the sorption experiment it was much longer (over 20 μs) due to the incorporation of an additional amplifier in the system required as the sample was very small. Variously 512 to 4096 points per decay were acquired with a dwell time of 1 μs and repetition time[10] (τ_{rd}) of 1 s. The number of averages depended on the sample size. For the sorption experiment 1000 scans were recorded due to the very small quantity. In temperature dependent investigations, 32 scans were sufficient.

The isopropanol exchange experiments[11] were performed with pulse gap in the range 10-35 μs and 256 scans.

[10] repetition time in entire thesis is treated as the time from the start of one sequence to the start of the next one

[11] measured by R. Kowalczyk

4.2.3. CPMG parameters

The NMR Carr-Purcell-Meiboom-Gill (CPMG) pulse sequence was applied to record the train of logarithmically spaced echoes.

The duration of the 90° radio frequency pulse was the same as for QE experiments. The 180° pulse was twice as long as 90° pulse for experiments performed on Maran spectrometer and twice as intense as 90° pulse for Kea^2 experiments.

The 180° pulse gaps (2τ) were increment logarithmically according to

$$2\,\tau_i = 2\,\tau_0 \cdot \alpha^i,\ \ i = 0 \ldots (N_E - 1) \tag{4.1}$$

where N_E is the number of echoes and α is a constant.

In the case of sorption experiments the 256 echoes with τ spaced from 30 to 100,000 μs were used. Typically, 1600 averages were acquired with a repetition time of 6.5 s. Each echo counted 32 data points with a dwell time of 1 μs. The curing temperature dependence measurements were performed by spacing τ from 26 μs to 22,000 or 5,000 μs. Typically, 420 echoes with 32 data points per echo were acquired. The repetition time was decreased from 4 to 2 s. The number of scans was increased from 128 to 320. The isopropanol exchange experiments[12] were performed by acquiring 512 echoes with τ spaced from 26 μs to 5,000 μs, repetition time of 2.5 s and up to 1024 scans.

4.2.4. T_1 recovery parameters

The activation energy at 28 and 90 days of cement hydration was measured by applying the T_1 saturation recovery pulse sequence on Maran spectrometer. In the case of 7 days old samples experiments have been performed by T_1 inversion recovery sequence on Kea^2 spectrometer.

The pulse characteristic was the same as described in previous sections. In all cases experiments were performed in 64 steps with 16 averages and repetition time of 1 s. For each step the distance from inversion pulse / saturation pulses to 90° FID pulse (τ_{rec}) was increased logarithmically

$$\tau_{rec} = \tau_{rec}^{o} \cdot \beta^i,\ \ i = 0 \ldots (N_{St} - 1) \tag{4.2}$$

where N_{St} is the number of applied steps and τ_{rec}^{o} is the minimum duration of the distance.

The values of τ_{rec} for 7 days old cement samples were spanned between 0.02 and 4,000 ms, while for 28 and 90 days old samples they were between 0.02 and 2,000 ms.

[12] measured by R. Kowalczyk

4.3. ANALYSIS OF NMR DATA

An analysis of the measured data was performed after subtraction of a residual NMR signal emanating from empty NMR tube(s). Quadrature echo signals were analysed in magnitude mode. The CPMG data were phased to minimise the imaginary signal. The T_1 recovery signal at each τ_{rec} was calculated as an average of first 10 points of FID decay.

4.3.1. Quad echo analysis

The recorded Quad Echo signal comprises of two parts: an echo due to the solid and an exponential decay due to the liquid. The exponential fraction is not affected by the second 90° pulse and therefore has the origin at the time of the first pulse. It decays with the relaxation time T_2^* determined by the magnet inhomogeneity. This signal is attributed to the mobile hydrogens. The application of the second 90° pulse refocuses the magnetisation of rigid dipole – dipole pairs within solid components. The solid signal originated from that fraction has an approximately Gaussian shape centred at the time 2τ and short time constant – Gaussian width (σ_{sol}) of 10 – 20 μs.

Hence the QE signal has been fitted to:

$$I_{Tot}(t,\tau) = I_{sol}(\tau)\cdot\exp\left[-\left(\frac{t-2\tau}{\sigma_{sol}}\right)^2\right] + I_{mob}(\tau)\cdot\exp\left(-\frac{t}{T_2^*}\right) \tag{4.3}$$

where I_{sol} and I_{mob} are the solid and mobile signal intensity, t is the time counted from the end of first 90° pulse, τ is the pulse gap.

The fitting procedure was performed by using code written in Matlab®. The code was designed to fit first the tail of exponential fraction, subtract that fit from total signal and then fit the Gaussian echo. The obtained fitting parameters ($I_{sol}, I_{mob}, \sigma_{sol}, T_2^*$) then served as the initial parameters for a full least square fitting of QE signal. To minimise the influence of magnet inhomogeneity on mobile signal intensity the analysis was made in time range below 200 μs. The sum of solid and mobile intensities is the total signal of all hydrogen within samples. However, the solid intensity is not totally refocused as with increasing τ it also relaxes. Therefore back-extrapolation of the echo intensity to pulse gap $\tau = 0$ is required. A Gaussian extrapolation was found to reflect best the content of solid and total water within sample. For completeness the mobile signal was also back extrapolated – the same results within measurement uncertainty were obtained by both the exponential and linear extrapolation.

4.3.2. CPMG and T_1 recovery analysis

4.3.2.1. Multi exponential fitting

The analysis of CPMG decay and T_1 recovery data is based on exponential fitting with multiple relaxation time components.

The CPMG experiments probe only the mobile water signal. The solid, chemically combined, signal is substantially relaxed by the time of the first echo (~ 60 μs) since its T_2 constant is ~10–20 μs. The CPMG decay intensity (I_{mob}) is expressed by the formula

$$I_{mob}(t) = I_o \int P(T_2) \cdot \exp\left(-\frac{t}{T_2}\right) dT_2 \tag{4.4}$$

where $P(T_2)$ is the probability of nuclei having T_2 and I_o in the overall intensity at time zero.

In the case of multi-model distribution of n specific T_2 values this may be rewritten as

$$I_{mob}(t) = \sum_{i=1}^{n} I_i \cdot \exp\left(-\frac{t}{T_{2,i}}\right) \tag{4.5}$$

where t is the time counted from 90° pulse, I_i is the intensity of i-th component, $T_{2,i}$ is the T_2 relaxation time of i-th component.

The similar expression for T_1 relaxation intensity (I_{TOT}) is

$$I_{TOT}(\tau_{rec}) = \sum_{i=1}^{n} I_i \cdot \left[1 - k \cdot \exp\left(\frac{\tau_{rec}}{T_{1,i}}\right)\right] \tag{4.6}$$

where τ_{rec} is the time between inversion pulse / saturation pulses and 90° FID pulse, $T_{1,i}$ is the T_1 relaxation time of i-th component and k is the parameter dependent on type of recovery, $k \approx 1$ for saturation and $k \approx 2$ for inversion recovery.

The k parameter in this study has been calculated for each data set of T_1 measurements as $k = 1 - b_1/b_2$ where b_1 is the value of I_{TOT} at $\tau_{rec} = 0$ and b_2 is the maximum value of I_{TOT} at longest time.

Origin® and Matlab® have pre-defined least square fitting procedures. However, using these procedures for analysis is difficult as the obtained intensities and relaxation times depend hugely on the pre-defined number of components and their initial guess values. Hence, the use of straight exponential fittings was minimised in this study. The exception was made for activation energy experiments where the number of components is determined from prior knowledge. The alternate methods used are Laplace transform analysis and exponential stripping.

4.3.2.2. Inverse Laplace Transform

Multi-exponential relaxation signal intensity for T_2 can be expressed as [106]

$$I(t) = \int P(T_2) \exp\left(-\frac{t}{T_2}\right) dT_2 + \epsilon(t) \qquad (4.7)$$

where I is measured signal as a function of decay time t, P is relaxation time (T_2) distribution function – probability density of hydrogen with specific relaxation time, and ϵ is the noise contribution (additive, zero mean and white Gaussian noise).

To solve equation 4.7 knowing the signal intensity and obtain the relaxation time (T_2) distribution function, P, the Inverse Laplace Transform (ILT) is used. However, the Laplace inversion is known to be ill-posed problem. Numerous algorithms have been put forward to solve the problem. That adopted here is due to Venkataramanan [97]. This algorithm makes the assumption that $P(T_2)$ is non-negative. Moreover, it introduces a regularisation parameter, α_R, which defines the smoothing of the distribution [107]. 'Similar arguments' apply to T_1 recovery analysis.

The outcome of ILT analysis depends on the α_R to a limited extend. In this thesis two Laplace Inversion programs run in Matlab® were used. Analysis of the sorption and activation energy experiments data was performed by using program supplied by Schlumberger-Doll Research. In the case of that program, if the α_R parameter is too big the spectrum is broad and peaks are not separated - they merge. If α_R is too small then the spectrum consists of many individual peaks which become very narrow. The solvent exchange experiments were analysed by program written at Victoria University of Wellington. Here, the smoothing parameter draws a distinction from former program: small α_R gives broad spectrum, big α_R – narrow spectrum. The maximum amplitude and the width of the peaks in the T_1 or T_2 spectrum are highly dependent on the α_R parameter. However the area of peaks shows much lower dependence on α_R. Therefore the intensities of the relaxation time components in this work were determined as the area – integral intensity, of each peak. An inaccuracy in α_R also leads to a pearling effect described as a tendency of the closely neighbouring peaks to move toward each other. This may introduces a systematic error in obtained T_2 values.

The uncertainty in the obtained spectrum may also arise from the measured echo data. In order to use the ILT analysis the signal to noise (S/N) ratio of acquired data should at least exceed the value of 500. Based on the personal experience of the author, it also is important to record the baseline of sufficient length.

The analysis of sorption and activation energy experiments were performed with α_R equalled to 10^{-5} and 10^{-4}, respectively (Schlumberger code). The range of T_2 relaxation time was 10^{-5} – 1 s, while for T_1 it was 10^{-5} – 10 s with 1000 steps distribution. The solvent exchange experiment analysis was performed in the same T_2 range as sorption experiments with $\alpha_R \sim 10^{11}$ - 10^{12} (Victoria code).

4.3.2.3. Exponential stripping

The exponential stripping method of analysis was used for temperature dependence and isopropanol exchange experiments where the signal to noise ratio of the data is not adequate for ILT analysis. However, the number of relaxation components was established by the results obtained earlier using ILT of similar cement paste samples.

The method is based on fitting the CPMG decay in steps. The procedure starts with fitting the tail of the decay, I_{TOT} ($t \geq t_{long}$), to the longest relaxation component only with a baseline. The fitting line calculated from the best fit parameters, I_{long}, $T_{2,long}$ and $I_{baseline}$, is then subtracted from the original data. The tail of residual data after subtraction is fitted to the next longest relaxation component (without baseline). This in turn is subtracted and procedure repeats iteratively until the shortest component has been fit.

Two sets of boundaries need to be considered and their choice is critical to the analysis.

The first are the lower limits of T_2 relaxation times for each component. They are selected based on experience gained from examination of other cement paste samples. The analysis was performed starting with the oldest samples (90 days of hydration). The lower boundary cut offs for C-S-H interlayer, gel, interhydrate and capillary pore water were set to 90, 250, 1500 and 10,000 μs, respectively based on earlier ILT analysis. Fitting was progressively performed for younger samples. The lower boundaries were varied in line with discovered T_2 of component. In the majority of the cases, especially for gel pore water, the T_2 values were found without encountering the boundary. The upper boundaries were not restricted allowing the T_2 values to be found.

The second boundary is the value of t_{long} for each fitting stage; the timeline of particular fittings. They were set based on the found T_2 values for the older sample. The fittings of the longer T_2 components start at time 3-5 times longer than the T_2 of the next shorter component.

The analysis protocols for CPMG and T_1 recovery experiments are summarised in table 4.4.

Table 4.4 Characteristic of experimental analysis.

Experiment	*Analysis method*
Sorption isotherm	ILT
Temperature dependence	Exponential stripping
Activation energy	ILT and multi-exponential fitting
Solvent exchange	ILT and exponential stripping

4.4. THERMOGRAVIMETRIC ANALYSIS

Thermogravimetric analysis (TGA) involves monitoring of changes in sample mass as the temperature is gradually raised. For better interpretation of data, in parallel with the TG curve, the derivative thermogravimetric (DTG) curve is registered and presents the changes in the rate of material decomposition.

In a TGA experiment the sample is placed on the pan - made with alumina when studying cement pastes, and then on an ultra-sensitive balance to follow the changes in sample weight during heating. The balance with pan is loaded into the electric oven containing a thermocouple to accurately measure temperature during experiment.

The mass loss of cementitious materials is usually caused by dehydration – loss of water molecules, dehydroxylation – loss of hydroxyl groups, and decarbonation - thermal dissociation of calcites. The changes in weight of different cement phases appear at various temperatures and overlap (fig. 4.1). It makes it difficult to distinguish and assign changes to specific component.

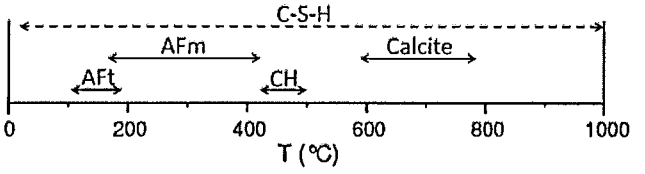

Figure 4.1 The range of temperature at which different phases loose mass (adopted from [108], [109]).

In this study TGA measurements were performed to define the content of Portlandite through loss of the water within it. At the temperature range when changes in CH mass happen, the decomposition of C-S-H also appears. However, as the rate of that decomposition is almost constant at those temperatures, it is overcome by applying the tangents method.

Experiments were made at University of Surrey[13] with TA Instruments Simultaneous Differential Technique SDT-Q600 Thermo Gravimetric Analyser with Differential Scanning Calorimeter (TGA-DSC). Samples were heated in temperature range between 20 and 1000°C at 10°C/min in the N_2 atmosphere (flow 100ml/min) to prevent carbonation. The temperature precision was 0.5°C and weight sensitivity was 0.1 μg.

4.5. X-RAY DIFFRACTION

X-Ray diffraction is a non-destructive technique based on the fact that each crystal is characterised by a collection of atomic planes that are spaced *d* apart.

X-rays are diffracted according to Bragg's Law:

[13] in collaboration with Violeta Doukova

$$n\lambda = 2d \cdot \sin\theta_i \qquad (4.8)$$

where n is the diffraction order (integer), λ is wavelength of the incident X-ray beam and θ_i is angle of incidence.

X-ray diffracted beams are detected and registered as XRD pattern - intensity (counts) as a function of diffraction angle $2\theta_i$. To identify the phase composition of measured sample the diffraction pattern is compared with known ICDD (International Centre for Diffraction Data) standards or other databases. The quantitative XRD analysis is performed by Rietveld method based on the least square fitting of the simulated and measured pattern.

In this study XRD measurements have been performed on cement powder to define their phase composition and on cement pastes to define degree of hydration[14] (α) and content of ettringite (f_{Ett}).

The XRD experiments were performed at EPFL[15] with Panalatical X'Pert Pro MPD diffractometer using a CuKα source (wavelength 1.54Å) with a fixed divergence slit of 0.5°. Samples were scanned between $2\theta_i$ = 7 and 70° using a X'Celerator detector. The rotation step size was 0.0167° ($2\theta_i$) and the time step was 77.5 s.

4.6. Sorption Analyser

The IGAsorp Moisture Sorption Analyser is a fully automated gravimetric analyser. It contains an ultra-sensitive microbalance which measures the changes in sample mass as humidity is changed. Those changes are measured with resolution of 0.1 μg. Constant monitoring of sample mass allows to determine when equilibrium has been reached [110].

The humidity in sample chamber is controlled and changed by mixing of dry and wet gas streams [110]. The wet stream is obtained by directing gas flow through water container. The flow rate is limited to 500 ml/min. To prevent carbonation of cement paste the nitrogen was used as a humidity controlling gas.

To perform the experiment, the sample is first placed in the conical holder with diameter of around 1 cm, hanged above humidity chamber and then the chamber is closed by moving up.

The IGAsorp Analyser was used in sorption experiment to equilibrate samples at desired humidity. The practice showed that the most time effective is to operate in the humidity range 80 to 5%. The humidity of 80% could be reached in the chamber after around 5 minutes whereas of 90% - after few hours.

[14] mass fraction of anhydrous cement consumed in the hydration reactions

[15] in collaboration with Arnaud Muller

4.7. TEMPERATURE CONTROL

Two experimental NMR parts of this work involved temperature as an important factor. These were the NMR measurements to investigate the influence of curing temperature on cement microstructure and to establish the activation energy.

The former were always performed at the same temperature as samples curing. The reason for that was to not alter the conditions of samples curing. In the second case, the relaxation parameters were measured during progressive increasing of sample / experimental temperature in the range -20°C to +60°C.

The temperature on the bench top spectrometer is controlled by three means depending on the desired value. In all cases the flow of nitrogen gas is directed through meter long heater and spectrometer probe. That flow is cooled down or heated up to achieve the fix temperature. In the range -20 to +5°C, the set temperatures are reached by controlled heating of the nitrogen gas directed in pipe through dewar with liquid nitrogen. For temperatures between 10 and 25°C flow goes through pipe merged in polystyrene box filled with ice and water. Increasing temperature is possible by heating the gas flow by one (30-40°C) or two (45-60°C) heaters.

During NMR experiments temperature is monitored by a sensor placed around 2-3 cm below the actual position of sample in bench top spectrometer. Considering the sensitivity of experiments to temperature, it was important to verify what the actual sample temperature was. The difference between real temperature and sensor display was measured in a separate experiment by using copper-constantan thermocouple. The schematic diagram of system is shown in figure 4.2. Cement sample was prepared with one end of thermocouple wires merged inside at the position of coil. The other end was kept at 0°C and thermocouple was connected to voltage meter.

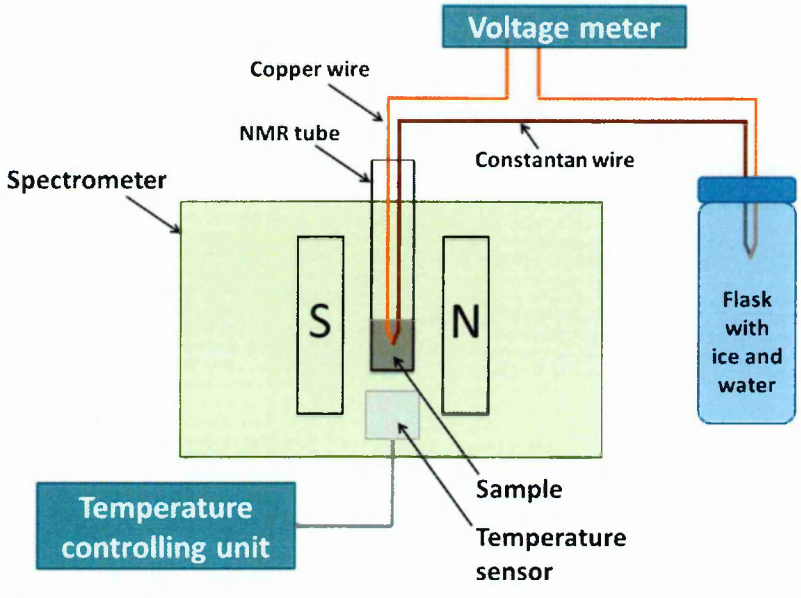

Figure 4.2 Schematic diagram of the system to calibrate the temperature: the copper – constantan thermocouple is merged into the cement sample and allows calculation of actual sample temperature, while the controlling unit displays the temperature recorded by sensor.

The voltage was recorded while the setting temperature was changed and equilibrated. The obtained voltage values (V [mV]) were converted to temperature (T [°C]) according to equation [111]:

$$T = A + B \cdot V - \frac{C}{V + D} - \frac{E}{V + F} \tag{4.9}$$

where A = 238.29°C, B = 13.364°C·mV^{-1}, C = 4776.4°C·mV, D = 21.867 mV, E = 154.83 °C·mV, F = 7.8242 mV

The calculated temperatures were plotted against the values of temperature displayed on controlling unit (fig. 4.3). The linear fittings to the data were performed. The formulas to calculate the set temperature (T_{set}) required to achieve desired experimental temperature (T_{real}) are:

$$\begin{aligned} T_{set} &= (T_{real} - 3.04)/0.94 && \text{for } -20 \leq T_{real} \leq +5°C && \text{(liquid } N_2\text{)} \\ T_{set} &= T_{real} - 0.94 && \text{for } 10 \leq T_{real} \leq 25°C && \text{(ice)} \\ T_{set} &= (T_{real} - 2.67)/0.93 && \text{for } 30 \leq T_{real} \leq 60°C && \text{(heater/s)} \end{aligned} \tag{4.10}$$

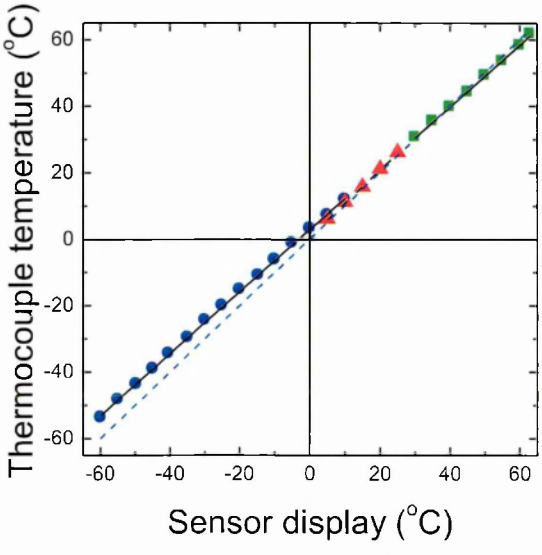

Figure 4.3 Temperature of thermocouple merged in cement sample and placed in spectrometer against the sensor display temperature of controlling system. Temperature of sample in spectrometer is controlled in three different ways: by using liquid nitrogen (blue circles), ice (red triangles) and heaters (green squares) combined with gas nitrogen flow. Dashed line is $y = x$ plot.

5. Sorption hysteresis

5.1. Calibration and assignment of signals

5.1.1. Is all the water detected by NMR?

Figure 5.1 shows exemplar QE data recorded during a sorption experiment for a sample of white cement paste equilibrated at 23% RH on the first desorption branch of sorption isotherm. The data acquisition parameters are given in section 4.2.2. Data are shown for τ values ranging from 12 to 45 μs. Each decay curve comprises an echo centred on a time 2τ and an exponential decay. Also shown are the echo and exponential decay fits to the data. Their sum is fitted according to equation (4.3).

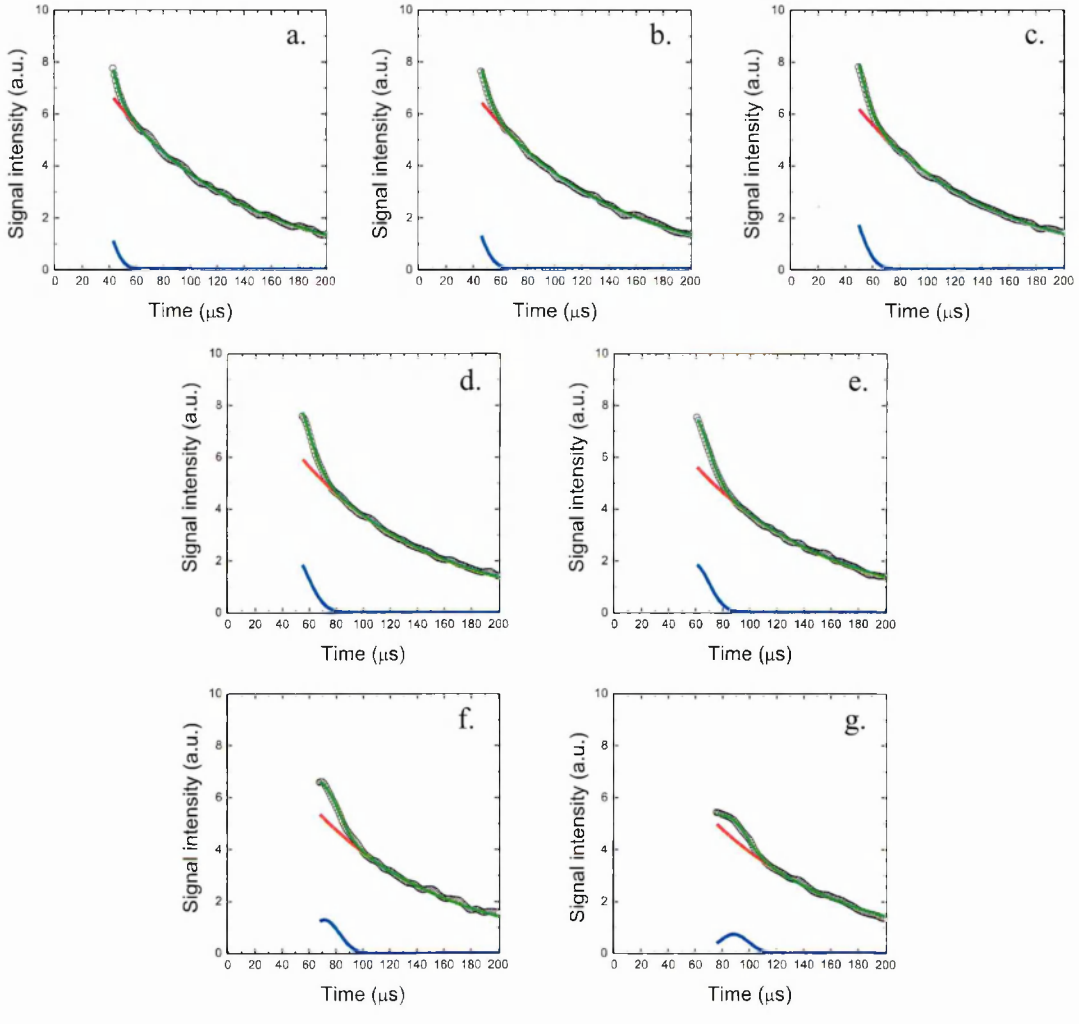

Figure 5.1 Quad echo signals recorded for white cement paste cure underwater (w/c_{mix} = 0.4) for 28 days and equilibrated at 23% relative humidity (black circles). Pulse gap (τ) was: a: 12μs, b: 15μs, c: 19μs, d: 24μs, e: 30μs, f: 37μs, g: 45μs. The lines present fitting for solid (blue) and mobile (red) components; the green line is the total intensity fit. The zero time is taken as the end of first 90° pulse of the sequence.

The pulse gap (τ) dependence of the solid echo and mobile decay amplitudes resultant from this fitting are shown in figure 5.2. It can be seen that the mobile amplitude has very weak dependence on pulse gap while the solid echo amplitude is strongly pulse gap dependent. Increase of pulse gap causes the decrease of solid amplitude; the solid signal relaxes. Hence, to gain the true solid signal, not influenced by relaxation process, the amplitude was back-extrapolated to zero pulse gap (τ = 0). This is shown by solid line in figure 5.2: single exponential decay. The exponential fitting was performed as it has been found to be the best fit for cement materials according to McDonald *et al* [26]. For consistency, the mobile fraction was also back-extrapolated. The linear and exponential fittings gave almost the same mobile amplitude (within 0.5% difference).

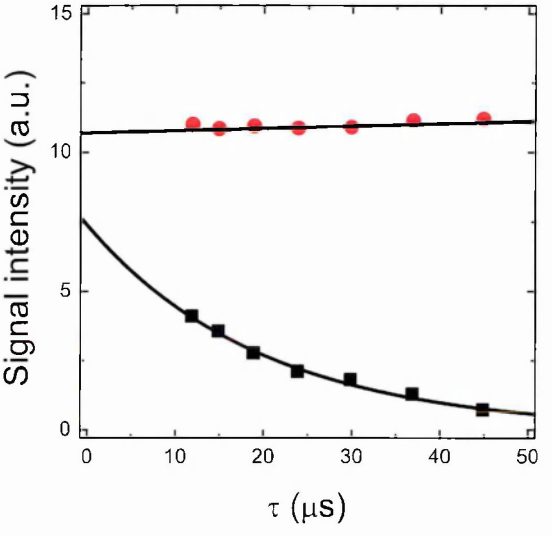

Figure 5.2 Solid echo (black squares) and mobile decay (red circle) signal amplitudes as a function of pulse gap (τ). The lines are the fits to the data: exponential for solid and linear for mobile signals.

It was critical for analysis to confirm that the NMR measurements 'see' all the water in the samples. In order to verify this, the total NMR signal - the sum of QE solid and mobile signals, was measured during progressive drying of a white cement paste (w/c_{mix} = 0.4). The samples were dried by equilibration at progressively lower RH in the IGAsorp Analyser. The total NMR signal intensity as a function of sample mass displays linear behaviour (figure 5.3). This is as expected since loss of each water molecule contributes a proportional loss of signal intensity. The best fit to the total intensity (I_{Tot}), excluding the point at 0.76 normalised sample mass, is expressed by equation $I_{Tot} = 3.158 \cdot m - 2.158$ with coefficient of determination (R^2) equal to 0.997. The intercept with the normalised sample mass axis allows calculation of the effective water to cement ratio. It is $(w/c)_{eff}$ = 0.463. The sample was made at $(w/c)_{mix}$= 0.4. The increase of this ratio reflects the subsequent curing of samples under saturated CH solution. The measurements of $(w/c)_{eff}$ based on the mass of paste samples after casting and after nominally 28 days of underwater curing were also performed and yield the same result. Taken together these results prove that there is no 'hidden' water reservoir within the sample that NMR cannot sense.

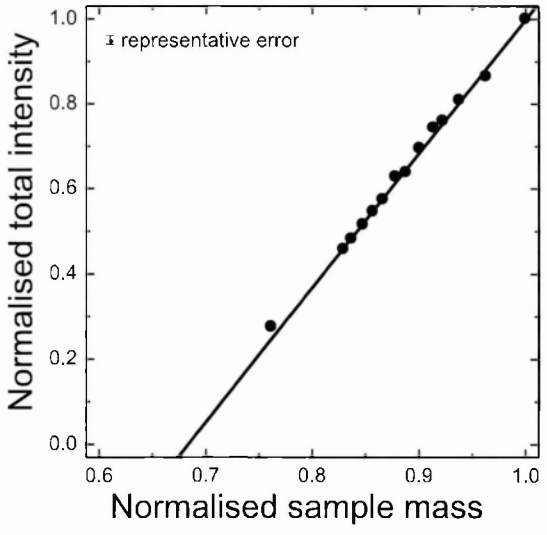

Figure 5.3 Changes in total NMR signal intensity as a function of normalised sample mass during drying of white cement paste.

5.1.2. Origin of the solid signal

The next step was to identify the origin of the QE solid signal. The QE measurements of powdered $Ca(OH)_2$ dried at 120°C for 48 hours were performed. The recorded signals are presented in figure 5.4. No mobile signal was observed. The echoes at the lower τ values were followed by a negative signal transient – a typical feature of a Pake doublet in the time domain. As the Pake doublet is characteristic of dipolar coupled spins pairs, and there is no mobile contribution to the signal, it confirmed that protons of Portlandite (CH) are chemically bound and entirely observed in solid part of the QE signal.

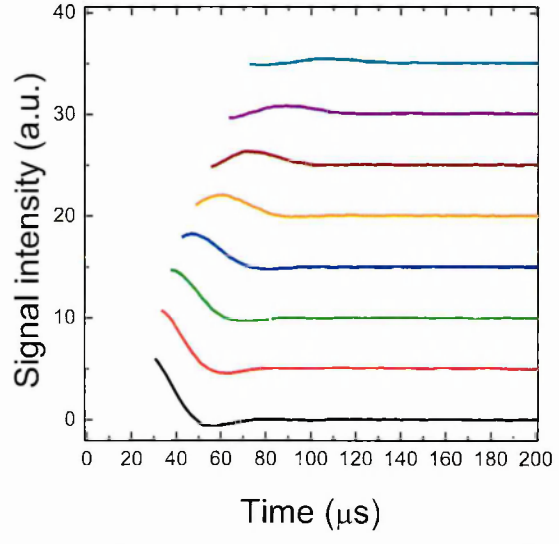

Figure 5.4 Stack plot of the Quad echo signals recorded for dried $Ca(OH)_2$. Pulse gap, τ, from bottom to top was: 12, 15, 19, 24, 30, 37, 45 and 54 μs.

Thermogravimetric analysis (TGA), X-ray diffraction (XRD) and calculation using thermodynamic model GEMS were performed on an as prepared (100% RH) sample by Arnaud Muller during the author's visit to EPFL. These techniques gave the mass fraction of CH in the paste as 22.5%, 23.7% and 24% respectively. The average fraction 23.4 ± 0.6% can be expressed as m_{CH} = 0.34 ± 0.01 g/g anhydrous cement. The mass fraction of ettringite measured by XRD was equal to 5.7±1.0% in the paste, equivalent to m_{Ett} = 0.083 ± 0.015 g/g anhydrous cement. The fraction of water combined into those two crystalline phases, CH and ettringite, is expressed as:

$$[(m_{CH} \cdot H_{CH}^{AMU}/CH^{AMU}) + (m_{Ett} \cdot H_{Ett}^{AMU}/Ett^{AMU})]/(w/c)_{eff} \quad (5.1)$$

where H_{CH}^{AMU} and H_{Ett}^{AMU} are the atomic mass units of water in CH and ettringite and CH^{AMU} and Ett^{AMU} are the atomic mass units of CH and ettringite.

The fraction of water obtained from equation (5.1) is equal to 26 ± 2% and stays in reasonable agreement with NMR solid intensity of 24.3%. It provides confidence that the NMR QE solid signal arises from Portlandite and ettringite, and hence does not comprise any contribution from C-S-H (further evidence is presented in section 6.3.3).

5.1.3. Differentiation of the mobile water component

The mobile water fraction measured by the QE experiment was further decomposed into water reservoirs characterised by different T_2 relaxation time by applying the CPMG pulse sequence. The echo decays were acquired and Laplace inverted as described in section 4.3.2.2.

An examplary CPMG data treatment for white cement paste sample equilibrated at 90% RH is presented in figure 5.5. The Inverse Laplace Transform (ILT) of the CPMG signal (fig. 5.5 c) decomposes the mobile fraction into three components with T_2 values of 126 ± 5, 412 ± 20 and 1800 ± 400 μs. The signal intensities normalised to the total CPMG intensity - mobile water, are 0.445, 0.546 and 0.009 respectively. The renormalisation of these fractions to the total intensity obtained from QE experiment yields 0.326, 0.399 and 0.007 respectively.

Figure 5.5 a and b shows the CPMG decay data and the fit based on the T_2 values and intensities obtained from ILT analysis. The coefficient of determination (R^2) for the fit presented was calculated according to:

$$R^2 = 1 - \frac{SS_R}{SS_{TOT}} = 1 - \sum_i (y_i - f_i)^2 \Big/ \sum_i (y_i - \bar{y})^2 \quad (5.2)$$

where SS_R and SS_{TOT} are the residual and total sum of squares, y_i and f_i are the observed and modelled values respectively and $\bar{y}$ is the mean of observed data. The R^2 for presented fit is equal to 0.999.

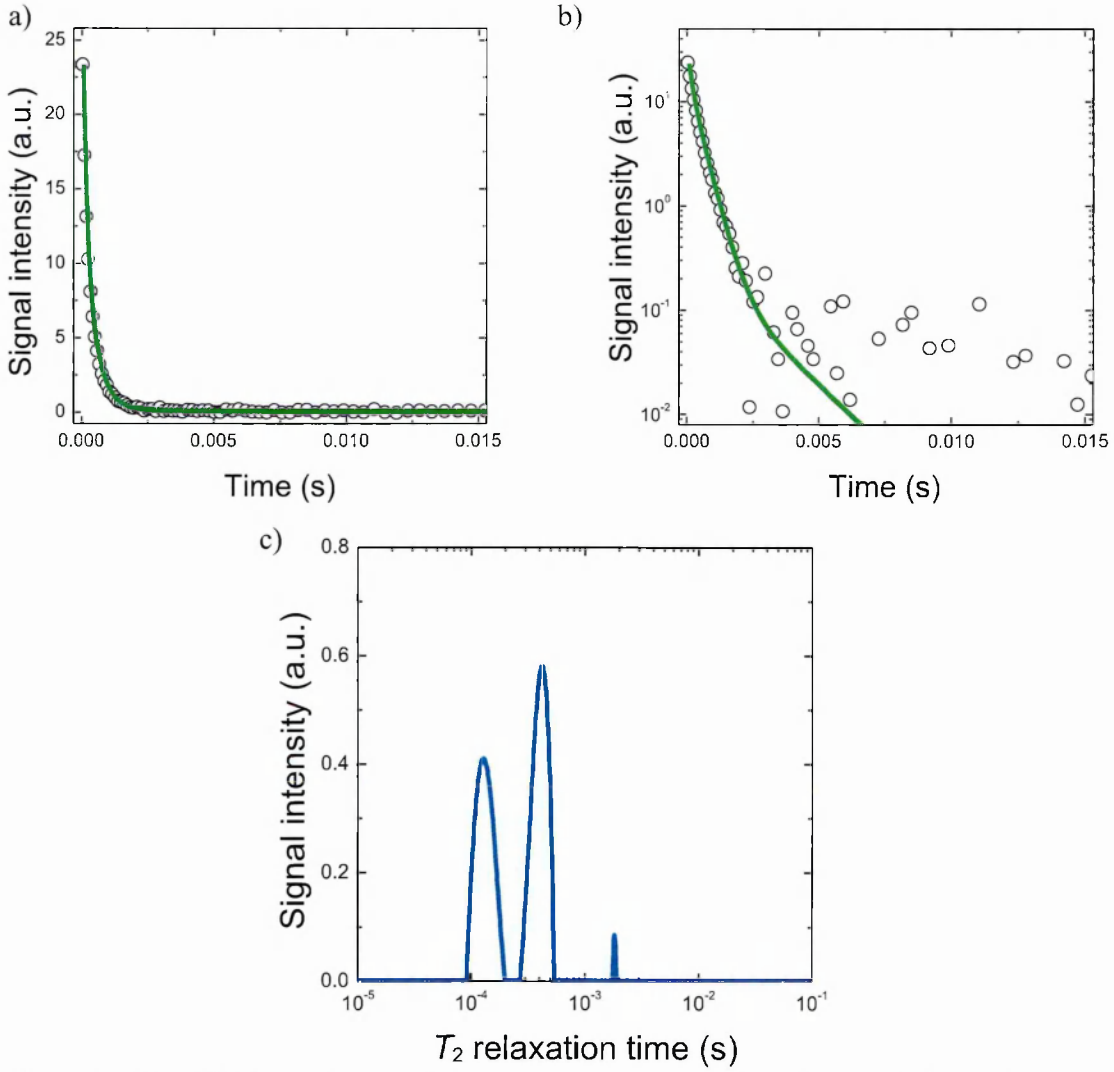

Figure 5.5 The CPMG signal recorded for white cement paste cure underwater (w/c_{mix} = 0.4) and equilibrated at 90% RH. The echoes decay data (circles) are presented in form of linear-linear (a) and log-linear (b) plots. Green lines are the fits based on T_2 and intensity values obtained from ILT. The inverse Laplace transform of the CPMG decay is presented in (c). In (b) negative baseline points are not shown.

The T_2 relaxation time of mobile water increases with the increase of pore size. The signal with the shortest T_2 is assigned to the smallest spaces whereas with the largest T_2 to the biggest spaces. Since all solid signal is account for CH and ettringite as shown in previous section (5.1.2), water filling C-S-H interlayer spaces and specifically any OH^- groups in interlayers cannot contribute to the solid signal. Studies by Monteilhet *et al* [95] and Valori *et al* [112] suggested that for cementitious materials the T_2 of order of few hundreds microseconds is characteristic for liquid in spaces of about few nanometers in C-S-H gel.

Taking these together, the T_2 relaxation time component with smaller T_2 (~ 120 μs) is assigned to water as well as to surface hydrogens and residual hydroxyl groups in interlayer pore spaces between calcium-silicate layers which exchange hydrogens. The components with

larger T_2 are assigned to water in C-S-H gel pores (~ 400 μs) and to water in interhydrate spaces (~ 1600 μs). Components with T_2 longer than those appearing in this sample originate from water in capillary pores and cracks. In this work the combined interhydrate and capillary pore water are defined as the 'free' water.

5.2. TOTAL INTENSITY HYSTERESIS LOOP

The normalised sample mass and total signal intensity have been plotted against relative humidity for cement samples spanning one and an half cycles of the desorption and adsorption isotherm – figure 5.6. The primary desorption shows the changes with humidity in the range from 100 to 0% RH. The data point at 100% RH represents the 'as prepared' cement paste and at 0% RH paste oven dried at 180°C. Other samples were equilibrated in the IGAsorp Analyser. The adsorption and secondary desorption were measured for the cycles between 5 and 80% RH.

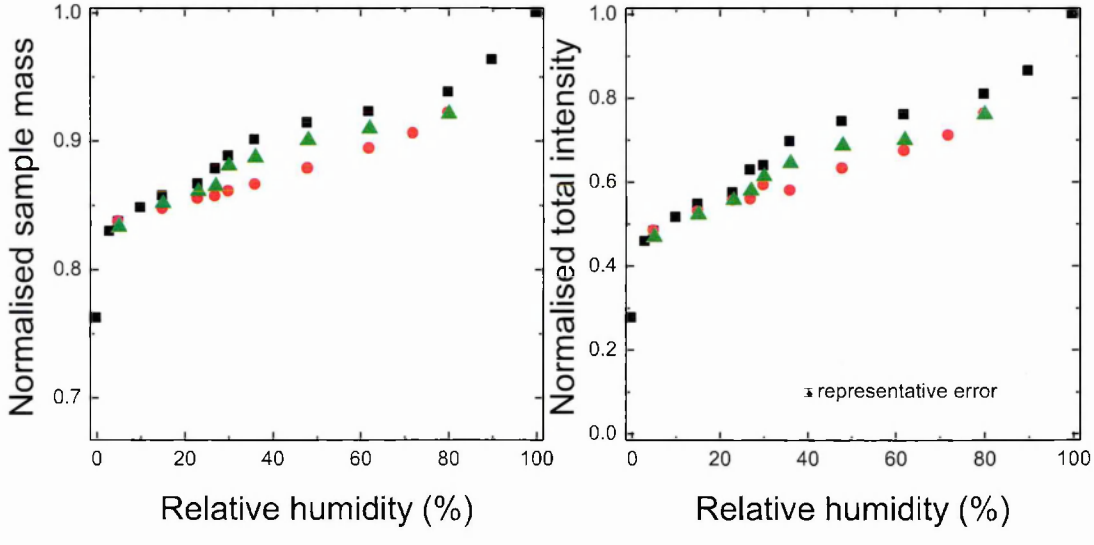

Figure 5.6 The normalised sample mass (left) and total NMR intensity (right) against relative humidity in progressively dried (black squares), wetted (red circles) and re-dried (green triangles) white cement paste.

The mass and NMR isotherm display an almost identical and characteristic hysteresis loop. This is not surprising as the sample mass and signal intensity are directly proportional.

The primary desorption results are consistent with larger pores emptying at high humidity (> 90%), smaller capillary and gel pores drying over a broad range down to 40% RH and finally loss of interlayer water at lower humidity (< 20%) [40].

The re-adsorption shows the signal and mass recovering to a lower value at any given humidity than was present during desorption. Initially up to around 20-25% RH water closely tracks the primary desorption. Above that value the adsorbed water increasingly lags behind the primary desorption. The maximum lag is equivalent to about 12% of the initial total water

content and occurs at about 40% RH. At the top of the loop at 80% RH the gap reduces to about 5% water content.

The existence of this loop in the NMR data confirms what is known from normal gravimetric data: the distribution of water in the different pore environments is different at any given RH on desorption and adsorption paths. The hysteresis between desorption and adsorption of cement based material has been reported in literature [113], [114]. The bigger hysteresis was also observed in middle range of humidity where the capillary condensation and evaporation are assumed to be dominating sorption mechanism. Below 33% humidity the hysteresis was reduced significantly and was less evident when adsorption started at higher RH values [114]. The possible reasons for hysteresis were explained by Feldman [113] in terms of irreversibility in removal and re-entering of water from interlayer spaces that collapse during drying or by Jennings [40] in terms of multi-size ink-bottle pores effect.

The secondary desorption presents the same trend as the original dehydration. However, as it starts at 80 not 100% RH, the water content is lower. In the humidity range below 30%, the water content tracks across to primary curve. The data reported in [114] showed that the secondary desorption from 100% RH initially overlaps the primary desorption but is shifted upwards, in comparison with primary desorption, at humidities below 44%. Nevertheless, if the starting humidity is lower the secondary desorption curve lays below primary desorption and the humidity at which they cross is lower. That agrees with the data reported here.

5.3. PORE-TYPE RESOLVED DESORPTION ISOTHERM

The NMR method has the advantage that it allows the isotherm to be resolved by pore type. Figure 5.7 shows the first pore-type resolved desorption isotherm to be measured in any cementitious material and possibly any nano-porous material. The total signal is decomposed into particular water populations: chemically combined water, C-S-H interlayer pore water, gel pore water and free (interhydrate and capillary) water.[16]

The plots show that the interhydrate and capillary porosity ('free' water) dries above 90% RH. That agrees with a calculation according to the Kelvin equation (eq. (2.6)) that all pores above 10 nm are empty at 90% RH. The gel pores become empty in the range between 100 and 25% RH equivalent to 1 and 0.6 relative water mass. The gel intensity plot plateaus for lower humidity, down to almost 0% RH, with a residual water content of about 5%. The origin of this gel intensity tail is not clear. It may indicate the presence of isolated smaller gel pores without connectivity to facilitate their drying. The other possibility, more favourable, is the presence of ink-bottle pores which cannot dry until drying of the smallest pores joining them with 'outside' occur. Almost no gel signal is observed at 0% RH for the oven dried sample.

A striking feature is that in the range 100 to 25% RH, as the gel signal decreases, an increase in the C-S-H interlayer signal is observed. This is explained by the relaxation behaviour of surface water molecules. When gel pores are full, gel surface water molecules

[16] sample at 100% RH was measured by Arnaud Muller during the author's visit to EPFL

are in rapid exchange with bulk gel pore water and therefore have the same T_2 relaxation time. However, as gel pores dry, there is a layer of less mobile water left on the pore surface. The surface layer molecules are no longer able to exchange with more mobile bulk water of gel pore. Hence, in NMR terms, they appear more like C-S-H interlayer water with shorter T_2 relaxation time.

Below 25% RH the C-S-H interlayer water signal decreases from about 0.3 to 0 at 0% RH. In this region, a similar rise in the component with the lowest T_2 relaxation time, chemically bound water is observed as the mobility of residual water in interlayer spacing is reduced.

At the lowest humidity, the intensity of chemically combined water decreases back to the starting value of 0.24.

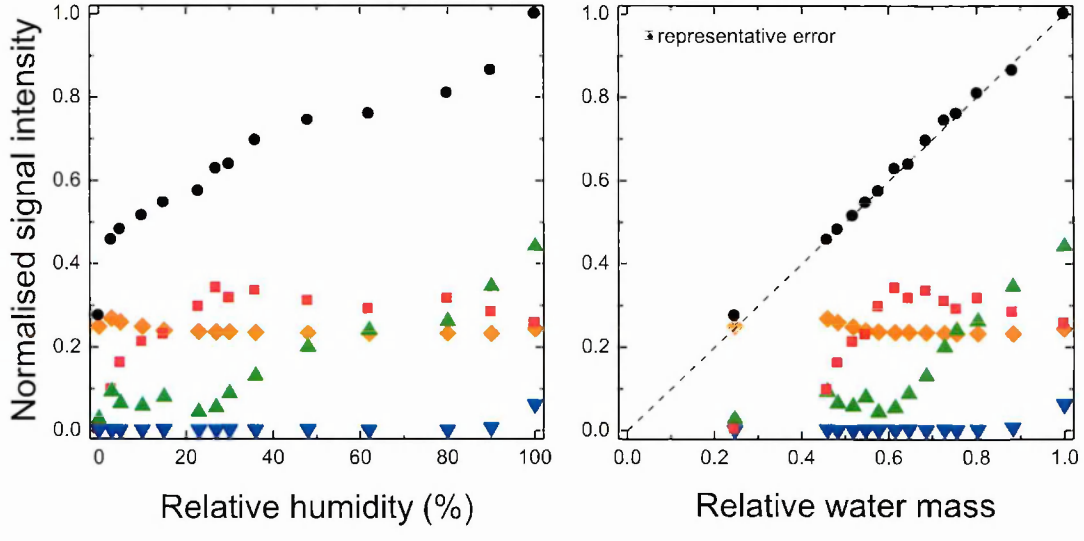

Figure 5.7 The normalised total signal intensity (black circle) as a function of relative humidity (left) and relative water mass (right). Total signal is further de-composed into chemically combined water (orange diamonds), C–S–H interlayer pore water (red squares), C–S–H gel pore water (green triangles) and 'free' water (blue inverted triangles).

The presented data allow a new schematic drawing of C-S-H morphology and water placement within C-S-H gel as 'seen' by NMR. This is shown in figure 5.8. The continuous network of C-S-H layers and gel pores is presented. At 100% RH all the surface water molecules in the interlayer and the gel pores are in rapid exchange with bulk pore water. They are seen as interlayer and gel water with two T_2 components respectively. When the humidity is decreased down to 25% the gel pores empty. The interlayer spaces are full of water. There is also a residual water layer on gel pore surface. This all appears as interlayer water in the T_2 spectrum. At even lower humidity, about 3%, the residual immobile water molecules left within structure appear solid like.

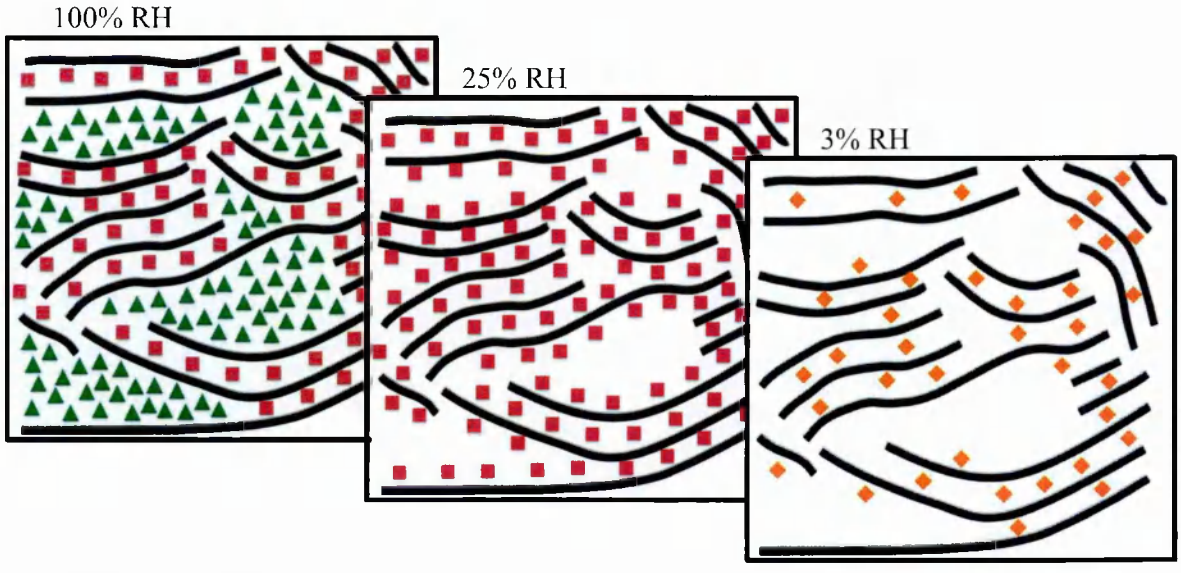

Figure 5.8 The schematic morphology of the C–S–H phase at 100, ~25 and ~3% RH. Black lines are Ca-O layers with SiO_4 tetrahedra on both sides. The C–S–H gel water molecules are presented by green triangles. Red squares are the water molecules filling C–S–H interlayer spaces and surface molecules in C–S–H gel pores at lower humidity. At the lowest humidity water molecules in interlayer spaces appear as solid-like and are shown as orange diamonds.

5.4. Isotherm loops for particular water reservoirs

The separately resolved first desorption, re-adsorption and second desorption isotherm loops for chemically combined water, C-S-H interlayer space water, C-S-H gel pore water and 'free' water as a function of relative humidity are presented in figure 5.9 a-d.

The intensity of the chemically combined water follows the same pattern, within experimental error, for each sorption process (fig. 5.9a). Below about 25% RH there is a slight (~0.04) increase in the signal, otherwise it is flat.

The interhydrate and capillary pores do not refill in the range of the loop studied, 5 to 80% RH. Their intensity stays at 0 at all humidities below 90% (fig. 5.9d).

Although there is a scatter in the data, the primary desorption, adsorption and secondary desorption of the C-S-H interlayer water intensities are the same to within measurement error below ~20% RH (fig. 5.9b). The interlayer intensity maxima appear at ~25% RH for all three sorption processes. Above this humidity, a decrease in intensity is observed. On the adsorption path intensity is always less than for primary desorption with typically 9-5% below. The secondary desorption signals are in between those two, closer to primary desorption. The interpretation of the adsorption results is complicated by the fact that the interlayer signal has two parts. The first is C-S-H interlayer water. The second is refilled surface layers in the gel pores that appear in this category of signal until the gel pores are fully refilled. Potentially this leads to a complex curve shape dependent on the order in which pores/surfaces refill.

The rehydration shows that the gel pores start to fill at a humidity point slightly moved forward (by 5% RH) in comparison to the point at which they became empty in a course of

drying (fig. 5.9c). Nevertheless the gel intensity is much lower than for the primary desorption up to 80% RH where it becomes the same. The maximum difference in the gel intensity – 8%, is reached at about 50% RH which is displaced upwards in comparison with the maximum lag of total signal intensity. Secondary desorption causes the gel pore water intensity to decrease faster down to 40% RH and then behave in the same way as during first desorption.

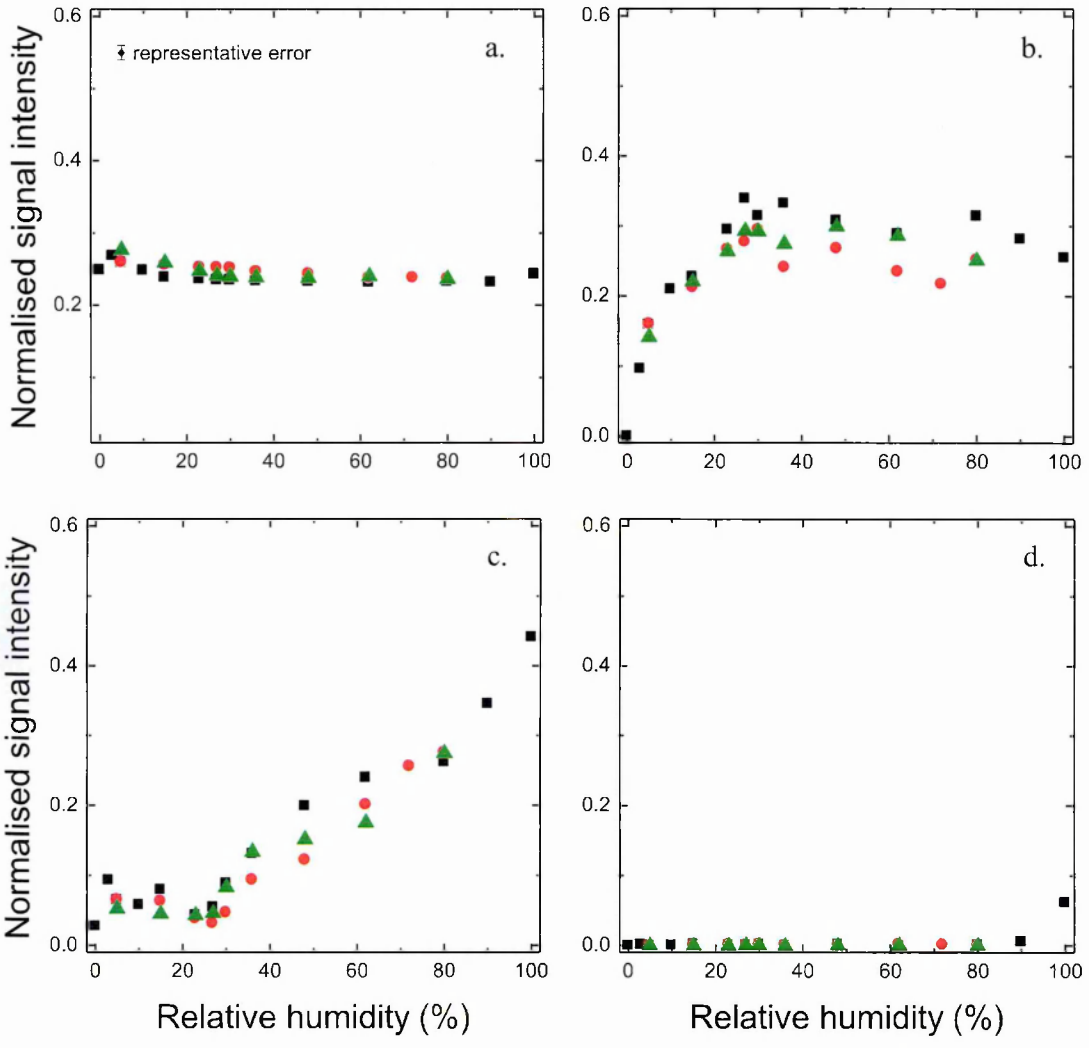

Figure 5.9 Signal intensity isotherm loops for chemically bound water (a), water in C–S–H interlayer (b) and gel (c) pores and 'free' water (d) during desorption (black squares), adsorption (red circles) and re-desorption (green triangles) as a function of relative humidity.

A better understanding of the effect of drying and wetting processes on the interlayer and gel pore water filling is provided by plotting the signal intensity as a function of relative water mass - figure 5.10 a-d.

Figure 5.10b shows that in the range of water mass fraction between 0.45 and about 0.55 the rate of filling interlayer spaces during adsorption is faster in comparison with the rate for both primary and secondary desorption branches. It is also observed that the maximum

interlayer water signal is reached earlier at about 0.55 water mass, in comparison with 0.6 for both desorption branches.

Above ~0.55 relative water mass, the gel pore water signals begin to increase. At any given water mass the gel signal is considerably higher during adsorption than primary desorption. The secondary desorption is similar to primary desorption (fig. 5.10c). Correspondingly, the interlayer like signal is lower for both wetting and re-drying cycles in comparison with primary desorption (fig. 5.10b). It reaches the lowest values for the former which intensities do not rise above that occurring at ~0.9 water mass fraction for primary desorption across the range 0.6 to 0.8 water mass. For later the values are averaged, more close to desorption.

These observations suggest that there is a much lower amount of interlayer-like monolayer water covering the surface of gel pores during adsorption compared to desorption. Hence the mechanism of filling the gel pores may be different during the adsorption process compared to emptying during desorption as discuss further in section 5.6.

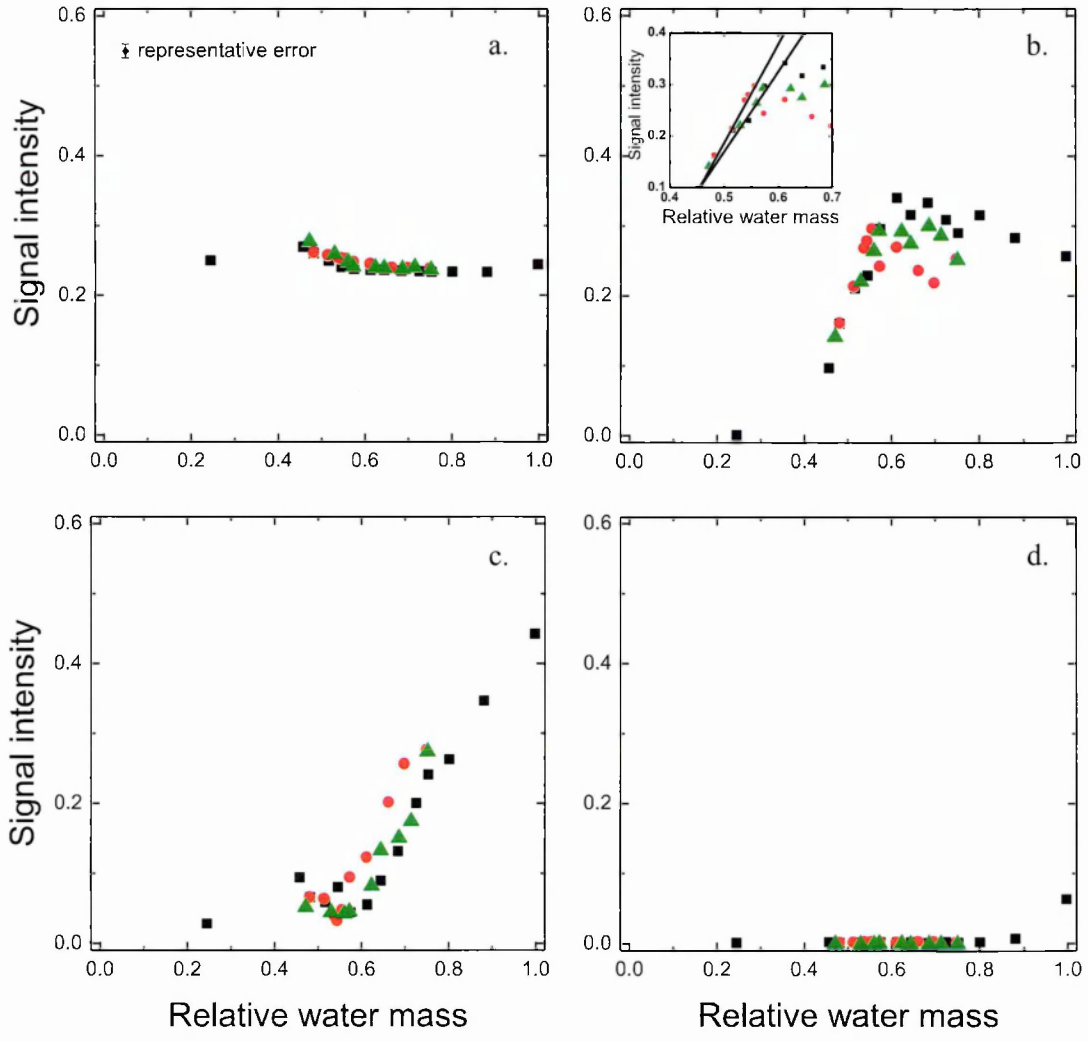

Figure 5.10 Signal intensity isotherm loops for chemically bound water (a), water in C–S–H interlayer (b) and gel (c) pores and 'free' water (d) during desorption (black squares), adsorption (red circles) and re-desorption (green triangles) as a function of relative water mass.

5.5. T_2 DISTRIBUTION

The T_2 relaxation time distribution of C-S-H interlayer and gel water provides further information. The graphs in figure 5.11 a-c shows the T_2 distribution where the markers present the time at which the maxima of ILT peaks appear and the bars are the widths of those peaks.

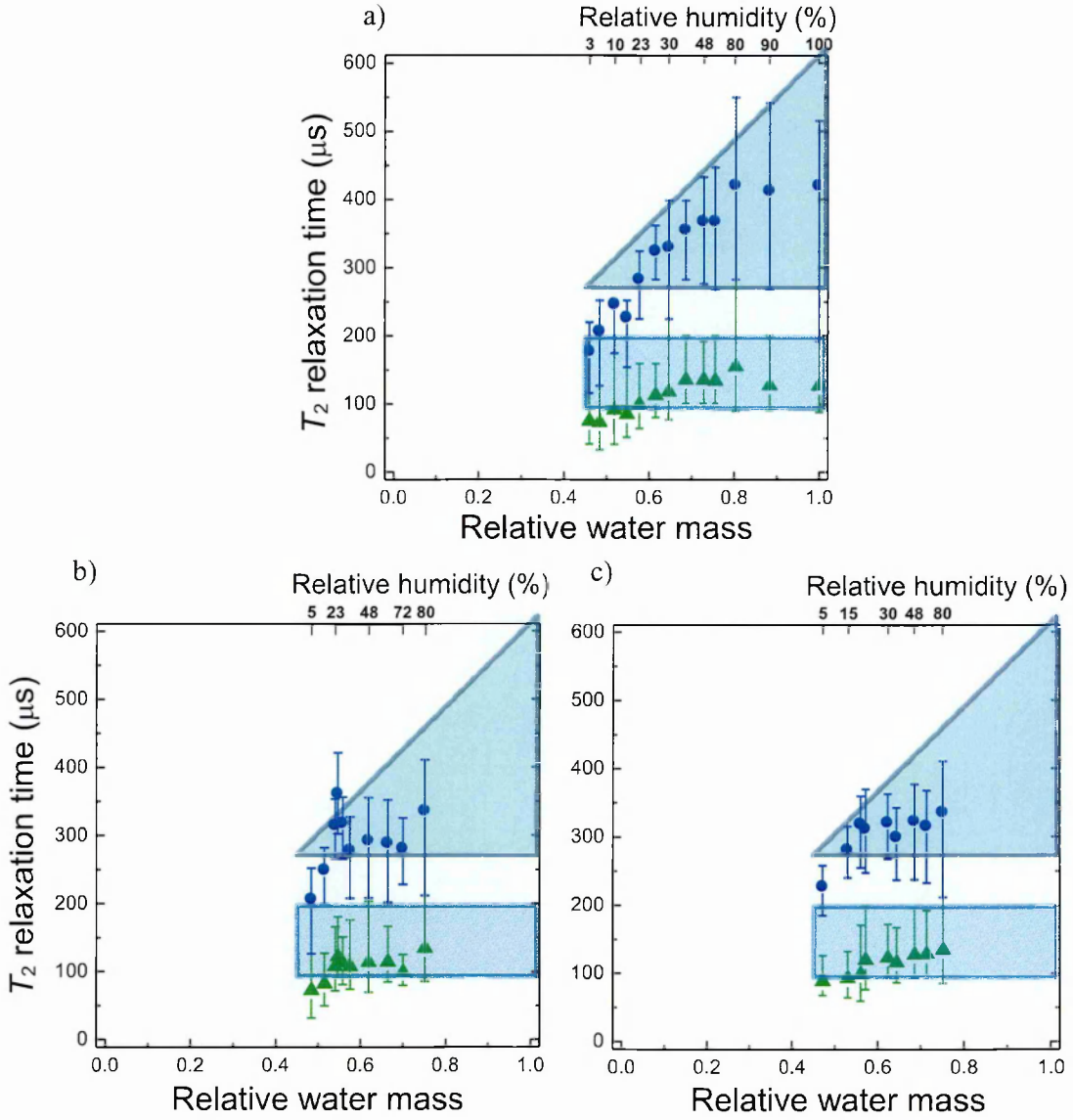

Figure 5.11 The T_2 relaxation time distribution as a function of relative water mass – lower axis, and RH – upper axis, during desorption (a), adsorption (b) and re-desorption (c) for C–S–H interlayer pore water (green triangles) and gel pore water (blue circles). The light blue boxes span the width of T_2 peaks of primary desorption and are provided as a guide to the eye.

During primary desorption the distribution of T_2 relaxation time for gel pore water shows a constant lower boundary of T_2 down to a relative water mass of about 0.6 at which point the gel signal intensity nears zero. This suggests a lower limit of filled pore sizes that does not change on desorption. The higher boundary of T_2 progressively decreases with reduction of

the water mass and relative humidity. This in turns suggests that the largest gel pores empty first. There is a wider distribution of filled pore sizes at high humidity compared to low humidity. The distribution of interlayer pore water stays constant down to a water mass of about 0.65 – 0.70 (humidity around 35%). Then its value starts to decrease. It reaches 75 μs at 3% RH. There may be several reasons for this. One possibility is that the surface mono-layer of water in empty pores has a slightly lower T_2 than that of the interlayer water (which is a few monolayers wide). The ILT is not able to separately resolve them both and hence the average decreases as the gel pore empties and surface layer increases. Another possibility is that pearling artificially increases the interlayer water T_2 at high humidity when there is a large gel pore signal.

Upon adsorption, the gel pore water T_2 distribution does not recover to the previous level. The lower boundary value is approximately constant at around 200 μs, ~75 μs less than during desorption. Apart from one data point measured at 27% RH with intensity less than 0.03, the T_2 times are also less than during desorption. Above a water mass fraction of 0.56 the times of peaks maxima are almost constant, close to the desorption lower boundary. Finally at water mass of 0.75 there is a substantial growth in T_2 value to almost the same value (~350 μs) as on desorption path. The constant T_2 value below 0.75 mass (equivalent 80% RH) may suggest that the surface to volume ratio of the pore water is also constant. The interlayer water T_2 achieves fairly constant value at 0.55 water mass, same mass at which the interlayer signal reaches the highest value.

The secondary desorption presents the data similar to the first desorption. The higher limit of the gel water T_2 decreases gradually. The lower limit is approximately constant at the ~50 μs lower T_2 with the huge majority of peak widths covering the same T_2 range.

5.6. ADSORPTION MECHANISM

The isotherm loops for interlayer and gel pore water allow an interpretation of the way the gel pores fills during adsorption. As shown in figure 5.10 b the maximum in interlayer water intensity is followed by sudden and significant drop of intensity (~0.05 at 36% RH). Afterwards the intensity seems to be constant in the range of experimental error (fig. 5.12) contrary to desorption processes where a gradient is observed. As the decrease in interlayer intensity is not observed, the intensity value is approximately the same as at 100% RH in 'as prepared' paste. The second desorption starts with an immediate rise of intensity. These observation suggest that the mechanism of adsorption differs from desorption and that interlayer signal belongs entirely to interlayer water and specifically not to surface water layer during adsorption above ~30% RH.

Additionally, the gel pore water intensity is shifted upwards during adsorption in comparison to both desorption branches (fig. 5.10 c). The shift in signal fraction is ~0.05 that corresponds to the value of decrease in interlayer water signal.

The decrease in interlayer signal accompanied by an increase of gel pore water intensity together strongly suggest that water layer created at the surface of gel pores is totally covered by the next layer of gel water at ~30% RH in the course of adsorption. The refilling of gel

pores may occur layer by layer in which case after the second layer of water is drawn into gel pores the concept of surface layer is not anymore valid. Mechanisms of pores emptying during desorption and filling during adsorption is schematically presented in figure 5.13.

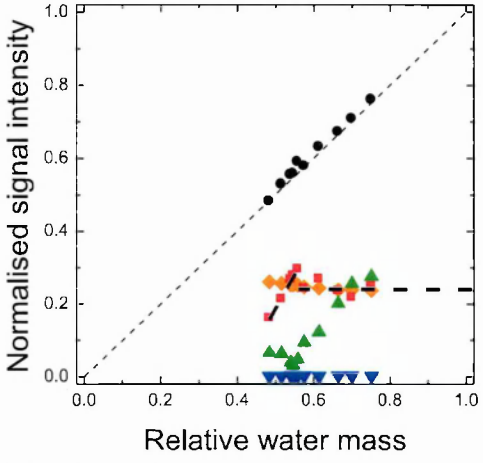

Figure 5.12 The fitting lines (thick dashed lines) of the interlayer signal for adsorption. Orange diamonds represent chemically combined water signal, red squares – the C–S–H interlayer pore water, green triangles – the C–S–H gel pore water and blue inverted triangles – the 'free' water signals. The black circles show the total water signal.

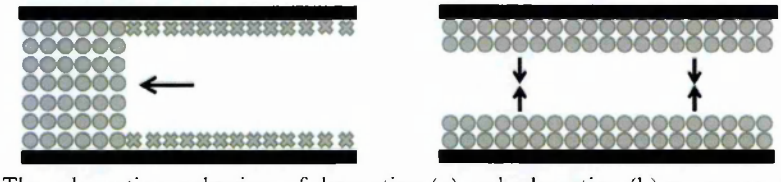

Figure 5.13 The schematic mechanism of desorption (a) and adsorption (b) processes. Circles represent mobile water molecules, crosses are immobile, surface water molecules.

5.7. Pore size and specific surface area calculations

5.7.1. Specific surface area based on adsorption isotherm

The specific surface area of cement paste is evaluated from the adsorption isotherm based on both sample mass and total signal intensity. The data is fitted according to BET theory in the humidity range < 45% - equation (2.4) in section 2.3.3 for amount of adsorbed water u (fig. 5.14).

The surface area (A) is calculated according to equation (2.5) in section 2.3.3, $A = N_A \cdot A_m \cdot u_m / M^{AMU}$ where N_A is Avogadro number, M^{AMU} – water molar mass, A_m - cross section area of water molecule ($10.6 \cdot 10^{-20}$ m^2 [59]).

The BET fitting parameters based on changes in total intensity are u_m = 0.041 and K = 7.19. The fitting of sample mass yields u_m = 0.037 and K = 5.54. The calculated specific surface areas are 144 ± 24 and 130 ± 5 m^2/g of dried paste (3% RH) according to changes in intensity and mass respectively.

The calculated SSAs based on the changes in total signal intensity and mass are in good agreement with each other. The BET surface areas agree with the range reported by Baroghel-Bouny [114] – 85-143 m^2/g of dried paste (3% RH).

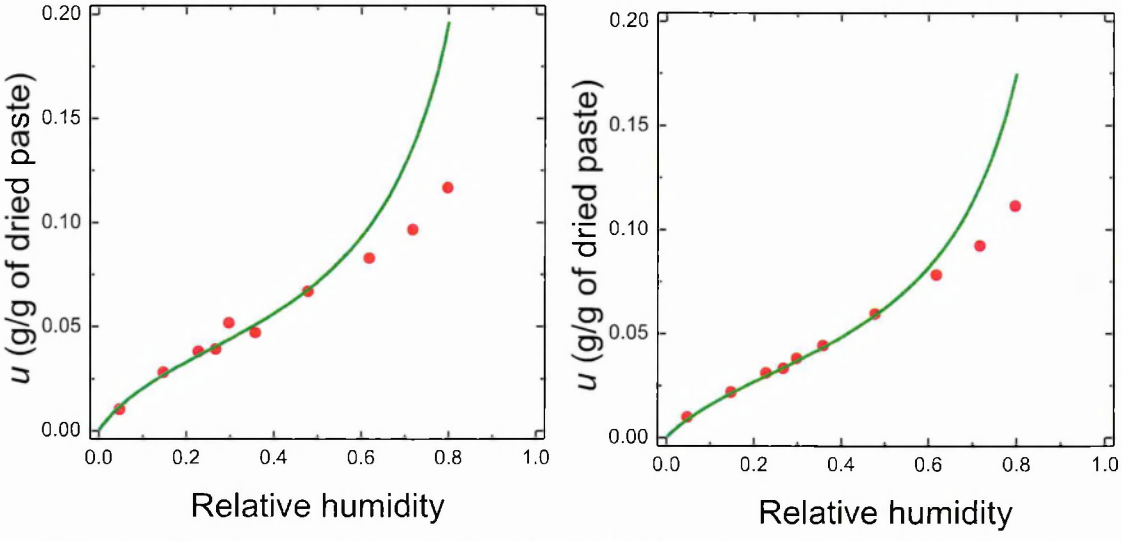

Figure 5.14 The adsorption isotherm in form of total NMR intensity sample mass (left) and sample mass (right). The green line presents the fitting according to BET equation.

5.7.2. Surface relaxation model

5.7.2.1. Pore size calculation

C-S-H interlayer and gel pore sizes were first calculated according to the fast exchange model of relaxation described in chapter 3.3.2 [27]. The model tells that, as water molecules undergo rapid exchange, the experimentally observed relaxation rate ($1/T_2$) is the volume weighted average of slowly relaxing bulk pore water and fast relaxing molecules on the pore surface. Considering that the $T_{2,bulk}$ relaxation time is very long, the contribution of bulk relaxation rate is negligible. This leads to the expression for observed relaxation rate:

$$\frac{1}{T_2} = \frac{\varepsilon S}{V} \cdot \frac{1}{T_{2,surf}} \tag{5.6}$$

where T_2 and $T_{2,surf}$ are the observed and surface relaxation times, S and V are the pore surface area and volume, ε is the thickness of water surface layer.

To calculate the surface-to-volume ratio, and hence pore size, the surface relaxivity ($\lambda = \varepsilon/T_{2,surf}$) is required. In this study, a water monolayer thickness (ε = 0.28 nm) and the relaxation time of the sample equilibrated at 3% RH ($T_{2,surf}$ = 75 μs) has been used for calibration. They yield surface relaxivity equal to $3.7 \cdot 10^{-3}$ nm/μs.

The pore size (d) is related directly to the surface-to-volume ratio. That relation depends on the shape of the pores. The calculation based on planar pores ($S/V = 2/d$) gives an equation for the width:

$$d = 2 \cdot \lambda \cdot T_2 \tag{5.4}$$

The C-S-H interlayer spacing based on the relaxation times (126 μs) is 0.94 ± 0.04 nm, gel pore size (420 μs) is 3.1 ± 0.2 nm and interhydrate size (1.4 ms) is 10.5 ± 1.8 nm.

5.7.2.2. Specific surface area calculation

Given the pore size the equation of specific surface area (A) can be evaluated. The volume of water in particular reservoirs is obtained by multiplication of signal intensities ($I_{CSH/gel}$) and effective water to cement ratio (w/c_{eff}). The SSA is calculated by dividing that volume by the width of pore expressed in cm. Further it is normalised to the volume of cement paste (V_p). The equation of SSA expressed in m^2 per cm^3 of paste can be written as

$$A_{CSH/gel} = \frac{I_{CSH/gel} \cdot \left(\frac{w}{c}\right)_{eff}}{2 \cdot \lambda \cdot T_{2,CSH/gel}} \cdot \frac{10^{-4}}{V_p} \tag{5.5}$$

The SSA for C-S-H interlayer pores is 175 ± 12 m^2/cm^3 of paste and for gel pores is 91 ± 4 m^2/cm^3 of paste. Equivalent values in different units are presented in table 5.1. The ratio of interlayer to gel SSAs is 1.9. The value of total specific area stays in good agreement with value obtained by Powers and Brownyard [32] – 170-195 m^2/g of anhydrous cement for 28 days old paste. It is however slightly lower than the values reported by Halperin *et al* [10] - 225 m^2/g of anhydrous cement, and slightly higher than that BET surface areas presented by Baroghel-Bouny [114] and calculated in section 5.7.1. based on adsorption branch.

Table 5.1 Specific surface area of C-S-H interlayer pores, gel pores and both together.

	Specific surface area in m^2 per				
	cm^3 of paste	g of paste	g of anhydrous cement	g of dried paste (180°C)	g of dried paste (3% RH)
Interlayer Pores	175±12	86	125	113	103
Gel Pores	91±4	44	65	58	54
Total	266	130	190	171	157

5.7.3. Amplitude model for calculation of pore size

The second model applied in order to obtain the C-S-H interlayer and gel pore sizes is the amplitude model described in section 3.4.3.2. This study extends and improves this approach.

5.7.3.1. Modification to the Amplitude model

The amplitude model by McDonald *et al* [26] presented in section 3.4.3.2 was relatively simplistic. The mobile signal was not differentiated between different pore types. In this thesis the application of CPMG pulse experiments facilitates such decomposition. Therefore, modifications to the calculation in the model are necessary.

The initial intensities in 'as prepared' paste (at 100% RH) for chemically combined water (I_{sol}), C-S-H interlayer pores (I_{CSH}), gel pores (I_{gel}) and 'free' water (I_{cap}) are expressed as:

$$I_{sol} = V_{sol} / V_{wp} = 0.243 \quad (5.6)$$

$$I_{CSH} = A_{CSH} \cdot (q + 2) \cdot d_{wat} / V_{wp} = 0.255 \quad (5.7)$$

$$I_{gel} = A_{gel} \cdot (p + 2) \cdot d_{wat} / V_{wp} = 0.441 \quad (5.8)$$

$$I_{cap} = V_{cap} / V_{wp} = 0.061 \quad (5.9)$$

where A_{CSH} and A_{gel} are the specific surface area of C-S-H interlayer and gel pores per unit volume of paste, V_{sol} and V_{cap} are volume of chemically bound and 'free' water per unit volume of paste, V_{wp} - volume of water in unit volume of paste (0.645 cm^3/cm^3 of paste), d_{wat} - the size of water molecule (0.28 nm). The definitions of p and q are presented in figure 5.15.

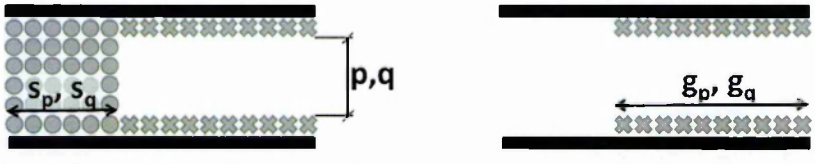

Figure 5.15 The parameters p and q are the gel and interlayer pore sizes respectively, without counting the surface water layer, expressed in number of water molecules; s_p and s_q are the fraction of specific surface area of gel and interlayer pores still filled with water during drying, g_p and g_q are the fraction of surface area covered by water layer.

The order at which water is removed is critical for analysis. Six stages of drying are identified and presented graphically in figure 5.16. (i) 'Free' water dries. (ii) Gel pores empty leaving a gel surface layer. (iii) The gel surface clears. (iv) The relatively mobile interlayer water is removed leaving a residual layer. (v) The residual interlayer water leaves. (vi) Chemically combined water from crystalline phases is removed.

The obtained NMR results do not show the fifth and sixth stages. Four stages in the data can at best be observed and further described including relevant equations:

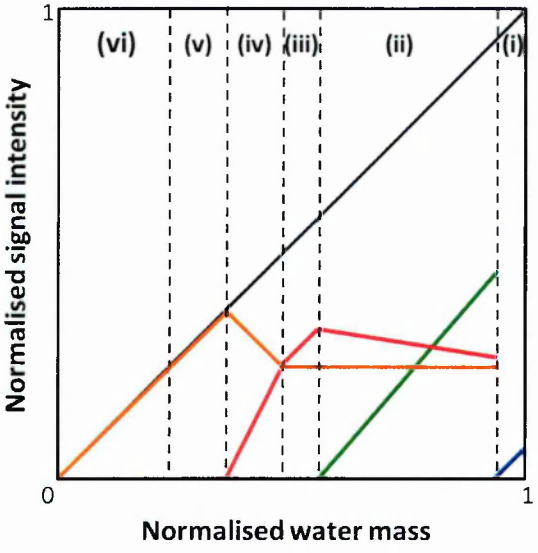

Figure 5.16. The scheme of five stages of cement paste drying according to NMR, description in text. Orange lines represent chemically combined water signal, red – the C–S–H interlayer pore water, green – the C–S–H gel pore water and blue– the 'free' water signals. The black line shows the total water signal.

(i) Evaporation of 'free' water occurs during primary desorption at the humidity above 90% RH. The normalised 'free' water mass, m_{cap}, is equivalent to its signal fraction at 100% RH (I_{cap}). However, it is not possible to extract any further information about pore size and the way they dry. This stage is not observed for secondary desorption as it is investigated in the RH range from 80 to 5%.

(ii) The bulk gel pore water fills the fraction $s_{p(ii)}$ of the gel surface area during drying (fig. 5.15). C-S-H interlayer water signal, $I_{CSH(ii)}$, consists of two parts: water fully filling interlayer spaces, $s_{q(ii)} = 1$, and two monolayers of water left on the gel pore surface fraction $1\text{-}s_{p(ii)}$. The water mass, $m_{(ii)}$, is lowered by 'free' water and progressively by drying of bulk gel pores water. This stage happens in the relative water mass range 0.94 to 0.6 (fig. 5.17). Hence:

$$I_{CSH(ii)} = \left[A_{CSH} \cdot (q+2) \cdot s_{q(ii)} + A_{gel} \cdot 2 \cdot \left(1 - s_{p(ii)}\right)\right] \cdot d_{wat}/\mathrm{V}_{wp} \quad (5.10)$$

$$I_{gel(ii)} = A_{gel} \cdot (p+2) \cdot s_{p(ii)} \cdot d_{wat}/\mathrm{V}_{wp} \quad (5.11)$$

$$m_{(ii)} = 1 - m_{cap} - A_{gel} \cdot p \cdot \left(1 - s_{p(ii)}\right) \cdot d_{wat}/\mathrm{V}_{wp} \quad (5.12)$$

$$I_{CSH(ii)} = a_{CSH(ii)} \cdot m_{(ii)} + b_{CSH(ii)} \quad (5.13)$$

$$I_{gel(ii)} = a_{gel(ii)} \cdot m_{(ii)} + b_{gel(ii)} \quad (5.14)$$

(iii) The gel surface water is removed gradually from $1\text{-}g_{p(iii)}$ surface fraction. The interlayer spaces remain saturated with water, $s_{q(iii)} = 1$, and the chemically combined water signal is constant. Hence the gradient of the interlayer signal should be 1. Considering the small mass range of this stage spanning at most two data points recorded within it, any further attempt to evaluate relations of pore parameters and intercepts of fitting lines is not rational and meaningful in this region. However, the existence of this region is critical to numerical solution of the model.

(iv) The relatively mobile interlayer water is removed in relative water mass range below 0.57 (fig. 5.17). A residual layer of water remains at surface fraction 1-$s_{q(iv)}$ of interlayer pores. This layer contributes to solid signal intensity, $I_{sol(iv)}$.

$$I_{CSH(iv)} = A_{CSH} \cdot (q+2) \cdot s_{q(iv)} \cdot d_{wat}/\mathrm{V}_{wp} \quad (5.15)$$

$$I_{sol(iv)} = V_{sol}/\mathrm{V}_{wp} + A_{CSH} \cdot 2 \cdot \left(1 - s_{q(iv)}\right) \cdot d_{wat}/\mathrm{V}_{wp} \quad (5.16)$$

$$m_{(iv)} = 1 - m_{cap} - \left[A_{gel} \cdot (p+2) + A_{CSH} \cdot q \cdot \left(1 - s_{q(iv)}\right)\right] \cdot d_{wat}/\mathrm{V}_{wp} + m_{gr} \quad (5.17)$$

$$I_{CSH(iv)} = a_{CSH(iv)} \cdot m_{(iv)} + b_{CSH(iv)} \quad (5.18)$$

$$I_{sol(iv)} = a_{sol(iv)} \cdot m_{(iv)} + b_{sol(iv)} \quad (5.19)$$

The model assumed that the gel intensity decreases to zero. In practice it does not. This leads to a systematic error in the resultant gel pore surface area. However, the earlier assumptions already made and the quality of the data do not warrant further analysis to incorporate this level of complexity. Nevertheless, the residual water mass m_{gr} have to be included into the total mass expressions for $m_{(iv)}$ (eq. (5.17)).It is taken as the average of the gel pore water intensity below relative water fraction 0.6, m_{gr} is ~0.06.

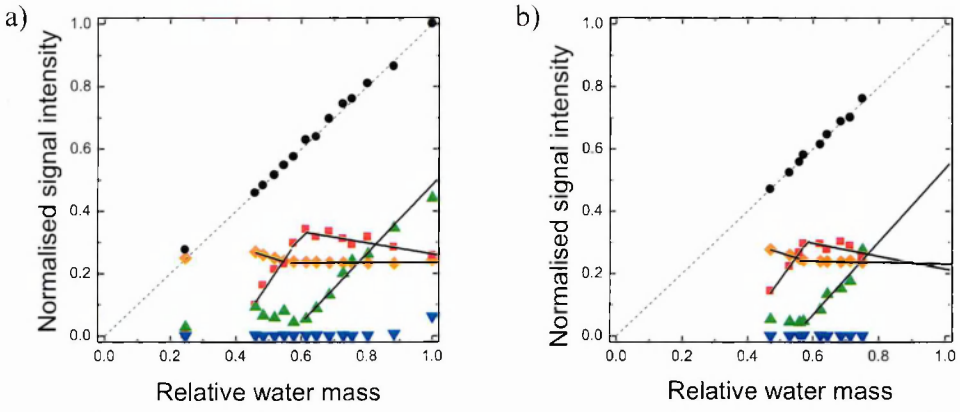

Figure 5.17 The fitting lines (solid lines) used to calculate the pore sizes from primary (a) and secondary desorption (b). Orange diamonds represent chemically combined water signal, red squares – the C–S–H interlayer pore water, green triangles – the C–S–H gel pore water and blue inverted triangles – the 'free' water signals. The black circles show the total water signal.

Solving equations (5.10) - (5.19) the expressions for fitting line slopes ($a_{CSH(ii)}$, $a_{gel(ii)}$, $a_{CSH(iv)}$, $a_{sol(iv)}$) and intercepts ($b_{CSH(ii)}$, $b_{gel(ii)}$, $b_{CSH(iv)}$, $b_{sol(iv)}$) are obtained:

$$a_{CSH(ii)} = -\frac{2}{p}; \quad a_{gel(ii)} = 1 + \frac{2}{p}; \quad (5.20)$$

$$a_{CSH(iv)} = 1 + \frac{2}{q}; \quad a_{gel(iv)} = \frac{V_{sol}}{\mathrm{V}_{wp}} - \frac{2}{q} \quad (5.21)$$

$$b_{CSH(ii)} = \frac{2}{p}\left(1 - m_{cap}\right) + A_{CSH} \cdot \frac{d_{wat}}{\mathrm{V}_{wp}} \cdot (q+2); \quad (5.22)$$

$$b_{gel(ii)} = -1 + m_{cap} + A_{gel} \cdot \frac{d_{wat}}{V_{wp}} \cdot (p+2) - \frac{2}{p} \cdot (1 - m_{cap}) \tag{5.23}$$

$$b_{CSH(iv)} = -1 + m_{cap} \cdot \left(1 + \frac{2}{q}\right) + A_{gel} \cdot \frac{d_{wat}}{V_{wp}} \cdot \left[p + 2 + \frac{2}{q}(p+2)\right] - \frac{2}{q} - m_{gr} \cdot \left(1 + \frac{2}{q}\right) + A_{CSH} \cdot \frac{d_{wat}}{V_{wp}} \cdot (q+2); \tag{5.24}$$

$$b_{sol(iv)} = \frac{V_{sol}}{V_{wp}} \cdot \frac{2}{q} + m_{gr}\left(\frac{2}{q} - 1\right) + A_{gel} \cdot \frac{d_{wat}}{V_{wp}} \cdot \left(\frac{4}{q} - 2\right) + A_{CSH} \cdot \frac{d_{wat}}{V_{wp}} \cdot \left(\frac{4}{q} - q \cdot s_{q(iv)}\right) \tag{5.25}$$

The pore characteristic parameters can be calculated from equations (5.6) - (5.9), (5.20) - (5.25) with additional conditions that:

$$I_{sol} + I_{CSH} + I_{gel} + I_{cap} = 1 \tag{5.26}$$

$$a_{CSH(ii)} + a_{gel(ii)} = 1 \tag{5.27}$$

$$a_{CSH(iv)} + a_{sol(iv)} = 1 \tag{5.28}$$

$$b_{CSH(ii)} + b_{gel(ii)} = 0 \tag{5.29}$$

5.7.3.2. Pore size calculation

In order to calculate the pore sizes the linear fits to interlayer, gel and chemically combined water intensities are performed and shown in figure 5.17. For primary desorption the fittings are made after 'free' water dries (without data point at water mass fraction 1) as it cannot be evaluated how this drying affects the behaviour of interlayer and gel pore signals.

Table 5.2 shows the gradients of the fitting lines for (ii) and (iv) stage of drying.

Table 5.2 Gradients and intercepts of fitting lines for (ii) and (iv) stage of drying.

	$a_{CSH(ii)}$	$a_{gel(ii)}$	$a_{CSH(iv)}$	$a_{sol(iv)}$	$b_{CSH(ii)}$	$b_{gel(ii)}$	$b_{CSH(iv)}$	$b_{sol(iv)}$
Desorption I	-0.180	1.103	1.557	0.335	0.443	-0.618	-0.609	0.422
Desorption II	-0.208	1.176	1.476	0.349	0.422	-0.639	-0.559	0.442

The gel pore size was calculated from equations (5.20) and (5.27) and interlayer pore size was based on eq. (5.21) and (5.28). The resultant pore sizes are presented in table 5.3. Errors in sizes were estimated based on the errors in the measured gradients of fitting lines for (ii) and (iv) stage of drying.

The gel pore size calculated from primary desorption is 4.5 nm. That is bigger than the value calculated from surface relaxation model – 3.1 nm, but close to the value obtained by

Table 5.3 Calculated size of C-S-H interlayer and gel pores.

Sorption cycle	Interlayer pore size [nm]	Gel pore size [nm]
Desorption I	1.5 ± 0.3	4.5 ± 1.6
Desorption II	1.6 ± 0.2	3.5 ± 1.5

McDonald *et al* [18] - 4.1 nm, when the amplitude model was developed based on oven drying of paste using simpler assumptions. The C-S-H interlayer pore size in 'as prepared' cement paste – before desorption, equals 1.5 nm. This value is the same as obtained by McDonald *et al* [18]. However, it is larger than expected and calculated from relaxation model. It is most likely because the assumptions of drying model break down in such a small space.

The results suggested that the mechanism of adsorption is not the same as for desorption (section 5.6). Therefore, the model cannot be used for the adsorption branch.

In figure 5.17 b it can be seen that secondary desorption proceeds in equivalent stages as primary desorption. It is assumed that the contribution of capillary water towards mass calculation is the same as for primary desorption. It is decided following the observation by Baroghel-Bouny [114] that initial water content is restored at 100% RH upon adsorption.

The gel pore size obtained from secondary desorption branch is affected by adsorption cycle. This is explained by adsorption mechanism - filling pores layer by layer. The adsorption was performed up to 80% RH hence the gel pores are not yet totally fill. The calculated values of gel pore size after adsorption and before secondary desorption is 3.5 nm.

Despite the size of interlayer pores based on primary desorption is lower than expected it is still possible to compare the values obtained from both desorption. After one sorption cycle the size comes back to the starting value.

5.7.3.3. Specific surface area calculation

The specific surface area of C-S-H interlayer pores (A_{CSH}) was calculated by simultaneous least-square fittings of equations (5.7), (5.22), (5.24), (5.26) and (5.29). The gel pores SSA (A_{gel}) was based on eq. (5.8), (5.23), (5.24), (5.26) and (5.29). The resultant specific surface areas are presented in table 5.4. Errors in specific surface areas were estimated based on the errors in the measured intercepts of fittings lines for (ii) and (iv) stage of drying and on the errors in C-S-H interlayer and gel pores estimated in previous section.

The calculated total surface area of C-S-H interlayer and gel pores from both desorption are very close. They are in the range of BET values measured by Baroghel-Bouny [114] but lower than that based on adsorption branch in this thesis (section 5.7.1). They are also below values reported by Powers and Brownyard [32], Halperin *et al* [10] and these based on surface relaxation model (section 5.7.2.2).

Table 5.4 Calculated specific surface area of C-S-H interlayer and gel pores.

Cycle	Desorption I			Desorption II		
	Specific surface area in m^2 per					
Pore types	cm^3 of paste	g of anh. cement	g of dried paste (3% RH)	cm^3 of paste	g of anh. cement	g of dried paste (3% RH)
Interlayer	128±30	92	76	112±40	80	66
Gel	65±10	47	38	89±20	64	53
Total	193	138	114	201	144	119

The values of C-S-H interlayer pores surface area are lower than obtained by the surface relaxation model by around 50-60 m^2/cm^3 of paste (27-36%). It is almost certainly because the width of the interlayer pores is higher than expected. If the assumption is made that the interlayer space size is 1 nm, the SSA calculated from primary desorption according to equation (5.7) and (5.22) would be 164 and 199 m^2/cm^3 of paste respectively, much closer to 175 m^2/cm^3 of paste obtained by relaxation model.

The gel pore surface area calculated from primary desorption data is lower by ~25% compare to the value based on surface relaxation model. While the one from secondary desorption is basically the same. There are two main sources of complexity in calculation of gel pore surface area. First is the residual water left in the smaller gel pores at water mass fraction below ~0.6. The second is unknown exact contribution of capillary water towards secondary desorption.

6. Influence of curing temperature on cement microstructure

6.1. C-S-H DENSITY AND COMPOSITION CALCULATION MODEL

The C-S-H density and composition calculation model, presented in section 6.1.1.-6.1.3., contains the products of joint research between the author and Arnaud Muller, fellow Transcend doctoral student at EPFL, Switzerland.

6.1.1. C-S-H density

Mass and volume balance equations for cement paste expressed per gram of anhydrous cement are written as:

$$1 + \frac{w_{mix}}{c} = (1 - \alpha) + \frac{w_{mix}}{c} \cdot \left[\beta_{sol} \cdot I_{sol} + \gamma_{CSH} \cdot I_{CSH} + \delta_w \cdot (I_{gel} + I_{cap})\right] \quad (6.1)$$

$$\frac{1}{\rho_c} + \frac{w_{mix}}{c \cdot \rho_w} = \frac{(1-\alpha)}{\rho_c} + \frac{w_{mix}}{c} \cdot \left[\frac{\beta_{sol} \cdot I_{sol}}{\rho_{sol}} + \frac{\gamma_{CSH} \cdot I_{CSH}}{\rho_{CSH}} + \frac{\delta_w \cdot (I_{gel} + I_{cap} + I_{void})}{\rho_w}\right] \quad (6.2)$$

where α is the degree of hydration, I are NMR intensity fractions and ρ are densities. The parameters β_{sol}, γ_{CSH} and δ_w are the reciprocals water mass fractions of solid, C-S-H and water. The subscripts c, w, *sol*, *CSH*, *gel*, *cap* and *void* correspond to cement, water, chemically combined water, C-S-H, gel pore water, 'free' water (capillary and interhydrate pore water) and chemical shrinkage voidage/filled porosity respectively.

The left side of equation (6.1) represents the sum of anhydrous cement (1) and water (w_{mix}/c) masses at the time of mixing. The right side is the sum of the masses of unreacted cement (1- α) and hydration products expressed in terms of signal intensities. In equation (6.2) the masses are divided by the respective densities to give the volume balance.

An important phenomenon to consider during hydration of cement paste is the chemical shrinkage. It is the volume reduction created because the volume of the hydration products is lower than the original volume of reactants: cement and water. Chemical shrinkage creates additional porosity – voids, inside cement paste in sealed cured systems. For *small* underwater cure paste samples voids are filled with water drawn into the sample [115]. Thus when following the hydration process of underwater cure paste the mass (m_{paste}) increases while the overall volume stays constant. Therefore, to balance the cement paste mass and volume equations, the chemical shrinkage is included only in the volume calculation.

The intensity fractions (I) of particular water reservoirs are normalised to the total intensity which does not include chemical shrinkage, hence $I_{sol} + I_{CSH} + I_{gel} + I_{cap} = 1$. The volume created by chemical shrinkage can be defined in terms of additional water signal intensity or mass $I_{void} = I_{total} - 1 = (w_{paste} - w_{mix})/w_{mix}$. The solid intensity originates from Portlandite (CH) and ettringite (Ett), so that $I_{sol} = I_{CH} + I_{Ett}$; $\beta_{sol} \cdot I_{sol} = \beta_{CH} \cdot I_{CH} + \beta_{Ett} \cdot I_{Ett}$; $\beta_{sol} \cdot I_{sol}/\rho_{sol} = \beta_{CH} \cdot I_{CH}/\rho_{CH} + \beta_{Ett} \cdot I_{Ett}/\rho_{CH}$. The constants $\rho_{c,w,CH,Ett}$ are equalled to 3.15, 1.00, 2.24 and 1.77 g/cm^3 respectively [28]. From the atomic masses, $\beta_{CH} = 74/18$, $\beta_{Ett} = 1255/576$ and $\delta_w = 1$.

This leaves four unknowns: α, γ_{CSH}, ρ_{CSH} and I_{CH} (or I_{Ett}, as knowing one, the other can be calculated through the relation for I_{sol}). The incorporation of additional, non-NMR, measurements is required. In this study, the degree of hydration (α) and the content of CH or ettringite (m_{CH} or m_{Ett}) is measured by XRD and, in case of CH, by TGA. The water intensity fraction of CH and ettringite are expressed by parallel sets of equations: $I_{CH} = m_{CH}/(w_{mix} \cdot \beta_{CH})$ with $I_{Ett} = I_{sol} - I_{CH}$; and $I_{Ett} = m_{Ett}/(w_{mix} \cdot \beta_{Ett})$ with $I_{CH} = I_{sol} - I_{Ett}$. As a result, the density and reciprocal water mass fraction of C-S-H can be calculated.

6.1.2. C-S-H composition

The C-S-H composition is written as $Ca_z(Si_y,Al_{(1-y)})O_{(z+y/2+3/2)}(H_2O)_x$. The reciprocal water content γ_{CSH} is expressed in terms of the water (x), calcium (z) and silicon (y) contents as

$$\gamma_{CSH} = \frac{56z + 9y + 51 + 18x}{18x} \tag{6.3}$$

where the numerical constants are derived from atomic masses of Ca, Si, Al, O and Hyd[17]; y is defined as $n_{Si}/(n_{Si} + n_{Al})$; and n is the molar content of respective element per mole of C-S-H.

An equality can be written for the Ca/(Si+Al) ratio for combined C-S-H and CH between reacted fractions of anhydrous cement and the hydration products[18]:

$$\frac{3\left(\frac{f_{C3S}}{C_3S^{AMU}}\right) + 2\left(\frac{\alpha' - f_{C3S}}{C_2S^{AMU}}\right) + 3\left(\frac{f_{C3A} - f_{C3A}^{Ett}}{C_3A^{AMU}}\right)}{\frac{f_{C3S}}{C_3S^{AMU}} + \frac{\alpha' - f_{C3S}}{C_2S^{AMU}} + 2\left(\frac{f_{C3A} - f_{C3A}^{Ett}}{C_3A^{AMU}}\right)} = \frac{\frac{I_{CH}n_{Hyd}}{2} + \frac{I_{CSH}n_{Hyd}z}{2x} + 3\left(\frac{f_{C3A} - f_{C3A}^{Ett}}{C_3A^{AMU}}\right)}{\frac{I_{CSH}n_{Hyd}y}{2x} + 2\left(\frac{f_{C3A} - f_{C3A}^{Ett}}{C_3A^{AMU}}\right)} \tag{6.4a}$$

[17] Hyd is used as an abbreviation of hydrogen, as H in cement notation means water, H_2O

[18] α' – mass of reacted C_3S and C_2S divided by mass of anhydrous cement

The nominator on the left side of equation (6.4a) comprises the number of calcium moles derived from reacted C_3S, C_2S and C_3A. The denominator is similarly constructed for the silicon and aluminium moles. On the right side the molar contents of Ca,Si and Al in CH and C-S-H are expressed in terms of NMR signal intensities, the C-S-H composition parameters (x, z, y) and molar content of hydrogen in the mixed paste ($n_{Hyd} = 2 \cdot w_{mix}/H^{AMU}$). Equation (6.4a) is written for the condition that degree of hydration is higher than the fraction of C_3S in anhydrous cement ($\alpha' > f_{C3S}$) and assuming that C_3S reacts before the more slowly reacting C_2S. Additionally, it is assumed that the fraction of C_3A which was not consumed to produce ettringite ($f_{C3A} - f_{C3A}^{Ett}$) is incorporated in C-S-H.

Equivalent expressions based on similar assumptions can be written for lower degree of hydration ($\alpha' < f_{C3S}$)

$$\frac{3\left(\frac{\alpha'}{C_3S^{AMU}}\right) + 3\left(\frac{f_{C3A} - f_{C3A}^{Ett}}{C_3A^{AMU}}\right)}{\frac{\alpha'}{C_3S^{AMU}} + 2\left(\frac{f_{C3A} - f_{C3A}^{Ett}}{C_3A^{AMU}}\right)} = \frac{\frac{I_{CH}n_{Hyd}}{2} + \frac{I_{CSH}n_{Hyd}z}{2x} + 3\left(\frac{f_{C3A} - f_{C3A}^{Ett}}{C_3A^{AMU}}\right)}{\frac{I_{CSH}n_{Hyd}y}{2x} + 2\left(\frac{f_{C3A} - f_{C3A}^{Ett}}{C_3A^{AMU}}\right)} \tag{6.4b}$$

A final equation is obtained from the equality $y = \frac{n_{Si}}{n_{Si}+n_{Al}} = 1 - \frac{n_{Al}}{n_{Si}+n_{Al}}$. If the sum of Al and Si molar content is written in terms of C-S-H intensity, then it follows that

$$y = 1 - \frac{4x \cdot (f_{C3A} - f_{C3A}^{Ett})}{I_{CSH}n_{Hyd}C_3A^{AMU}} \tag{6.5}$$

Simultaneous solution of equations (6.1), (6.2), (6.3), (6.4) and (6.5) enables the C-S-H density and composition to be calculated.

6.1.3. C-S-H 'solid' and 'bulk' density

The C-S-H density derived as in section 6.1.1. includes the calcium and silicon backbones of the structure and the water within interlayer spaces as shown in figure 6.1 left. It especially excludes water, as well as any OH groups, on the surfaces of C-S-H agglomerates as the water (hydrogens or perhaps magnetisation) is in rapid exchange with the bulk gel pore water and has longer T_2. This density is called C-S-H 'solid' density in this work.

The alternative C-S-H composition: $Ca_z\ (Si_y,Al_{(1-y)})\ O_{(z+y/2+3/2)}\ (H_2O)_{x'}$, including the gel pore water, has water content x' and the C-S-H 'bulk' density ρ'_{CSH} (fig. 6.1 right)

$$x' = \frac{x \cdot \left(I_{CSH} + I_{gel}\right)}{I_{CSH}} \tag{6.6}$$

and

$$\rho'_{CSH} = \frac{\gamma_{CSH} \cdot I_{CSH} + \delta_w \cdot I_{gel}}{\frac{\gamma_{CSH} \cdot I_{CSH}}{\rho_{CSH}} + \frac{\delta_w \cdot I_{gel}}{\rho_w}} \tag{6.7}$$

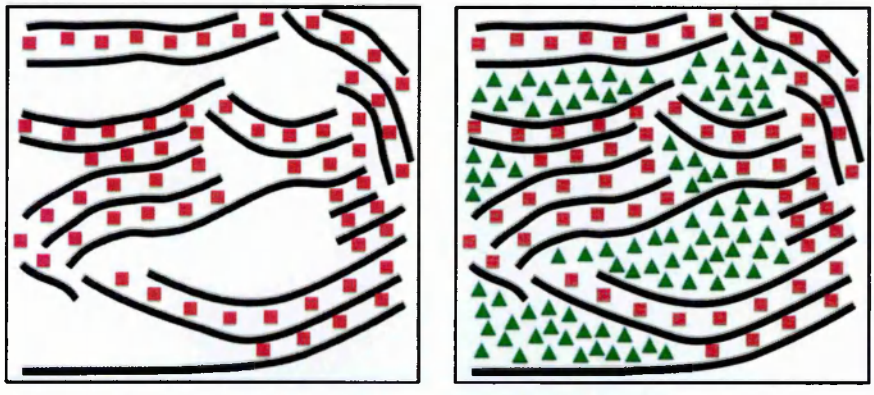

Figure 6.1 A scheme of water location inside C–S–H at 100% humidity for C–S–H 'solid' (left) and 'bulk' (right) density calculation. It shows that for C–S–H 'solid' density only water molecules in interlayer spaces (red squares) are included in calculation, while for C-S-H 'bulk' density water in interlayer and gel pores (green triangles) is considered.

6.2. Microstructure, C-S-H density and composition at 20°C

6.2.1. Evolution of different water populations

The examplary QE data recorded by Kea^2 spectrometer for white cement paste cured underwater at 20°C for 28 days are shown in figure 6.2. Here, the dead time is shorter (10 μs) than in previous experiments thus the solid echo is clearly visible. Data are presented for τ ranging from 12 to 54 μs. The echo, exponential decay and combined fits to the data are shown. The back-extrapolation of the solid echo and mobile intensity to $\tau = 0$ were performed by Gaussian and linear fit to the data, respectively (figure 6.3).

The mobile fraction measured by QE was further decomposed by exponential stripping of CPMG decay data as described in section 4.3.2.3. This method of analysis was chosen due to inadequate signal to noise ratio of the data for ILT analysis.

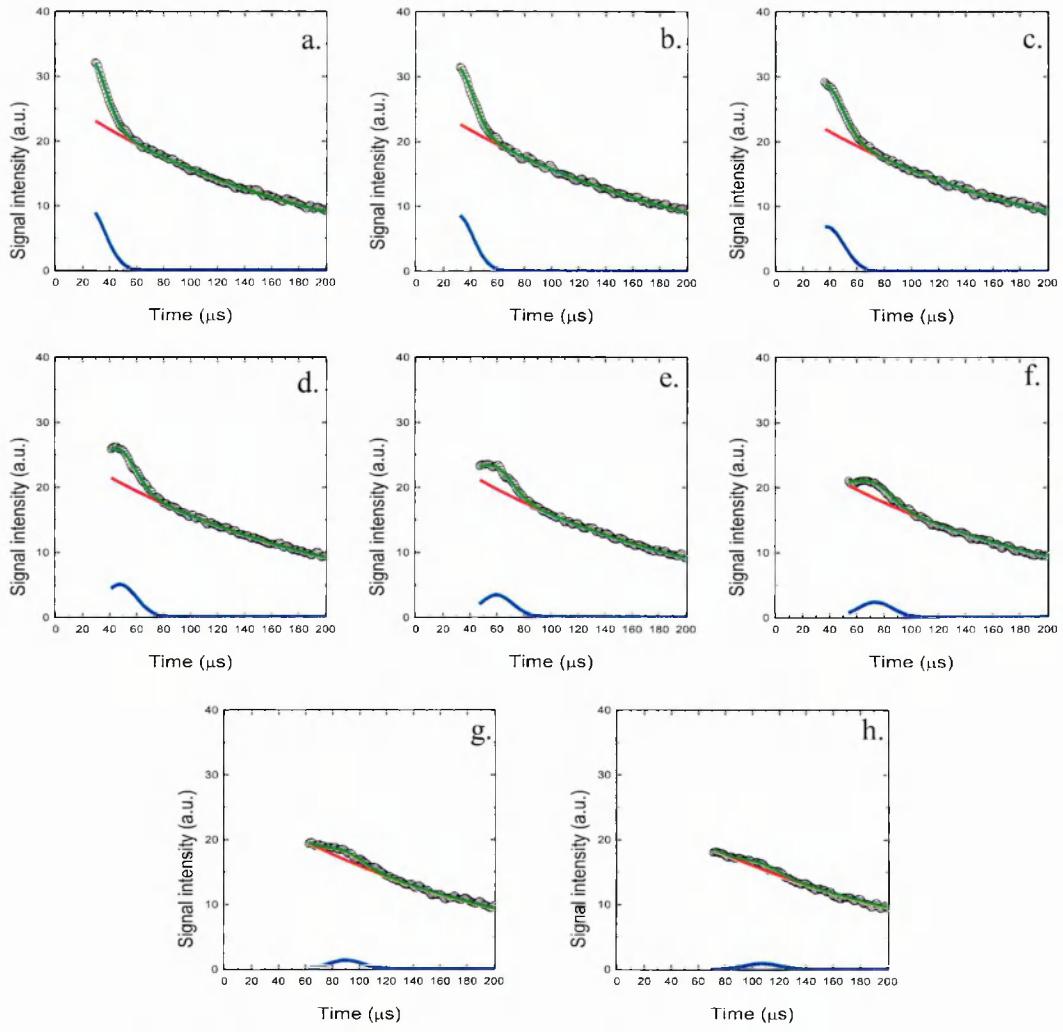

Figure 6.2 Quad echo signals recorded for 28 days old white cement paste (black circles) at eight values of τ: a: 12μs, b: 15μs, c: 19μs, d: 24μs, e: 30μs, f: 37μs, g: 45μs, h: 54μs. The lines present fitting for solid (blue) and mobile (red) components; the green line is the total intensity fit. The zero time is taken as the end of first 90° pulse of the sequence.

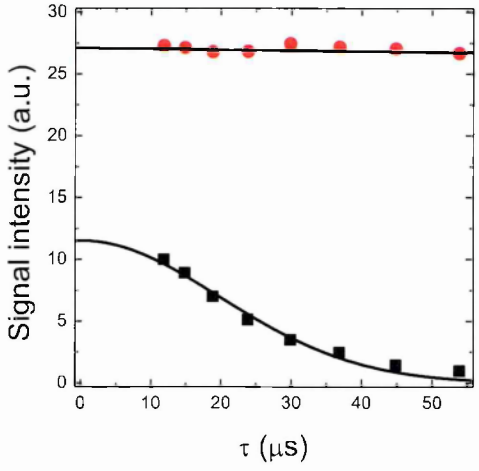

Figure 6.3 Solid echo (black squares) and mobile decay (red circle) signal amplitudes as a function of pulse gap (τ). The lines are the fits to the data: Gaussian for solid and linear for mobile signals.

Figure 6.4 shows the CPMG decay stripping for 28 days old white cement paste, the same as in examples of QE analysis. First, the interhydrate and capillary pore water were fitted to the decay beyond about 1.5 ms. The fitting line calculated based on obtained T_2 relaxation times ($T_{2,inthyd}$ = 1.6 ms, $T_{2,cap}$ = 28 ms) and intensities (I_{inthyd} = 4%, I_{cap} = 1%)[19] was subtracted from original decay. The residual data, starting from t_{long} = 300 μs, was fitted and gained parameters of gel pore water ($T_{2,gel}$ = 291 μs, I_{gel} = 47%). Further subtraction leaves the data to yield the C-S-H interlayer parameters ($T_{2,CSH}$ = 91 μs, I_{CSH} = 23%).

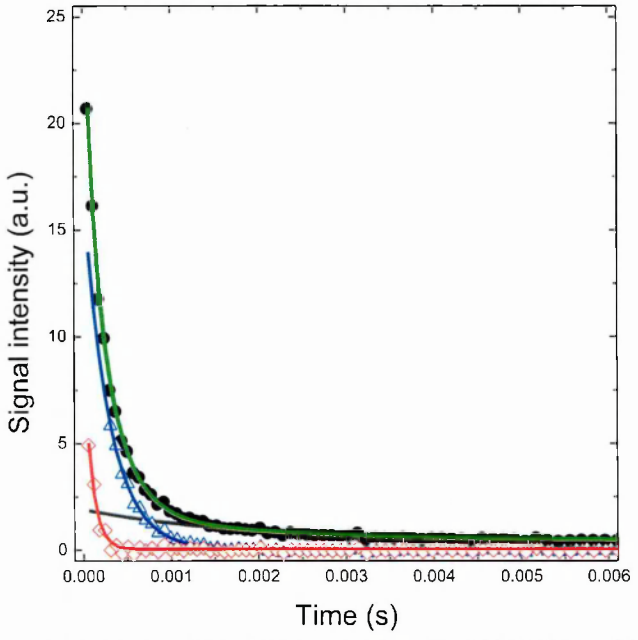

Figure 6.4 Graph presents the exponential stripping procedure for CPMG decay (black circles) of 28 days old white cement paste cure underwater (w/c_{mix} = 0.4). The grey line is the 'free' water fit and blue triangles are the data after subtraction of that fit from CPMG decay. Blue line presents the fit of gel water intensity which further was subtracted, leaving red diamonds. Red line shows the fit for interlayer water signal. The green line is the total fit make as sum of the capillary, gel and interlayer fits.

NMR data were acquired during cement hydration starting from 2 h up to 90 days. Figure 6.5 presents the evolution of water populations for white cement paste mixed at w/c_{mix} ratio 0.4 and cured underwater at 20°C. The signal intensities are normalised to the intensity/water mass at the mixing time to show the actual changes and the uptake of water due to chemical shrinkage.

The 'free' water intensity is the sum of interhydrate and capillary pore water intensities with the low contribution of latter, about 2-1%, over whole hydration time. The 'free' water intensity decreases rapidly during first 3 days of hydration when the 'free' water is consumed by 57, 17 and 9% each day. After the third day the rate of consumption is significantly lower, below 3% per day, and gradually decreases with time. The signal of water in crystalline phases increases continuously throughout the entire examined hydration time. The C-S-H interlayer water appears after 6 h of hydration and rises gradually during the first 12 days.

[19] note: in the C-S-H density and composition calculation model the sum of I_{inthyd} and I_{cap}, is given as I_{cap}

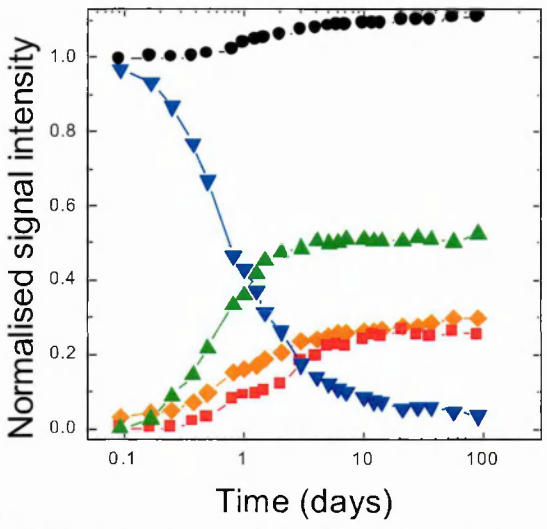

Figure 6.5 The evolution of different water population for white cement paste mixed at w/c_{mix} ratio 0.4 and cured underwater at 20°C. Orange diamonds represent chemically combined water signal, red squares – the C–S–H interlayer pore water, green triangles – the C–S–H gel pore water and blue inverted triangles – the 'free' water signals. The black circles show the total water signal normalized to the initial mass of water at the mixing point. Lines are guide for eyes.

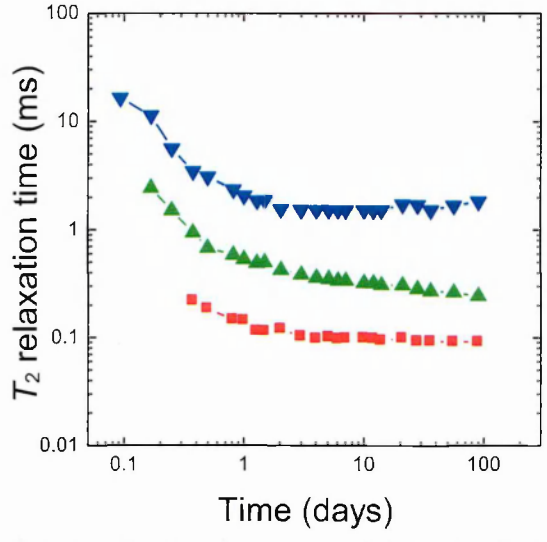

Figure 6.6 The evolution of T_2 relaxation time for water populations of white cement paste mixed at w/c_{mix} ratio 0.4 and cured underwater at 20°C. Red squares represent the T_2 relaxation time for C–S–H interlayer pore water, green triangles for C–S–H gel pore water and blue inverted triangles for 'free' water.

After that time there is only slight increase. The gel pore water signal increases at a very high rate up to 2 days and stays approximately constant after 4 days. The ratio of gel pore to interlayer water decreases from almost 9 at 9 hours of hydration through 4 at 2 days and down to 2 for later hydration ages.

Figure 6.6 shows the corresponding T_2 relaxation times of the C-S-H interlayer, gel and 'free' – interhydrate, pore water. The T_2 of the dominating 'free' water component falls rapidly during the first day of hydration. After two days its T_2 already reaches the asymptotic

value of about 1.5-1.6 ms that corresponds to pore size[20] of 11.2-11.9 ± 1.8 nm. The gel T_2 drops considerably from around 2.5 ms (18.7 ± 0.7 nm) to 0.5 ms (3.7 ± 0.2 nm) over first 24 hours and then slowly but progressively down to about 0.3 ms (~2.2 ± 0.2 nm). The values of T_2 for interlayer water are almost constant from the moment when the component appears: ~220 μs at 9h, ~100 μs at 3 days and ~90 μs at 90 days that corresponds to pore sizes of: ~1.6 ± 0.2 nm at 9h, ~0.75 ± 0.04 nm at 3 days and ~0.67 ± 0.04 nm at 90 days.

6.2.2. Density and C-S-H composition

The C-S-H density and composition were calculated for the white cement paste (w/c_{mix} = 0.4) used in the sorption experiment at 28 days of hydration and 100% RH: sample S28 (section 5.3) and for the samples used in the temperature dependence study both at 28 and 90 days of hydration: samples T28 and T90 (section 6.2.1).

The signal intensity fraction due to chemical shrinkage voids was calculated from the increase of water to cement ratio (w/c_{paste}). The degree of hydration (α) was measured by XRD. The verification of crystalline phases fraction (m_{CH} and m_{Ett}) was performed by TGA and XRD measurements.

Table 6.1 shows the measured parameters. The NMR intensities are presented in table 6.2. The negative sign in the capillary intensity implies that water which is drawn into sample is used in the hydration process.

Table 6.1. Parameters for application of the C-S-H density and composition model for white cement paste at 20°C.

Sample	Age [days]	$(w/c)_{paste}$ [g/g$_{anh}$] (±0.002)	α (±0.02)	m_{CH} [g/g$_{anh}$] (±0.010)	m_{Ett} [g/g$_{anh}$] (±0.010)
S28	28	0.463[21]	0.77	0.342	0.083
T28	28	0.439[22]	0.85	0.270	0.086
T90	90	0.443[22]	0.90	0.311	0.086

Table 6.2. The intensities used to calculate C-S-H density and composition at 20°C. The error in intensities is around ±0.010 based on standard deviation of the data for multiple samples.

Sample	Age [days]	I_{sol}	I_{CH}	I_{Ett}	I_{CSH}	I_{gel}	I_{Cap}	I_{void}	I_{tot}
S28[23]	28	0.281	0.185	0.096	0.295	0.510	-0.086	0.157	1.157
T28[24]	28	0.276	0.164	0.112	0.252	0.512	-0.040	0.097	1.097
T90[24]	90	0.297	0.189	0.108	0.252	0.525	-0.074	0.109	1.109

[20] pore sizes calculated using surface relaxivity equal to $3.7 \cdot 10^{-3}$ nm/μs as obtained in section 5.7.2.1

[21] calculated from changes of total signal intensity during desorption experiment as presented in section 5.1.1.

[22] obtained from the sample mass changes

[23] $I_{Ett} = m_{Ett} / (w_{mix} \cdot \beta_{Ett})$ and $I_{CH} = I_{sol} - I_{Ett}$

[24] $I_{CH} = m_{CH} / (w_{mix} \cdot \beta_{CH})$ and $I_{Ett} = I_{sol} - I_{CH}$

Solving equations (6.1) to (6.5) the resultant C-S-H 'solid' density and composition for underwater cured, never dried paste sample S28 are 2.68 ± 0.03 g/cm^3 and $Ca_{z=1.54}(Si_{y=0.96},Al_{(1-y)=0.04})\ O_{(z+y/2+3/2)=3.51}\ (H_2O)_{x=1.92}$. Water content excluding gel pore water is $x = 1.92 \pm 0.05$. Including the gel water, the C-S-H 'bulk' density and water content (eq. (6.6-6.7)) are $\rho'_{CSH} = 1.89 \pm 0.02$ g/cm^3 and $x' = 5.25 \pm 0.04$. (Errors represent the standard deviation of the data for multiple samples measured in course of temperature dependent investigation). The calculated parameters are reproduced as the top line of the table 6.3, and may be compared with the subsequent lines which are for samples T28 and T90.

Table 6.3. The C-S-H density and composition for white cement paste at 20°C.

Sample	ρ_{CSH} [g/cm^3]	$Ca_z(Si_y,Al_{(1-y)})\ O_{(z+y/2+3/2)}\ (H_2O)_x$	ρ'_{CSH} [g/cm^3]	x'
S28	2.68	$Ca_{z=1.54}(Si_{y=0.96},Al_{(1-y)=0.04})\ O_{(z+y/2+3/2)=3.51}\ (H_2O)_{x=1.92}$	1.89	5.25
T28	2.60	$Ca_{z=1.78}(Si_{y=0.98},Al_{(1-y)=0.02})\ O_{(z+y/2+3/2)=3.77}\ (H_2O)_{x=1.51}$	1.91	4.58
T90	2.65	$Ca_{z=1.65}(Si_{y=0.98},Al_{(1-y)=0.02})\ O_{(z+y/2+3/2)=3.64}\ (H_2O)_{x=1.39}$	1.93	4.29

If it is assumed that the lateral extent of gel pores and interlayer spaces is similar as suggested by figure 6.1 then the calculated stacks of C-S-H layers can only comprise two to three layers. Taking the layer repeat distance 1.4 nm of C-S-H mineral analogue, tobermorite-14, the C-S-H stack thickness is 2.8 - 4.2 nm. This thickness is close to the C-S-H globule size in Jennings Colloidal Model, CM-II [6]. Assuming C-S-H stacks of three layers, their volume excluding external water layers is $V = 3 \cdot 1.4 \cdot 10^{-9}$ m^3/m^2 of layer. The additional volume of two external monolayers of water can be expressed as $\Delta V = 2 \cdot 0.28 \cdot 10^{-9}$ m^3/m^2 of layer. Hence, if the outer surface water layer is included, the NMR density ρ_{CSH} is decreased to

$$\rho_{CSH}^{ext} = \frac{4.2 \cdot \rho_{CSH} + 0.56}{4.76} \tag{6.8}$$

The NMR calculated C-S-H 'solid' densities (with average $\rho_{CSH} = 2.64 \pm 0.03$ g/cm^3) are slightly higher than the values obtained by SANS measurements for a fully saturated CM-II globule density 2.604 g/cm^3 [7], also excluding any water on the outer surface of particles. If the correction for outer surface water is applied the average ρ_{CSH}^{ext} is equalled to 2.45 ± 0.03 g/cm^3. This value is very close to density of saturated globule with a monolayer of water on the surface at 11% RH reported by Jennings, 2.47 g/cm^3 [6] and by Feldman, 2.43-2.45 g/cm^3 [75].

The density of saturated C-S-H gel, including gel pore water, measured by NMR is about 1.90 ± 0.02 g/cm^3 with water content 4.58-5.25 at 28 days of hydration. It is close to the CM-II model quoted value 1.83 g/cm^3 with water content 5 when the large gel pores (LGP) are

included [6] and measured by Young and Hansen [72] value of 1.85-1.90 g/cm^3 for saturated (90% RH) C-S-H of fully hydrated C_3S paste with water content of ~4.0.

Water content of sample S28, $x = 1.92 \pm 0.05$, is a little over the content determined by SANS ($x = 1.8$) [7]. The water content values for samples T28 and T90 are somehow lower. The reason for that is not fully understood. However, the sensitivity analysis presented in section 6.4.5 shows the complexity of the analysis and its high dependence on input parameters. It is possible that there is systematic error in one of the input parameters causing discrepancy of x and x' results. Otherwise, comparing the results of T28 and T90 with the relation of Ca/Si and H_2O/Si reviewed by Chen [74] they are in very good agreement and this is the sample S28 that lies out of reported trend.

The values of the Ca/(Si+Al) ratio (calcium content - z) are in fairly good agreement with the results of Rayment and Majumdar [70] who yielded the average Ca/(Si +Al + S + Fe) ratio of inner and outer C-S-H ranging from 1.70 at $w/c = 0.3$ to 1.48 at $w/c = 0.6$.

6.2.3. C-S-H water content at different humidities

The first pore-type resolved desorption isotherm from section 5.3 and the NMR calculation model for C-S-H composition provide opportunity to draw the first water content isotherm for C-S-H differentiated by water environments – figure 6.7. The water contents have been recalculated based on the sum of interlayer, gel and solid-like surface water signals at 100% RH treated as the water content x'. Whereas, the C-S-H water mass originates from subtraction of capillary and chemically combined water contribution from total water mass.

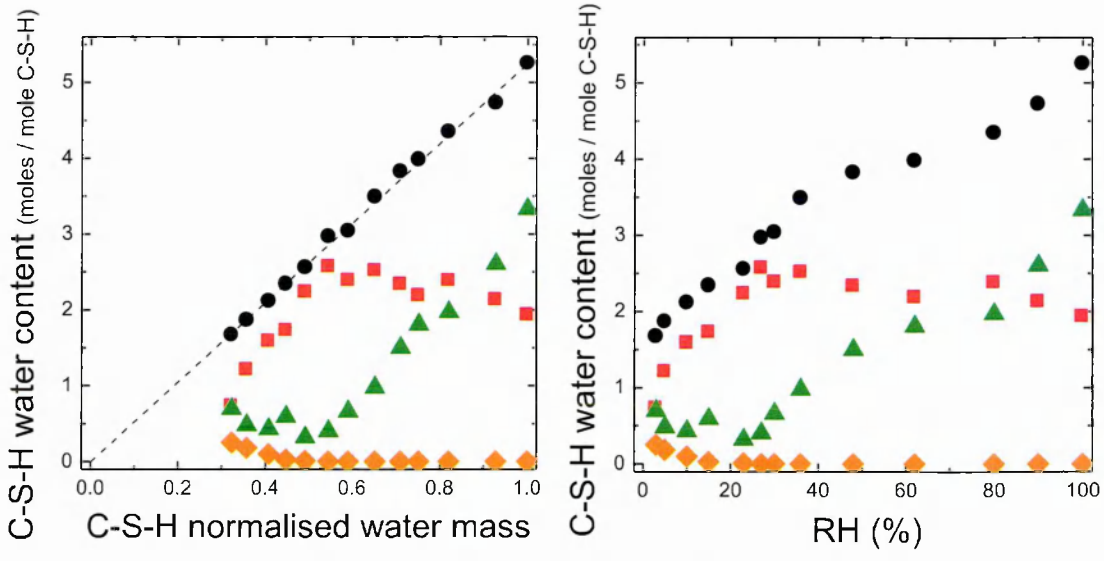

Figure 6.7 The C-S-H water content isotherm as a function of C-S-H water mass (left) and relative humidity (right). The black circles represent the C-S-H water content x', including gel pores, which is divided into interlayer 'solid' water content x (red squares), gel water content (green triangles) and solid-like surface water (orange diamonds).

At 100% RH water content excluding and including gel pores water is $x = 1.92$ and $x' = 5.25$ respectively. When looking at the presented data, one has to remember that the

apparent increase in interlayer water content is actually the appearance of a surface layer of water in the emptying gel pores. A surface layer, in NMR terms, appears interlayer space – like. The other complication is the residual water staying in very small gel pores below 25% RH. The origin of this tail is not clear. It may indicate the presence of the isolated smaller gel pores without connectivity that cannot dry or of ink-bottle pores.

The obtained curve for water content, including gel pores, mirrors the curve presented by Jennings [6] which shows evolution of total water within C-S-H without division into particular components. At 11% RH, the water content is given as 2.1 by Jennings [6] for saturated C-S-H globule with a monolayer of water on the surface, as 2.0 by Feldman and Ramachandran [73] and 2.1 by Young and Hansen [72] in hydrated C_3S. The NMR results yield the water content, including gel pores, $x' = 2.11$ at 10% RH, while the interlayer water content is 1.58. The former is in good agreement with literature value. However the water included in the calculation is the sum of interlayer, residual gel and solid-like surface water.

6.3. Evolution of water population for white cement paste at different temperature

The QE and CPMG NMR experiments were performed to identify quantitatively the influence of curing temperature on the population of water inside cement pastes over the time of hydration (2 h – 90 days). The applied curing temperatures were 10, 20, 30, 40, 50 and 60°C. The measurements were performed on white cement paste mixed at $w/c_{mix} = 0.4$ and cured underwater.

6.3.1. Uptake of water during hydration

The volume created by chemical shrinkage was defined based on the mass of water drawn into the sample to fill the voids. Figure 6.8 shows the increase of water mass as a function of hydration time for white cement pastes mixed at w/c_{mix} ratio 0.4 and cured underwater at different temperatures. Depending on the curing temperature, as the hydration proceeds, the different mass of water is drawn inside underwater cured sample.

The increase of curing temperature causes water uptake to start at earlier hydration times suggesting faster hydration at higher temperature. The acceleration of the hydration process at higher temperatures has been previously reported based on the measurements of chemical shrinkage [116], degree of hydration [109], [117], TGA [117] and strength development [117], [118]. The speed of that uptake is higher at the beginning and it slows down considerably later. With time, at lower curing temperature, the total water ingress rises to values comparable or higher than that found at higher curing temperatures at earlier times. The same behaviour for chemical shrinkage was observed by Geiker and Knudsen [116] through weighing of samples immersed in liquid paraffin. The higher mass can be seen for pastes cured at 40°C in comparison with 50 and 60°C already after half day of hydration (fig. 6.8). Nevertheless, at the later hydration time, beyond 60 days, the water mass at 40°C is slightly lower than for paste cured at 20°C. The continuous increase of water mass at 10°C is

observed through whole hydration time. However, in the experimental time it rises only above mass for paste at 50 and 60°C.

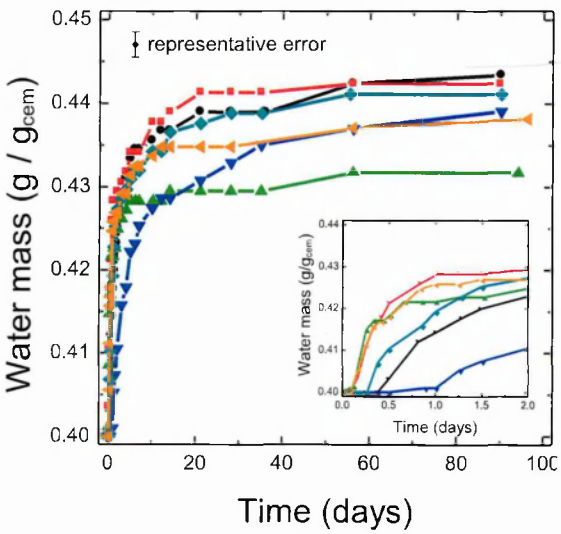

Figure 6.8 Uptake of water as a function of hydration time for white cement pastes mixed at w/c_{mix} ratio 0.4 and cured underwater at different temperature: blue inverted triangles: 10°C; black circles: 20°C; cyan diamonds: 30°C; red squares: 40°C; orange left-triangles: 50°C; and green triangles: 60°C.

6.3.2. 'Free' water evolution

One way to interpret the influence of temperature is by comparing the time at which a given amount of 'free' pore water[25] is consumed inside the sample. The age of sample at which the initial fraction of 'free' water is consumed by 50% and 80% decreases with increase in curing temperature in the range 10 to 60°C. However, the striking feature is that the consumption of 90% of 'free' water is achieved at much longer ages for samples cured at elevated temperatures (Figure 6.9).

Figure 6.10 presents the evolution of 'free' water intensity throughout experimental hydration time. At higher temperature and initial stages of hydration 'free' water is consumed faster. However, when samples are older there is more 'free' water left at elevated temperatures. Data suggests that coarser porosity is created and that it is subsequently much harder to fill this porosity with hydration products. The increased coarser porosity at higher temperatures has been previously reported in literature based mainly on SEM observation [109], [117], [119], [120] but also MIP results [119].

[25] 'free' water is the sum of interhydrate and capillary pore water intensities with the low contribution of latter, about 3-1%, over whole hydration time at all examined curing temperatures

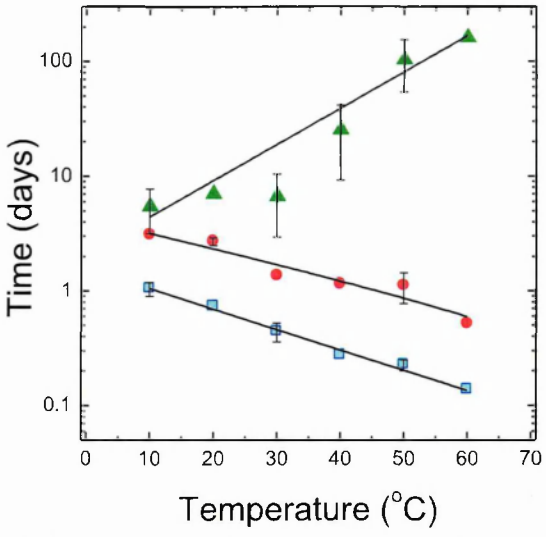

Figure 6.9 Consumption of 'free' water for white cement pastes mixed at w/c_{mix} ratio 0.4 and cured underwater at different temperature. The hydration time of sample at which the initial fraction of 'free' water is consumed by 50% is shown as blue squares, by 80% as red circles and by 90% as green triangles. The black lines are exponential fits to the data. (The consumption of 'free' water by 90% at 60°C is obtained by extrapolation as it was not achieved within experimental time).

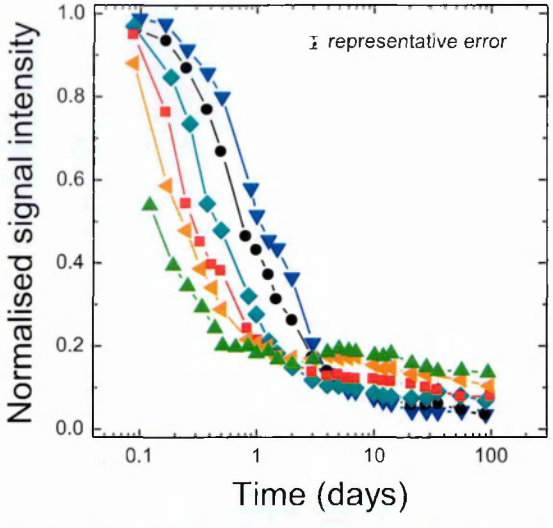

Figure 6.10 Evolution of 'free' water as a function of hydration time for white cement pastes mixed at w/c_{mix} ratio 0.4 and cured underwater at different temperature: blue inverted triangles: 10°C; black circles: 20°C; cyan diamonds: 30°C; red squares: 40°C; orange left-triangles: 50°C; and green triangles: 60°C. Lines are guides for eyes.

6.3.3. Chemically combined water evolution

The development of chemically combined water within CH and ettringite proceeds faster and earlier when the curing temperature is increased (figure 6.11). However, beyond about 5 days of hydration, when the intensity is ~24-25%, the trend reverses. From that point on the quantity of water associated with those phases increases more slowly at elevated temperature

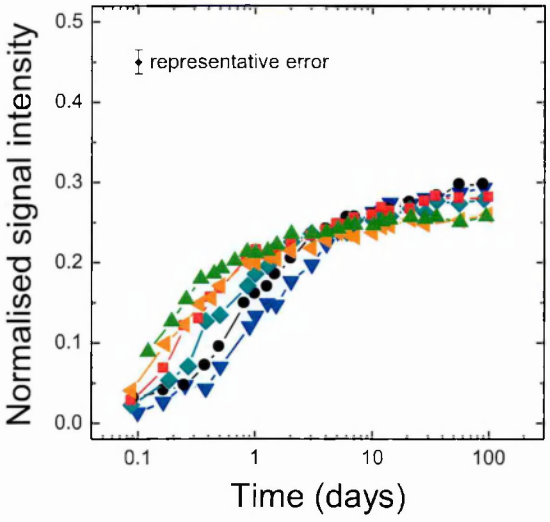

Figure 6.11 Evolution of chemically combined water as a function of hydration time for white cement pastes mixed at w/c_{mix} ratio 0.4 and cured underwater at different temperature blue inverted triangles: 10°C; black circles: 20°C; cyan diamonds: 30°C; red squares: 40°C; orange left-triangles: 50°C; and green triangles: 60°C. Lines are guides for eyes.

and as a result has lower values.

The verification of the amount and origin of the chemically combined water was performed by TGA and XRD measurements at 28 and 90 days of hydration. The results are presented in table 6.4. The obtained Portlandite and ettringite mass fractions are recalculated to evaluate the fractions of water within them based on their molecular composition, atomic masses and water to cement ratio at mixing point. The XRD patterns did not show the presence of calcium aluminate and monosulfoaluminate at any curing temperature. The sum of water fraction within CH and ettringite determined by TGA and XRD is within 3% of the NMR solid signal fraction.

The CH content as measured by TGA at University of Surrey gives systematically higher results than that measured at EPFL. The reasons for that are not fully understood. There are several factors to take into account. First, samples were posted to EPFL and hence curing temperatures were not maintained. Second, for all samples measured at EPFL hydration was stopped by isopropanol exchange in contrast to the measurement performed on not altered samples at University of Surrey. It has be reported in literature that the alcohols exchange, including isopropanol, may alter the portlandite and calcite determination by TGA method [121]. Finally, the measurements were performed in the temperature range up to 950 and 1000°C at EPFL and Surrey respectively. That this last explanation is not the source of discrepancy was confirmed by the analysis in the same temperature range. Nevertheless, the striking feature is the consistency between the TGA and XRD measurements facilitated at EPFL. However, the quantitative XRD analysis depends on parameters chosen for the Rietveld analysis and that may suggest a systematic calibration factor shifting results.

The results (table 6.4) show that the water content of CH and hence CH content at different curing temperature are fairly constant. The same observation are presented in [109], [120].

Table 6.4. CH and ettringite mass fractions measured by TGA and XRD, their water mass fractions calculated from mass fractions and measured solid NMR signals for white cement pastes mixed at w/c_{mix} ratio 0.4 and cured underwater at different temperature. The fraction of CH water at 90 days was calculated based on TGA measured at Surrey, while at 28 days on average XRD and TGA results obtained at EPFL.

Temp [°C]	*Age* [days]	*Mass fraction* [g/g_{anh}] (±0.010)				*Fraction of water*			*NMR solid signal* (±0.010)
		CH			*Ett*	*CH*	*Ett*	*CH + Ett*	
		TGA	*XRD*	*TGA*	*XRD*				
		measured at Surrey	*measured at EPFL*						
10	28		0.262	0.261	0.084	0.159	0.096	0.255	0.280
	90	0.298	0.261			0.181		0.277	0.293
20	28		0.276	0.264	0.086	0.164	0.099	0.263	0.276
	90	0.311				0.189		0.288	0.297
30	28		0.270	0.264	0.081♦	0.162	0.093	0.255	0.262
	90	0.311	0.278			0.189		0.282	0.279
40	28		0.273♦	0.272♦	0.074♦	0.166	0.085	0.250	0.276
	90	0.309				0.188		0.273	0.281
50	28		0.274	0.277	0.069	0.167	0.079	0.246	0.248
	90	0.307	0.279			0.187		0.266	0.259
60	28		0.277♦	0.280♦	0.055	0.169	0.063	0.233	0.254
	90	0.309				0.188		0.251	0.258

♦ estimated by linear interpolation of data at different temperatures

With increase in temperature, there is a significant decrease in the ettringite content. The lower ettringite content at elevated temperatures was also found by Lothenbach *et al* [117] and Galluci *et al* [109]. The decrease could be associated with the thermodynamic instability of ettringite at different, higher temperatures. The thermal stability of the pure ettringite phase was investigated by Zhou and Glasser [122]. They show that at relative humidity over 80% and temperature below 75°C ettringite water content is fairly unchanged at about 31.6. The thermal stability of ettringite was also examined in the presence of water and gypsum. Hall *et al* [123] found that the ettringite decomposition occurs rapidly at 114°C and results in release of water and formation of monosulfoaluminate hydrate (AFm) and bassanite. The X-ray study by Christensen *et al* [124] followed the hydrothermal reactions of C_3A-gypsum and Portland cement with water. The former showed no precipitation of ettringite in whole temperature range investigated (25-120°C). However, for C_3A doped with Na^+ the ettringite forms in increasing amount up to 46°C. Following that the AFm grows in depletion of ettringite and finally above 68°C ettringite is not observed. During hydration of cement paste the ettringite is formed up to ~ 48°C when the conversion of ettringite to AFm starts. It remains in the structure up to ~70-75°C.

6.3.4. C-S-H interlayer and gel water evolution

The C-S-H interlayer and gel pore water appear earlier and develop at a higher rate when the curing temperature is increased (figure 6.12). However with time the intensities of gel and interlayer water for samples cured at lower temperature gradually exceed values for the higher temperatures. Eventually, after about 20 days of hydration for C-S-H interlayer water and 2 days for gel water, intensities are higher for samples cured at progressively lower temperature. The spread of the intensities at 90 days of hydration is ~5%. It is also observed that the change in the rate of gel pore formation happens earlier at higher temperature.

The ratio of C-S-H gel to interlayer signal decreases faster for paste cured at elevated temperature. For mature pastes, the ratio reaches value of about 2 at every temperature: 10°C: ~1.9, 60°C: ~2.2.

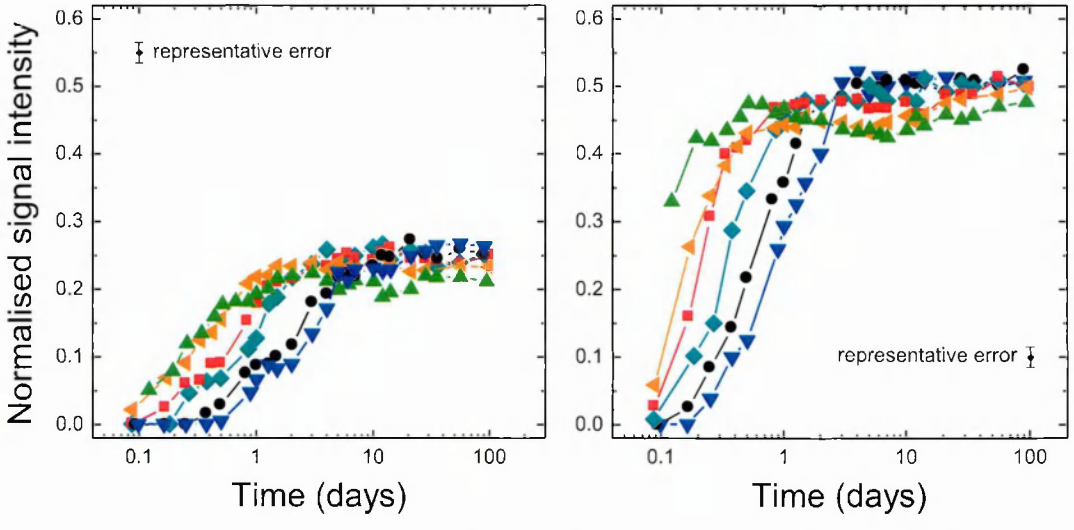

Figure 6.12 Evolution of C-S-H interlayer (left) and gel (right) pore water as a function of hydration time for white cement pastes mixed at w/c_{mix} ratio 0.4 and cured underwater at different temperature: blue inverted triangles: 10°C; black circles: 20°C; cyan diamonds: 30°C; red squares: 40°C; orange left-triangles: 50°C; and green triangles: 60°C.

6.3.5. T_2 relaxation times

Figure 6.13 illustrates how the associated T_2 relaxation times of interlayer, gel and 'free' water vary with hydration time at different curing temperatures.

Initially, the T_2 relaxation times of 'free' – interhydrate, water drop faster with the increase in curing temperature. Beyond about two days the reservoirs maintain the same T_2 times implying constraining of capillary pore sizes. The exceptions are the T_2 relaxation times at 10°C. Their higher values at longer hydration times are explained by a still significant ingress of water due to chemical shrinkage as indicated by increasing water uptake in figure 6.8. At elevated temperatures the T_2 of gel pore water also has the smaller values and decreases more quickly as the hydration process is accelerated. However, after about a week, the trend reverses. The pastes cured at higher temperatures are characterised by the longer T_2 indicating

that gel pore sizes may be bigger. The T_2 of water within C-S-H interlayer spaces stays almost the same at all temperatures after 3 days of hydration.

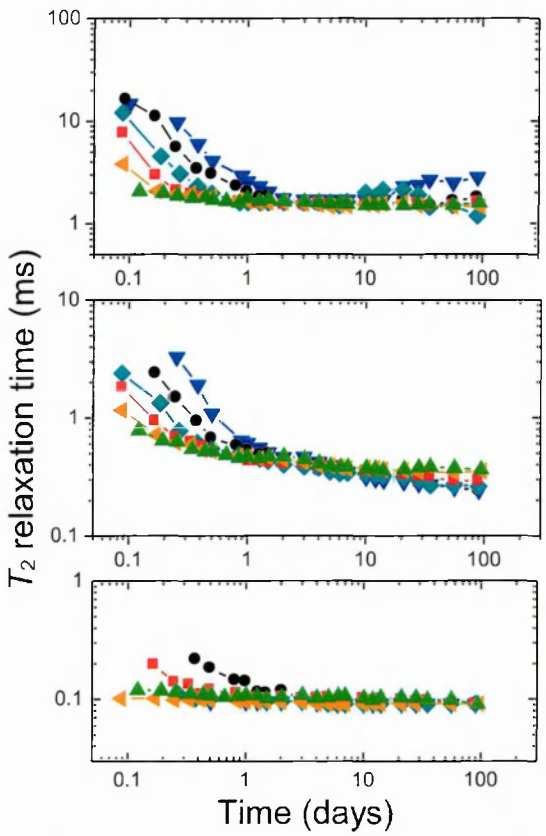

Figure 6.13 The evolution of T_2 relaxation time for water populations of white cement pastes mixed at w/c_{mix} ratio 0.4 and cured underwater at different temperature. The upper graph shows the T_2 of 'free' water, the middle graph - T_2 of C–S–H gel pore water and the lower graph – T_2 of C–S–H interlayer space water. Blue inverted triangles: 10°C; black circles: 20°C; cyan diamonds: 30°C; red squares: 40°C; orange left-triangles: 50°C; and green triangles: 60°C. Lines are guides for eyes.

6.4. Density and composition vs temperature

The C-S-H density and composition for white cement paste cured at various temperatures were calculated based on model described in section 6.1.

6.4.1. Input data

Additional XRD and TGA measurements were performed to obtained the degree of hydration α, (table 6.5) and water content within CH (section 6.3.3 table 6.4) of samples at 28 and 90 days of hydration. The mass of samples was recorded to enable calculation of $(w/c)_{paste}$ (table 6.5) which served to calculate the signal due to water filling chemical shrinkage voids.

Table 6.5. Water uptake and degree of hydration for white cement pastes mixed at w/c_{mix} ratio 0.4 and cured underwater at different temperature.

Temp [°C]	*Age* [days]	$(w/c)_{paste}$ [g/g_{anh}] (±0.002)	α (±0.02)§
10	28	0.433	0.81
	90	0.439	0.87
20	28	0.439	0.85
	90	0.443	0.90♦
30	28	0.439	0.86
	90	0.442	0.93
40	28	0.441	0.88♦
	90	0.442	0.94♦
50	28	0.435	0.90
	90	0.438	0.94
60	28	0.429	0.92♦
	90	0.432	0.95♦

§ - measured at EPFL by Arnaud Muller

♦ - estimated by linear fitting of data at different temperatures

The intensities of water population used in calculation are presented in table 6.6.

Table 6.6 The intensities used to calculate C-S-H density and composition at 28 and 90 days of hydration. The error in intensities is around ±0.010.

Temp [°C]	*Age* [days]	I_{sol}	I_{CH}	I_{Ett} ǂ	I_{CSH}	I_{gel}	I_{cap}	I_{void}	I_{tot}
10	28	0.280	0.159	0.121	0.256	0.504	-0.040	0.082	1.082
	90	0.293	0.181	0.122	0.263	0.508	-0.064	0.098	1.098
20	28	0.276	0.164	0.112	0.252	0.512	-0.040	0.097	1.097
	90	0.297	0.189	0.108	0.252	0.525	-0.074	0.109	1.109
30	28	0.262	0.162	0.100	0.253	0.506	-0.021	0.097	1.097
	90	0.279	0.189	0.090	0.250	0.503	-0.033	0.104	1.104
40	28	0.276	0.166	0.110	0.243	0.487	-0.005	0.103	1.103
	90	0.281	0.188	0.093	0.249	0.498	-0.028	0.106	1.106
50	28	0.248	0.167	0.080	0.227	0.482	0.044	0.087	0.087
	90	0.259	0.187	0.072	0.232	0.498	0.011	0.095	1.095
60	28	0.254	0.169	0.085	0.219	0.451	0.075	0.074	1.074
	90	0.258	0.188	0.070	0.211	0.477	0.055	0.080	1.080

ǂ $I_{Ett} = I_{sol} - I_{CH}$

6.4.2. Density of C-S-H at various temperature

The data presented in section 6.4.1. allows calculation of the C-S-H density according to equations (6.1, 6.2, 6.7). Figure 6.14 shows the C-S-H 'solid' density, excluding gel water, and C-S-H 'bulk' density, including gel water, for white cement paste cured at different temperatures. Presented error represents the average standard deviation value. The sensitivity of the resultant C-S-H densities on input parameters is described in more details in section 6.4.5.

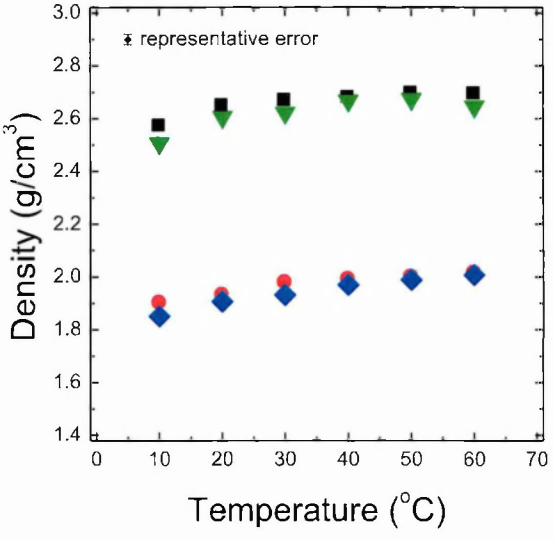

Figure 6.14 C–S–H density as a function of the curing temperature for 28 days (triangles and diamonds) and 90 days old (squares and circles) white cement pastes mixed at w/c_{mix} ratio 0.4 and cured underwater. The blue diamonds and red circles represent the C–S–H bulk density, inclusive of the gel water; green triangles and black squares represent the C–S–H 'solid' density, exclusive of the gel pore water.

The C-S-H 'solid' density increases with increase of temperature. One explanation could be that the interlayer space filled by water is smaller at higher temperature. That this is unlikely is shown as the T_2 relaxation time of interlayer water does not vary with increase of curing temperature. However, its intensity is lower. Hence, the increase of density may arise from an arrangement of calcium silicate (l) and water (l-1) layers. The increase may be explained by the higher ratio of $l/(l\text{-}1)$ at the elevated temperature (figure 6.15) as the calcium silicate layer is more dense than water.

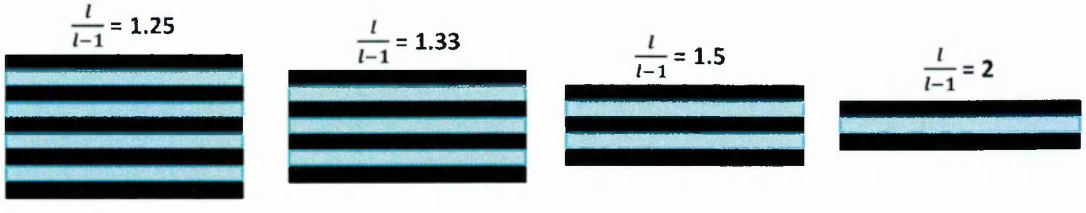

Figure 6.15 An arrangement of calcium silicate layers (l) –black strips, and water (l-1) layers – blue doted strips, presenting the increase of the $l/(l\text{-}1)$ ratio.

The C-S-H 'bulk' density also increases with temperature. The reason for that is twofold. On one hand, the higher 'solid' density contributes greatly to the rise of 'bulk' density. The density grows further as there is less gel pore water at higher temperatures. The rise of 'bulk' density between 10 and 60°C is equal to 0.16 and 0.11 g/cm^3 at 28 and 90 days of hydration respectively. The increase in bulk density with temperature was reported in recent study by Galluci *et al* [109] for sealed cement paste hydrated for 90 days. The calculation was based on SEM and XRD measurements. Nevertheless, the difference in obtained densities at 5 and 60°C (0.34 g/cm^3) is higher than calculated in this thesis.

6.4.3. Composition of C-S-H at various temperature

The water content within C-S-H excluding, x, and including, x', gel pore water is presented in figure 6.16. Presented error represents the standard deviation value. The sensitivity of the resultant C-S-H water content on input parameters is further described in in section 6.4.5.

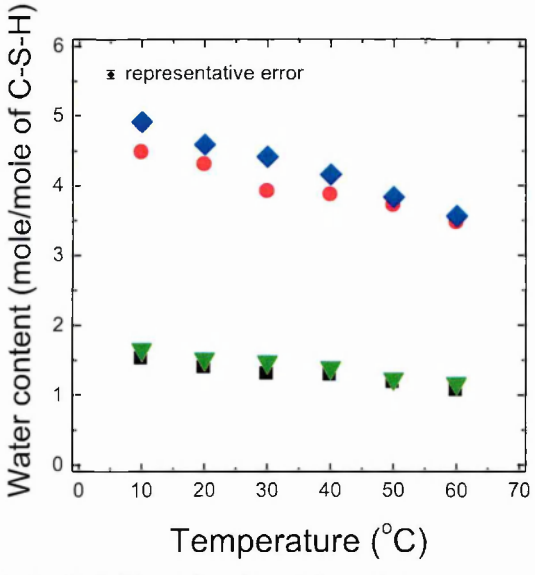

Figure 6.16 Water content in the C–S–H as a function of the curing temperature for 28 days (triangles and diamonds) and 90 days old (squares and circles) white cement pastes mixed at w/c_{mix} ratio 0.4 and cured underwater. The blue diamonds and red circles represent the water in the C–S–H, including the gel water (x'); green triangles and black squares represent water in the C–S–H excluding the gel pore water (x).

The x and x' follow the inverse trend of the density curves. The 'solid' water content declines with temperature indicating that the stack of C-S-H contains fewer layers and therefore fractionally less interlayers filled with water compared to these layers, $(l\text{-}1)/l$. The water content with gel water included also decreases with temperature. Again, it is the joint effect of reduction in number of locally aggregated C-S-H layers and gel water content. The decrease in the H_2O content of C-S-H was reported by Gallucci *et al* [109]. Based on TGA and XRD measurements authors defined the H_2O/SiO_2 ratio of sealed cement pastes hydrated for 90 days to decrease from 3.3 at 5°C to 2.3 at 60°C. The difference in the C-S-H water content between pastes cured at the lowest and highest temperature applied reported by Galluci *et al* and obtained in this study is the same and equalled to 1.0. Nevertheless the

comparison of absolute values is not possible as Galluci *et al* defined the water content as for filled interlayer spaces with the water layer remaining on the gel pore surface included.

The Ca/(Si+Al) ratio, z, remains fairly constant with increasing temperature (figure 6.17 left). It average value at 28 days of hydration is 1.78 ± 0.01 and at 90 days it is lower with 1.67 ± 0.01. The Si content, y, remains fairly constant over whole temperature range as well as at 28 and 90 days of hydration (figure 6.17 right). The average y value is equal to 0.97 ± 0.01. The Ca/(Si + Al) ratio of the sealed cement paste with w/c ratio 0.4 was reported by Gallucci *et al* [109]. Based on SEM-EDS analysis it remains the same in temperature range 5 to 60°C at around 1.8. Lothenbach *et al* [117] used the same method to estimate the ratio for sealed Portland-limestone cement paste. The ratio was found to not differ significantly (1.62 to 1.72) with increase of temperature (5 to 40°C); it remains fairly constant in the range of experimental errors.

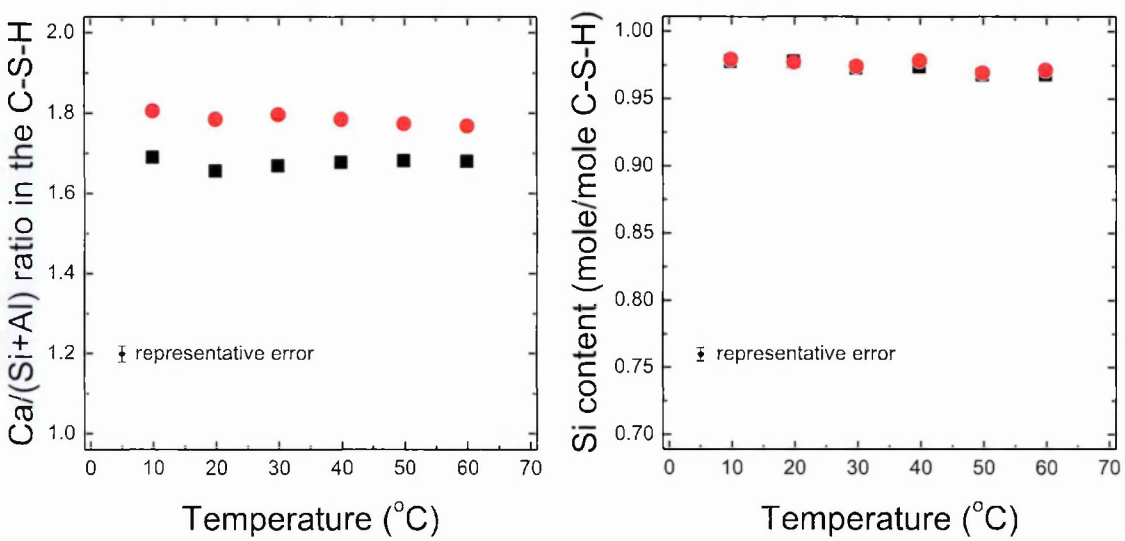

Figure 6.17 Ca/(Si+Al) ratio (left) and Si content (right) in the C–S–H as a function of the curing temperature for 28 days (red circle) and 90 days old (black squares) white cement pastes mixed at w/c_{mix} ratio 0.4 and cured underwater.

6.4.4. Mass and volume composition of cement paste at various temperature

The phase composition diagrams for both mass and volume at various curing temperature are presented in figure 6.18 for 28 and 90 days of hydration. The diagrams show that pastes cured at higher temperature are more reacted. The constant amount of CH and decrease in ettringite content with temperature are observed. It is noticed that the mass and volume of C-S-H is greater at the elevated temperature, while the gel water content is slightly reduced. Pastes exposed to the higher temperature are characterised by larger content of sum 'free' and voids water – coarser porosity.

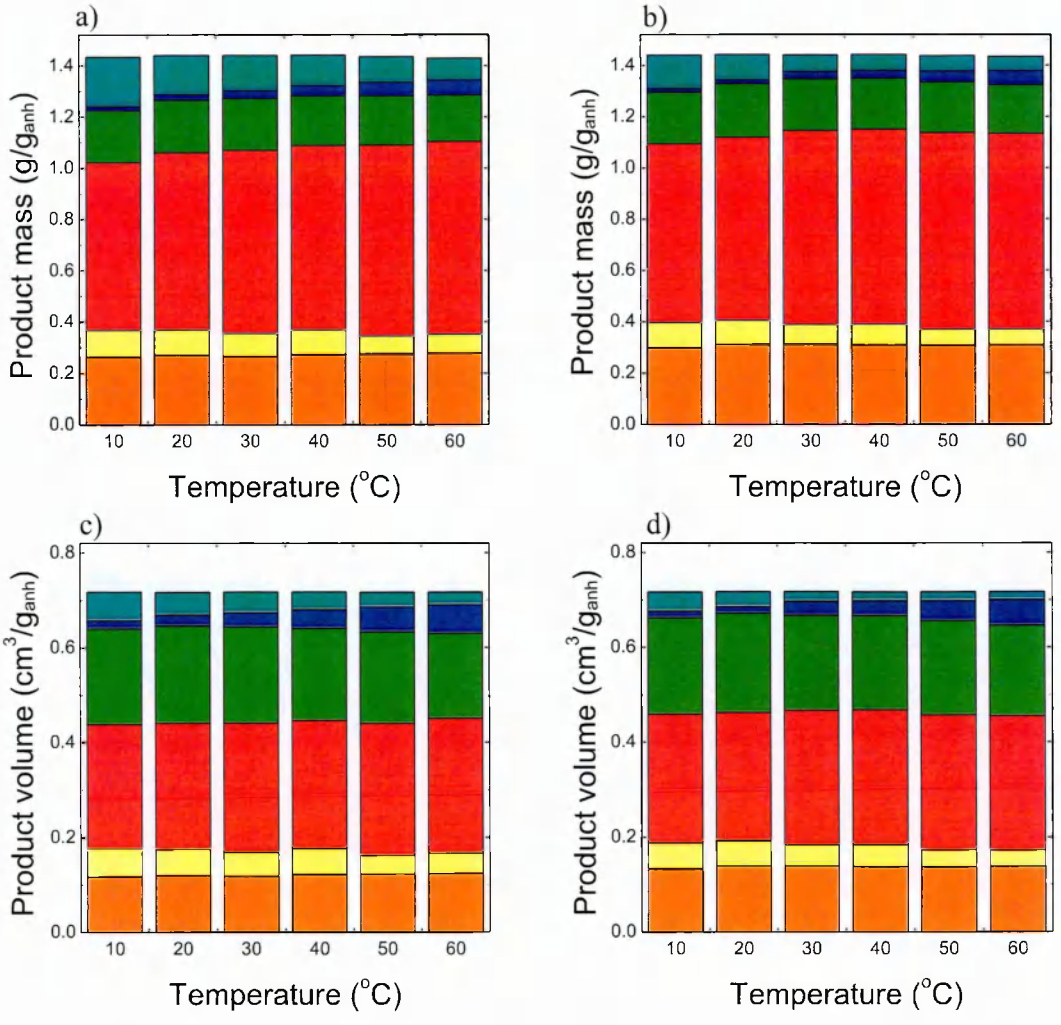

Figure 6.18 Mass and volume composition for 28 days (a and c) and 90 days old (b and d) white cement pastes mixed at w/c_{mix} ratio 0.4 and cured underwater. From bottom: the orange region corresponds to Portlandite, yellow to ettringite, red to the C–S–H, green to gel pore water, blue to joint 'free' and voids water and dark cyan to unreacted cement.

6.4.5. Sensitivity analysis of C-S-H density and composition model

Investigation of the influence of input parameters on the resultant densities and composition of C-S-H is of high importance to this study.

The statistical analysis of the C-S-H densities and composition uncertainties is tedious and extremely complex. It arises from complex dependency between C-S-H characteristics and the uncertainty of many input parameters including α, w_{mix}/c, $(w/c)_{paste}$, I_{CH}, I_{Ett}, I_{CSH}, I_{gel}, I_{cap}, I_{void}, γ_{CSH}, f_{C3S}, f_{C3A}, f_{C3A}^{Ett}, n_{Hyd}. As an example, the uncertainty analysis for the C-S-H 'solid' density is shown through equations (6.9)-(6.12). This includes the expressions for reciprocal of C-S-H 'solid' density, the general and detailed uncertainty of reciprocal and finally uncertainty of C-S-H 'solid' density, respectively.

$$\frac{1}{\rho_{CSH}} = \frac{1}{\rho_w \cdot \gamma_{CSH} \cdot I_{CSH}} + \frac{\alpha}{\frac{w_{mix}}{c} \cdot \rho_c \cdot \gamma_{CSH} \cdot I_{CSH}} - \frac{\beta_{CH} \cdot I_{CH}}{\rho_{CH} \cdot \gamma_{CSH} \cdot I_{CSH}} - \frac{\beta_{Ett} \cdot I_{Ett}}{\rho_{Ett} \cdot \gamma_{CSH} \cdot I_{CSH}} - \frac{\delta_w \cdot (I_{gel} + I_{cap} + I_{void})}{\rho_w \cdot \gamma_{CSH} \cdot I_{CSH}} \quad (6.9)$$

$$u\left(\frac{1}{\rho_{CSH}}\right) = \sqrt{\sum_v \left[\frac{\mathrm{d}(1/\rho_{CSH})}{\mathrm{d}v} \cdot u(v)\right]^2} \quad (6.10)$$

where u is uncertainty and v is variable.

For density calculation v includes: α, w_{mix}/c, I_{gel}, I_{cap}, I_{void}, I_{CH}, I_{Ett}, I_{CSH} and γ_{CSH} leading to:

$$\begin{aligned} u\left(\frac{1}{\rho_{CSH}}\right) = \Bigg\{ & \left[\frac{1}{\frac{w_{mix}}{c} \cdot \rho_c \cdot \gamma_{CSH} \cdot I_{CSH}} \cdot u(\alpha)\right]^2 \\ & + \left[\frac{-\alpha}{\left(\frac{w_{mix}}{c}\right)^2 \cdot \rho_c \cdot \gamma_{CSH} \cdot I_{CSH}} \cdot u\left(\frac{w_{mix}}{c}\right)\right]^2 + \left[\frac{-\delta_w}{\rho_w \cdot \gamma_{CSH} \cdot I_{CSH}} \cdot u(I_{gel})\right]^2 \\ & + \left[\frac{-\delta_w}{\rho_w \cdot \gamma_{CSH} \cdot I_{CSH}} \cdot u(I_{cap})\right]^2 + \left[\frac{-\delta_w}{\rho_w \cdot \gamma_{CSH} \cdot I_{CSH}} \cdot u(I_{void})\right]^2 \\ & + \left[\frac{-\beta_{CH}}{\rho_{CH} \cdot \gamma_{CSH} \cdot I_{CSH}} \cdot u(I_{CH})\right]^2 + \left[\frac{-\beta_{Ett}}{\rho_{Ett} \cdot \gamma_{CSH} \cdot I_{CSH}} \cdot u(I_{Ett})\right]^2 \\ & + \Bigg[\Bigg(\frac{-1}{\rho_w \cdot \gamma_{CSH} \cdot (I_{CSH})^2} + \frac{-\alpha}{\frac{w_{mix}}{c} \cdot \rho_c \cdot \gamma_{CSH} \cdot (I_{CSH})^2} + \frac{\beta_{CH} \cdot I_{CH}}{\rho_{CH} \cdot \gamma_{CSH} \cdot (I_{CSH})^2} \\ & \quad + \frac{\beta_{Ett} \cdot I_{Ett}}{\rho_{Ett} \cdot \gamma_{CSH} \cdot (I_{CSH})^2} + \frac{\delta_w \cdot (I_{gel} + I_{cap} + I_{void})}{\rho_w \cdot \gamma_{CSH} \cdot (I_{CSH})^2}\Bigg) \cdot u(I_{CSH})\Bigg]^2 \\ & + \Bigg[\Bigg(\frac{-1}{\rho_w \cdot (\gamma_{CSH})^2 \cdot I_{CSH}} + \frac{-\alpha}{\frac{w_{mix}}{c} \cdot \rho_c \cdot (\gamma_{CSH})^2 \cdot I_{CSH}} + \frac{\beta_{CH} \cdot I_{CH}}{\rho_{CH} \cdot (\gamma_{CSH})^2 \cdot I_{CSH}} \\ & \quad + \frac{\beta_{Ett} \cdot I_{Ett}}{\rho_{Ett} \cdot (\gamma_{CSH})^2 \cdot I_{CSH}} + \frac{\delta_w \cdot (I_{gel} + I_{cap} + I_{void})}{\rho_w \cdot (\gamma_{CSH})^2 \cdot I_{CSH}}\Bigg) \cdot u(\gamma_{CSH})\Bigg]^2\Bigg\}^{1/2} \end{aligned} \quad (6.11)$$

$$u(\rho_{CSH}) = \sqrt{\left[-{\rho_{CSH}}^2 \cdot u\left(\frac{1}{\rho_{CSH}}\right)\right]^2} \quad (6.12)$$

However, analysis pre-supposed that the uncertainties in all the variables are independent. This is not the case because $\sum I=1$. Expressions for uncertainties in other derived parameters are even more complex.

Due to that complexity of statistical analysis the sensitivity of the calculated C-S-H characteristics is presented by the percentage changes caused by the changes of the input

parameters. Table 6.7 demonstrates the percentage changes of C-S-H 'solid' and 'bulk' densities (ρ_{CSH}, ρ_{CSH}') as well as water (x, x'), calcium (z) and silicon (y) contents for C-S-H. The 5% increase of degree of hydration, water to cement ratio of paste, content of CH (with dropping content of ettringite), solid intensity (with simultaneous decrease of mobile intensity) and C-S-H interlayer water intensity (with decrease of gel water intensity) is implemented in a sensitivity analysis now presented.

Through analysis it was portrait that the C-S-H 'solid' and 'bulk' densities depend to the highest degree on the water to cement ratio of the paste which causes about 7% and 3% increase respectively. It arises as in the calculation model the measured fractional intensities are renormalised to the water content at the mixing time. Hence by misjudging the w/c_{paste} by +5% the intensity of ettringite, C-S-H interlayer and gel pore water populations would rise, capillary water intensity would decrease and CH intensity would not change as it is based on TGA and XRD measurements. The change of w/c_{paste} also causes the 56% increase of the voids intensity, I_{void}. Separately considered, a 5% imprecision in the voids intensity, and hence chemical shrinkage volume, affects ρ_{CSH} and ρ_{CSH}' by 0.7 and 0.4% respectively, and does not influence on any composition parameter. The calculated densities also depend on the accuracy of degree of hydration, 5% overvaluing causes 1 and 2% increase in ρ_{CSH} and ρ_{CSH}'.

The water contents rely on the precision of α and w/c_{paste} measurements causing 6% decrease for former and 6% increase for later input. Additionally, the 'solid' water content would change by 5% if the interlayer water intensity, I_{sh}, had 5% inconsistency. The calcium content, z, is dependent essentially on the content of crystalline phases - CH and ettringite. The inaccuracy in the solid intensity has the least impact on the calculated C-S-H densities and composition.

Table 6.8 presents percentage changes in C-S-H densities and composition parameters caused by simultaneous changes of two input parameters. It is shown that the joint change of the degree of hydration α and w/c_{paste} causes the highest change amongst all presented combination of parameters. When w/c_{paste} is increased by 5% and α is decreased by 5% the C-S-H 'solid' and 'bulk' water contents increase by over 14%. The contents are also altered to high extend (by 11-12% and 6% respectively) by simultaneous increase of w/c_{paste} and I_{sh} as well as by decrease of α and increase of I_{sh}. The 'solid' and 'bulk' C-S-H densities are affected by 5-9% and 1-5%, respectively, by all combination of the w/c_{paste} parameter. The overestimation of w/c_{paste} and underestimation of I_{sh} has the highest influence (~9%) amongst them on 'solid' C-S-H density. The calcium content, z, would rise by 3-4% if the α and m_{CH} are misjudge in opposite manner. The silicon content, y, stays almost unchanged; changes are less than 1%, despite the dynamic nature of all input parameters.

Table 6.7 Sensitivity analysis of C-S-H density and composition calculation based on 28 days old paste cured at 20°C with initial parameters ρ_{CSH} = 2.60 g/cm^3, ρ_{CSH}' = 1.91 g/cm^3, x = 1.51, x' = 4.58, z = 1.78 and y = 0.98. The parameters were changed by +5% (↑) or -5% (↓). Presented are the percentage changes in densities and elements contents. ('c' means that this is the parameter which compensate the 5% change of the given parameter so that $I_{sol} + I_{CSH} + I_{gel} + I_{cap} = 1$ or $I_{Ett} = I_{sol} - I_{CH}$).

Parameters Changed by 5%	ρ_{CSH}	ρ_{CSH}'	x	x'	y	z
α ↑	1.0 ↑	1.8 ↑	-6.3 ↓	-6.3 ↓	0.2 ↑	0.6 ↑
w/c_{paste} ↑	7.1 ↑	2.7 ↑	6.3 ↑	6.3 ↑	0.5 ↑	0.1 ↑
m_{CH} ↑ m_{Ett} c	-0.2 ↓	-0.3 ↓	-0.7 ↓	-0.7 ↓	-0.3 ↓	-2.8 ↓
I_{sol} ↑ I_{mob} ↓	-0.1 ↓	0.1 ↑	-0.5 ↓	-0.5 ↓	0.5 ↑	0.1 ↑
I_{sh} ↑ I_{gel} c	-1.1 ↓	0.0	5.0 ↑	0.0	0.0	0.0

Table 6.8 Extension of the sensitivity analysis of C-S-H density and composition presented in table 6.7. Presented are the percentage changes in densities and elements contents caused by simultaneous changes of two input parameters.

	ρ_{CSH}		ρ_{CSH}'		x		x'		y		z	
Changed Parameters	α ↑	α ↓	α ↑	α ↓	α ↑	α ↓	α ↑	α ↓	α ↑	α ↓	α ↑	α ↓
w/c_{paste} ↑	7.8 ↑	6.3 ↑	4.5 ↑	0.8 ↑	-0.5 ↓	14.1 ↑	-0.5 ↓	14.1 ↑	0.6 ↑	0.4 ↑	0.8 ↑	-0.6 ↓
w/c_{paste} ↓	-5.0 ↓	-7.6 ↓	-0.8 ↓	-4.6 ↓	-12.0 ↓	0.7 ↑	-12.0 ↓	0.6 ↑	-0.3 ↓	-0.7 ↓	0.5 ↑	-0.8 ↓
m_{CH} ↑ m_{Ett} c	0.9 ↑	-1.3 ↓	1.6 ↑	-2.2 ↓	-7.0 ↓	6.4 ↑	-7.0 ↓	6.4 ↑	-0.1 ↓	-0.5 ↓	-2.0 ↓	-3.7 ↓
m_{CH} ↓ m_{Ett} c	1.2 ↑	-0.9 ↓	2.1 ↑	-1.6 ↓	-5.7 ↓	8.1 ↑	-5.7 ↓	8.1 ↑	0.4 ↑	0.1 ↑	3.3 ↑	2.4 ↑
I_{sol} ↑ I_{mob} ↓	1.0 ↑	-1.2 ↓	1.9 ↑	-1.9 ↓	-6.8 ↓	6.8 ↑	-6.8 ↓	6.8 ↑	0.6 ↑	0.4 ↑	0.8 ↑	-0.6 ↓
I_{sol} ↓ I_{mob} ↑	1.1 ↑	-1.0 ↓	1.7 ↑	-2.0 ↓	-5.8 ↓	7.7 ↑	-5.8 ↓	7.7 ↑	-0.3 ↓	-0.7 ↓	0.5 ↑	-0.8 ↓
I_{sh} ↑ I_{gel} c	-0.1 ↓	-2.3 ↓	1.8 ↑	-1.9 ↓	-1.6 ↓	12.6 ↑	-6.3 ↓	7.3 ↑	0.2 ↑	-0.2 ↓	0.6 ↑	-0.7 ↓
I_{sh} ↓ I_{gel} c	2.2 ↑	0.1 ↑	1.8 ↑	-1.9 ↓	-11.0 ↓	1.9 ↑	-6.3 ↓	7.3 ↑	0.2 ↑	-0.2 ↓	0.6 ↑	-0.7 ↓

	ρ_{CSH}		ρ_{CSH}'		x		x'		y		z	
Changed Parameters	w/c_{paste} ↑	w/c_{paste} ↓	w/c_{paste} ↑	w/c_{paste} ↓	w/c_{paste} ↑	w/c_{paste} ↓	w/c_{paste} ↑	w/c_{paste} ↓	w/c_{paste} ↑	w/c_{paste} ↓	w/c_{paste} ↑	w/c_{paste} ↓
m_{CH} ↑ m_{Ett} c	7.0 ↑	-6.4 ↓	2.4 ↑	-2.9 ↓	5.5 ↑	-6.8 ↓	5.5 ↑	-6.8 ↓	0.2 ↑	-0.8 ↓	-2.7 ↓	-2.9 ↓
m_{CH} ↓ m_{Ett} c	7.2 ↑	-6.0 ↓	3.0 ↑	-2.3 ↓	7.0 ↑	-5.5 ↓	7.1 ↑	-5.5 ↓	0.8 ↑	-0.2 ↓	3.0 ↑	2.7 ↑
I_{sol} ↑ I_{mob} ↓	7.1 ↑	-6.3 ↓	2.8 ↑	-2.6 ↓	5.9 ↑	-6.7 ↓	5.9 ↑	-6.7 ↓	1.0 ↑	0.0	0.3 ↑	0.0
I_{sol} ↓ I_{mob} ↑	7.1 ↑	-6.1 ↓	2.6 ↑	-2.7 ↓	6.7 ↑	-5.6 ↓	6.7 ↑	-5.6 ↓	0.0	-1.0 ↓	0.0	-0.3 ↓
I_{sh} ↑ I_{gel} c	5.7 ↑	-7.1 ↓	2.7 ↑	-2.6 ↓	11.6 ↑	-1.5 ↓	6.3 ↑	-6.1 ↓	0.5 ↑	-0.5 ↓	0.1 ↑	-0.1 ↓
I_{sh} ↓ I_{gel} c	8.6 ↑	-5.3 ↓	2.7 ↑	-2.6 ↓	1.0 ↑	-10.8 ↓	6.3 ↑	-6.1 ↓	0.5 ↑	-0.5 ↓	0.1 ↑	-0.1 ↓

	ρ_{CSH}		ρ_{CSH}'		x		x'		y		z	
Changed Parameters	m_{CH} ↑ m_{Ett} c	m_{CH} ↓ m_{Ett} c	m_{CH} ↑ m_{Ett} c	m_{CH} ↓ m_{Ett} c	m_{CH} ↑ m_{Ett} c	m_{CH} ↓ m_{Ett} c	m_{CH} ↑ m_{Ett} c	m_{CH} ↓ m_{Ett} c	m_{CH} ↑ m_{Ett} c	m_{CH} ↓ m_{Ett} c	m_{CH} ↑ m_{Ett} c	m_{CH} ↓ m_{Ett} c
I_{sol} ↑ I_{mob} ↓	-0.2 ↓	0.1 ↑	-0.2 ↓	0.4 ↑	-1.2 ↓	0.3 ↑	-1.2 ↓	0.3 ↑	0.2 ↑	0.8 ↑	-2.7 ↓	3.0 ↑
I_{sol} ↓ I_{mob} ↑	-0.1 ↓	0.2 ↑	-0.4 ↓	0.2 ↑	-0.3 ↓	1.2 ↑	-0.3 ↓	1.2 ↑	-0.8 ↓	-0.2 ↓	-2.9 ↓	2.7 ↑
I_{sh} ↑ I_{gel} c	-1.3 ↓	-1.0 ↓	-0.3 ↓	0.3 ↑	4.2 ↑	5.8 ↑	-0.7 ↓	0.7 ↑	-0.3 ↓	0.3 ↑	-2.8 ↓	2.9 ↑
I_{sh} ↓ I_{gel} c	1.0 ↑	1.4 ↑	-0.3 ↓	0.3 ↑	-5.7 ↓	-4.3 ↓	-0.7 ↓	0.7 ↑	-0.3 ↓	0.3 ↑	-2.8 ↓	2.9 ↑

	ρ_{CSH}		ρ_{CSH}'		x		x'		y		z	
Changed Parameters	I_{sol} ↑ I_{mob} ↓	I_{sol} ↓ I_{mob} ↑	I_{sol} ↑ I_{mob} ↓	I_{sol} ↓ I_{mob} ↑	I_{sol} ↑ I_{mob} ↓	I_{sol} ↓ I_{mob} ↑	I_{sol} ↑ I_{mob} ↓	I_{sol} ↓ I_{mob} ↑	I_{sol} ↑ I_{mob} ↓	I_{sol} ↓ I_{mob} ↑	I_{sol} ↑ I_{mob} ↓	I_{sol} ↓ I_{mob} ↑
I_{sh} ↑ I_{gel} c	-1.2 ↓	-1.1 ↓	0.1 ↑	-0.1 ↓	4.5 ↑	5.4 ↑	-0.5 ↓	0.5 ↑	0.5 ↑	-0.5 ↓	0.1 ↑	-0.1 ↓
I_{sh} ↓ I_{gel} c	1.1 ↑	1.3 ↑	0.1 ↑	-0.1 ↓	-5.5 ↓	-4.6 ↓	-0.5 ↓	0.5 ↑	0.5 ↑	-0.5 ↓	0.1 ↑	-0.1 ↓

6.5. Evolution of water population for white cement paste with 10% of silica fume

Preparation of cement paste with silica fume involved addition of superplasticizer. The amount of superplasticizer added was 0.1% by weight of the binder. This is equivalent to 0.25% of the mass of water for $w/b = 0.4$. This quantity of superplasticizer is sufficiently low so as not to be considered as a separate component in relaxation analysis.

6.5.1. Uptake of water during hydration

The water ingress during hydration for cement paste with addition of 10% silica fume (SF) mixed at $w/b_{mix} = 0.4$ and cured at different temperature is presented in figure 6.19.

The uptake of water starts at earlier hydration time and proceeds more quickly for pastes cured at elevated temperature. However, samples cured at lower temperature catch up and in some cases overtake their higher temperature counterparts and finally uptake more water. In comparison with plain white cement paste, more water is drawn into samples.

Pastes cured at the highest temperature presents a distinguishing behaviour. Their water mass increases significantly during first 4h of hydration and consequently shows water content values higher by about 0.015 g/g_{anh}. The observation is believed to be caused by the observed cracking of the SF samples cured at 60°C.

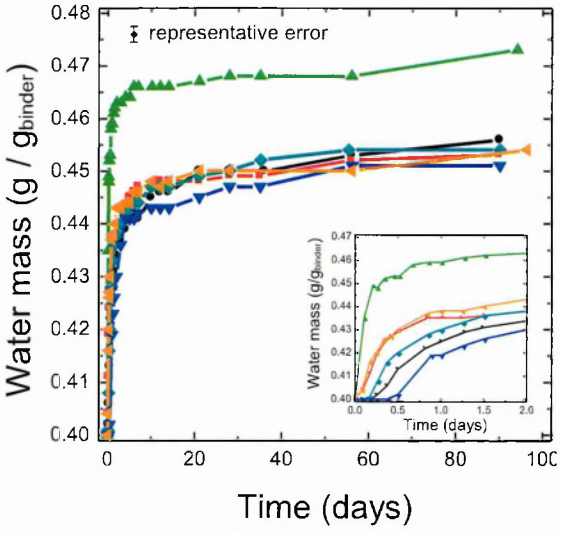

Figure 6.19 Uptake of water mass as a function of hydration time for white cement pastes with addition of 10% silica fume mixed at w/b_{mix} ratio 0.4 and cured underwater at different temperature: blue inverted triangles: 10°C; black circles: 20°C; cyan diamonds: 30°C; red squares: 40°C; orange left-triangles: 50°C; and green triangles: 60°C.

6.5.2. 'Free' water evolution

The 'free' water[26] signal evolution for pastes with addition of silica fume is presented in figure 6.20.

At early age, 'free' water is consumed faster at higher temperature compared to lower temperature. The hydration time at which 'free' water is consumed by 50% is about 3, 5, 8 and 13 hours at 60, 40, 30 and 20°C respectively. The characteristic feature is the minimum in the 'free' water intensity followed by weak local maximum and subsequent steady decline, more visible for samples cured at higher temperatures. The reason for this behaviour is not clear. One may think that as the samples are cured underwater there is ingress of water which accounts for these behaviours. However, the changes in the total signal intensity shown in an upper plot of figure 6.20 are not adequate to explain free water data. It is noticed that the hydration times at which minima in 'free' water signal appear, at different temperatures, coincide with times of maxima in chemically combined water signal presented in the following section. It suggests that the appearance of trough and increase of signal is the consequence of a pozzolanic reaction of CH and SF. It may imply that the product of reaction is the C-S-H with interhydrate spaces in between. The following decline in signal indicates that the 'free' water is again consumed in hydration process.

When samples are older, more 'free' water remains at higher curing temperature. However, the difference in 'free' water content at different temperature is reduced notably with time.

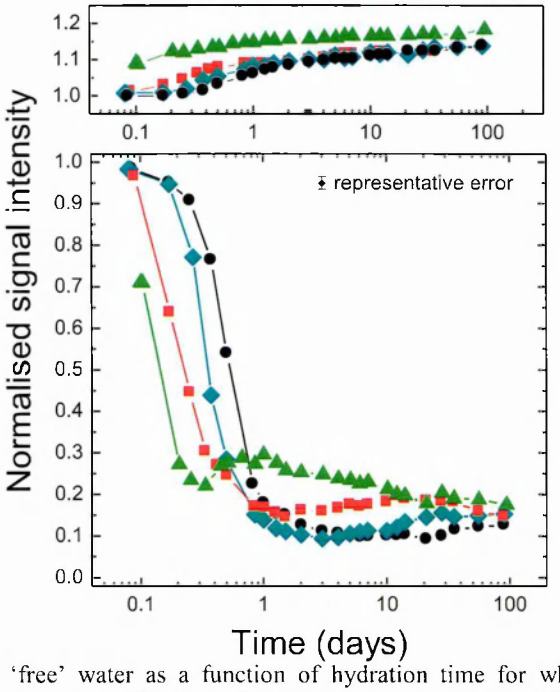

Figure 6.20 Evolution of 'free' water as a function of hydration time for white cement pastes with addition of 10% silica fume mixed at w/b_{mix} ratio 0.4 and cured underwater at different temperature: black circles: 20°C; cyan diamonds: 30°C; red squares: 40°C and green triangles: 60°C. The upper plot shows the evolution of total signal intensity. Lines are guides for eyes.

[26] 'free' water is the sum of interhydrate and capillary pore water intensities with the low contribution of latter, about 3-1%, over whole hydration time at all examined curing temperatures

6.5.3. Chemically combined water evolution

Figure 6.21 shows the evolution of chemically combined water intensity. At early stage of hydration the crystalline phases are created faster at elevated temperatures. Nonetheless, progressively with time and lower curing temperature solid water fractions are larger than at higher temperatures. It is observed that there is an apparent maximum in the signal fraction, which moves toward shorter hydration times with rise of curing temperature (10°C: ~60 days, 20°C: ~28 days, 30°C: ~5 days, 40°C: ~36 hours, 50°C: ~20 hours, 60°C: ~12 hours). Maxima

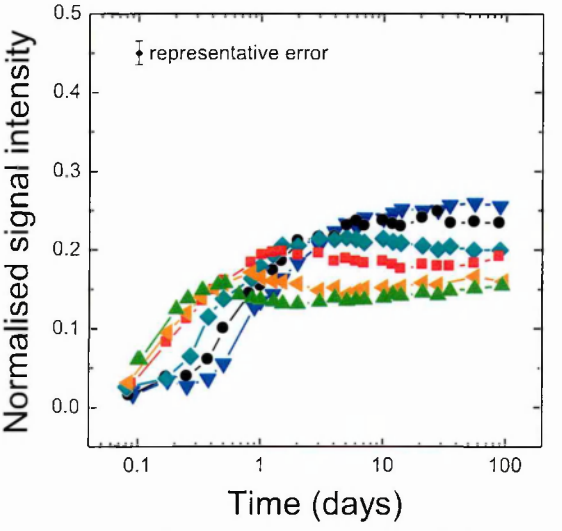

Figure 6.21 Evolution of chemically combined water as a function of hydration time for white cement pastes with addition of 10% silica fume mixed at w/b_{mix} ratio 0.4 and cured underwater at different temperature: blue inverted triangles: 10°C; black circles: 20°C; cyan diamonds: 30°C; red squares: 40°C; orange left-triangles: 50°C; and green triangles: 60°C. Lines are guides for eyes.

Table 6.9 The mass and water content of CH measured by TGA; the NMR solid signal; ettringite water content calculated as the difference of solid signal and CH water content; and ettringite content based on its water content; at 90 days of hydration for white cement pastes with addition of 10% silica fume mixed at w/b_{mix} ratio 0.4 and cured underwater at different temperature.

Temp [°C]	m_{CH} [g/g_{bin}] (±0.010)	*Water Content*[27] *at 90days*			m_{Ett} [g/g_{bin}]
		TGA CH (I_{CH})	**NMR solid (I_{sol})**	***Ett*** **(I_{sol} - I_{CH})**	
10	0.235	0.143	0.255	0.113	0.098
20	0.217	0.132	0.229	0.097	0.084
30	0.201	0.122	0.199	0.076	0.066
40	0.193	0.117	0.180	0.063	0.055
50	0.190	0.116	0.159	0.044	0.038
60	0.184	0.112	0.154	0.042	0.037

[27] 1 - water content at the mixing time, w/b_{mix} = 0.4

coincidence with the minima in free water signal intensity. These maxima and subsequent decline of intensity indicates the consumption of CH in a pozzolanic reaction with silica fume to create C-S-H. For mature paste significantly lower chemically combined water content is observed for paste cured at elevated temperature.

The TG analysis of pastes at 90 days of hydration permit calculation of the water fraction in CH. Based on the analysis results for plain white cement paste, the ettringite water fraction was determined as a difference between NMR solid signal and CH water fraction. The results presented in Table 6.9 shows that with increase of curing temperature the CH and ettringite water fractions and hence the CH and ettringite contents decrease.

6.5.4. C-S-H interlayer and gel water evolution

The evolution of C-S-H interlayer and gel pore water signal for white cement paste prepared with addition of silica fume is presented in figure 6.22.

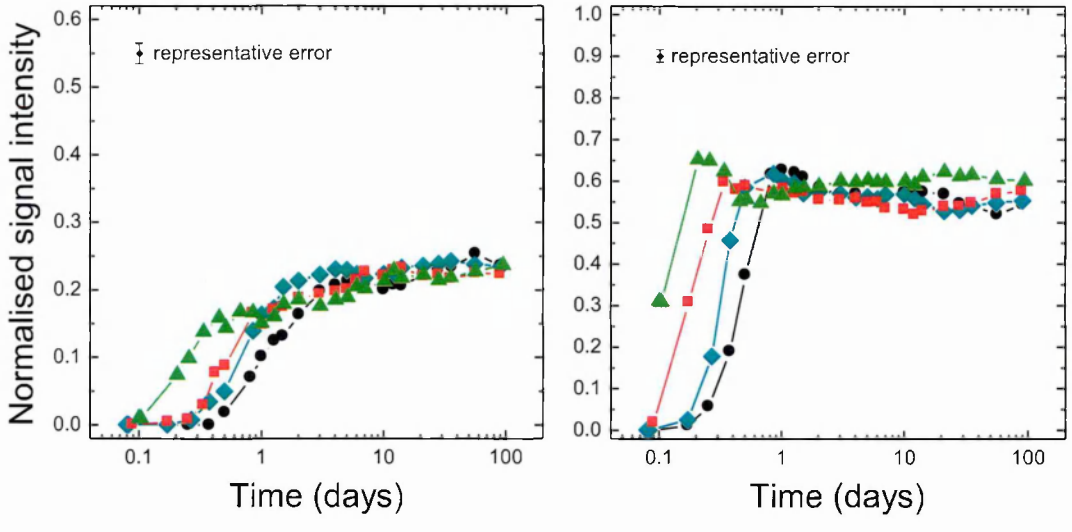

Figure 6.22 Evolution of C-S-H interlayer (left) and gel (right) pore water as a function of hydration time for white cement pastes with addition of 10% silica fume mixed at w/b_{mix} ratio 0.4 and cured underwater at different temperature: black circles: 20°C; cyan diamonds: 30°C; red squares: 40°C and green triangles: 60°C.

At higher curing temperatures, the acceleration of C-S-H interlayer and gel pore development takes place. For mature pastes, after 10 days of hydration, the interlayer water signal rises steadily and similarly across all temperatures. The gel water signal, at first, grows attaining a maximum value and thereafter declines. This indicates the consumption of gel water. For pastes cured at 60, 40 and 30°C the gel signal increases again beyond 1, 10 and 20 days respectively, at the times when the 'free' water signal begin to decrease again. This is a result of a complex process of hydration in presence of silica fume: the C-S-H is created as cement phases hydrate as well as due to CH and SF reaction.

6.5.5. T_2 relaxation times

Figure 6.23 illustrates how the associated T_2 relaxation times of interlayer, gel and 'free' water vary with hydration time at different curing temperatures for white cement pastes with addition of 10% silica fume.

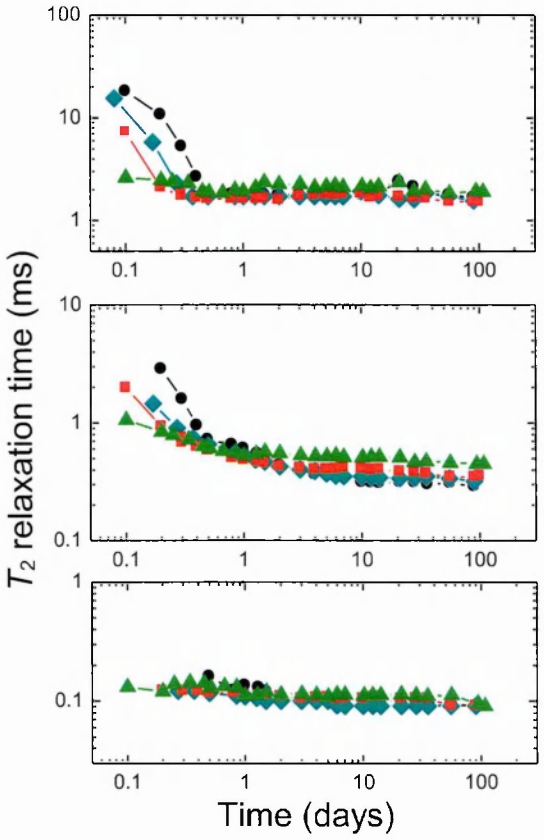

Figure 6.23. The evolution of T_2 relaxation time for water populations of white cement pastes with addition of 10% silica fume mixed at w/b_{mix} ratio 0.4 and cured underwater at different temperature. The upper graph shows the T_2 of 'free' water, the middle graph - T_2 of C–S–H gel pore water and the lower graph – T_2 of C–S–H interlayer space water. Black circles: 20°C; cyan diamonds: 30°C; red squares: 40°C; and green triangles: 60°C. Lines are guides for eyes.

At early hydration time, the T_2 relaxation times of 'free' – interhydrate, water decrease faster as curing temperature increases. Beyond about 12 hours the reservoirs are characterised by the same T_2 times suggesting same capillary pore sizes. Initially at higher temperatures, the T_2 of gel pore water also has the smaller values as the hydration process is accelerated. At later ages of pastes, the trend reverses and pastes cured at higher temperatures are characterised by the longer T_2 implying larger gel pore sizes. The T_2 of water within C-S-H interlayer spaces stays almost the same at all temperatures with slight decrease with time.

6.6. COMPARISON: WHITE CEMENT PASTE VS WHITE CEMENT PASTE WITH SILICA FUME

6.6.1. Evolution of water populations at 20°C

Figure 6.24 compares the evolution of NMR water populations during hydration for plain white cement paste and white cement paste with silica fume (SF) cured underwater at 20°C. The same populations are observed with differences in intensities. The total signal intensity for paste with SF is higher than for plain paste suggesting higher chemical shrinkage.

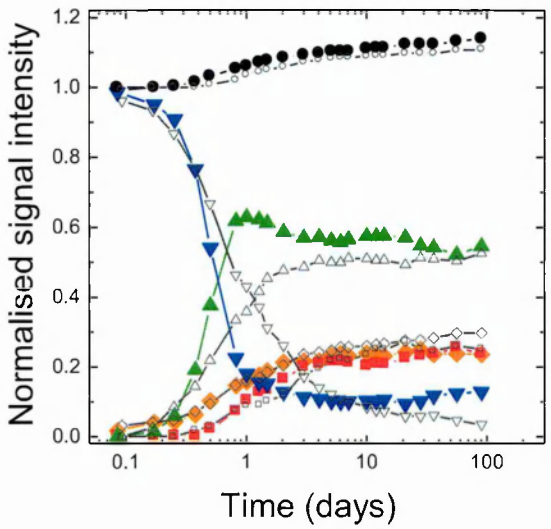

Figure 6.24 The evolution of different water population for white cement paste with 10% addition of silica fume mixed at w/b_{mix} ratio 0.4 and cured underwater at 20°C. Orange diamonds represent chemically combined water signal, red squares – the C–S–H interlayer pore water, green triangles – the C–S–H gel pore water and blue inverted triangles – the 'free' water signals. The black circles show the total water signal normalized to the initial mass of water at the mixing point. Open black symbols are corresponding signals for reference white cement paste cured at 20°C.

Initially, up to 9 hours, the 'free' water intensities are very close. Later, the consumption is much faster for paste containing silica fume. At 1 day of hydration there is only 18% of 'free' water left in comparison with 43% for plain paste. After 3 days the intensity remains at fairly constant level of 10%, while for plain cement it decreases gradually down to 3% at 90 days. The development of the 'free' water signal indicates the 'finer' porosity of the SF paste between 0.5 and 7 days in comparison with plain cement paste. Beyond 7 days the situation reverses – plain cement paste shows less capillary porosity.

Addition of silica fume causes more prompt development of gel pores. Throughout the whole experimental time the gel water intensity is higher than for white cement paste. Moreover, it presents different behaviour: the intensity attains a maximum after 20h and beyond that point it gradually decreases. In contrast for plain cement the gel intensity increases up to 4 days and stays relatively constant afterwards without a maximum.

The C-S-H interlayer water signal follows the same trend for both mixes and is only slightly lower in the presence of SF.

The intensities of crystalline phases increase at the same rate in both pastes during the first 2 days. Following that, as a result of silica fume impact, the increase in signal lessens. Hence, the difference in signals for both pastes increases with time with the gap of 7% at 90 days.

The associated T_2 relaxation times for water within C-S-H interlayer spaces, gel and interhydrate pores are presented in figure 6.25. The 'free' – interhydrate, water T_2 relaxation times are the same at the beginning of hydration for paste with and without silica fume. They are slightly smaller between 0.3 and 2 days and higher beyond 2 days in presence of SF. However, they reach fairly constant value already after 12 hours in comparison with two days for paste without SF. The T_2 of the gel water is slightly higher after 20 days. The C-S-H interlayer water is characterised by almost the same relaxation times throughout whole hydration process.

The reasons for changes in water intensities and T_2 relaxation times in the presence of SF are twofold. The cement hydration is accelerated as the fine silica fume provides additional nucleation sites for C-S-H. Further modifications of microstructure are caused by the pozzolanic reaction of silica fume and CH that results in creation of C-S-H.

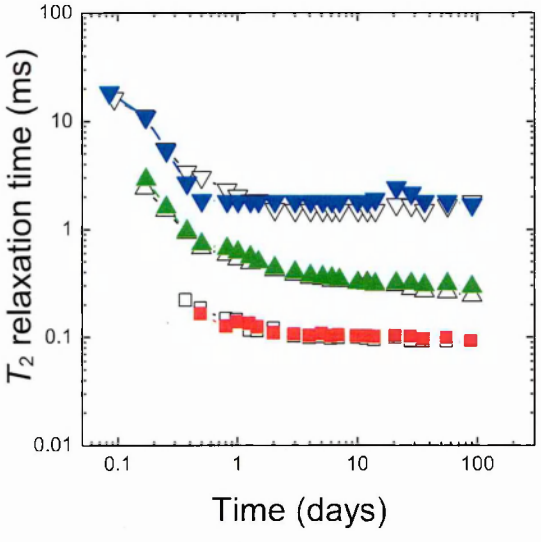

Figure 6.25 The evolution of T_2 relaxation time for white cement paste with 10% addition of silica fume mixed at w/b_{mix} ratio 0.4 and cured underwater at 20°C. Red squares represent the T_2 of C–S–H interlayer pore water, green triangles – the C–S–H gel pore water and blue inverted triangles – the 'free' water. Open black symbols are corresponding times for reference white cement paste cured at 20°C.

6.6.2. The comparison for the full range of temperature

The comparison of the NMR results for white cement paste with and without addition of silica fume at different temperatures is presented in figure 6.26.

The significant differences in the amount of chemically combined water are noticeable. At earlier ages, the signal in presence of SF follows the signal for plain white cement. However, after 2 days at 20°C, 36 h at 30°C, 36h at 40°C and 6h at 60°C the lower values are observed. The maximum difference in intensities is about 10%.

The consumption of 'free' water is faster for pastes with SF at the beginning of hydration. The inflection point appears at progressively longer times with decrease of temperature: ~10h for 60°C and 7 days for 20°C. Beyond that point there is more 'free' water within structure of SF pastes.

It is also shown that pastes contain more gel pore water at the same temperature and time when the silica fume is incorporated. The difference becomes gradually smaller with hydration time. The content of C-S-H interlayer water is influenced by addition of silica fume to the smallest extend. The intensities are just slightly lower by 1-3%.

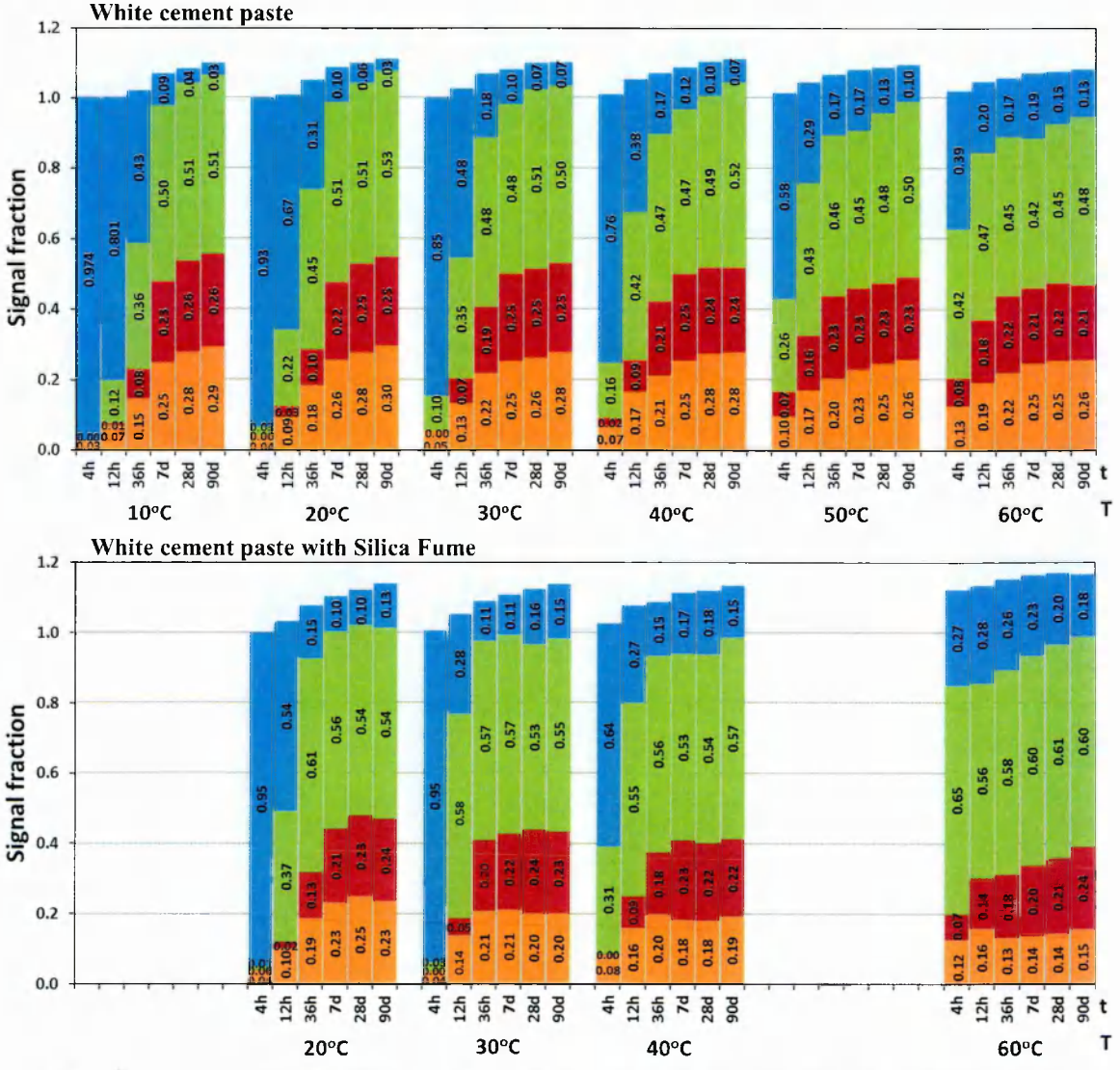

Figure 6.26 The evolution of different water population for white cement paste (top) and white cement paste with silica fume (bottom) over the time of hydration for samples cured underwater at various temperature. Total signal is de-composed into chemically combined water (orange), water in C–S–H interlayer spaces (red), C–S–H gel pores (green) and 'free' water (blue). The total signal fractions go above 1 indicating the underwater curing.

7. Other experimental insight

7.1. Activation energy of water dynamic

7.1.1. Verification of experiments integrity

7.1.1.1. Water T_1 relaxation time as a function of temperature

Inversion recovery measurements of distilled water were performed at different temperature (T) to validate the behaviour of the T_1 relaxation time against literature data [125]. Figure 7.1 presents the change in T_1 relaxation time expressed as $\ln\left(T_1(T_{ref})/T_1(T)\right)$ to account for different frequencies at which experiments were performed (28 vs 20 MHz). Good agreement is found between data sets.

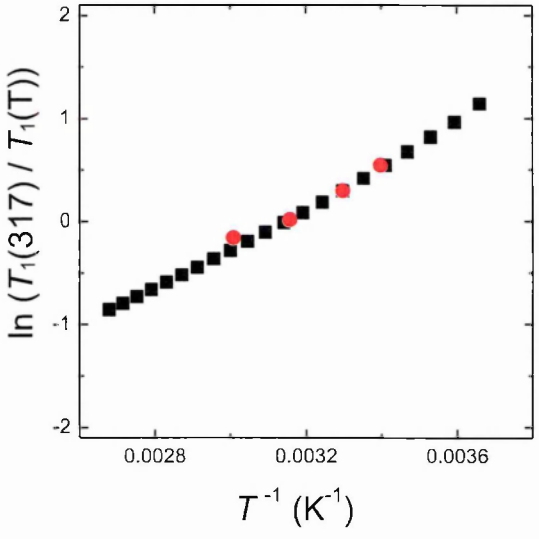

Figure 7.1 The changes in the T_1 relaxation time of water as a function of temperature. Red circles are the author experimental data, black squares are the data reported by Krynicki [125].

7.1.1.2. The total signal intensity as a function of temperature

The activation energy experiments presented in the following section were performed by T_1 recovery. The total signal intensity - 'net' magnetization, M_o, along the z direction is the measure of the excess of parallel state magnetic moments population. Considering the Boltzmann's distribution equation (section 3.1) and the fact that energy difference between α and β spin states, ΔE, is much lower than the thermal energy, kT, the expression for M_o as a function of temperature is well approximated by [78]:

$$M_o = N \cdot \frac{(\gamma \cdot \hbar)^2 \cdot B_o}{4 \cdot k_B \cdot T} = C \cdot \frac{1}{T} \tag{7.1}$$

where N is the total number of nuclei in sample, B_o is magnetic field, γ is the gyromagnetic ratio, k_B is Boltzmann constant, $\hbar$ is the Planck constant divided by 2π and C is constant.

Figure 7.2 a and b demonstrate that the measured total signal intensity for mature white cement paste, at 28 and 90 days of hydration, behaves linearly and increases proportionally with increase in $1/T$ according to equation (7.1). The saturation recovery technique was used to measure those samples. Data sets took two days to record. A further set was recorded at days 7 and 8 using inversion recovery. However, it showed too much systematic variation during measurements due to ongoing hydration to be trusted. These measurements are not included.

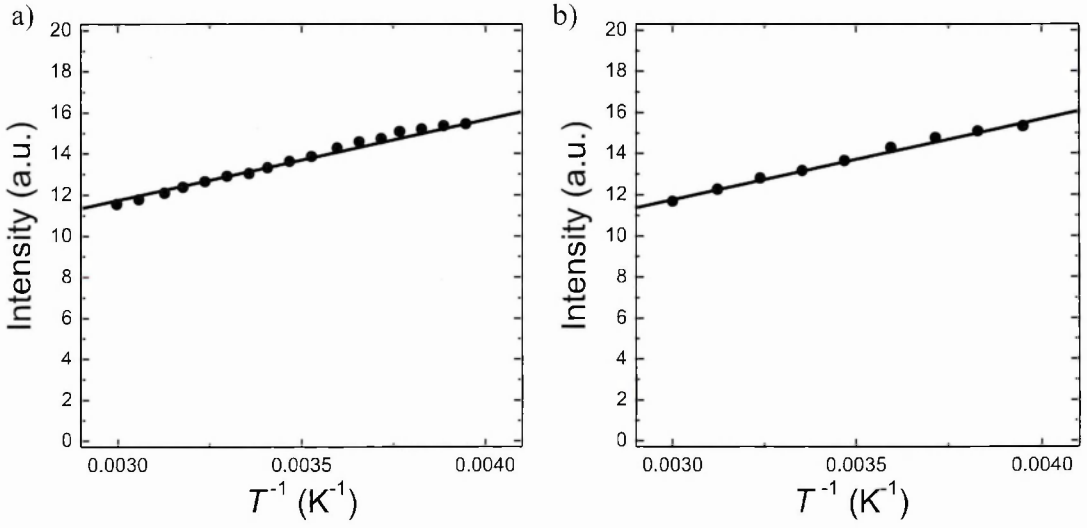

Figure 7.2 Total signal intensity for white cement paste cured underwater (w/c_{mix} = 0.4) for 28 (a) and 90 (b) days of hydration as a function of temperature at which measurements were performed.

7.1.2. Activation energy

7.1.2.1. The analysis of T_1 relaxation measurements

The T_1 recovery measurements were performed in the experimental temperature range from -20 to +60°C. The data were originally analysed by Inverse Laplace Transform (ILT). However they showed fluctuations in intensities of the C-S-H interlayer and gel pore water due to low signal to noise ratio. Hence, the fractional intensities for particular water populations were averaged and intensities recalculated. Further, multi-exponential analyses with constrained intensities were performed. The T_1 relaxation times obtained in such way served to plot the $\ln(1/T_1)$ dependence on temperature (figure 7.3) used in further calculations.

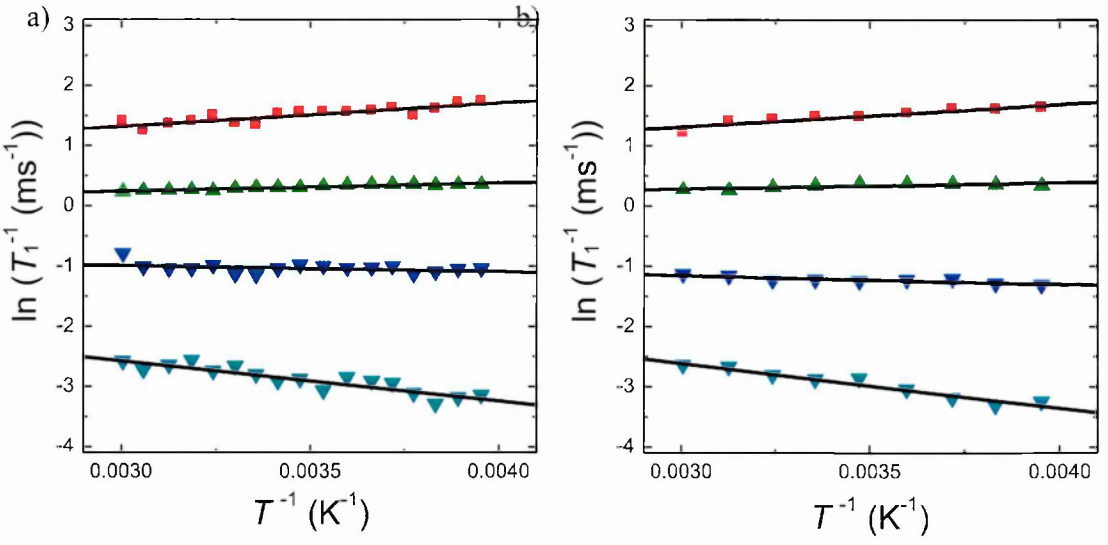

Figure 7.3 The changes in $\ln(1/T_1)$ as a function of temperature for white cement paste at 28 (a) and 90 (b) days of hydration based on multi-exponential analysis with constrained intensities. Lines are the linear fit to the data.

7.1.2.2. Activation energy

The basic law of chemistry, developed by Svente Arrhenius, relates the constant rate of reaction (k) with temperature (T) at which the reaction/process occurs

$$k = A \cdot e^{-\frac{E_A}{k_B \cdot T}} \tag{7.2}$$

where A is prefactor and E_A is the activation energy.

This law can be adapted for NMR analysis. As water, or more precisely hydrogens, in different pore environments have specific relaxation rates ($1/T_1$), by looking at the changes in these rates with temperature it is possible to calculate the activation energy for relaxation processes in associated pore types. The correlation time (τ_c) of molecular motion causing relaxation can be written as an Arrhenius type rate process

$$\tau_c = \tau_o \cdot e^{\frac{E_A}{k_B \cdot T}} \tag{7.3}$$

According to BPP theory [89], the T_1 relaxation time for magnetic dipole-dipole interactions is expressed in terms of spectral density function $J^{\times}(\omega)$, given in section 3.3.1, and hence is related to correlation time as:

$$\frac{1}{T_1} = C \cdot J^{\times}(\omega) = C' \cdot \left(\frac{2 \cdot \tau_c}{1 + \omega^2 \cdot {\tau_c}^2}\right) \tag{7.4}$$

where C and C' is constant.

The T_1 relaxation time as a function of τ_c shows a minimum at $\omega_o \cdot \tau_c \approx 1$ (section 3.3.1. figure 3.11). Therefore depending on the $\omega_o \cdot \tau_c$ value relaxation rate can be expressed as:

$$\omega_o \tau_c \ll 1 \rightarrow ln\left(\frac{1}{T_1}\right) = C'' + \frac{E_A}{k_B \cdot T}; \qquad \omega_o \tau_c \gg 1 \rightarrow ln\left(\frac{1}{T_1}\right) = C'' - \frac{E_A}{k_B \cdot T} \tag{7.5}$$

where C'' is constant.

The evaluated relation of relaxation rate considers only ^{1}H dipolar spin-pair interactions through the molecular rotations and translational motions. Considering the measurements of distilled water which is characterised by long T_1 and T_2 relaxation in the fast motion regime, the gradient sign is consistent with equation (7.5).

For cementitious materials the mechanism of relaxation and the obtained values of T_1 are induced/dominated by ^{1}H interaction with paramagnetic impurities, S, and modulated by translational diffusion of the mobile spins, I, with reference *to* S as described in section 3.3.3. For relaxation of spins in cement paste pores the correlation time, τ_c, may be taken to be the surface hopping time, τ_m, of Korb's model. The expression $\omega_o \cdot \tau_c$ becomes $\omega_S \cdot \tau_m$, where $\omega_S \approx 650 \cdot \omega_o$ is the electron resonance frequency.

7.1.2.3. The activation energy calculation for cement paste

The fitting lines of function $\ln(1/T_1) = A \pm E_A/(k_B \cdot T)$ for mobile relaxation time components of white cement paste are shown in figure 7.3a at 28 days and figure 7.3b at 90 days of hydration. The gradients of these lines are presented in table 7.1.

Table 7.1. The gradients of the fitting lines of $\ln(1/T_1)$ as a function of temperature for cement paste at 28 (fig 7.3 a) and 90 (fig. 7.3 b) days of hydration and activation energy of water transport in associated pores calculated based on these gradients.

Pore water	Gradient		Activation energy [eV]	
	28 days	90 days	28 days	90 days
C-S-H interlayer	392.0	375.2	0.034 ±0.003	0.032 ±0.002
C-S-H gel	137.2	106.0	0.012 ±0.001	0.009 ±0.002
Interhydrate	-99.6	-146.2	0.009 ±0.002	0.013 ±0.002
Capillary	-663.2	-740.1	0.057 ±0.005	0.064 ±0.007

The first observation is the change in gradient from positive values for C-S-H interlayer and gel pore water to negative for two capillary reservoirs. This suggests that the relaxation times of cement paste pore water are placed in close proximity of the T_1 ($\omega_o \cdot \tau_c$) minimum. At 20 MHz and taking $\tau_m \approx 1$ ns [99] $\omega_S \cdot \tau_m$ has a value of ≈ 80 that is much greater than 1. This clarifies the gradient sign for interhydrate and capillary water. Nevertheless the change of the sign for interlayer and gel pore water is surprising and not fully understood at this stage of work. Ongoing Molecular Dynamics and Monte Carlo simulation studies of relaxation in small pores by TRANSCEND student Serge Henri Cachia (Project 1) and EPSRC student Nicholas Howlett may help clarify the situation.

The activation energies of molecular motion within cement paste porosities, calculated based on gradients, are presented in table 7.1 and in figure 7.4 as a function of hydration time and T_1 relaxation time at 298 K. Water in capillary pores, with higher T_1 and pore size of order of micrometres, is characterised by the greatest activation energy. With increase of hydration time the values of capillary activation energies stay fairly constant within range of experimental accuracy. The calculated values (~0.060 eV) are about one third of that for bulk water. For water in spaces with smaller pore sizes the activation energy may go through a minimum. The lowest values are observed for water in interhydrate pores which size is about 10 nm and gel pores with size of ~3 nm. Following that the activation energy is higher in C-S-H interlayer spaces. It is also noted that the C-S-H interlayer, gel and interhydrate water activation energies do not vary significantly within hydration time at which experiments were performed in this study.

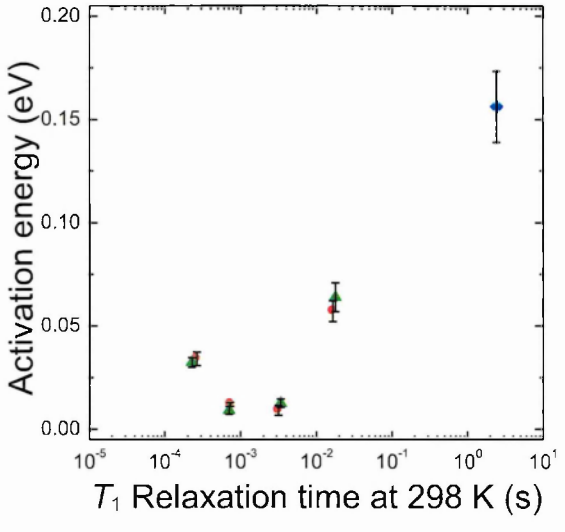

Figure 7.4 The activation energy dependence on T_1 relaxation time for white cement paste 28 (red circles) and 90 (green triangles) days of hydration. The blue diamond represents the approximated water activation energy based on fitting line of $\ln(1/T_1)$ of experimental data presented in figure 7.1.

The activation energy for relaxation in bulk fluid is determined by the activation energy for rotational and translational motion of spins in bulk. The activation energy for surface adsorbed species is that for surface diffusion. Since the observed relaxation rate is the

weighted average of surface and bulk relaxation, this suggests that the surface mobility has lower activation energy than the bulk, as more confined water has a lower energy. This is perhaps surprising and is a subject of ongoing MD simulations by Serge Henri Cachia. The increase for interlayer water may reflect that the relaxation model breaking down in such a small space, especially given water associated with interlayer calcium.

7.2. WATER - ISOPROPANOL EXCHANGE

This section contains the product of joint research between author and Dr Radoslaw Kowalczyk. The author's contribution was the experimental examination of the time dependency of exchange and the exponential stripping analysis of both deuterated and protonated sample data (latter for comparison with ILT). More details on the sample preparation, experiments and analysis are presented in [105] (Appendix 2).

7.2.1. Protonated cement paste

The T_2 relaxation time distributions for cement pastes prepared with H_2O are presented in figure 7.5 and table 7.2. The distribution of as prepared paste (top graph) shows peaks associated with chemically combined water (24% with T_2 ~10 μs), C-S-H interlayer (21%, 90 μs), gel (44%, 300 μs), interhydrate (8%, 1 ms) and capillary pore (3%, 4 and 15 ms) water.

The isopropanol exchange (middle graph of figure 7.5 and 2nd line in table 7.2) causes a slight decrease in the total signal intensity in comparison with as prepared paste. The reduction could be explained by lower proton density of isopropanol ($0.105N_A$ cm^{-3} where N_A is Avogadro number) than of water ($0.111N_A$ cm^{-3}). The 3% decline in intensity would be achieved by exchanging 60% of mobile water with isopropanol. However, the T_2 distribution reveals important changes in populations. The interhydrate and capillary liquid intensities increase markedly from a sum of 11% to 39%. At the same time, the intensity of liquid within gel pores decreases drastically by 28%. Only a small change is observed (by 3%) in interlayer intenity. The solid signal is unchanged.

One may think that there is increase in the amount of large pores and a parallel decrease of gel pore volume due to damage to pore network. That this is unlikely is proven by the result of back exchanging an isopropanol exchanged sample with water (bottom graph of figure 7.5). In the 3rd line of the table it is shown that gel, interhydrate and capillary water intensities are reversed almost to the level of as prepared paste. This suggests that larger pores, even for underwater cured samples, are inaccessible to water and are hence empty. It arises because the very small permeability of paste restrains curing water from getting into and saturating the capillary porosity. At reduced relative humidity the Kelvin Laplace equation ensures that large pores are not liquid filled. Even at 98% RH, pores with size above 53 nm are empty of liquid water. However, isopropanol can access these bigger pores as its contact angle is smaller compared to water [126].

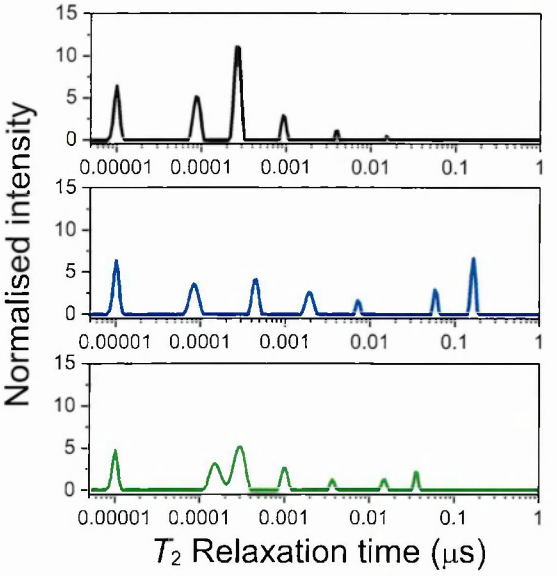

Figure 7.5 The T_2 relaxation times distribution of as prepared paste with H_2O (top), exchanged with isopropanol (middle) and exchanged back with H_2O (bottom) – analysis performed by Dr R. Kowalczyk.

Table 7.2 Signal intensities of different water populations in as prepared and isopropanol exchanged pastes normalised to ignited paste mass and 'as prepared' paste with H_2O.

Sample	I_{sol}	I_{CSH}	I_{gel}	$I_{Int\text{-}hyd}$	I_{cap}	I_{tot}
as prepared H_2O	0.24	0.21	0.44	0.08	0.03	1.00
+ IPA	0.24	0.18	0.16	0.11	0.28	0.97
+ IPA + H_2O back exchanged	0.21	0.18	0.37	0.10	0.11	0.97
as prepared D_2O	0.01	0.01	0.03	0.00	0.02	0.07
+ H_2O	0.21	0.18	0.40	0.09	0.10	0.98
+ IPA(D)	0.02	0.11		0.06	0.24	0.43
+IPA	0.18	0.11	0.14	0.13	0.15	0.71

The expected capillary liquid fraction can be calculated. Assuming that 0.38 gram of water are required to fully hydrate 1 gram of cement [28] and taking the water to cement ratio at the mixing time (w/c_{mix} = 0.46), then there are 0.08 cm^3 of water available to create interhydrate and capillary pores at full cement hydration (α = 100%). Additionally, the chemical shrinkage creates the voids accessible to isopropanol in the amount of $0.075 \cdot \alpha$ g/cm^3 of anhydrous cement[28]. Therefore, there is 0.155 cm^3 of capillary porosity at full hydration, or 29% of the total liquid volume. However, considering that paste did not reach the full hydration, the realistic degree of hydration (α = 85%) leads to capillary liquid volume 0.201 cm^3 and fraction of 38%. This is in very good agreement with the sum of interhydrate and capillary liquid intensity in the isopropanol exchanged paste (39%).

[28] defined by Arnaud Muller and presented in [128]

The changes in gel pore intensity upon isopropanol exchange can be explained as the isopropanol draws water out of gel pores but cannot itself get into the smaller gel pores. That isopropanol only fills the bigger gel pores are evidenced by longer T_2 of gel liquid and the fact that the isopropanol has a molecular size too big to access the smaller gel pores. Considering that the solvent do not enter smaller gel pores and that the intensity of the C-S-H interlayer is changed minimally, the water in the interlayer spaces is not replaced by isopropanol.

7.2.2. Deuterated cement paste

In order to distinguish which pores are filled by water and which by isopropanol the exchange experiments were repeated on the samples made with D_2O.

The as prepared D_2O paste shows negligible signal (4^{th} line in table 7.2). The minimal signal present is caused by hydrogen-deuterium (Hyd-D) exchange during sample preparation and curing. When deuterated paste is exchanged with H_2O the signals from the original water populations are recorded (1^{st} and 5^{th} line in table 7.2). The recovery of chemically combined water signal suggests that the solid phases have high SSA, enabling Hyd-D chemical exchange, and hence they exist in nanocrystalline forms. The solid, C-S-H interlayer and gel water intensities are slightly lower than for as prepared H_2O paste. However, the total interhydrate and capillary intensity is almost double. This suggests that the paste prepared with D_2O hydrates more slowly than that with H_2O, as already reported [127]. It is further evidenced as the T_2 relaxation times of gel, interhydrate and capillary water, and hence pore sizes, are bigger for deuterated paste (375 μs, 2.6 and 15.5 ms against 300 μs, 1.0 and 4 ms).

The partially deuterated isopropanol, $(CH_3)_2CDOD$, was used to register only the isopropanol – water molecular exchange and to prevent the Hyd-D chemical exchange (as the hydrogens likely to undergo such exchange are deuterated). The analysis (6^{th} line in table 7.2) shows the minimal chemically combined signal – in contrast to H_2O replacement, proving that the Hyd-D chemical exchange did not occur. The modest signal was obtained from C-S-H gel (11%). It is assumed to originate from the isopropanol entering the larger gel pores. Results can be compared with solvent replaced H_2O paste by multiplying by 8/6 (number of Hyd in isopropanol by number of Hyd in deuterated isopropanol). The multiplication yields 15% of intensity for C-S-H gel water which is in good agreement with the gel intensity for H_2O paste exchanged with isopropanol (16%). This strongly suggests that isopropanol molecules do not replace water within C-S-H interlayer spaces and demonstrates the connectivity of C-S-H gel pore network with larger interhydrate and capillary pores. The total signal intensity acquired from interhydrate and capillary liquid is equalled to 30%. Multiplication gives 40% which is also closed to 39% for H_2O paste.

The deuterated paste was also exchanged with regular isopropanol (7^{th} line in table 7.2). The analysis shows that signals recover hugely for all population demonstrating both isopropanol – water molecular and Hyd-D chemical exchange processes. The increase in chemically combined and interlayer intensities indicates the appearance of Hyd-D chemical exchanged as now all hydrogens sites are protonated. However, these intensities do not reach the intensity levels of H_2O paste suggesting that the chemical exchange is not yet completed.

The gel intensity is slightly smaller than for solvent replaced H_2O paste (14% -16%). However the larger pores are not yet filled to the same level (28% - 39%).

7.2.3. Time dependency of exchange

The full equilibration of the solvent replacement is a very slow process for the large cement paste samples. Figure 7.6 presents how the combined signal intensities of liquids in capillary and interhydrate and in C-S-H interlayer and gel pores change over exchange time for white cement paste mixed at w/c_{mix} = 0.4 and cured underwater. The measured sample had length and diameter of 8 mm. This size is considerably bigger in comparison with millimetre pieces of paste measured in previous sections when the exchange occurred after 3 days.

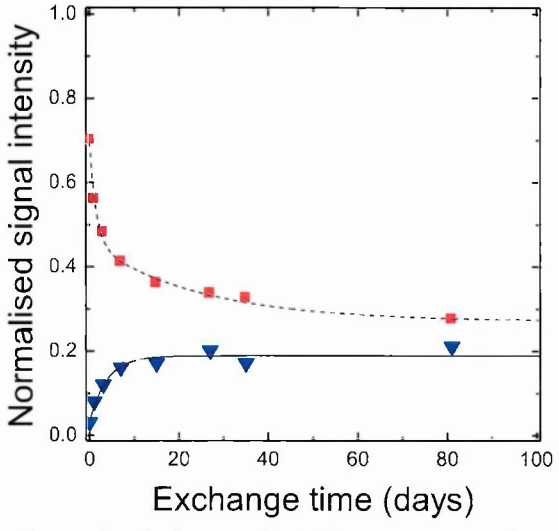

Figure 7.6 The increase of sum interhydrate and capillary pore water intensity (blue triangles) and decrease of sum C-S-H interlayer and gel pore water intensity (red squares) for isopropanol exchange of large paste sample. The lines are the exponential fits – solid with one and dashed with two components.

The sum interhydrate and capillary intensity increases significantly from ~3 to 20% showing again that even though the sample is cure underwater many of large pores are not filled with water. The calculated fraction of capillary water, as presented in section 7.3.1, for fully hydration paste in that case is 20%. The exchange was performed on 6 month old sample, the hydration is almost completed (definitely over 90% as shown for 90 days old paste in section 6.6.1). Hence, experimental and estimated fractions are in good agreement.

The decrease of combined fraction of C-S-H interlayer and gel liquid (from ~70% to 27%) again suggests that isopropanol draws water out of C-S-H gel but not replace it to the same extend. The exponential fits yield the time constant of the signals changes. The capillary pores are filled by isopropanol with a time constant of about 4 days for the 8 mm sample. Water is drawn out from gel pores within 1.5 days. The longest process (25 days) is surprisingly the equilibration of water within interlayer spaces and on the surface of gel pores which appears interlayer-like during drying. The full equilibration of solvent exchange in sample of larger, centimetre size takes about two months.

8. Summary / Conclusion

It has been shown in this thesis that NMR Relaxometry provides a great level of valuable information concerning cement microstructure as a function of hydration time, temperature, relative humidity and mix composition. Furthermore, better insight into pore-water interactions in cementitious materials was obtained.

It was shown that NMR experiments are quantitative. The linear dependence of total signal intensity with sample mass during drying proved that NMR senses all water within samples. The origin of the solid Quad Echo signal was verified by thermogravimetric analysis and X-ray diffraction. The signal arises entirely from Portlandite and ettringite, and does not comprise any contribution from C-S-H. Five distinct NMR hydrogen populations were observed and assigned as chemically combined water, C-S-H interlayer, gel and interhydrate pore water and finally water in larger capillary pores and cracks.

8.1. Sorption isotherm

The NMR Relaxometry has revealed the first pore-type resolved sorption isotherm of any cementitious material. Such an isotherm facilitates the assessment of porosity types that are dried or filled at different humidity conditions. The striking feature of the data is the re-assignment of the NMR signal of the surface water layer remaining in gel pores during drying to the C-S-H interlayer water signal. The results allow an interpretation of the way the pores empty during desorption and fill during adsorption branches. Six stages of desorption process were identified. It was observed that drying progresses through the removal of the bulk pore water with a water layer remaining at the pore surfaces. For adsorption the results suggests refilling of gel pores layer by layer. The results allow schematic presentation of the C-S-H morphology. It is similar to the picture of C-S-H proposed by Feldman and Sereda [38] and consistent with interpretation of their model.

Pore sizes in 'as prepared' cement paste were independently calculated based on the T_2 relaxation times in accordance with fast exchange model of relaxation and based on the rate of signal amplitude loss during drying. The relaxation time model gives the C-S-H interlayer spacing of 0.94 ± 0.04 nm and gel pore size of 3.1 ± 0.2 nm. The value of gel pore size obtained by amplitude model from primary desorption branch is higher - 4.5 ± 1.6 nm, but close to that obtained by McDonald *et al* [18]. The amplitude model gives the 1.5 ± 0.3 nm for C-S-H interlayer pore size. That is larger than expected and than the value from the relaxation model calculation. It is attributed to the breakdown of the drying model assumptions in small interlayer space.

The specific surface area was calculated by three means: BET theory; fast exchange model of relaxation; and amplitude model. The amplitude model gives systematically lower values in comparison with the other two methods. This is explained by the high sensitivity of SSA analysis on pore size and attributed to the higher size of C-S-H interlayer pores than expected. The total specific surface area evaluated based on mass and intensity BET fits and on relaxation times yields close values of 130 ± 5, 144 ± 24 and 157 ± 9 m^2/g of dried paste (3%

RH) respectively. These values were shown to be relatively close to previous estimates by Baroghel-Bouny [114] and by Powers and Brownyard [32] but lower than that measurements by Halperin *et al* [10]. The analysis allows differentiation of SSA between C-S-H interlayer and gel pores. Given the pore widths from fast exchange model, the specific surface areas are 91 ± 4 m^2/cm^3 of paste for gel pores and 175 ± 12 m^2/cm^3 for C-S-H interlayer pores.

8.2. Influence of curing temperature on cement microstructure

The quantitative NMR data lead to a full description of cement paste and C-S-H characteristics. The density, Ca/(Si+Al) ratio and water content of C-S-H were measured in never dry white cement pastes using NMR Relaxometry supported by TGA and XRD analysis. The NMR evaluated C-S-H 'solid' and 'bulk' densities in cement paste cured at 20°C for 28 days are 2.64 ± 0.03 g/cm^3 and 1.90 ± 0.02 g/cm^3. The values of C-S-H 'solid' density are at the upper end of earlier estimates by helium piknometry [28], [75], [76] but are in good agreement with the well cited measurement using SANS by Jennings [7]. The 'bulk' density is close to the CM-II model value [6] and that measured by Young and Hansen [72].

Changes of curing temperature cause important alteration to the C-S-H characteristics and cement paste. With increase of curing temperature the increase of both C-S-H 'solid' and 'bulk' densities was revealed with accompanying decrease in C-S-H water content. It was interpreted as evidence for fewer locally stacked calcium silicate layers and further explained by a slightly lower amount of the gel pore water at the elevated temperature. The increase of C-S-H 'bulk' density and decline of water content with temperature was also observed by Galluci *et al* [109]. The calcium and silicon content remain constant despite the changes in curing temperatures. The cement paste composition is affected. An increase of curing temperature accelerates cement hydration and growth of hydrates. Pastes cured at higher temperature are 'more' hydrated. At mature age, they are characterised by larger capillary porosity, greater amount of C-S-H phase and lower content of ettringite and gel pores.

The combined results of the desorption and C-S-H composition studies allowed the creation of the C-S-H 'solid' and 'bulk' water content desorption isotherm that can be evaluated to define the C-S-H composition at various humidities. In particular water content at 10% RH is measured as 2.11 moles/mole of C-S-H. It is in agreement with values at 11% RH reported by Jennings [6], Feldman and Ramachandran [73] and Young and Hansen [72].

^{1}H NMR Relaxometry enabled determination of the evolution of the nanoscale porosity for white cement pastes and comparison between pastes with and without addition of silica fume, cured at different temperatures. In general, with the hydration time, the consumption of interhydrate/capillary pore water and the development of three water populations (chemically combined water within crystalline phases; and water in interlayer spaces and gel pores of C-S-H) were registered. For white cement paste the amount of chemically combined water and C-S-H interlayer water increase continuously in course of hydration. Initially the content of gel pore water increases more rapidly and later becomes approximately constant (after ~4 days at 20°C). The observation of two nanoscale pore types intrinsic to the C-S-H is distinctive in comparison with Jennings' CM-II model [6] that identifies four populations:

interlayer spaces; intra-globular pores; small pores between globules (SGP) and large pores between globule flocs (LGP). The gel pores as measured in this thesis are comparable in size with SGP while the interhydrate size is in the range of the LGP size. However, as the latter is consumed in the hydration process, it is not treated as part of C-S-H structure in this study.

The evolution of NMR signals for white cement paste with silica fume shows the formation of C-S-H due to pozzolanic reaction of silica fume with CH and acceleration of hydration due to silica fume filler effect. The major influence of silica fume is observed in the reduced amount of chemically combined water and much higher of gel pore water in comparison with plain white cement paste. The maximum gel pore water content for paste cured at 20°C appears earlier than for plain white cement, already at ~20h, and coincidental in time with the change in capillary water consumption and stability of interhydrate pore size. In mature pastes with silica fume considerably higher capillary porosity is seen. However the sizes of C-S-H interlayer, gel and interhydrate/capillary pores are very similar as for plain cement paste. The investigation of SF pastes with increase of curing temperature reveals more complex hydration behaviour as there are two factors contributing: the C-S-H is created due to silicates reaction with water and silica fume reaction with CH.

8.3. Activation energy of water dynamic

The activation energy for water relaxation processes in C-S-H interlayer, gel, interhydrate and capillary pores was determinate based on T_1 relaxation time measurements. The prior verification of acquired data for water against literature and the linear increase of total signal intensity with increase in $1/T$ gave the confidence in obtained results.

It is observed that the activation energy decreases with confinement of space to the certain pore size / T_1 level at which it may go through a minimum and after which the energy reaches higher values for water within even smaller spaces. The results suggest that the translational and rotational motion of spins has higher activation energy than the surface diffusion. The increase of activation energy for interlayer water may reflect that the relaxation model breaks down in such a small space. Otherwise the activation energy and mechanism of spin relaxation in cement paste pores may be explained as an effect of balance between surface diffusion and rotational-translation interactions.

8.4. Water - isopropanol exchange

NMR relaxation analysis was performed to assess the mechanism of water-isopropanol replacement method used for arresting cement hydration. The results showed that water-isopropanol exchange essentially do not alter the water within the C-S-H interlayer spaces. However, isopropanol draws water out of C-S-H gel pores and refill the bigger, more accessible amongst them. It invades the interhydrate and capillary pores giving significantly higher intensity than in 'as prepared' paste. That suggests the presence of the large capillary pores in cement paste that are inaccessible to water and explains the lower capillary porosity recorded by NMR than expected from Powers and Brownyard model [32], [34].

The connectivity of C-S-H gel pore network with larger interhydrate and capillary pores was revealed through the exchange of deuterated paste with deuterated isopropanol. It also demonstrated that isopropanol molecules do not enter the C-S-H interlayer spaces and do not replace water within those spaces. Furthermore, the chemical exchange between deuterons and protons proves experimentally for the first time the interconnectivity of C-S-H interlayer and gel pores with interhydrate and capillary pores.

8.5. FUTURE WORK

It has been shown in this thesis that NMR relaxometry is an excellent source of valuable information about cement microstructures, especially C-S-H, and water within them. The NMR relaxometry opens the door to a routine way of cementitious materials characterisation needed by researchers and industry to rapidly describe novel cements. Nevertheless there are several factors to consider in context of making NMR the routine test. In particular NMR laboratories use different variants of pulse sequence; perform the experiments by using spectrometers with different operating characteristics; and analyse the data following different protocols. Additional level of variation arises from the examined samples themselves: their sizes; geometry; preparation; and curing conditions. All these make the comparison between different NMR laboratories and instruments difficult and the interpretation of results complex. The need to standardise the NMR characterisation of cementitious materials was identified. The project with aim to fulfil that gap and define, validate and disseminate the appropriate protocols for NMR measurements and analysis has already begun in collaboration between University of Surrey and National Physical Laboratory.

The research presented in this thesis could be complemented and extended in many aspects. The possible extensions are: examination of the influence of curing temperature on the C-S-H characteristics for cement paste with addition of silica fume; calculation of the pore sizes for cement paste with silica fume; deeper investigation of empty capillary pores etc.

The other proposition could be examination of the activation energy for water relaxation at younger pastes ages. Nevertheless the activation energy results are surprising and at first the deeper understanding of the experimentally yielded values of activation energy and their behaviour with the decrease of pore size is required. Ongoing Molecular Dynamics and Monte Carlo simulation studies of relaxation in small pores of calcium silicate hydrates by Serge Henri Cachia and Nicholas Howlett may help to clarify the results.

Other areas for further studies includes: a re-evaluation of T_2-T_2 experiments in the light of this work and of the simulations of Serge Henri Cachia and Nicholas Howlett; and further investigation of the lateral extend of C-S-H pores using double quantum and diffusion methods. In a wider aspect the next important stage is to create the link between the resultant information and knowledge gained from this thesis and the properties of cementitious materials and concrete structures.

Appendixes

Appendix 1:

A.C.A. Muller, K. L. Scrivener, A. M. Gajewicz, P. J. McDonald, "Use of bench-top NMR to measure the density, composition and desorption isotherm of C-S-H in cement paste", *Microporous and Mesoporous Materials*, vol. 178, pp. 99-103, 2013

Appendix 2:

R. M. Kowalczyk, A. M. Gajewicz, P. J. McDonald, "The mechanism of water-isopropanol exchange in cement pastes evidenced by NMR relaxometry", *RSC Advances*, vol. 4, pp. 20709-20715, 2014

Appendix 3:

A.C.A. Muller, K. L. Scrivener, A. M. Gajewicz, P. J. McDonald, "Densification of C-S-H measured by ^{1}H NMR Relaxometry," *The Journal of Physical Chemistry C*, vol. 117, pp. 403–412, 2013

MATERIAL REDACTED AT REQUEST OF UNIVERSITY

Bibliography

[1] "World Business Council for Sustainable Development, Cement Sustainability Initiative, http://www.wbcsdcement.org," 2014.

[2] K. L. Scrivener, "Introduction : basic concepts." 1st Marie-Curie RTN training course, Denmark, 2006.

[3] J.-P. Mercier, G. Zambelli, and W. Kurz, *Introduction à la science des matériaux*. Lausanne: Presses Polytechniques et Universitaires Romandes, 1999.

[4] H. G. van Oss, "U. S. Geological Survey, Mineral Commodity Summaries," 2014.

[5] I. G. Richardson, "The calcium silicate hydrates," *Cem. Concr. Res.*, vol. 38, pp. 137–158, 2008.

[6] H. M. Jennings, "Refinements to colloid model of C-S-H in cement: CM-II," *Cem. Concr. Res.*, vol. 38, no. 3, pp. 275–289, 2008.

[7] A. J. Allen, J. J. Thomas, and H. M. Jennings, "Composition and density of nanoscale calcium-silicate-hydrate in cement," *Nat. Mater.*, vol. 6, pp. 311–316, 2007.

[8] A. Muller, K. L. Scrivener, and P. J. McDonald, "Porosity characterisation across different binders by a multi-technic approach." Poster on 2nd Official Transcend Meeting, Morges, 2012.

[9] "MC ITN TRANSCEND http://www.nanocem.org/index.php?id=282," 2014.

[10] W. P. Halperin, J. Y. Jehng, and Y.-Q. Song, "Application of spin-spin relaxation to measurement of surface area and pore size distributions in a hydrating cement paste," *Magn. Reson. Imaging*, vol. 14, pp. 169–173, 1994.

[11] P. D. M. Hughes, "A study of water transport in zeolite 4A powder beds and sodium silicate films using broadline Magnetic Resonance Imaging; PhD thesis," University of Surrey, 1996.

[12] M. Fleury, S. Gautier, F. Norrant, and E. Kohler, "Characterisation of Nanoporous Systems with Low Field NMR: Application to Kaolinite and Smectite Clays," in *International Symposium of the Society of Core Analysts*, 2011, pp. 1–12.

[13] F. Jaeger, A. Shchegolikhina, H. Van As, and G. E. Schaumann, "Proton NMR Relaxometry as a Useful Tool to Evaluate Swelling Processes in Peat Soils," *Open Magn. Reson. J.*, pp. 27–45, 2010.

[14] D. V. Ellis and J. M. Singer, *Well Logging for Earth Scientists*. Dordrecht: Springer, 2008.

[15] V. Baukh, H. P. Huinink, O. C. G. Adan, S. J. F. Erich, and L. G. J. van der Ven, "Water-Polymer Interaction during Water Uptake," *Macromolecules*, vol. 44, pp. 4863–4871, 2011.

[16] H. C. Bertram, S. B. Engelsen, H. Busk, A. H. Karlsson, and H. J. Andersen, "Water properties during cooking of pork studied by low-field NMR relaxation: effects of curing and the RN⁻-gene," *Meat Sci.*, vol. 66, pp. 437–46, 2004.

[17] M. Jones, "Mobile nuclear magnetic resonance characterisation of water distribution and movement in living trees and felled timber; PhD thesis," University of Surrey, 2012.

[18] R. Blinc, M. Burgar, G. Lahajnar, M. Rozmarin, V. Rutar, I. Kocuvan, and J. Ursic, "NMR Relaxation Study of Adsorbed Water in Cement and C_3S Pastes," *J. Am. Ceram. Soc.*, vol. 61, pp. 35–37, 1978.

[19] L. J. Schreiner, J. C. Mactavish, L. Miljkovic, M. M. Pintar, R. Blinc, G. Lahajnar, D. Lasic, and L. W. Reever, "NMR line shape-spin-lattice relaxation correlation study of Portland cement hydration," *J. Am. Ceram. Soc.*, vol. 68, pp. 10–16, 1985.

[20] D. D. Lasic, J. M. Corbett, J. Jian, J. C. MacTavish, M. M. Pintar, R. Blinc, and G. Lahajnar, "NMR Spin Grouping in Hydrating Cement at 200 MHz," *Cem. Concr. Res.*, vol. 18, pp. 649–653, 1988.

[21] L. Miljkovict, D. Lasic, J. C. Mactavish, M. M. Pintar, R. Blinc, and G. Lahajnar, "NMR study of hydrating cement: A spin-spin study of the early hydration stage," *Cem. Concr. Res.*, vol. 18, pp. 951–956, 1988.

[22] A. J. Bohris, U. Goerk, P. J. McDonald, M. Mulheron, B. Newling, and B. L. E. Page, "A Broad Line NMR and MRI Study of Water and Water Transport in Portland Cement Pastes," *Magn. Reson. Imaging*, vol. 16, pp. 455–461, 1998.

[23] A. Plassais, M.-P. Pomiès, N. Lequeux, P. Boch, J.-P. Korb, and D. Petit, "Micropore size analysis in hydrated cement paste by NMR," *C. R. Acad. Sci. Paris, Chim. / Chem. 4*, vol. 4, pp. 805–808, 2001.

[24] J. Greener, H. Peemoeller, C. Choi, R. Holly, E. J. Reardon, C. M. Hansson, and M. M. Pintar, "Monitoring of Hydration of White Cement Paste with Proton NMR Spin–Spin Relaxation," *J. Am. Ceram. Soc.*, vol. 83, pp. 623–627, 2000.

[25] R. Holly, E. J. Reardon, C. M. Hansson, and H. Peemoeller, "Proton Spin-Spin Relaxation Study of the Effect of Temperature on White Cement Hydration," *J. Am. Ceram. Soc.*, vol. 90, pp. 570–577, 2007.

[26] P. J. McDonald, V. Rodin, and A. Valori, "Characterisation of intra- and inter-C–S–H gel pore water in white cement based on an analysis of NMR signal amplitudes as a function of water content," *Cem. Concr. Res.*, vol. 40, pp. 1656–1663, 2010.

[27] F. D. Orazio, S. Bhattacharja, and W. P. Halperin, "Molecular diffusion and nuclear-magnetic-resonance relaxation of water in unsaturated porous silica glass," *Phys. Rev. B*, vol. 42, pp. 9810–9818, 1990.

[28] H. F. W. Taylor, *Cement chemistry*. London: Academic Press Limited, 1990.

[29] K. L. Scrivener, "Hydration and Microstructure." 1st Marie-Curie ITN training course, Maastricht, 2011.

[30] J. W. Bullard, H. M. Jennings, R. A. Livingston, A. Nonat, G. W. Scherer, J. S. Schweitzer, K. L. Scrivener, and J. J. Thomas, "Mechanisms of cement hydration," *Cem. Concr. Res.*, vol. 41, pp. 1208–1223, 2011.

[31] K. L. Scrivener, "Backscattered electron imaging of cementitious microstructures: understanding and quantification," *Cem. Concr. Compos.*, vol. 26, pp. 935–945, 2004.

[32] T. C. Powers and T. L. Brownyard, "Studies of the Physical Properties of Hardened Portland Cement Paste Part 3. Theoretical Interpretation of adsorption Data," *J. Am. Concr. Inst.*, vol. 18, pp. 469–504, 1946.

[33] T. C. Powers and T. L. Brownyard, "Studies of the Physical Properties of Hardened Portland Cement Paste Part 9. General Summary of Findings on the Properties of Hardened portland Cement Paste," *J. Am. Concr. Inst.*, vol. 18, pp. 971–992, 1947.

[34] T. C. Hansen, "Physical structure of hardened cement paste. A classical approach," *Mater. Constr.*, vol. 19, pp. 423–436, 1986.

[35] P. K. Mehta and P. J. M. Monteiro, *Concrete Structure, Properties and Materials*. New Jersey: Prentice-Hall, 1993.

[36] T. C. Powers, "Structure and Physical Properties of Hardened Portland Cement Paste," *J. Am. Ceram. Soc.*, vol. 41, pp. 1–6, 1958.

[37] O. M. Jensen, "Powers' model." Lecture COE Hokkaido University, 2005.

[38] R. F. Feldman and P. J. Sereda, "A model for hydrated portland cement paste as deduced from sorption- length change and mechanical properties," *Mater. Constr.*, vol. 1, pp. 509–520, 1968.

[39] R. F. Feldman and P. J. Sereda, "A New Model for Hydrated Portland Cement and its Practical Implications," *Eng. J.*, vol. 53, pp. 53–59, 1970.

[40] H. M. Jennings, "A model for the microstructure of calcium silicate hydrate in cement paste," *Cem. Concr. Res.*, vol. 30, pp. 101–116, 2000.

[41] P. D. Tennis and H. M. Jennings, "A model for two types of calcium silicate hydrate in the microstructure of Portland cement pastes," *Cem. Concr. Res.*, vol. 30, pp. 855–863, 2000.

[42] J. J. Thomas, H. M. Jennings, and A. J. Allen, "The surface area of hardened cement paste as measured by various techniques," *Concr. Sci. Eng.*, vol. 1, pp. 45–64, 1999.

[43] X. Cong and R. J. Kirkpatrick, "^{29}Si MAS NMR Study of the Structure of Calcium Silicate Hydrate," *Adv. Cem. Based Mater.*, vol. 3, pp. 144–156, 1996.

[44] S. Grangeon, F. Claret, C. Lerouge, F. Warmont, T. Sato, S. Anraku, C. Numako, Y. Linard, and B. Lanson, "On the nature of structural disorder in calcium silicate hydrates with a calcium/silicon ratio similar to tobermorite," *Cem. Concr. Res.*, vol. 52, pp. 31–37, Oct. 2013.

[45] J. J. Chen, J. J. Thomas, H. F. W. Taylor, and H. M. Jennings, "Solubility and structure of calcium silicate hydrate," *Cem. Concr. Res.*, vol. 34, pp. 1499–1519, 2004.

[46] T. Maeshima, H. Noma, M. Sakiyama, and T. Mitsuda, "Natural 1.1 and 1.4 nm tobermorites from Fuka, Okayama, Japan: Chemical analysis, cell dimensions, ^{29}Si NMR and thermal behavior," *Cem. Concr. Res.*, vol. 33, pp. 1515–1523, 2003.

[47] I. G. Richardson, "The nature of C-S-H in hardened cements," *Cem. Concr. Res.*, vol. 29, pp. 1131–1147, 1999.

[48] M. Geiker, "Porosity development and moisture fixation, mechanisms." 1st Marie-Curie ITN training course, Maastricht, 2011.

[49] *CEB - Design Guide - Durable concrete structures. Chapter 2.* London: Thomas Telford Services Ltd, 1992.

[50] *Manual of Symbols and Terminology for Physicochemical Quantities and Units - Appendix II Definitions, Terminology and Symbols in Colloid and Surface Chemistry - Part I.* prepared for publication by D. H. Everett, London: International Union of Pure and Applied Chemistry - Devision of Physical Chemistry, 1971.

[51] M. Geiker, "Porosity and water fixation; characterization." 1st Marie-Curie ITN training course, Maastricht, 2011.

[52] M. Petri, "Metody badan porowatosci," in *Materialy Budowlane Podstawy technologii i metody badan*, J. Malolepszy, Ed. Krakow: AGH Uczelniane Wydawnictwo Naukowo Dydaktyczne, 2008, pp. 270–277.

[53] S. Diamond, "Mercury porosimetry an inappropriate method for the measurement of pore size distributions in cement-based materials," *Cem. Concr. Res.*, vol. 30, pp. 1517–1525, 2000.

[54] E. W. Washburn, "The Dynamics of Capillary Flow," *Phys. Rev.*, vol. 17, pp. 273–283, 1921.

[55] R. A. Cook and K. C. Hover, "Mercury porosimetry of hardened cement pastes," *Cem. Concr. Res.*, vol. 29, pp. 933–943, 1999.

[56] C. Gallé, "Effect of drying on cement-based materials pore structure as identified by mercury intrusion porosimetry A comparative study between oven-, vacuum-, and freeze-drying," *Cem. Concr. Res.*, vol. 31, pp. 1467–1477, 2001.

[57] R. A. Cook and K. C. Hover, "Mercury porosimetry of cement-based materials and associated correction factors," *Constr. Build. Mater.*, vol. 7, pp. 231–240, 1993.

[58] K. L. Scrivener and E. Gallucci, "Microstructural Characterisation Methods for Cementitious Materials." 1st Marie-Curie ITN training course, Maastricht, 2011.

[59] L. Wadsö, "Sorption I." 3rd Marie-Curie ITN training course, Lund, 2011.

[60] S. Brunauer, P. H. Emmett, and E. Teller, "Adsorption of Gases in Multimolecular Layers," *J. Am. Chem. Soc.*, vol. 60, pp. 309–319, 1938.

[61] L. Wadsö, "Capillarity," no. July. 3rd Marie-Curie ITN training course, Lund, 2011.

[62] G. G. Litvan, "Variability of the Nitrogen Surface Area of Hydrated Cement Paste," *Cem. Concr. Res.*, vol. 6, pp. 139–143, 1976.

[63] A. M. Kjeldsen and M. Geiker, "On the interpretation of low temperature calorimetry data," *Mater. Struct.*, vol. 41, pp. 213–224, 2007.

[64] Z. Sun and G. W. Scherer, "Pore size and shape in mortar by thermoporometry," *Cem. Concr. Res.*, vol. 40, pp. 740–751, 2010.

[65] D. P. Bentz, "NISTIR 7267 Low Temperature Calorimetry Studies of Hydrating Portland Cement Pastes," *Natl. Inst. Stand. Technol.*, pp. 1–125, 2005.

[66] A. J. Allen and J. J. Thomas, "Analysis of C–S–H gel and cement paste by small-angle neutron scattering," *Cem. Concr. Res.*, vol. 37, pp. 319–324, 2007.

[67] H. F. W. Taylor, "Hydrated Calcium Silicates. Part I. Compound Formation at Ordinary Temperatures.," *J. Chem. Soc.*, pp. 3682–3690, 1950.

[68] W. Kurdowski, "Faza C-S-H – stan zagadnienia. Część 1; C-S-H – state of art. Part 1," *Cem. Wapno Bet.*, vol. 4, pp. 216–222, 2008.

[69] A. Nonat, "The structure and stoichiometry of C-S-H," *Cem. Concr. Res.*, vol. 34, pp. 1521–1528, Sep. 2004.

[70] D. L. Rayment and A. J. Majumdar, "The composition of the C-S-H phases in portland cement pastes," *Cem. Concr. Res.*, vol. 12, pp. 753–764, 1982.

[71] I. G. Richardson, "Tobermorite/jennite- and tobermorite/calcium hydroxide-based models for the structure of C-S-H: applicability to hardened pastes of tricalcium silicate, β-dicalcium silicate, Portland cement, and blends of Portland cement with blast-furnace slag, metakaol," *Cem. Concr. Res.*, vol. 34, pp. 1733–1777, 2004.

[72] J. F. Young and W. Hansen, "Volume Relationships for C-S-H Formation Based on Hydration Stoichiometries," *Mater. Res. Soc. Proc.*, vol. 85, pp. 313–321, 1986.

[73] R. F. Feldman and V. S. Ramachandran, "A Study of the State of Water and Stoichiometry of Bottle Hydrated Ca_3SiO_5," vol. 4, pp. 155–166, 1974.

[74] J. J. Chen, "The Nanostructure of Calcium Silicate Hydrate; PhD thesis," Chapter 2.3, Northwestern University, 2003.

[75] R. F. Feldman, "Helium Flow and Density Measurement of the Hydrated Triclcium Silicate - Water System," *Cem. Concr. Res.*, vol. 2, pp. 123–136, 1972.

[76] R. F. Feldman, "Density and porosity studies of hydrated portland cement," *Cem. Technol.*, vol. 3, pp. 5–14, 1972.

[77] B. Blümich, *Essential NMR for Scientists and Engineers*. Springer, 2005.

[78] R. H. Harris, *Nuclear Magnetic Resonance Spectroscopy*. London: Longman, 1986.

[79] P. T. Callaghan, *Principles of Nuclear Magnetic Resonance Microscopy*. Oxford Science Publications, 2011.

[80] B. Cowan, *Nuclear Magnetic Resonance and Relaxation*. Cambridge University Press, 1997.

[81] T. C. Farrer and E. D. Becker, *Pulse and Fourier Transform NMR Introduction to Theory and Methods*. New York - London: Academic Press, 1971.

[82] A. Valori, P. J. McDonald, and K. L. Scrivener, "The morphology of C–S–H: Lessons from ^{1}H nuclear magnetic resonance relaxometry," *Cem. Concr. Res.*, vol. 49, pp. 65–81, 2013.

[83] E. L. Hahn, "Spin echoes," *Phys. Rev.*, vol. 80, p. 580–, 1950.

[84] H. Y. Carr and E. M. Purcell, "Effects of Diffusion on Free Preession in Nuclear Magnetic Resonance Experiments," *Phys. Rev.*, vol. 94, pp. 630–638, 1954.

[85] S. Meiboom and D. Gill, "Modified Spin-Echo Method for Measuring Nuclear Relaxation Times," *Rev. Sci. Instrum.*, vol. 29, pp. 688–691, 1958.

[86] J. G. Powles and J. H. Strange, "Zero Time Resolution Nuclear Magnetic Resonance Transient in Solids," *Proceedings of the Physical Society*, vol. 82, pp. 6–15, 1963.

[87] N. Boden and M. Mortimer, "An NMR 'Solid' Echo Experiment for the Direct Measurement of the Dipolar Interaction Between Spin-1/2 Pairs in Solid," vol. 21, pp. 538–540, 1973.

[88] A. Abragam, *Principles of Nuclear Magnetism*. New York: Oxford University Press, 1961.

[89] N. Bloembergen, E. M. Purcell, and R. V. Pound, "Relaxation Effects in Nuclear Magnetic Resonance Absorption," *Phys. Rev.*, vol. 73, pp. 679–712, 1948.

[90] D. A. Faux, P. J. McDonald, N. C. Howlett, J. S. Bhatt, and S. V. Churakov, "Nuclear magnetic resonance relaxometry of water in two- and quasi-two-dimensions," *Phys. Rev. E - Stat. Nonlinear, Soft Matter Phys.*, vol. 87, pp. 062309–1–18, 2013.

[91] J.-P. Korb, M. Whaley-Hodges, and R. G. Bryant, "Translational diffusion of liquids at surfaces of microporous materials: Theoretical analysis of field-cycling magnetic relaxation measurements," vol. 56, pp. 1934–1945, 1997.

[92] P. J. McDonald, J.-P. Korb, J. Mitchell, and L. Monteilhet, "Surface relaxation and chemical exchange in hydrating cement pastes: a two-dimensional NMR relaxation study," *Phys. Rev. E. Stat. Nonlin. Soft Matter Phys.*, vol. 72, pp. 011409–1–9, 2005.

[93] J.-P. Korb, M. Whaley-Hodges, and R. Bryant, "Translational Diffusion of Liquids at Surface of Microporous materials: New Theoretical Analysis of Field Cycling Magnetic Relaxation Measurements," *Magn. Reson. Imaging*, vol. 16, pp. 575–578, 1998.

[94] P. J. McDonald, J. Mitchell, M. Mulheron, P. S. Aptaker, J.-P. Korb, and L. Monteilhet, "Two-dimensional correlation relaxometry studies of cement pastes performed using a new one-sided NMR magnet," *Cem. Concr. Res.*, vol. 37, pp. 303–309, 2007.

[95] L. Monteilhet, J.-P. Korb, J. Mitchell, and P. J. McDonald, "Observation of exchange of micropore water in cement pastes by two-dimensional T_2-T_2 nuclear magnetic resonance relaxometry," *Phys. Rev. E*, vol. 74, pp. 061404–1–9, 2006.

[96] H. Peemoeller, R. K. Shenoy, and M. M. Pintar, "Two-dimensional NMR time evolution correlation spectroscopy in wet lysozyme," *J. Magn. Reson.*, vol. 45, pp. 193–204, Nov. 1981.

[97] L. Venkataramanan, Y.-Q. Song, and M. D. Hurlimann, "Solving Fredholm integrals of the first kind with tensor product structure in 2 and 2.5 dimensions," *IEEE Trans. Signal Process.*, vol. 50, no. 5, pp. 1017–1026, 2002.

[98] A. Valori, P. J. McDonald, and V. Rodin, "On the interpretation of ^{1}H 2-dimensional NMR relaxation exchange spectra in cements: is there exchange between pores with two characteristic sizes or Fe^{3+} concentrations?," *Cem. Concr. Res.*, vol. 40, pp. 1375–1377, 2010.

[99] F. Barberon, J.-P. Korb, D. Petit, V. Morin, and E. Bermejo, "Probing the Surface Area of a Cement-Based Material by Nuclear Magnetic Relaxation Dispersion," *Phys. Rev. Lett.*, vol. 90, pp. 116103–1–4, 2003.

[100] J.-P. Korb, P. J. McDonald, L. Monteilhet, A. G. Kalinichev, and R. J. Kirkpatrick, "Comparison of proton field-cycling relaxometry and molecular dynamics simulations for proton–water surface dynamics in cement-based materials," *Cem. Concr. Res.*, vol. 37, pp. 348–350, 2007.

[101] S. Bhattacharja, M. Moukwa, F. D'Orazio, J.-Y. Jehn, and W. P. Halperin, "Microstructure Determination of Cement Pastes by NMR and Conventional Techniques," *Adv. Cem. Based Mater.*, vol. 1, pp. 67–76, 1993.

[102] R. M. E. Valckenborg, "Pore water distribution in mortar during drying as determined by NMR," *Mater. Struct.*, vol. 34, no. 244, pp. 599–604, 2005.

[103] V. Kocaba, "MC-RTN Procedure for mixing of cement pastes," 2007.

[104] A. C. A. Muller, "Personal comunnication - Mixing cement paste with addition of silica fume," 2012.

[105] R. M. Kowalczyk, A. M. Gajewicz, and P. J. McDonald, "The mechanism of water–isopropanol exchange in cement pastes evidenced by NMR relaxometry," *RSC Adv.*, vol. 4, pp. 20709–20715, 2014.

[106] Y.-Q. Song, L. Venkataramanan, and L. Burcaw, "Determining the resolution of Laplace inversion spectrum," *J. Chem. Phys.*, vol. 122, pp. 104104–1–8, Mar. 2005.

[107] S. Godefroy, B. Ryland, and P. T. Callaghan, "2D Laplace Inversion Instruction Manual," Victoria University of Wellington, Wellington, 2008.

[108] B. Z. Dilnesa, "Application of Thermogravimetric Method in Cement Science," *http://www.empa.ch/plugin/template/empa/*/95268/---/l=1.*.

[109] E. Gallucci, X. Zhang, and K. L. Scrivener, "Effect of temperature on the microstructure of calcium silicate hydrate (C-S-H)," *Cem. Concr. Res.*, vol. 53, pp. 185–195, 2013.

[110] "http://www.metalpoweranalytical.com/moisture_sorption_analysis.htm," 2014..

[111] M. R. Boudry, "A simple conversion formula for type 'T' (copper-constantan) thermocouple readings," *J. Phys. E.*, vol. 9, pp. 1064–1065, 1976.

[112] A. Valori, "Characterisation of cementitious materials by ^{1}H NMR; PhD thesis," University of Surrey, 2009.

[113] R. F. Feldman, "Assessment of experimental evidence for models of hydrated portland cement," *Highw. Res. Rec.*, vol. 370, pp. 8–24, 1972.

[114] V. Baroghel-Bouny, "Water vapour sorption experiments on hardened cementitious materials Part I: Essential tool for analysis of hygral behaviour and its relation to pore structure," *Cem. Concr. Res.*, vol. 37, pp. 414–437, 2007.

[115] H. Chen, M. Wyrzykowski, K. L. Scrivener, and P. Lura, "Modeling of Internal Relative Humidity Evolution in Cement Patses at Early Age," in *Second International Conference on Microstructural-related Durability of Cementitious Composites*, April 2012, pp. 140–147.

[116] M. Geiker and T. Knudsen, "Chemical Shrinkage of Portland Cement Pastes," *Cem. Concr. Res.*, vol. 12, pp. 603–610, 1982.

[117] B. Lothenbach, F. Winnefeld, C. Alder, E. Wieland, and P. Lunk, "Effect of temperature on the pore solution, microstructure and hydration products of Portland cement pastes," *Cem. Concr. Res.*, vol. 37, pp. 483–491, 2007.

[118] M. Zajac, S. Garrault, and A. Nonat, "Effect of the hydration temperature on mechanical resistance of Portland cement mortar and paste," *Cem. Wapno Bet.*, vol. 2, pp. 68–75, 2007.

[119] K. O. Kjellsen, R. J. Detwiler, and O. E. Gjorv, "Pore Structure of Plain Cement Pastes Hydrated at Different Temperatures," *Cem. Concr. Res.*, vol. 20, pp. 927–933, 1990.

[120] K. O. Kjellsen, R. J. Detwiler, and O. E. Gjørv, "Development of microstructures in plain cement pastes hydrated at different temperatures," *Cem. Concr. Res.*, vol. 21, pp. 179–189, 1991.

[121] L. D. Mitchell and J. C. Margeson, "The effects of solvents on C–S–H as determined by thermal analysis," *J. Therm. Anal. Calorim.*, vol. 86, pp. 591–594, 2006.

[122] Q. Zhou and F. P. Glasser, "Thermal stability and decomposition mechanisms of ettringite at <120°C," *Cem. Concr. Res.*, vol. 31, pp. 1333–1339, 2001.

[123] C. Hall, P. Barnes, A. D. Billimore, A. C. Jupe, and X. Turrillas, "Thermal decomposition of ettringite $Ca_6[Al(OH)_6]_2(SO_4)_3 \cdot 26H_20$," *J. Chem. Soc. Faraday Trans.*, vol. 92, pp. 2125–2129, 1996.

[124] A. N. Christensen, T. R. Jensen, and J. C. Hanson, "Formation of ettringite, $Ca_6Al_2(SO_4)_3(OH)_{12} \cdot 26H_2O$, AFt, and monosulfate, $Ca_4Al_2O_6(SO_4) \cdot 14H_2O$, AFm-14, in hydrothermal hydration of Portland cement and of calcium aluminum oxide-calcium sulfate dihydrate mixtures studied by in situ synchrotron X-ray powder," *J. Solid State Chem.*, vol. 177, pp. 1944–1951, 2004.

[125] K. Krynicki, "Proton Spin-Lattice Relaxation in Pure Water Between 0°C and 100°C," *Physica*, vol. 32, pp. 167–178, 1966.

[126] H. J. Busscher, G. A. M. Kip, A. van Silfhout, and J. Arends, "Spreading Pressures of Water and n-Propanol on Polymer Surfaces," *J. Colloid Interface Sci.*, vol. 114, pp. 1–7, 1986.

[127] J. J. Thomas and H. M. Jennings, "Effects of D_2O and Mixing on the Early Hydration Kinetics of Tricalcium Silicate," *Chem. Mater.*, vol. 11, pp. 1907–1914, 1999.

[128] A. C. A. Muller, K. L. Scrivener, A. M. Gajewicz, and P. J. McDonald, "Densification of C-S-H measured by ^1H NMR Relaxometry," *J. Phys. Chem. C*, vol. 117, pp. 403–412, 2013.